FAST AND EFFICIENT SOLUTIONS OF MULTISCALE ELECTROMAGNETIC PROBLEMS

A DISSERTATION SUBMITTED TO
THE GRADUATE SCHOOL OF ENGINEERING AND SCIENCE
OF BILKENT UNIVERSITY
IN PARTIAL FULFILLMENT OF THE REQUIREMENTS FOR
THE DEGREE OF
DOCTOR OF PHILOSOPHY
IN
ELECTRICAL AND ELECTRONICS ENGINEERING

By
Bahram Khalichi
September 2020

Fast and Efficient Solutions of Multiscale Electromagnetic Problems
By Bahram Khalichi
September 2020

We certify that we have read this dissertation and that in our opinion it is fully adequate, in scope and in quality, as a dissertation for the degree of Doctor of Philosophy.

Vakur Behçet Ertürk(Advisor)

Özgür Salih Ergül(Co-Advisor)

Ekmel Özbay

Orhan Arıkan

Seyit Sencer Koç

Hatice Özlem Aydın Çivi

Approved for the Graduate School of Engineering and Science:

Ezhan Karaşan
Director of the Graduate School

ABSTRACT

FAST AND EFFICIENT SOLUTIONS OF MULTISCALE ELECTROMAGNETIC PROBLEMS

Bahram Khalichi
Ph.D. in Electrical and Electronics Engineering
Advisor: Vakur Behçet Ertürk
Co-Advisor: Özgür Salih Ergül
September 2020

Frequency-domain surface integral equations (SIEs) used together with the method of moments (MoM), and/or its accelerated versions, such as the multilevel fast multipole algorithm (MLFMA), are usually the most promising choices in solving electromagnetic problems including perfect electric conductors (PEC). However, the electric-field integral equation (EFIE) (as one of the most popular SIEs) is susceptible to the well-known low-frequency (LF) breakdown problem, which prohibits its use at low frequencies and/or dense discretizations. Although the magnetic-field integral equation (MFIE) is less affected from the LF-breakdown, it is usually criticized for being less accurate, and being applicable only to closed surfaces. In addition, the conventional MLFMA which enables the solution of electrically large problems with an extremely large number of unknowns by reducing the computational complexity for memory requirements and CPU time suffers from the LF breakdown when applied to the geometries with electrically small features.

We proposed a mixed-form MLFMA and incorporated it with the recently introduced potential integral equations (PIEs), which are immune to the LF-breakdown problem, to obtain an efficient and accurate broadband solver to analyze electromagnetic scattering/radiation problems from PEC surfaces over a wide frequency range. The mixed-form MLFMA uses the conventional MLFMA at middle/high frequencies and the nondirective stable plane wave MLFMA (NSPWMLFMA) at low frequencies (i.e., electrically small boxes). We demonstrated that the proposed algorithm is accurate enough to be applied for both open and closed surfaces. In addition, we modified and utilized incomplete tree structures in conjunction with the mixed-form MLFMA to have a novel broadband incomplete-leaf (IL) MLFMA (IL-MLFMA) for the fast and accurate solution of multiscale scattering/radiation problems using PIEs. The proposed method is capable of handling multiscale electromagnetic problems containing fine

geometrical details in their structures. The algorithm is population based and deploys a nonuniform clustering that enables to use deep levels safely and, when necessary, without compromising the accuracy, and hence the error is controllable. As a result, by using the proposed IL-MLFMA for PIEs (i) the efficiency is improved and (ii) the memory requirements are significantly reduced (order of magnitude) while the accuracy is maintained.

Keywords: Potential integral equations, multilevel fast multipole algorithm, low-frequency breakdown, nondirective stable plane wave MLFMA, incomplete tree, multiscale electromagnetic problems.

ÖZET

ÇOK ÖLÇEKLİ ELEKTROMANYETİK PROBLEMLERİN HIZLI VE VERİMLİ ÇÖZÜMÜ

Bahram Khalichi
Elektrik-Elektronik Mühendisliği, Doktora
Tez Danışmanı: Vakur Behçet Ertürk
İkinci Tez Danışmanı: Özgür Salih Ergül
Eylul 2020

Frekans bölgesindeki yüzey integral denklemleriyle (YİD) beraber kullanılan momentler metodu (MM) ve/veya bunun hızlandırılmış sürümü olan çok seviyeli hızlı çokkutup yöntemi (ÇSHÇY), mükemmel elektrik iletkenleri de dahil olmak üzere elektromanyetik problemlerin çözümünde genellikle en umut verici seçeneklerdir. Fakat, elektrik alan integral denklemi (EAİD) (en popüler YİD'lerden biri), iyi bilinen düşük frekans bozulması problemine karşı hassas olduğundan düşük frekanslarda ve/veya yoğun ayrıklaştırmalarda kullanımı kısıtlanmaktadır. Manyetik alan integral denklemleri (MAİD) düşük frekans bozulmasından daha az etkilenmesine rağmen, daha az isabetli olmasından ve sadece kapalı yüzeylere uygulanabilirliğinden dolayı genellikle eleştirilmektedir. Buna ek olarak, elektriksel boyutu yüksek ve çok sayıda bilinmeyen içeren problemlerin çözümündeki hesaplama karmaşıklığını hem hafıza hem de zaman için azaltan geleneksel ÇSHÇY, küçük parçalardan oluşan geometrilere uygulandığında düşük frekans bozulmasından etkilenmektedir. önerilen karma ÇSHÇY'ye, son dönemlerde tanıtılan ve düşük frekans bozulmaları yaratmayan potansiyel integral denklemleri (PİD) dahil edilerek mükemmel elektrik iletkeni yüzeyler için geniş frekans aralığında elektromanyetik saçılım/yayınım problemlerini analiz etmek için kullanılan verimli ve isabetli geniş bantlı çözücü elde edilmiştir. Karma ÇSHÇY, orta ve yüksek frekanslarda geleneksel ÇSHÇY kullanırken, düşük frekanslarda (başka bir deyişle elektriksel olarak küçük kutularda) yönsüz sabit düzlem dalgası ÇSHÇY (YSDDÇSHÇY) kullanmaktadır. önerilen algoritmanın hem açık hem de kapalı yüzeylerde uygulanabilecek kadar isabetli olduğu gösterilmiştir. Buna ek olarak, tamamlanmamış ağaç yapısı, karma ÇSHÇY ile birleştirilerek çok ölçekli saçılım/yayınım problemlerinin PİD kullanılarak hızlı ve isabetli çözümü için özgün geniş bantlı tamamlanmamış-yaprak (TY) ÇSHÇY (TY-ÇSHÇY)

elde edebilmiştir. önerilen yöntem, yapısında küçük detaylar içeren ölçekli elektromanyetik problemlerle başa çıkabilecek kapasiteye sahiptir. Bu algoritma popülasyona dayanmaktadır ve düzensiz kümeleme uygulamaktadır. Düzensiz kümeleme, derin seviyelerin güvenli ve gerektiğinde isabetlilikten ödün vermeden kullanımını sağladığı için hata kontrol edilebilirdir. Sonuç olarak, önerilen PİD için TY-ÇSHÇY kullanılarak (i) verim iyileştirilmiştir ve (ii) hafıza ihtiyacı, isabetlilik belirli bir düzeyde tutularak önemli ölçüde düşürülmüştür.

Anahtar sözcükler: Potansiyel integral denklemleri, çok seviyeli hızlı çokkutup yöntemi, düşük frekans bozulması, yönsüz sabit düzlem dalgası ÇSHÇY, tamamlanmamış ağaç, ölçekli elektromanyetik problemler.

Acknowledgement

First and foremost, I would like to express my deepest gratitude to my supervisor, Prof. Vakur B. Ertürk for his endless supervision, support, encouragement, and patience during these years. I greatly appreciate his comments and ideas from which I have learned a lot. Additionally, I would like to appreciate my co-supervisor Prof. Özgür Ergül for his endless guidance, comments, and ideas. My supervisors have definitely been the most inspirational person in my educational life.

I am indebted to my PhD committee (TIK) members, Prof. Orhan Arıkan, Prof. Ayhan Altıntaş, and Prof. Sencer Koç who provided me with their precious suggestions during the past years. I also would like to thank Prof. Ekmel Özbay and Prof. Özlem Aydın Çivi for accepting to serve as jury members in my PhD thesis defense.

I would like to thank my friends and colleagues who create memorable episode of my life: Alireza Sadeghi Tarakameh, Mahsa Nasiri, Mahdi Shakiba Herfeh, Reza Babaloo, Ehsan Kazemivalipour, Amir Ghobadi, Sina Abedini Dereshgi, Maryam Salim, Mohammad Kazemi, Mohammad Kaveh, Laleh Eskandarian, Wiria Soltanpoor, Ali Maleki Gargari, Iman Marivani, Mohammadreza Mohaghegh Neyshabouri, Seçil Eda Doğan, Zeinab Eftekhari, Burak Özbey, Polat Goktaş. They all stood by me through the twists and turns of life.

Last but not least, I must express my very profound gratitude to my family: my beloved mother, my father whom I missed during my PhD, my brother and my sister, and at the end my love Fariba who has been my best friend during the past few years, and her love, great companionship and encouragements helped me get through this stage. Without their support, I wouldn't have gotten where I am. Thank you all.

Contents

1 Introduction **1**

1.1 Literature Review 5

1.1.1 Surface Integral Equations 5

1.1.2 FMM and LF problem of MLFMA 8

1.1.3 Fast Solutions of Multisacle Electromagnetic Problems . . 11

2 Basics of EM Theory **14**

2.1 Introduction 14

2.2 Maxwell's Equations 14

2.3 The Scalar Helmholtz Equation 18

2.4 Far-Zone Fields 21

3 Surface Integral Equations **22**

3.1 Introduction 22

3.2 Surface Equivalence Theorem 23

3.2.1 Physical Equivalence Theorem 24

3.2.2 Electric-field Integral Equation 26

3.2.3 Magnetic-field Integral Equation 27

3.2.4 Combined-field Integral Equation 28

3.2.5 Low-frequency Breakdown of EFIE 29

3.2.6 Inaccuracy Problem of MFIE 32

4 Potential Integral Equations **34**

4.1 Introduction 34

4.2 Derivation of Potential Integral Equations 34

4.2.1 Method of Moments 44

4.2.2 Discretization of Potential Integral Equations 47
4.2.3 Electromagnetic Excitation 51
4.2.4 Iterative Solvers and Condition Number 55
4.2.5 Numerical Results 58

5 Multilevel Fast Multipole Algorithm 62
5.1 Introduction and Concept 62
5.2 Basic Steps in MLFMA 65
5.2.1 Multipole Expansions of a Plane Wave 67
5.2.2 Addition Theorem 68
5.2.3 Diagonalization of the Free-Space Green's Function 69
5.2.4 Tree Structure and Stages of MLFMA 70
5.3 Fast Implementations of Potential Integral Equations 72
5.3.1 Low-frequency Breakdown of MLFMA 75

6 Broadband Solutions of Potential Integral Equations With Mixed-form MLFMA 76
6.1 Introduction 76
6.2 Nondirective Stable Plane Wave MLFMA (NSPWMLFMA) for PIEs 77
6.3 Preconditioning for PIEs solved via Mixed-Form MLFMA 83
6.4 Numerical Results 85

7 Solutions of Multiscale Electromagnetic Problems 92
7.1 Introduction 92
7.2 Implementations 93
7.3 Numerical Results 100

8 Conclusion and Future Work 113
8.1 Conclusion 113
8.2 Future Work 114

A 129

List of Figures

3.1 Arbitrarily-shaped conducting geometries. 23

3.2 (a) Actual sources $\boldsymbol{J}_1$ and $\boldsymbol{M}_1$ radiating fields $\boldsymbol{E}_1$ and $\boldsymbol{H}_1$ to the infinite medium with the constitutive parameters of μ_1 and ε_1. (b) The equivalent problem when the actual sources are replaced with the current densities over the imaginary surface. The equivalent current densities are radiating the same fields $\boldsymbol{E}_1$ and $\boldsymbol{H}_1$ outside the region and $\boldsymbol{E}$ and $\boldsymbol{H}$ inside the region. (c) Since the volume within S is not the region of interest, and the equivalent current densities are obtained using tangential components of both electric and magnetic fields, we can assume that $\boldsymbol{E}$ and $\boldsymbol{H}$ are zero (This is known as Love's equivalence principle). (d) The equivalent electric-current density is zero if we replace the region with an electric conductor. (e) The equivalent magnetic-current density is zero if we replace the region with a magnetic conductor. 24

3.3 Physical equivalence theorem. (a) A scattering problem (original problem) consisting of a PEC scatterer which is illuminated by incident fields $\boldsymbol{E}^{inc}$ and $\boldsymbol{H}^{inc}$. The incident fields are created by the electric and magnetic sources ($\boldsymbol{J}$ & $\boldsymbol{M}$) radiating into an infinite region. Presence of the scatterer creates scattered fields $\boldsymbol{E}^{scat}$ and $\boldsymbol{H}^{scat}$. The total fields outside the scatterer are the superposition of the incident fields and the scattered fields. (b) The equivalent problem can be defined by introducing equivalent surface currents ($\boldsymbol{J}_S$ & $\boldsymbol{M}_S$) over the boundary. These currents radiate in a homogeneous space and create $-\boldsymbol{E}^{inc}$ and $-\boldsymbol{H}^{inc}$ fields inside the object and $\boldsymbol{E}^{scat}$ and $\boldsymbol{H}^{scat}$ fields outside the object. 25

4.1 Geometry to obtain the surface PIEs. 35
4.2 Configuration of region and medium to obtain surface PIEs for a PEC scatterer. 40
4.3 (a) Triangular discretization of a sphere using various mesh sizes. (b) Modeling of a complicated benchmark object known as stealth airborne target Flamme with planar triangular meshes [5]. 46
4.4 An RWG function defined on a pair of triangles sharing an edge. . 47
4.5 Configuration of a Hertzian dipole at the origin and a Hertzian dipole radiating from its far zone. 52
4.6 An illustration of a delta-gap source defined on a pair of triangles. 55
4.7 Far-zone scattered electric-field result obtained via PIE/MoM, for the uniformly discretized PEC sphere illuminated by an x-polarized uniform plane wave propagating along the z-direction (a) at 6 GHz. (b) at 3 GHz. 60
4.8 Far-zone scattered electric-field result obtained via PIE/MoM, for the uniformly discretized PEC sphere illuminated by an x-polarized uniform plane wave propagating along the z-direction at different frequencies. 61

5.1 (a) A spherical object enclosed by a cubic box and recursive clustering based on dividing the box into eight identical subboxes. (b) Construction of a hierarchy of boxes called as tree structures. (c) A discretized sphere and (d) its corresponding clustering where the empty boxes are omitted. (e) Near-zone boxes colored in yellow and far-zone boxes colored in blue for a given testing box (in red) based on the one-box-buffer scheme. 64
5.2 Integration path for the equation given in (5.5b) [120]. 66
5.3 A schematic description of the diagonalized form of the free-space Green's function and calculation of interaction between a pair of RWG functions located at far boxes based on the one-box-buffer scheme. 71
5.4 Aggregation, translation, and disaggregation processes inside a typical MLFMA scenario [121]. 73

6.1 (a) Diagonal terms of near-field matrix ($\bar{\mathbf{\Gamma}}_{\boldsymbol{J},\boldsymbol{J}}$) which are used to construct the left preconditioner at level 2, (b) Block diagonal terms of near-field matrix ($\bar{\mathbf{\Gamma}}_{\boldsymbol{J},\boldsymbol{J}}$) which are used to construct the left preconditioner at level 2, (c) level 3, and (d) level 4 according to (6.18). 84

6.2 Far-zone scattered electric field results obtained from numerical and analytical solutions for a PEC sphere of diameter 10 cm (a) at 3 GHz and (b) 30 MHz. 86

6.3 Far-zone scattered electric field results obtained from numerical solutions for a PEC plate with edge size of 10 cm discretized with different mesh sizes including fine and coarse cases (a) at 3 GHz and (b) 3 MHz. 87

6.4 Matrix-vector multiplication times for both a PEC tilted plate and a PEC sphere at two different frequencies (3 GHz and 3 MHz for tilted PEC plate, and 3 GHz and 30 MHz for the PEC sphere). For the PEC tilted plate, the number of unknowns is increasing from 1960 to 511360 by refining the discretization from $\lambda/20$ to $\lambda/320$ at 3 GHz and from 1960 to 127680 by refining the discretization from $\lambda/20000$ to $\lambda/160000$ at 3 MHz. Minimum box sizes in the tree structures for 3 GHz and 3 MHz are $\lambda/256$ and $\lambda/32000$, respectively. For the PEC sphere, these numbers are as follows: the number of unknowns is increasing by refining the discretizations from 13405 ($l_\lambda = \lambda/30$) to 364865 ($l_\lambda = \lambda/150$) at 3 GHz, and from 3305 ($l_\lambda = \lambda/1400$) to 54365 ($l_\lambda = \lambda/5600$) at 30 MHz. Minimum box sizes in the tree structures for 3 GHz and 30 MHz are $\lambda/256$ and $\lambda/6400$, respectively. 88

6.5 RCS results obtained by using two different mesh sizes $l_\lambda = \lambda/100$ and $l_\lambda = \lambda/200$, which are corresponding to 23175 and 119175 unknowns at 600 MHz. The coarse and fine discretized objects are solved by using MoM and 8-level mixed-form MLFMA with approximate minimum box sizes of $\lambda/128$ in the tree structure. . . 89

6.6 Geometry of a mushroom-type structure. 90

6.7 Far-zone scattered electric field result obtained from 8-level mixed-form MLFMA solution of the PEC mushroom-type structure at 3 GHz. 90
6.8 Linear current distribution of the mushroom-type structure illuminated by a uniform plane wave polarized in x-direction. . . . 91

7.1 (a) 3-D view and corresponding (b) 2-D view of nonuniform clustering in incomplete-tree structure where overpopulated boxes require more divisions to reach the assigned population threshold (overpopulated (or OCBs) are colored with darker gray in the same level). 95
7.2 A typical 2-D incomplete-tree structure with recognized OCBs, TBs, and PBs [121]. 96
7.3 A pictorial example to illustrate (i) the parent TBs of RWG and pulse basis functions, and (ii) how their interactions are classified (i.e., near- or far-field interactions). 97
7.4 (a) 2-D view of a nonuniform clustering where the darker regions correspond to the denser discretizations. (b-d) Several representations of near-field and far-field boxes of different testing boxes colored in pink. 99
7.5 Geometry of nonuniformly discretized sphere with a multiscale factor of 100 possessing a dense discretization around the south pole. 101
7.6 (a) The geometry of PEC circular cone including the number of unknowns and mesh sizes for each colored region. (b) Far-zone scattered electric-field results obtained via PIE/MoM, PIE/mixed-form MLFMA and PIE/IL-MLFMA for the nonuniformly discretized PEC circular cone illuminated by an x-polarized uniform plane wave propagating along the z-direction at 1 GHz. . 104

7.7 Normalized electric-field intensities in dB on the x-z plane for the circular cone geometry with the plane-wave illumination at 1 GHz. The near-field results are obtained via (a) PIE/MoM, (b) PIE/IL-MLFMA with MBP of 50 (corresponding to 9 active levels), (c) 5-level PIE/mixed-form MLFMA, and (d) 6-level PIE/mixed-form MLFMA. 106

7.8 Far-zone scattered electric-field results obtained by using PIE/MoM, PIE/mixed-form MLFMA and PIE/IL-MLFMA for the nonuniformly discretized NASA Almond geometry illuminated by two Hertzian dipoles at 5 GHz. 107

7.9 (a) Absolute value of the normalized current distributions over the nouniformly discretized NASA Almond geometry at 5 GHz excited by a pair of Hertzian Dipoles. The results are obtained by using (a) PIE/MoM, (b) PIE/IL-MLFMA, (c) 5-level PIE/mixed-form MLFMA, and (d) 6-level PIE/mixed-form MLFMA. 108

7.10 (a) A cavity-backed slot antenna based on the SIW technology excited by a Hertzian dipole located in the middle of the structure. Absolute value of the normalized current distributions on the (b) top and (c) bottom surfaces obtained via PIE/IL-MLFMA, and the same current distributions on the (d) top and (e) bottom surfaces of the antenna obtained by using HFSS at 9 GHz. (f) Normalized radiation patterns with respect to θ when $\phi = 0$, and π (i.e., over x-z plane) obtained via PIE/IL-MLFMA and FEM. 109

7.11 Normalized radiation patterns with respect to θ when $\phi = 0$, and π (i.e., over x-z plane) obtained via PIE/IL-MLFMA and FEM. . 110

7.12 (a) A nonuniformly discretized $16\lambda \times 16\lambda \times 3.8\lambda$ airplane illuminated by a uniform plane wave propagating parallel to the x-z plane (with an angle of incidence 100° with respect to the z-axis) at 600 MHz. (b) RCS (in dBsm) patterns of this airplane at x-z, y-z and x-y planes. 111

List of Tables

4.1 Information for a uniformly discretized PEC sphere with the diameter of 0.1 m, which is illuminated by an x-polarized uniform plane wave propagating along the z-direction at different frequencies. 59

6.1 Number of iterations based on the residual error 10^{-3} for the solution of the PEC sphere problem. 83

7.1 Statistics for scattering simulations of a nonuniform discretized sphere with diameter of 10 cm and multiscale factor of 100 illuminated by an x-polarized uniform plane wave propagating along the z-direction at 3 GHz. Different number of RWGs populations (corresponding to the different simulation levels) are chosen for the simulation with error tolerance of 1e-4 103

List of Abbreviations

ACE:	Accelerated Cartesian Expansion
A-EFIE:	Augmented electric-field integral equation
CCIE	Current and charge integral equation
CEM:	Computational electromagnetics
CFIE:	Combined-field integral equation
CP:	Calderón Preconditioner
EFIE:	Electric-field integral equation
FFT:	Fast Fourier transform
FIPWA:	Fast inhomogeneous plane wave algorithm
FMM:	Fast multipole method
GMRES:	Generalized minimal residual (method)
H-MLFMA:	Hierarchical MLFMA
IE:	Integral equation
IL:	Incomplete leaf
IL-MLFMA:	Incomplete-leaf multilevel fast multipole algorithm
ILU:	Incomplete lower upper decomposition
LF:	Low frequency
LF-MLFMA:	Low-frequency multilevel fast multipole algorithm
MBP:	maximum box population

MFIE:	Magnetic-field integral equation
MLFMA:	Multilevel fast multipole algorithm
MoM:	Method of moments
MVM:	Matrix-vector multiplication
NSPWMLFMA:	Nondirective stable plane-wave MLFMA
OCBs:	Overcrowded boxes
PBs:	Pruned boxes
PEC:	Perfect electric conductor
PIEs:	Potential integral equations
RMS:	Root mean square
RWG:	Rao-Wilton-Glisson (function)
SIE:	Surface integral equation
SPIE:	Separated potential integral equation
TBs:	Truncated boxes
UMLFMA:	uniform multilevel fast multipole algorithm

Chapter 1

Introduction

Maxwell's equations have been proven to be valid and successful in the description of macroscopic electromagnetic fields [1, 2]. However, analytical solutions to Maxwell's equations can be applied only to simple geometries. Nowadays, thanks to computer technology, computational electromagnetics (CEM) become more intriguing and increasingly important for modern applications and researches such as scattering, radiation, and guiding problems [3–8]. Full-wave numerical methods in CEM are mainly categorized into integral-equation (IE) [3–6] and partial differential-equation (PDE) [7,8] methods based on different ways of discretization of Maxwell's equations. The main difference here is that IE-based methods solve Maxwell's equations formulated as IEs for equivalent sources, while PDE-based methods such as the finite-element method and the method of finite difference directly solve Maxwell's equations in differential form. Unlike PDE methods that employ volumetric discretizations of the entire space by considering radiation boundary conditions, IE methods have the advantage of surface discretizations of homogeneous problems (less number of unknowns than volumetric discretizations) leading to surface integral equations (SIEs) that inherently satisfy the radiation boundary condition. SIEs only consider the boundaries of the different regions and take into account the equivalent sources on the boundaries that lead to less number of unknowns. Therefore, they are very useful and efficient in providing solutions for many open-region scattering and radiation problems.

Different SIEs such as the Electric-Field Integral Equation (EFIE) and the Magnetic-Field Integral Equation (MFIE) are widely utilized to solve a large variety of electromagnetic problems [3–6]. However, EFIE is susceptible to the well-known low-frequency (LF) breakdown problem, which prohibits its use at lower frequencies and/or dense discretizations [5, 9–11]. Although MFIE is less affected by the LF breakdown, it is usually criticized for being less accurate compared to its counterpart EFIE, and it is applied only to closed surfaces [5, 12–17]. Consequently, one of the challenging problems in IEs is to come up with well-behaving or well-conditioned formulations that can be used from zero to microwave frequencies.

IEs cannot be solved analytically for most electromagnetic problems. Therefore, computational methods such as the method of moments (MoM) can be employed to discretize and convert IEs into a linear system of equations and then to obtain a solution [3,4]. Apart from the versatility and accuracy of MoM in the solutions of IEs, it yields a dense matrix equation with an $\mathcal{O}(N^2)$ complexity for memory consumption where N is the number of unknowns. The resultant matrix equation can be solved directly or iteratively which requires $\mathcal{O}(N^3)$ operations for direct solutions (e.g., Gaussian elimination or the Lower Upper Decomposition), and $\mathcal{O}(N^2)$ operations for computing matrix-vector multiplication (MVM) at each iteration when an iterative solution is sought. As a results, IEs suffers from high computational complexity regarding the memory consumption and CPU time [5, 6].

To enable the solution of extremely large and densely discretized electromagnetic problems, Fast Multipole Method (FMM) was presented and developed [5, 6, 18–24], which accelerate the MVMs with a complexity of $\mathcal{O}(N^{3/2})$. The recursive clustering idea of FMM in combination with different decomposition representations of the free-space Green's function was developed to obtain the Multilevel Fast multipole Algorithm (MLFMA) [5, 6, 25–28] with a computational complexity of $\mathcal{O}(N\log N)$. MLFMA computes the interactions between basis (radiating) and testing (receiving) functions in a group-by-group manner and a recursive three-stage fashion called as aggregation, translation, and disaggregation stages. This is accomplished by dividing the geometry of

the problem into a hierarchy of boxes (called tree structure) and invoking the diagonalized form of the free-space Green's function (propagating plane-wave decomposition). However, because of the diagonalization, MLFMA breaks down at lower frequencies due to numerical instabilities [29,30]. It occurs when the box sizes are smaller than a certain critical electrical size (usually smaller than $\lambda/8$) which does not allow us to efficiently simulate electromagnetic problems with considerable subwavelength geometrical details.

In this thesis, considering the above-mentioned advantages and disadvantages of SIEs in solutions of electromagnetic problems, our objective is to introduce a state-of-the-art algorithm and to develop a broadband solver that enables us to investigate real-life multiscale problems including open and closed surfaces in an efficient and accurate way. Considering the fact that rigorous analysis of multiscale geometries in a wide frequency range is one of the most challenging issues in CEM, such an algorithm and a solver based on that will certainly meet the increasing demands coming from both industry and academia. This algorithm will have the capability to be applied to a broad range of applications such as measuring radar cross-section (RCS) [2], design and analysis of antennas and microwave components [2, 31, 32], biomedical applications [33–37], specific absorption rate prediction [38–44], and coil analysis in the context of magnetic resonance imaging (MRI) [45–48], etc.

As the first part of this thesis, a mixed-form MLFMA was incorporated with the Potential Integral Equations (PIEs, $\boldsymbol{A} - \Phi$ formulation [49–52]) to obtain an efficient and accurate solver to solve electromagnetic scattering from perfect electric conductors (PECs) over a wide frequency range. PIEs are chosen since they do not suffer from the LF inaccuracy and they are applicable to both open and closed surfaces. In addition, the mixed-form MLFMA uses the conventional MLFMA at middle/high frequencies and the nondirective stable plane wave MLFMA (NSPWMLFMA) [53–56] at low frequencies (i.e., electrically small boxes: Box size $= B_\lambda < \lambda/8$). Although there are many different studies available in the literature to treat the LF breakdown of MLFMA [29, 57–64], NSPWMLFMA is preferred due to its error controllability and suitability for being combined with the conventional MLFMA to obtain a robust broadband

mixed-form MLFMA solver for $\boldsymbol{A} - \Phi$ formulations. The proposed method can be applied to large variety of electromagnetic problems including both open and closed surfaces.

Despite stable computations of near-field and far-field interactions via PIEs and broadband mixed-from MLFMA, nonuniform discretizations that are typical in multiscale problems bring additional challenges when standard tree structures with fixed-size boxes and regular divisions of parent boxes into subboxes are employed [65–72]. In other words, deploying fixed-size boxes in the tree structures of the proposed broadband solver brings only two inefficient/inaccurate options.

- Large boxes with a limited number of levels can be utilized to maintain accuracy. However, the solver becomes inefficient due to nonuniform distributions of the unknowns. In highly dense regions, there will be many triangles in relatively large boxes resulting in an $\mathcal{O}(N^2)$ complexity.
- Extended numbers of levels can be utilized to reach small numbers of unknowns in leaf-level boxes. However, the solver becomes inaccurate since many leaf-level boxes cannot enclose relatively larger discretization elements especially in the coarsely discretized regions.

Therefore, in the second part of the thesis, we significantly modified the recently introduced incomplete tree structures (for MFIE) [73–76], and used them in conjunction with the mixed-form MLFMA [77, 78] for PIEs to have a truly broadband and an accurate electromagnetic solver for addressing real-life multiscale electromagnetic problems. The proposed mixed-from MLFMA with an incomplete tree structure [79, 80], referred to as incomplete-leaf (IL) MLFMA for the rest of the thesis, is population-based and free of the above-mentioned issues for multiscale problems due to using variable box sizes. The algorithm deploys nonuniform clustering where the required numbers of levels are determined based on a predetermined box populations. The modified IL-MLFMA for PIEs can handle challenging discretizations and it can be one of the most powerful electromagnetic solvers for PEC objects with open and closed geometries to meet

the requirements of a broad range of applications from scattering problems to biomedical applications.

1.1 Literature Review

1.1.1 Surface Integral Equations

Common SIEs such as EFIE and MFIE are usually utilized to solve a large variety of conducting and homogeneous problems due to only surface discretization instead of the entire space containing the problem [3, 4, 81]. EFIE is applicable to both open and closed surfaces, and it can handle multiply connected (toroidal) geometries unlike MFIE [17, 82]. It can also be combined with MFIE giving rise to the Combined-Field Integral Equation (CFIE), which is free from spurious-resonance solution [4, 81]. However, the numerical solution of EFIE suffers from the LF breakdown, an ill-conditioning phenomenon caused by a dense discretization with respect to the wavelength or by the weak coupling of the electric and magnetic fields near zero frequencies [9–11]. In other words, EFIE suffers from the LF breakdown when the electrical size of the object is much smaller than the wavelength (i.e., the object requires fine discretizations to capture electrically small geometrical features). From the mathematical point of view, the reason behind the LF breakdown of EFIE is due to the finite machine precision and poor frequency scaling in the representation of the EFIE formulation, in which the magnetic vector potential term (contribution of the current) is in the order of $\mathcal{O}(\omega)$ and the scalar potential term (contribution of charge) is in the order of $\mathcal{O}(\frac{1}{\omega})$, where ω is the angular frequency ($\omega = 2\pi f$, f : frequency). Therefore, in the numerical solution of EFIE at low frequencies, the contribution coming from the magnetic vector potential to the resultant impedance matrix is significantly smaller than the contribution coming from the scalar potential. However, the contribution of the magnetic vector potential during the numerical process can be as important as the contribution of the scalar potential. This loss of contribution from the magnetic vector potential

makes the solution inaccurate. Furthermore, the scalar potential part has a null space because of its divergence operator [9] and when the contribution of the magnetic vector potential is lost, the resultant impedance matrix is nearly singular and difficult to invert at low frequencies. Since MFIE cannot be replaced with EFIE due to its less accuracy and limited applications to closed surfaces [12–17], one of the challenging problems is to come up with a well-behaving (i.e., well-conditioned) SIE which can be used from zero to microwave frequencies. In majority of the established works, the objective is to extend the validity of IEs to low frequencies [83–87]. This can be accomplished by changing the EFIE system to a different one that is solvable.

One of the most popular approaches to solve the LF-breakdown problem of EFIE is the loop-tree/loop-star decomposition method [83, 84]. In this approach, the current will be decomposed into its solenoidal (divergence-free) and irrotational (curl-free) components. Loop and star basis functions are utilized to expand the solenoidal and irrotational components of the current on the surface of the scatterer, respectively. Therefore, by using higher-order basis functions, the contribution of the vector potential is separated from the scalar potential and the instability of EFIE at low frequencies can be solved. However, finding the global loops is a kind of unintentionally created limitation for the loop-tree/loop-star decomposition method. The difficulty of finding global loops was solved by using the projection method in [82]. Apart from this problem, representations in terms of higher-order basis functions are improper at higher frequencies. It means that this method is not efficient within a broad frequency region.

Another approach is based on using the current and the charge as separate unknowns which is known as a Current and Charge Integral Equation (CCIE) [88, 89]. This stable, broadband and second kind Fredholm surface integral equation can be applied to composite metallic and dielectric objects. However, CCIE may suffer from inaccuracies at very low frequencies [9] and topological LF breakdown occurs in multiply connected domains [17].

Similar to CCIE, Augmented Electric-Field Integral Equation (A-EFIE) introduces charges as additional unknowns and employs the continuity equation

to solve the LF-breakdown problem [90–92]. Introducing new unknowns cause separation of the current and the charge or equivalently vector and scalar potentials from each other. The advantage of A-EFIE compared to the loop-tree/loop-star decomposition method is achieving the LF stability without searching for loop-tree/loop-star basis functions and can be easily integrated into the existing MoM solvers. But still, in both CCIE and A-EFIE, only solenoidal current is solved at low frequencies due to the decoupling of the current and charge. Therefore, more different applications are required to be examined to show the accuracy of these methods [9]. For instance, topological LF breakdown and plane wave scattering are investigated for A-EFIE in [91]. They utilized perturbation method with A-EFIE to retrieve small currents with high accuracy when the vector potential contribution is negligible.

Calderón Preconditioner (CP) based methods form another choice for addressing the LF-breakdown problem of EFIE [17,82,86,87,92]. Using CP based methods results in a well-conditioned second kind Fredholm integral equation and reduces the number of required iterations in an iterative solver. However, as a disadvantage claimed in [9], this method solves a modified system of equations rather than the original problem. This causes an unexpected problem such as independency of current distribution from frequency at very low frequencies, resulting in a large error in the far-field computations [9]. Inaccuracy of CP-EFIE was investigated in [87] and similar to A-EFIE, the accuracy of the calculated current increases by using perturbation methods. CP-EFIE does not include charge as an additional unknown which makes it more advantageous in comparison with A-EFIE. But still, topological LF breakdown is a problem and more complicated objects should be investigated to find the accuracy of CP based methods [82].

Separated Potential Integral Equation (SPIE), based on the separation of vector and scalar potentials, is another approach for circumventing the LF-breakdown problem [93]. A modified version of this method can be obtained by applying charge neutrality and creating an augmented matrix. According to [93], it shows better performance in terms of convergence and condition number in comparison to A-EFIE.

The recently introduced PIEs [49] by Prof. Chew's research group can be used to solve electromagnetic problems in a broad spectrum of frequencies involving the LF regime [49–52,77,78,94–96]. PIEs are derived by using the surface equivalence theorem and by satisfying the boundary conditions on the scalar potential (Φ) and the tangential component of the magnetic vector potential ($\hat{\boldsymbol{n}} \times \boldsymbol{A}$) instead of the tangential components of the electric ($\hat{\boldsymbol{n}} \times \boldsymbol{E}$) and magnetic fields ($\hat{\boldsymbol{n}} \times \boldsymbol{H}$). This method can be one of the most promising choices for solving electromagnetic problems in a wide frequency regime, since it does not suffer from LF inaccuracies and it is applicable to both open and closed surfaces.

1.1.2 FMM and LF problem of MLFMA

Solution of SIEs using MoM leads to matrix equations where an efficient solution in terms of computational complexity and memory requirement can be achieved by using FMM and its multilevel version MLFMA [5,6,18–24]. For this purpose, factorization and diagonalization of the free-space scalar Green's function are utilized together with the clustering idea to accelerate the MVMs in an iterative solver which enables MLFMA to solve larger problems with a computational complexity of $\mathcal{O}(N\log N)$ [5, 6, 25–28]. In conventional implementations of MLFMA, the clustering idea (called tree structure) is constructed by placing the whole object in a cubic box and recursively dividing the box (called parent box) into eight identical subboxes (called child boxes). Only nonempty boxes are considered to be divided into subboxes and after the division process, empty subboxes are omitted. Clustering idea and the diagonalization/factorization of the free-space Green's function cause to calculate far-field interactions among the separated radiating (basis) and receiving (testing) elements in a group-by-group manner consisting of three stages, called aggregation, translation, and disaggregation [5,6].

In comparison to the factorization of the free-space Green's function where the multipole representation is used, the diagonalization converts the spherical waves into plane waves (represents the addition theorem [1,2] in terms of plane waves

instead of multipoles) and makes MLFMA more efficient in solving large scale electromagnetic problems at intermediate and high frequencies. However, due to the diagonalization, MLFMA suffers from the LF breakdown which does not allow us to efficiently simulate problems containing considerable subwavelength geometrical details that requires electrically small boxes in the tree structure of MLFMA. It means that dividing boxes into arbitrarily small subboxes ($B_\lambda < \lambda/8$) is not feasible [29, 30]. Although MLFMA with multipole representation is stable at low frequencies due to the nondiagonal translation, it is very slow in the intermediate- and high-frequency regions. Therefore, the requirement for solving scattering/radiation problems with a large number of unknowns in a broad frequency band is to overcome the LF breakdown of MLFMA.

The LF breakdown of MLFMA can be explained as follows; in the standard addition theorem used in FMM (by considering $e^{-i\omega t}$ time convention), the multiplication of the first kind spherical Bessel and Hankel functions in the translation operator balances each other, in the particular scenario, the value of the Bessel function approaches zero when the argument of the Bessel function becomes small, and hence for the same argument, the value of the Hankel function becomes very large. Consequently, their product can remain bounded in the double-precision arithmetic platform [5]. Unfortunately, this phenomenon becomes impossible when the plane-wave expansion in MLFMA is utilized instead of multipole expansion despite the fact that using infinite precision can solve the LF breakdown of MLFMA [97–99]. In common, there are two approaches to circumvent the LF breakdown of MLFMA: 1) Spectral representation of the free-space Green's function. 2) Multipole representation of the free-space Green's function.

A method called as fast inhomogeneous plane wave algorithm (FIPWA) which is in the context of the first approach is one of the developed methods with diagonal translations to solve the LF breakdown of MLFMA by considering both propagating and evanescent waves [57, 59, 61, 62]. Since the method is based on the spectral representation of the free-space Green's function, it has a drawback that six different expansions of the Green's function in six different directions must be used to cover all translation directions in the entire space.

Spectral representation of the free-space Green's function with sampling the evanescent part using the generalized Gaussian quadrature rule is presented in [57]. The method is inefficient at higher frequencies due to the use of multipole series for the aggregation and the disaggregation stages. Spectral representation of the free-space Green's function with sampling the evanescent part using less efficient quadrature is used in [59] to overcome the LF breakdown. To improve the efficiency of the method at higher levels, evanescent waves are partially or fully extrapolated from the propagating waves based on the electrical size of the cubes. Darve and Have solved the LF breakdown of MLFMA [61] by using the spectral representation of the free-space Green's function where they utilized spherical harmonics and Singular Value Decomposition (SVD) method in propagating and evanescent parts, respectively. Wallen and Sarvas utilized the spectral representation of the free-space Green's function where they implemented a fast Fourier transform-based approach in propagating part and six expansions to cover the entire space for the evanescent part [62].

All above-mentioned methods differ significantly in their numerical implementations and require new interpolation/anterpolation for their multilevel implementations. But still, as stated in [67], at high frequencies MLFMA should be used instead of the method based on the spectral representation of the Green's function. Therefore, making a bridge between the plane and partial wave expansions in the high- and low-frequency regimes adds an additional cost to the system. Therefore, it will be more valuable to extend the validity range of MLFMA to low frequencies.

In the second category, multipole decomposition of the free-space Green's function is exploited to alleviate the LF breakdown problem of MLFMA. However, in these methods, nondiagonal translations lead to a rapidly increasing computational cost in the intermediate and high-frequency regimes [22–24, 58].

New approaches using alternative expansions and decompositions are also available in the literature for stable implementation of MLFMA at low frequencies. Among them, LF-MLFMA with suitable scaling factors was introduced by Chew [58] that ensures stable computations at low frequencies.

However, later on, it was demonstrated that this approach is not suitable for multiscale problems. Moreover, uniform MLFMA (UMLFMA) was proposed by Xuan et al [62, 100]. This method unlike the previous approaches, shifts the integration path into a complex plane instead of using the spectral representation and scaling factors. This direction-independent method uses numerically constructed translation operators to solve the LF breakdown of MLFMA. Unfortunately, this method is claimed to be poorly error-controllable [53].

Bogaert solved the LF-breakdown problem of the traditional MLFMA by proposing Nondirective Stable Plane Wave MLFMA (NSPWMLFMA), a broadband algorithm yielded by deforming the integration path of θ component to the complex plane to consider the effects of the evanescent waves [53–55]. For this purpose, the addition theorem is manipulated to construct a numerically stable translation operator along the z direction in a closed-form representation by calculating Fourier series expansions for the θ component. This is the most significant advantage of NSPWMLFMA in comparison to UMLFMA where the translation operators are constructed numerically. By deforming the integration path into the complex plane, evanescent waves are taken into account and then the LF-breakdown problem of MLFMA is solved by normalizing the Fourier coefficients which are now dependent on spherical Hankel and real exponential functions. NSPWMLFMA can be combined with the conventional MLFMA easily which makes NSPWMLFMA as a promising candidate for broadband applications. However, the only difficulty of NSPWMLFMA is the dependency of the translation operator on the directions. However, this problem is solved by utilizing the QR-decomposition method [53, 56].

1.1.3 Fast Solutions of Multisacle Electromagnetic Problems

In fact, we want a truly broadband and an accurate electromagnetic solver for multiscale geometries. Therefore, capturing the fine but important features of geometries requires nonuniform discretization [64, 101–106]. Moreover, uniform

discretization of such kind of structures leads to very tiny triangular meshes which increases the required number of unknowns tremendously. However, deploying fixed-size boxes without a multiscale construction of the tree structure in the broadband MLFMA solvers leads to the aforementioned two inefficient and/or inaccurate options for the solution of real-life multiscale electromagnetic problems. Accordingly, hierarchical MLFMA (H-MLFMA) has been proposed for the solution of multiscale problems in [107]. It benefits from two distinct types of basis functions called plane-wave and skeleton basis functions for propagating and evanescent waves, respectively. These different basis functions are based on the electrical size of the elements. However, using two distinct types of basis functions is a kind of unintentionally created limitation for the implementation of H-MLFMA-based solvers.

The concept of using a simple hybrid tree structure with only two different box sizes at the leaf level was proposed for multiscale problems in [72]. Vikram et. al., developed a broadband MLFMA with nonuniform clustering for multiscale geometries. The algorithm ensures that the number of unknowns per leaf-level boxes is approximately the same [68–71]. This method was developed as a hybrid scheme by combining Accelerated Cartesian Expansion (ACE) with FMM for multiscale problems, which requires transition level between them. In this method, Cartesian harmonics are used as an equivalent form of the spherical harmonics at low frequency. Far apart from its accuracy, the method cannot be easily combined with existing MLFMA solvers which decreases the efficiency of utilizing this method.

Although the nonuniform clustering and the efficient organization of near- and far-field boxes can provide accurate and efficient solutions for real-life multiscale problems and lead to benefit from the true power of broadband MLFMA [73–76], these issues have not been considered in sufficient depth until a broadband MLFMA (called as IL-MLFMA) with an incomplete tree structure was introduced by our research group for MFIE. To construct a population-based incomplete tree structure, we first define a predetermined threshold that gives us the allowed maximum number of unknowns in a box, call it maximum box population (MBP), and then we define three kinds of boxes based on the predetermined

threshold. The defined boxes are; overcrowded boxes, truncated boxes, and pruned boxes. Overcrowded boxes contain more or equal number of unknowns than the predetermined threshold and those are the ones that are divided into subboxes. Truncated boxes contain fewer number of unknowns than the predetermined threshold and pruned boxes are the boxes that they would exist if the tree structure were complete. In contrast to available approaches exploited to attack multiscale problems, IL-MLFMA can readily solve nonuniform discretized objects with a high ratio of multiscale factor and it can be modified to be combined with the other existence MLFMA solvers without any limitations.

The organization of this dissertation is as follows: In chapter 2, we provide the fundamentals of electromagnetic theory. In chapter 3, we briefly review different types of SIEs and their corresponding properties. We proceed by introducing recently developed PIEs in chapter 4, where the derivation and implementation are given. Chapter 5 covers the conventional MLFMA, and chapter 6 presents our proposed broadband solver based on PIEs accelerated by mixed-form MLFMA. In chapter 7, a novel incomplete tree structure for the solution of multiscale electromagnetic problems using PIEs is proposed. Finally in chapter 8, we have the conclusion of the dissertation.

Chapter 2

Basics of EM Theory

2.1 Introduction

Maxwell's equations as the foundation of classical electromagnetism have been proven to be valid and successful in the description of macroscopic electromagnetic fields. The analytical solutions of Maxwell's equations have been derived and scrutinized in the literature for simple geometries [1, 2]. In this chapter, in order to have a coherent notation as well as provide a solid foundation for the rest of the thesis, the analytical solutions of Maxwell's equations in an infinitely large, homogeneous, isotropic medium will be derived and discussed. The solution will be provided in the frequency domain. An $e^{-i\omega t}$ time convention, where $\omega = 2\pi f$ with f being the operating frequency, is assumed and suppressed throughout this thesis.

2.2 Maxwell's Equations

Maxwell's equations in the frequency domain can be written as

$$\nabla \times \boldsymbol{E}(\boldsymbol{r}) = i\omega \boldsymbol{B}(\boldsymbol{r}) - \boldsymbol{M}(\boldsymbol{r}) \tag{2.1a}$$

$$\nabla \times \boldsymbol{H}(\boldsymbol{r}) = -i\omega \boldsymbol{D}(\boldsymbol{r}) + \boldsymbol{J}(\boldsymbol{r}) \tag{2.1b}$$

$$\nabla \cdot \boldsymbol{D}(\boldsymbol{r}) = \rho_e(\boldsymbol{r}) \tag{2.1c}$$

$$\nabla \cdot \boldsymbol{B}(\boldsymbol{r}) = \rho_m(\boldsymbol{r}). \tag{2.1d}$$

In (2.1a)-(2.1d), as first-order partial coupled differential equations, $\boldsymbol{r}$ is the position vector, ε (permittivity) and μ (permeability) are the constitutive parameters of the medium, $\boldsymbol{J}(\boldsymbol{r})$ and $\rho_e(\boldsymbol{r})$ are the electric-current and electric-charge densities, respectively. In addition, $\boldsymbol{M}(\boldsymbol{r})$ and $\rho_m(\boldsymbol{r})$ are the magnetic-current and magnetic-charge densities introduced by applying the equivalence theorem on dielectric objects, respectively, $\boldsymbol{E}(\boldsymbol{r})$ and $\boldsymbol{H}(\boldsymbol{r})$ are the electric and magnetic fields, while $\boldsymbol{D}(\boldsymbol{r})$ and $\boldsymbol{B}(\boldsymbol{r})$ are the electric-flux (displacement vector) and magnetic-flux densities, respectively. The coupling of electric and magnetic fields with each other in the curl equations, known as Faraday's law of induction (2.1a) and Maxwell-Ampere's law (2.1b). The constitutive relations inside a linear, isotropic, and homogeneous medium (known as a simple medium) are given by

$$\boldsymbol{D}(\boldsymbol{r}) = \varepsilon \boldsymbol{E}(\boldsymbol{r}) \tag{2.2a}$$

$$\boldsymbol{B}(\boldsymbol{r}) = \mu \boldsymbol{H}(\boldsymbol{r}). \tag{2.2b}$$

It is possible to eliminate $\boldsymbol{D}(\boldsymbol{r})$ and $\boldsymbol{B}(\boldsymbol{r})$ from the curl equations in (2.1) by using constitutive equations (2.2). Therefore, the curl equations for a simple medium can be written as

$$\nabla \times \boldsymbol{E}(\boldsymbol{r}) = i\omega\mu \boldsymbol{H}(\boldsymbol{r}) - \boldsymbol{M}(\boldsymbol{r}) \tag{2.3a}$$

$$\nabla \times \boldsymbol{H}(\boldsymbol{r}) = -i\omega\varepsilon \boldsymbol{E}(\boldsymbol{r}) + \boldsymbol{J}(\boldsymbol{r}). \tag{2.3b}$$

Taking the divergence of (2.3a) and (2.3b), and then using (2.1c) and (2.1d) in the resultant equations, one can obtain the continuity equations given by

$$\nabla \cdot \boldsymbol{J}(\boldsymbol{r}) = i\omega\rho_e(\boldsymbol{r}) \tag{2.4a}$$

$$\nabla \cdot \boldsymbol{M}(\boldsymbol{r}) = i\omega\rho_m(\boldsymbol{r}), \tag{2.4b}$$

which present the relation between the charge and current densities, and yield the law of conservation of charge. The vector wave equation in terms of electric field can also be obtained by taking the curl of (2.3a) and substituting (2.1c), (2.3b), and (2.4a) into it together with the vector identity ($\nabla \times \nabla \times \boldsymbol{a} = \nabla\nabla \cdot \boldsymbol{a} - \nabla^2\boldsymbol{a}$) resulting

$$\nabla^2\boldsymbol{E}(\boldsymbol{r}) + k^2\boldsymbol{E}(\boldsymbol{r}) = -i\omega\mu\left[\boldsymbol{J}(\boldsymbol{r}) + \frac{1}{k^2}\nabla\left(\nabla \cdot \boldsymbol{J}(\boldsymbol{r})\right)\right] + \nabla \times \boldsymbol{M}(\boldsymbol{r}), \tag{2.5}$$

where $k = \omega\sqrt{\mu\varepsilon}$ is the wavenumber of the medium. A similar vector wave equation in terms of magnetic field can also be obtained by taking the curl of (2.3b) and substituting (2.1d), (2.3a), and (2.4b) into it together with the above-mentioned vector identity resulting

$$\nabla^2\boldsymbol{H}(\boldsymbol{r}) + k^2\boldsymbol{H}(\boldsymbol{r}) = -i\omega\varepsilon\left[\boldsymbol{M}(\boldsymbol{r}) + \frac{1}{k^2}\nabla(\nabla \cdot \boldsymbol{M}(\boldsymbol{r}))\right] - \nabla \times \boldsymbol{J}(\boldsymbol{r}). \tag{2.6}$$

On the other hand, Maxwell's equations can be written in terms of potentials by using the supposition theorem for electric and magnetic sources. If we consider the fictitious magnetic sources in (2.1) are zero, magnetic-flux density in (2.1d) will be a solenoidal vector field, and hence by using the null identity ($\nabla \cdot \nabla \times \boldsymbol{a} = 0$), we have

$$\boldsymbol{H}(\boldsymbol{r}) = \frac{1}{\mu}\nabla \times \boldsymbol{A}_m(\boldsymbol{r}), \tag{2.7}$$

in which $\boldsymbol{A}_m(\boldsymbol{r})$ is the magnetic vector potential. Inserting the (2.7) into (2.3a), where $\boldsymbol{M}(\boldsymbol{r}) = 0$, we obtain

$$\nabla \times [\boldsymbol{E}(\boldsymbol{r}) - i\omega\boldsymbol{A}_m(\boldsymbol{r})] = 0. \tag{2.8}$$

The obtained irrotational field (curl-free vector field) can be written as the gradient of a scalar function (as a consequence of another null identity given by $\nabla \times \nabla a = 0$)

$$\boldsymbol{E}(\boldsymbol{r}) = i\omega \boldsymbol{A}_m(\boldsymbol{r}) - \nabla \phi_e(\boldsymbol{r}), \tag{2.9}$$

where $\phi_e(\boldsymbol{r})$ is known as the electric scalar potential. Following the same procedure and assuming the electric sources are zero, one can obtain

$$\boldsymbol{E}(\boldsymbol{r}) = -\frac{1}{\varepsilon} \nabla \times \boldsymbol{A}_e(\boldsymbol{r}) \tag{2.10a}$$

$$\boldsymbol{H}(\boldsymbol{r}) = i\omega \boldsymbol{A}_e(\boldsymbol{r}) - \nabla \phi_m(\boldsymbol{r}), \tag{2.10b}$$

where $\boldsymbol{A}_e(\boldsymbol{r})$ and $\phi_m(\boldsymbol{r})$ are the electric vector potential and magnetic scalar potential, respectively. Combination of (2.9) with (2.10a), and (2.7) with (2.10b) result in the total electric and magnetic fields, respectively, created by the electric and magnetic potentials as

$$\boldsymbol{E}(\boldsymbol{r}) = iw \boldsymbol{A}_m(\boldsymbol{r}) - \nabla \phi_e(\boldsymbol{r}) - \frac{1}{\varepsilon} \nabla \times \boldsymbol{A}_e(\boldsymbol{r}) \tag{2.11a}$$

$$\boldsymbol{H}(\boldsymbol{r}) = iw \boldsymbol{A}_e(\boldsymbol{r}) - \nabla \phi_m(\boldsymbol{r}) + \frac{1}{\mu} \nabla \times \boldsymbol{A}_m(\boldsymbol{r}). \tag{2.11b}$$

In (2.7) and (2.10a), the curl of auxiliary electric vector potential $\boldsymbol{A}_e(\boldsymbol{r})$ and magnetic vector potential $\boldsymbol{A}_m(\boldsymbol{r})$ are determined. However, the divergences of the auxiliary vector fields are also required to be defined. This can be accomplished by using the Lorenz gauge as

$$\nabla \cdot \boldsymbol{A}_m(\boldsymbol{r}) = i\omega\varepsilon\mu\phi_e(\boldsymbol{r}) \tag{2.12a}$$

$$\nabla \cdot \boldsymbol{A}_e(\boldsymbol{r}) = i\omega\varepsilon\mu\phi_m(\boldsymbol{r}). \tag{2.12b}$$

Using Maxwell's equations in (2.3), and substituting the relations in (2.7), (2.9), and (2.10) into it, and then utilizing the gauge conditions [given in (2.12)] together with the vector identity ($\nabla \times \nabla \times \boldsymbol{a} = \nabla\nabla \cdot \boldsymbol{a} - \nabla^2 \boldsymbol{a}$), a set of four well-known

vector and scalar wave equations can be derived as

$$\nabla^2 \boldsymbol{A}_e(\boldsymbol{r}) + k^2 \boldsymbol{A}_e(\boldsymbol{r}) = -\varepsilon \boldsymbol{M}(\boldsymbol{r}), \tag{2.13a}$$

$$\nabla^2 \boldsymbol{A}_m(\boldsymbol{r}) + k^2 \boldsymbol{A}_m(\boldsymbol{r}) = -\mu \boldsymbol{J}(\boldsymbol{r}), \tag{2.13b}$$

$$\nabla^2 \phi_e(\boldsymbol{r}) + k^2 \phi_e(\boldsymbol{r}) = -\frac{1}{\varepsilon} \rho_e(\boldsymbol{r}), \tag{2.13c}$$

$$\nabla^2 \phi_m(\boldsymbol{r}) + k^2 \phi_m(\boldsymbol{r}) = -\frac{1}{\mu} \rho_m(\boldsymbol{r}). \tag{2.13d}$$

Each vector wave equation in (2.13a) and (2.13b) can be decomposed into three separate scalar Helmholtz (wave) equations in Cartesian coordinate system. In addition, once the vector potentials are determined, the corresponding scalar potentials attained in (2.13c) and (2.13d) will be calculated by means of the gauge conditions given in (2.12).

One can use one of the vector wave equations presented in (2.5), (2.6), (2.13a) and (2.13b), to calculate the electromagnetic fields in a specific region with appropriate boundary conditions. However, solutions of the wave equations based on the scalar and vector potentials given in (2.13), and then inserting the potential expressions into (2.11), are simpler than the solution of the vector wave equations in terms of electric and magnetic fields. The solution of the vector potential wave equations can be obtained using the scalar Green's function as will be explained in the following section.

2.3 The Scalar Helmholtz Equation

Vector potential wave equations given in (2.13a) and (2.13b) can be decomposed into three scalar Helmholtz equations in Cartesian coordinate system. For example, one can obtain three inhomogeneous scalar Helmholtz equations from

(2.13b) in Cartesian coordinate system as

$$\nabla^2 A_{m_x}(\boldsymbol{r}) + k^2 A_{m_x}(\boldsymbol{r}) = -\mu J_x(\boldsymbol{r}) \tag{2.14a}$$

$$\nabla^2 A_{m_y}(\boldsymbol{r}) + k^2 A_{m_y}(\boldsymbol{r}) = -\mu J_y(\boldsymbol{r}) \tag{2.14b}$$

$$\nabla^2 A_{m_z}(\boldsymbol{r}) + k^2 A_{m_z}(\boldsymbol{r}) = -\mu J_z(\boldsymbol{r}). \tag{2.14c}$$

Each equation in (2.14) for an arbitrary source distribution $\boldsymbol{J}$ within an infinite medium with constitutive parameters ε and μ is in the form of

$$\nabla^2 f(\boldsymbol{r}) + k^2 f(\boldsymbol{r}) = -s(\boldsymbol{r}). \tag{2.15}$$

Equation (2.15) can be solved in a closed-form representation using the Green's function as

$$f(\boldsymbol{r}) = \iiint d\boldsymbol{r'} s(\boldsymbol{r'}) g(\boldsymbol{r}, \boldsymbol{r'}), \tag{2.16}$$

where $g(\boldsymbol{r}, \boldsymbol{r'})$ is the free-space scalar Green's function and is given by

$$g(\boldsymbol{r}, \boldsymbol{r'}) = \frac{e^{ikR}}{4\pi R} = \frac{e^{ik|\boldsymbol{r}-\boldsymbol{r'}|}}{4\pi|\boldsymbol{r}-\boldsymbol{r'}|} \qquad (\boldsymbol{R} = \boldsymbol{r} - \boldsymbol{r'}), \tag{2.17}$$

where $\boldsymbol{r}$ and $\boldsymbol{r'}$ represent the observation and source points, respectively. Therefore, the solution of the vector potential wave equations are obtained as

$$\boldsymbol{A}_e(\boldsymbol{r}) = \frac{\varepsilon}{4\pi} \int d\boldsymbol{r'} \boldsymbol{M}(\boldsymbol{r'}) \frac{e^{ik|\boldsymbol{r}-\boldsymbol{r'}|}}{|\boldsymbol{r}-\boldsymbol{r'}|} \tag{2.18a}$$

$$\boldsymbol{A}_m(\boldsymbol{r}) = \frac{\mu}{4\pi} \int d\boldsymbol{r'} \boldsymbol{J}(\boldsymbol{r'}) \frac{e^{ik|\boldsymbol{r}-\boldsymbol{r'}|}}{|\boldsymbol{r}-\boldsymbol{r'}|}. \tag{2.18b}$$

In a similar fashion, the solution of (2.13c) and (2.13d) can be obtained as

$$\begin{aligned}\phi_e(\boldsymbol{r}) &= \frac{1}{4\pi\varepsilon}\int d\boldsymbol{r'}\rho_e(\boldsymbol{r'})\frac{e^{ik|\boldsymbol{r}-\boldsymbol{r'}|}}{|\boldsymbol{r}-\boldsymbol{r'}|} \\ &= \frac{1}{4\pi i\omega\varepsilon}\int d\boldsymbol{r'}\nabla'\cdot\boldsymbol{J}(\boldsymbol{r'})\frac{e^{ik|\boldsymbol{r}-\boldsymbol{r'}|}}{|\boldsymbol{r}-\boldsymbol{r'}|} \qquad (2.19a)\\ \phi_m(\boldsymbol{r}) &= \frac{1}{4\pi\mu}\int d\boldsymbol{r'}\rho_m(\boldsymbol{r'})\frac{e^{ik|\boldsymbol{r}-\boldsymbol{r'}|}}{|\boldsymbol{r}-\boldsymbol{r'}|} \\ &= \frac{1}{4\pi i\omega\mu}\int d\boldsymbol{r'}\nabla'\cdot\boldsymbol{M}(\boldsymbol{r'})\frac{e^{ik|\boldsymbol{r}-\boldsymbol{r'}|}}{|\boldsymbol{r}-\boldsymbol{r'}|}, \qquad (2.19b)\end{aligned}$$

where the equation of continuity for both electric and magnetic sources are employed to arrive at the final expressions given in (2.19a) and (2.19b). Substituting (2.18) and (2.19) into (2.11), the total electric and magnetic fields due to arbitrary electric and magnetic sources can be derived as

$$\begin{aligned}\boldsymbol{E}(\boldsymbol{r}) &= ik\eta\int d\boldsymbol{r'}\left[\boldsymbol{J}(\boldsymbol{r'})+\frac{1}{k^2}\nabla'\cdot\boldsymbol{J}(\boldsymbol{r'})\nabla\right]g(\boldsymbol{r},\boldsymbol{r'}) \\ &\quad -\int d\boldsymbol{r'}\nabla g(\boldsymbol{r},\boldsymbol{r'})\times\boldsymbol{M}(\boldsymbol{r'}) \qquad (2.20a)\\ \boldsymbol{H}(\boldsymbol{r}) &= ik\eta^{-1}\int d\boldsymbol{r'}\left[\boldsymbol{M}(\boldsymbol{r'})+\frac{1}{k^2}\nabla'\cdot\boldsymbol{M}(\boldsymbol{r'})\nabla\right]g(\boldsymbol{r},\boldsymbol{r'}) \\ &\quad +\int d\boldsymbol{r'}\nabla g(\boldsymbol{r},\boldsymbol{r'})\times\boldsymbol{J}(\boldsymbol{r'}), \qquad (2.20b)\end{aligned}$$

where $\eta=\sqrt{\dfrac{\mu}{\varepsilon}}$ is the intrinsic impedance of the medium. Equations (2.20a) and (2.20b) can be expressed in a simpler form by using integro-differential operators defined as

$$\mathcal{T}\{\boldsymbol{X}\}(\boldsymbol{r}) = ik\int d\boldsymbol{r'}\left[\boldsymbol{X}(\boldsymbol{r'})+\frac{1}{k^2}\nabla'\cdot\boldsymbol{X}(\boldsymbol{r'})\nabla\right]g(\boldsymbol{r},\boldsymbol{r'}) \qquad (2.21a)$$

$$\mathcal{K}\{\boldsymbol{X}\}(\boldsymbol{r}) = \int d\boldsymbol{r'}\boldsymbol{X}(\boldsymbol{r'})\times\nabla' g(\boldsymbol{r},\boldsymbol{r'}). \qquad (2.21b)$$

Finally, the electric and magnetic fields can be written in a compact form as

$$\boldsymbol{E}(\boldsymbol{r}) = \eta\mathcal{T}\{\boldsymbol{J}\}(\boldsymbol{r})-\mathcal{K}\{\boldsymbol{M}\}(\boldsymbol{r}) \qquad (2.22a)$$

$$\boldsymbol{H}(\boldsymbol{r}) = \eta^{-1}\mathcal{T}\{\boldsymbol{M}\}(\boldsymbol{r})+\mathcal{K}\{\boldsymbol{J}\}(\boldsymbol{r}). \qquad (2.22b)$$

2.4 Far-Zone Fields

In the far-zone region of an antenna or a scatterer, where $|\boldsymbol{r}| = r >> r' = |\boldsymbol{r'}|$ and $|\boldsymbol{r}| = r >> \lambda$ (or $kr >> 1$), the scalar free-space Green's function and its gradient can be approximated as

$$g(\boldsymbol{r}, \boldsymbol{r'}) = \frac{e^{ik|\boldsymbol{r}-\boldsymbol{r'}|}}{4\pi|\boldsymbol{r}-\boldsymbol{r'}|} \approx \frac{e^{ikr}}{4\pi r} e^{-ik\hat{\boldsymbol{r}}\cdot\boldsymbol{r'}} \tag{2.23a}$$

$$\nabla g(\boldsymbol{r}, \boldsymbol{r'}) = \frac{(\boldsymbol{r}-\boldsymbol{r'})(ik|\boldsymbol{r}-\boldsymbol{r'}|-1)e^{ik|\boldsymbol{r}-\boldsymbol{r'}|}}{4\pi|\boldsymbol{r}-\boldsymbol{r'}|^3} \approx \hat{\boldsymbol{r}} ik \frac{e^{ikr}}{4\pi r} e^{-ik\hat{\boldsymbol{r}}\cdot\boldsymbol{r'}}. \tag{2.23b}$$

Substituting (2.23a) and (2.23b) into $\mathcal{T}\{\boldsymbol{X}\}(\boldsymbol{r})$ and $\mathcal{K}\{\boldsymbol{X}\}(\boldsymbol{r})$, far-zone approximations of the operators can be obtained as

$$\mathcal{T}\{\boldsymbol{X}\}(\boldsymbol{r}) = ik\frac{e^{ikr}}{4\pi r}\left\{\int d\boldsymbol{r'}\left[\boldsymbol{X}(\boldsymbol{r'})e^{-ik\hat{\boldsymbol{r}}\cdot\boldsymbol{r'}} + \hat{\boldsymbol{r}}\frac{ik}{k^2}\nabla'\cdot\boldsymbol{X}(\boldsymbol{r'})e^{-ik\hat{\boldsymbol{r}}\cdot\boldsymbol{r'}}\right]\right\} \tag{2.24a}$$

$$\mathcal{K}\{\boldsymbol{X}\}(\boldsymbol{r}) = ik\frac{e^{ikr}}{4\pi r}\hat{\boldsymbol{r}} \times \int d\boldsymbol{r'}\boldsymbol{X}(\boldsymbol{r'})e^{-ik\hat{\boldsymbol{r}}\cdot\boldsymbol{r'}}. \tag{2.24b}$$

The final expression for the $\mathcal{T}\{\boldsymbol{X}\}(\boldsymbol{r})$ operator can be obtained from (2.24a) by using the vector identity, given by $\nabla\cdot(\psi\boldsymbol{a}) = \psi\nabla\cdot\boldsymbol{a} + \boldsymbol{a}\cdot\nabla\psi$ and applying the divergence theorem for the second term of (2.24a) resulting

$$\mathcal{T}\{\boldsymbol{X}\}(\boldsymbol{r}) = ik\frac{e^{ikr}}{4\pi r}\int d\boldsymbol{r'}\left[\boldsymbol{X}(\boldsymbol{r'})e^{-ik\hat{\boldsymbol{r}}\cdot\boldsymbol{r'}} - \hat{\boldsymbol{r}}\hat{\boldsymbol{r}}\cdot\boldsymbol{X}(\boldsymbol{r'})e^{-ik\hat{\boldsymbol{r}}\cdot\boldsymbol{r'}}\right]. \tag{2.25}$$

Equations (2.24b) and (2.25) can be used together with (2.22) to calculate the electric and magnetic fields in the far-field region. The expressions for $\mathcal{T}\{\boldsymbol{X}\}(\boldsymbol{r})$ and $\mathcal{K}\{\boldsymbol{X}\}(\boldsymbol{r})$ operators infer that the variable r is now separated from the other variables and the electromagnetic fields in (2.22) decay to zero as the observation point goes to infinity, $r = |\boldsymbol{r}| \to \infty$. Finally, the far-zone electric and magnetic fields are defined as the electric and magnetic fields multiplied by the distance from the object when the observation point (distance) goes to infinity.

$$\boldsymbol{E}^{\infty}(\theta,\varphi) = \lim_{r\to\infty}\left\{re^{-ikr}\boldsymbol{E}(r,\theta,\varphi)\right\} \tag{2.26a}$$

$$\boldsymbol{H}^{\infty}(\theta,\varphi) = \lim_{r\to\infty}\left\{re^{-ikr}\boldsymbol{H}(r,\theta,\varphi)\right\} \tag{2.26b}$$

Chapter 3

Surface Integral Equations

3.1 Introduction

In the previous chapter, solutions of Maxwell's equations in an unbounded medium are illustrated. In this chapter, solutions of scattering and radiation problems involving arbitrarily shaped conducting geometries are considered as presented in Fig. 3.1. For this purpose, it is often useful and convenient to replace the original electromagnetic problem with an equivalent one by employing equivalent current densities over the imaginary surfaces that solve the problem in the region of interest. These equivalent electric- and magnetic-current densities are able to mathematically modify or eliminate the presence of the object of interest in original problems. Since in this thesis we are only involved in the solution of perfect electrically conducting (PEC) bodies, we will focus on the surface equivalence theorem as a fundamental block for deriving different types of surface integral equations to solve scattering/radiation problems [81].

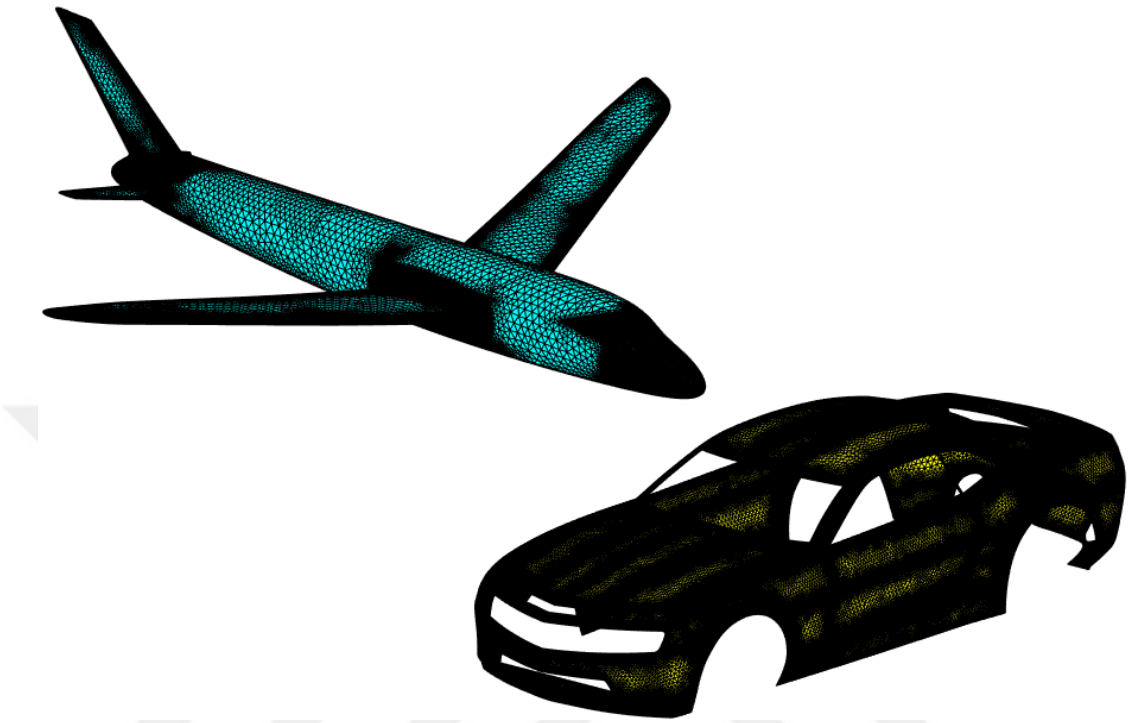


Figure 3.1: Arbitrarily-shaped conducting geometries.

3.2 Surface Equivalence Theorem

According to the uniqueness theorem [1, 2], distribution of electromagnetic fields in a lossy region is uniquely specified by the sources inside the region and by satisfying the boundary conditions (the electromagnetic fields in lossless regions are considered as a particular case when the losses go to zero). Furthermore, uniqueness theorem is considered as a fundamental block for the surface equivalence theorem where the actual sources are replaced by the equivalent ones over the imaginary boundaries. Suitable electric- and magnetic-current densities are defined over the surfaces to obtain the electromagnetic fields in the region of interest. The current densities are defined using the tangential components of the electric and magnetic fields over the imaginary surface in such a way that the fields inside the closed surface can be considered to be zero, and then the fields outside the region are equal to the radiation produced by the actual sources. The procedure is illustrated in Fig. 3.2.

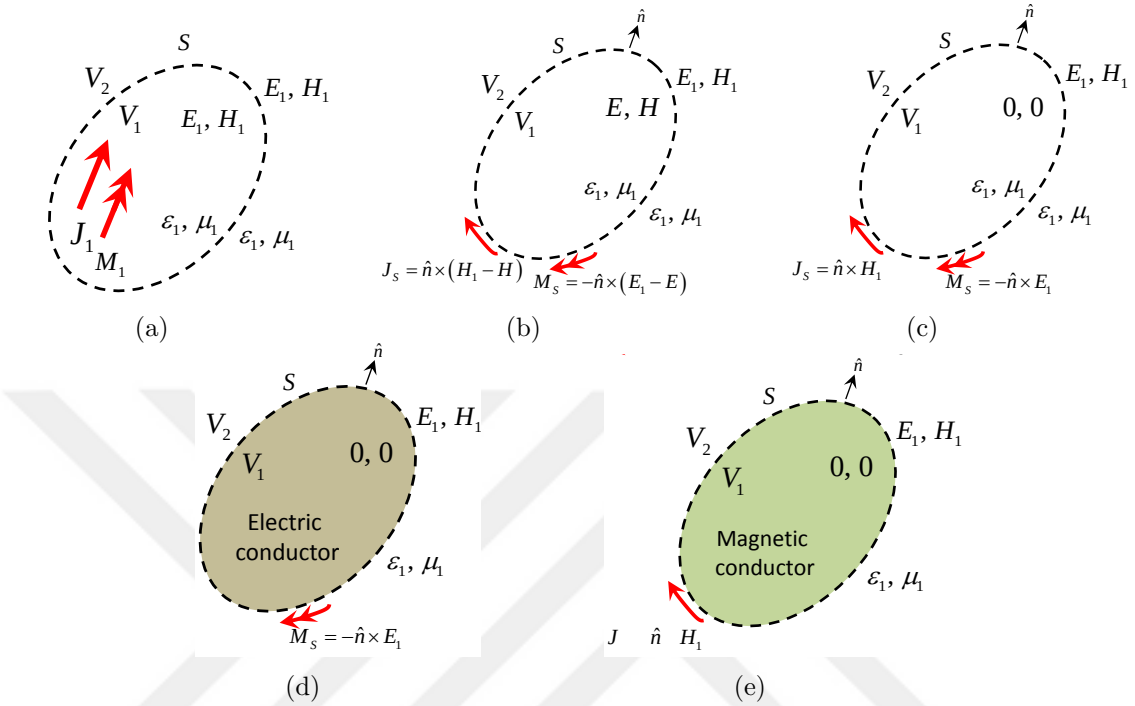


Figure 3.2: (a) Actual sources $\boldsymbol{J}_1$ and $\boldsymbol{M}_1$ radiating fields $\boldsymbol{E}_1$ and $\boldsymbol{H}_1$ to the infinite medium with the constitutive parameters of μ_1 and ε_1. (b) The equivalent problem when the actual sources are replaced with the current densities over the imaginary surface. The equivalent current densities are radiating the same fields $\boldsymbol{E}_1$ and $\boldsymbol{H}_1$ outside the region and $\boldsymbol{E}$ and $\boldsymbol{H}$ inside the region. (c) Since the volume within S is not the region of interest, and the equivalent current densities are obtained using tangential components of both electric and magnetic fields, we can assume that $\boldsymbol{E}$ and $\boldsymbol{H}$ are zero (This is known as Love's equivalence principle). (d) The equivalent electric-current density is zero if we replace the region with an electric conductor. (e) The equivalent magnetic-current density is zero if we replace the region with a magnetic conductor.

3.2.1 Physical Equivalence Theorem

Another fundamental concept in the area of scattering problems called the physical equivalence theorem [1, 2] would be considered here, which is closely related to the surface equivalence theorem. A scattering problem can be considered as a radiation problem (its equivalent form) based on the defined equivalent current densities. These currents are radiating to a region of interest, and they are obtained via satisfying the boundary conditions on the surface of the scatterer. Now, consider a scattering problem as presented in Fig. 3.3

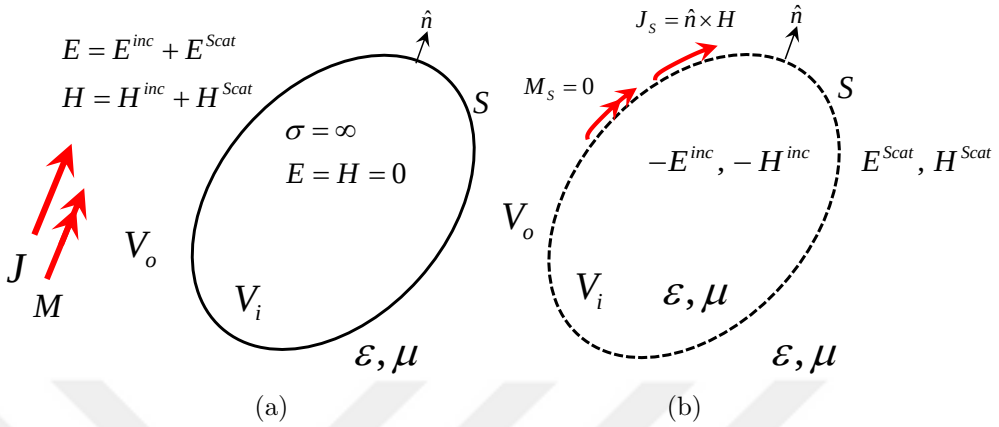


Figure 3.3: Physical equivalence theorem. (a) A scattering problem (original problem) consisting of a PEC scatterer which is illuminated by incident fields $\boldsymbol{E}^{inc}$ and $\boldsymbol{H}^{inc}$. The incident fields are created by the electric and magnetic sources ($\boldsymbol{J}$ & $\boldsymbol{M}$) radiating into an infinite region. Presence of the scatterer creates scattered fields $\boldsymbol{E}^{scat}$ and $\boldsymbol{H}^{scat}$. The total fields outside the scatterer are the superposition of the incident fields and the scattered fields. (b) The equivalent problem can be defined by introducing equivalent surface currents ($\boldsymbol{J}_S$ & $\boldsymbol{M}_S$) over the boundary. These currents radiate in a homogeneous space and create $-\boldsymbol{E}^{inc}$ and $-\boldsymbol{H}^{inc}$ fields inside the object and $\boldsymbol{E}^{scat}$ and $\boldsymbol{H}^{scat}$ fields outside the object.

where the radiation of electric $\boldsymbol{J}$ and magnetic $\boldsymbol{M}$ sources into an infinite region with constitutive parameters ε and μ create incident fields $\boldsymbol{E}^{inc}$ and $\boldsymbol{H}^{inc}$ in the region. The presence of a PEC scatterer inside the region creates scattered fields $\boldsymbol{E}^{scat}$ and $\boldsymbol{H}^{scat}$ outside the object as illustrated in Fig. 3.3(a). The scattered electromagnetic fields inside the object are zero due to the infinite conductivity of the object. Appropriate equivalent surface currents on the surface of the PEC object, as they satisfy the boundary conditions, can permit us to eliminate the original problem [Fig. 3.3(a)] and replace it with the equivalent problem as presented in Fig. 3.3(b). The equivalent electric and magnetic currents are calculated by

$$\boldsymbol{J}_S = \hat{\boldsymbol{n}} \times (\boldsymbol{H}^{inc} + \boldsymbol{H}^{scat}) = \hat{\boldsymbol{n}} \times (\boldsymbol{H}^{scat} - (-\boldsymbol{H}^{inc})) \tag{3.1a}$$

$$\boldsymbol{M}_S = -\hat{\boldsymbol{n}} \times (\boldsymbol{E}^{inc} + \boldsymbol{E}^{scat}) = -\hat{\boldsymbol{n}} \times (\boldsymbol{E}^{scat} - (-\boldsymbol{E}^{inc})) = 0. \tag{3.1b}$$

Magnetic current is zero because of the image theory [1, 2]. In (3.1a), $\boldsymbol{J}_S$ implies that it radiates the scattered fields outside and the negative incident fields inside

the eliminated object. Therefore, considering the effect of original sources, the total fields inside and outside of the PEC object would be zero and $\boldsymbol{E}, \boldsymbol{H}$, respectively, as shown in the original problem in Fig. 3.3(a). Physical equivalence principle replaces the original problem with an equivalent one; nevertheless, the equivalent current $\boldsymbol{J}_S$ depends on both the unknown scattered and known incident fields.

3.2.2 Electric-field Integral Equation

An electric current will be induced on the surface of a PEC scatterer when it is illuminated by an incident field. The radiated electric field is obtained from the induced surface current via (2.20a). By using the physical equivalence principle [see Fig. 3.3(b)] and enforcing the boundary condition for the tangential component of the total electric field [see equation (3.1b)] on the surface of the PEC scatterer, one can derive the well-known EFIE [4, 5] as

$$0 = \hat{\boldsymbol{n}} \times \left[\boldsymbol{E}^{inc}(\boldsymbol{r}) + \boldsymbol{E}^{scat}(\boldsymbol{r})\right] \tag{3.2a}$$

$$-\hat{\boldsymbol{n}} \times \boldsymbol{E}^{inc}(\boldsymbol{r}) = \hat{\boldsymbol{n}} \times \eta \mathcal{T}\{\boldsymbol{J}\}(\boldsymbol{r'}) \tag{3.2b}$$

$$-\hat{\boldsymbol{n}} \times \boldsymbol{E}^{inc}(\boldsymbol{r}) = \hat{\boldsymbol{n}} \times ik\eta \int d\boldsymbol{r'} \left[\boldsymbol{J}(\boldsymbol{r'}) + \frac{1}{k^2}\nabla' \cdot \boldsymbol{J}(\boldsymbol{r'})\nabla\right] g(\boldsymbol{r}, \boldsymbol{r'}), \tag{3.2c}$$

where $\hat{\boldsymbol{n}}$ denotes the normal unit vector on the surface of the scatterer and $\boldsymbol{E}^{scat}(\boldsymbol{r})$ is calculated using (2.20a). In (3.2c), the surface electric-current density $\boldsymbol{J}(\boldsymbol{r'})$ is the unknown. The above integral equation is called the normal EFIE (N-EFIE) since it is sampled using a rotated version of the tangential electric field. Tangential EFIE (T-EFIE) can be obtained as

$$0 = \hat{\boldsymbol{n}} \times \hat{\boldsymbol{n}} \times \left[\boldsymbol{E}^{inc}(\boldsymbol{r}) + \boldsymbol{E}^{scat}(\boldsymbol{r})\right] \tag{3.3a}$$

$$-\hat{\boldsymbol{n}} \times \hat{\boldsymbol{n}} \times \boldsymbol{E}^{inc}(\boldsymbol{r}) = \hat{\boldsymbol{n}} \times \hat{\boldsymbol{n}} \times \eta \mathcal{T}\{\boldsymbol{J}\}(\boldsymbol{r'}) \tag{3.3b}$$

$$-\hat{\boldsymbol{n}} \times \hat{\boldsymbol{n}} \times \boldsymbol{E}^{inc}(\boldsymbol{r}) = \hat{\boldsymbol{n}} \times \hat{\boldsymbol{n}} \times ik\eta \int d\boldsymbol{r'} \left[\boldsymbol{J}(\boldsymbol{r'}) + \frac{1}{k^2}\nabla' \cdot \boldsymbol{J}(\boldsymbol{r'})\nabla\right] g(\boldsymbol{r}, \boldsymbol{r'}). \tag{3.3c}$$

Each formulation in (3.2) and (3.3) possesses distinct numerical properties where the diagonal entries of the discretized N-EFIE are zero in contrast to quasi-diagonally dominant matrix obtained from T-EFIE [5].

3.2.3 Magnetic-field Integral Equation

In a similar fashion, using the physical equivalence theorem and enforcing the boundary condition for the tangential component of the total magnetic field on the surface of a conducting scatterer lead to the normal MFIE (N-MFIE) [5] given by

$$\boldsymbol{J}(\boldsymbol{r}) = \hat{\boldsymbol{n}} \times \left[\boldsymbol{H}^{scat}(\boldsymbol{r}) - (-\boldsymbol{H}^{inc}(\boldsymbol{r}))\right] \tag{3.4a}$$

$$-\hat{\boldsymbol{n}} \times \boldsymbol{H}^{inc}(\boldsymbol{r}) = -\boldsymbol{J}(\boldsymbol{r}) + \lim_{r \to S^+} \hat{\boldsymbol{n}} \times \int d\boldsymbol{r'} \nabla g(\boldsymbol{r}, \boldsymbol{r'}) \times \boldsymbol{J}(\boldsymbol{r'}) \tag{3.4b}$$

$$\hat{\boldsymbol{n}} \times \boldsymbol{H}^{inc}(\boldsymbol{r}) = \boldsymbol{J}(\boldsymbol{r}) + \lim_{r \to S^+} \hat{\boldsymbol{n}} \times \int d\boldsymbol{r'} \nabla' g(\boldsymbol{r}, \boldsymbol{r'}) \times \boldsymbol{J}(\boldsymbol{r'}), \tag{3.4c}$$

where S^+ is a surface approaching S from the outside, and $\boldsymbol{H}^{scat}(\boldsymbol{r})$ can be calculated using (2.20b). The integral equation in (3.4c) should be evaluated as the observation point (position vector $\boldsymbol{r}$) approaches the source point (position vector $\boldsymbol{r'}$) from outside of the surface S. After the singularity extraction (approaching the surface from the outside region) due to the singular behavior of the free-space Green's function in the kernel of the integral, we have

$$\hat{\boldsymbol{n}} \times \boldsymbol{H}^{inc}(\boldsymbol{r}) = \boldsymbol{J}(\boldsymbol{r}) - \frac{\Omega_o}{4\pi} \boldsymbol{J}(\boldsymbol{r}) + \hat{\boldsymbol{n}} \times \int_{PV} d\boldsymbol{r'} \nabla' g(\boldsymbol{r}, \boldsymbol{r'}) \times \boldsymbol{J}(\boldsymbol{r'}) \tag{3.5a}$$

$$\hat{\boldsymbol{n}} \times \boldsymbol{H}^{inc}(\boldsymbol{r}) = \boldsymbol{J}(\boldsymbol{r}) - \frac{\Omega_o}{4\pi} \boldsymbol{J}(\boldsymbol{r}) - \hat{\boldsymbol{n}} \times \mathcal{K}^{PV}\{\boldsymbol{J}\}(\boldsymbol{r'}), \tag{3.5b}$$

where $\mathcal{K}^{PV}$ is the principal value of the $\mathcal{K}$ operator given in (2.21b), and Ω_o is the exterior solid angle, and for smooth surfaces, the exterior solid angle is equal 2π. Tangential MFIE (T-MFIE) can be obtained similar to the procedure explained for T-EFIE. Discretized N-MFIE is well-conditioned for Galerkin testing in comparison to T-MFIE due to having a diagonally dominant matrix. In addition, discretized N-MFIE should bear a better condition number with respect to the

discretized T-EFIE, due to the presence of unknown parameter (current density) outside the integral known as the second kind Fredholm integral equation.

3.2.4 Combined-field Integral Equation

EFIE and MFIE suffer from spurious internal resonance problem when applied to perfect electric conducting bodies with closed surfaces [81]. In this case, the uniqueness of the solutions are not guaranteed at some discrete singular frequencies (and their vicinities) that correspond to the interior resonant modes of the object. Therefore, at the interior resonant frequencies, MoM solutions of EFIE and MFIE lead to singular matrices, and hence, nontrivial solutions introduce errors on the near-field and/or far-field results. The problem will be more serious when the interval between the two adjacent singular (resonant) frequencies decreases as the operating frequency increases for a fixed-size scatterer or as the size of the scatterer grows for a constant operating frequency.

The internal resonance problem of EFIE is related to the fictitious PEC cavity, formed even for a solid PEC scatterer by applying the physical equivalence theorem [81]. In this scenario, when a scatterer is illuminated at the same resonant frequencies of the corresponding PEC cavity, the tangential component of the electric field is not sufficient to uniquely satisfy the boundary condition, and hence electromagnetic fields leak into the PEC cavity. Considering the fact that the medium is lossless, having energy inside the cavity causes nontrivial interior solutions and uniqueness is not satisfied at these resonant frequencies. This is indicating the presence of null-space solutions for matrix equations obtained via MoM solution of EFIE. The existence of nontrivial interior solution for EFIE corresponds to the existence of non-radiating current on the boundary and nontrivial electromagnetic field inside the cavity which introduces an error on the near-field results. However, we may still obtain the correct scattered field even though the current is wrong and nonunique. Furthermore, the matrix system representing EFIE becomes non-convergent or ill-conditioned.

Similarly, MFIE also suffers from a nontrivial (i.e., null-space) solution at the

resonant frequency of the PMC (perfect magnetic conductor) cavity [81]. The null-space solution of MFIE is quite different and can be proved by performing a Gedanken experiment [108]. Contrary to EFIE, presence of the nontrivial interior solution for MFIE corresponds to the nonunique radiating current which generates a strong scattered field outside the scatterer and affects both near- and far-field results.

The internal resonance problem of EFIE and MFIE can be alleviated by adding some losses to the background medium based on satisfying the uniqueness theorem. In addition, enforcing the boundary conditions for both tangential components of the electric and magnetic fields can eliminate the spurious solutions. This can be accomplished by a linear combination of EFIE and MFIE (the nullspaces of EFIE and MFIE differ from each other) to construct the combined field integral equation (CFIE) as follows:

$$\text{CFIE} = \alpha\text{T-EFIE} + \eta(1-\alpha)\text{N-MFIE}, \tag{3.6}$$

where the constant α is chosen between 0 and 1, and η is the intrinsic impedance of medium.

3.2.5 Low-frequency Breakdown of EFIE

The numerical solution of EFIE suffers from the LF breakdown, an ill-conditioning phenomenon caused by a dense discretization with respect to the operating wavelength (or by the weak coupling of the electric and magnetic fields near zero frequencies) [9–11,82]. From the mathematical point of view, the reason behind the LF breakdown of EFIE is due to the finite machine precision and poor frequency scaling in the EFIE formula given in (3.3c), in which the magnetic vector potential term (contribution of the current) is in the order of $\mathcal{O}(\omega)$ and the scalar potential term (contribution of charge) is in the order of $\mathcal{O}(\frac{1}{\omega})$. Therefore, in the MoM solution of EFIE at low frequencies, the contribution coming from the magnetic vector potential to the impedance matrix is significantly smaller than the contribution coming from the scalar potential. Nevertheless, the contribution

of the magnetic vector potential during the numerical process can be as significant as the contribution of the scalar potential. Because when $\omega \to 0$, due to the weak coupling of the electric and magnetic fields, the current distribution can be decomposed into its solenoidal (divergence-free) and irrotational (nonsolenoidal or curl-free) components where these two components are completely decoupled at the zero frequency. As a consequence, the divergence-free component creates only a magnetic field, while the irrotational component creates only an electric field. Moreover, the divergence of the irrotational component should go to zero with vanishing frequency to satisfy the continuity equation or produce a physically finite charge. Therefore, the irrotational current should be dependent on ω [10] while such a frequency scaling is not required for the solenoidal component. For the sake of simplicity, we try to illustrate the aforementioned discussion by using the following formulation:

$$-\hat{\boldsymbol{n}} \times \hat{\boldsymbol{n}} \times \boldsymbol{E}^{inc}(\boldsymbol{r}) = \hat{\boldsymbol{n}} \times \hat{\boldsymbol{n}} \times ik\eta \int d\boldsymbol{r'} \left[\boldsymbol{J}(\boldsymbol{r'}) + \frac{1}{k^2} \nabla' \cdot \boldsymbol{J}(\boldsymbol{r'}) \nabla \right] g(\boldsymbol{r}, \boldsymbol{r'}) \tag{3.7a}$$

$$\begin{aligned} -\hat{\boldsymbol{n}} \times \hat{\boldsymbol{n}} \times \lim_{\omega \to 0} \boldsymbol{E}^{inc}(\boldsymbol{r}) = \lim_{\omega \to 0} [& \hat{\boldsymbol{n}} \times \hat{\boldsymbol{n}} \times i\omega\mu \int d\boldsymbol{r'} \left(\boldsymbol{J}_{sol}(\boldsymbol{r'}) + \boldsymbol{J}_{irr}(\boldsymbol{r'}) \right) g(\boldsymbol{r}, \boldsymbol{r'}) \\ & + \frac{i}{\omega\varepsilon} \int d\boldsymbol{r'} \nabla \cdot \left(\boldsymbol{J}_{sol}(\boldsymbol{r'}) + \boldsymbol{J}_{irr}(\boldsymbol{r'}) \right) \nabla g(\boldsymbol{r}, \boldsymbol{r'})] \end{aligned} \tag{3.7b}$$

$$\begin{aligned} -\hat{\boldsymbol{n}} \times \hat{\boldsymbol{n}} \times \lim_{\omega \to 0} \boldsymbol{E}^{inc}(\boldsymbol{r}) = \lim_{\omega \to 0} [& \hat{\boldsymbol{n}} \times \hat{\boldsymbol{n}} \times i\omega\mu \int d\boldsymbol{r'} (\underbrace{\boldsymbol{J}_{sol}(\boldsymbol{r'})}_{\substack{\text{Creates only} \\ \text{the magnetic field}}} + \underbrace{\boldsymbol{J}_{irr}(\boldsymbol{r'})}_{\substack{\text{It goes to zero} \\ \text{when } \omega \to 0}}) g(\boldsymbol{r}, \boldsymbol{r'}) \\ & + \frac{i}{\omega\varepsilon} \int d\boldsymbol{r'} \underbrace{\nabla \cdot \left(\boldsymbol{J}_{sol}(\boldsymbol{r'}) + \boldsymbol{J}_{irr}(\boldsymbol{r'}) \right)}_{\substack{\text{The divergence part should go to zero as } \omega \to 0, \\ \text{therefore, } \boldsymbol{J}_{irr}(\boldsymbol{r'}) \text{ is dependent on } \omega \text{ [10]}, \\ \text{and it creates only the electric field.}}} \nabla g(\boldsymbol{r}, \boldsymbol{r'})]. \end{aligned} \tag{3.7c}$$

The discretized form of (3.7a) with Rao-Wilton-Glisson (RWG) basis function, $\boldsymbol{b}^{\mathrm{RWG}}(\boldsymbol{r'})$, and testing it again with RWG testing function, $\boldsymbol{t}^{\mathrm{RWG}}(\boldsymbol{r'})$ (i.e., Galerkin

MoM procedure), we obtain

$$-\left\langle \boldsymbol{t}_m^{\mathrm{RWG}}(\boldsymbol{r}), \hat{\boldsymbol{n}} \times \hat{\boldsymbol{n}} \times \boldsymbol{E}^{inc}(\boldsymbol{r}) \right\rangle = \left\langle \boldsymbol{t}_m^{\mathrm{RWG}}(\boldsymbol{r}), \hat{\boldsymbol{n}} \times \hat{\boldsymbol{n}} \times i\omega\mu \int d\boldsymbol{r'} \boldsymbol{b}_n^{\mathrm{RWG}}(\boldsymbol{r'}) g(\boldsymbol{r}, \boldsymbol{r'}) \right\rangle \tag{3.8a}$$

$$+ \left\langle \boldsymbol{t}_m^{\mathrm{RWG}}(\boldsymbol{r}), \frac{i}{\omega\varepsilon} \int d\boldsymbol{r'} \nabla \cdot \boldsymbol{b}_n^{\mathrm{RWG}}(\boldsymbol{r'}) \nabla g(\boldsymbol{r}, \boldsymbol{r'}) \right\rangle$$

$$-\int d\boldsymbol{r} \boldsymbol{t}_m^{\mathrm{RWG}}(r) \cdot \boldsymbol{E}^{inc}(\boldsymbol{r}) = \underbrace{i\omega\mu \int d\boldsymbol{r} \boldsymbol{t}_m^{\mathrm{RWG}}(\boldsymbol{r}) \cdot \int d\boldsymbol{r'} \boldsymbol{b}_n^{\mathrm{RWG}}(\boldsymbol{r'}) g(\boldsymbol{r}, \boldsymbol{r'})}_{\text{Contribution of the magnetic vector potential}} \tag{3.8b}$$

$$+ \underbrace{\frac{i}{\omega\varepsilon} \int d\boldsymbol{r} \nabla \cdot \boldsymbol{t}_m^{\mathrm{RWG}}(\boldsymbol{r}) \cdot \int d\boldsymbol{r'} \nabla \cdot \boldsymbol{b}_n^{\mathrm{RWG}}(\boldsymbol{r'}) g(\boldsymbol{r}, \boldsymbol{r'})}_{\text{Contribution of the electric scalar potential}} .$$

As illustrated in (3.7) and (3.8), by moving toward the low frequencies, the magnetic vector potential produces a smaller electric field [irrotational current creates an electric field $\mathcal{O}(\omega)$], although it generates a nonvanishing magnetic field. This loss of the contribution from the magnetic vector potential makes the solution inaccurate. Furthermore, the scalar potential part has a nullspace because of its divergence operator and when the contribution of the magnetic vector potential is lost, the resultant impedance matrix is nearly singular and its inversion is challenging at low frequencies [9]. Therefore, accurate calculation of the magnetic vector potential requires precise computation of both solenoidal and irrotational components of the current density which means both inductive and capacitive effects should be accurately determined due to the equally importance of each part at low frequencies (decomposing the current into its solenoidal and irrotational components correspond to the separation of scattering problem into inductive and capacitive parts at low frequencies). As a result, one of the approaches for circumventing the LF breakdown of EFIE is based on the expansion of the current density using different types of basis functions that correspond to solenoidal and irrotational components.

Note that the LF breakdown of EFIE can occur when the size of a scatterer is much smaller than the operating wavelength or if it contains electrically small geometrical details that require very fine discretizations [11]. Therefore, the LF breakdown can occur at higher frequencies in the presence of electrically very small discretizations. The tiny meshes increase the condition number of the resultant impedance matrix and cause an ill-conditioning problem, and then poor convergence in the iterative solvers and inaccurate results even in the direct methods.

3.2.6 Inaccuracy Problem of MFIE

In the solutions of electromagnetic problems modeled by arbitrarily shaped planar triangles, MFIE is usually criticized for being less accurate compared to EFIE if the same basis function (divergence-conforming RWG basis function which will be discussed later) is utilized to expand the unknown surface current distribution on planar triangular subdomains [12–17]. This means that the calculated root mean square error on the far-field results obtained via MFIE is several orders of magnitude larger than that results obtained from EFIE. MFIE even with denser discretizations would not be able to achieve the same accuracy of that of EFIE [5]. This problem will be more crucial if the geometry contains sharp wedges and corners. It is demonstrated that the accuracy of MFIE is dependent on the choice of the basis and testing functions. Hence, the accuracy of MFIE can be significantly improved if the basis and testing functions are restricted to be curl-conforming [16]. In addition, MFIE is applicable only to closed geometries which is another shortcoming of MFIE.

It is worthy to be noted here that the LF breakdown is not limited to EFIE, and MFIE also suffers from the LF-breakdown problem at very low frequencies (near zero frequency). This is due to the fact that the reconstruction of electric field requires accurate calculations of the current and charge distributions on surfaces. However, using MFIE, we can calculate the current distribution accurately at very low frequencies, where the charge distribution will be inaccurate due to losing its dependency to the frequency. This problem can be solved either by applying modifications to the basis functions and using a perturbation method or by simultaneously defining the charge and current as unknowns to have a straightforward and analytically justified method for avoiding the LF breakdown. Furthermore, the null-space solutions of the static MFIE lead to topological breakdown when applied to multiply-connected or toroidal geometries.

The inaccuracy problem of MFIE can also contaminate CFIE. Consequently, improving the accuracy of the MFIE solution is essential in order to obtain an accurate CFIE solution.

As a result, proposing well-conditioned IE formulations with the capability of being used in a wide range of frequency spectrum has been considered for a long time. In the next chapter, we will talk about PIEs as a promising choice for the solution of

electromagnetic problems in a broad frequency regime without facing the LF-breakdown and inaccuracy problems [49–52, 77, 78, 94–96, 109, 110].

Chapter 4

Potential Integral Equations

4.1 Introduction

Well-established SIEs formulated in terms of $\boldsymbol{E}(\boldsymbol{r})$ and $\boldsymbol{H}(\boldsymbol{r})$ suffer from the LF-breakdown and inaccuracy problems, as mentioned in the previous chapter. Nevertheless, recently introduced PIEs are capable of circumventing the LF breakdown of EFIE and inaccuracy of MFIE without using higher-order basis functions such as Calderón preconditioned technique [86,87] and mixed discretization [13,16]. In addition, PIEs can be applied to both open and closed geometries. Therefore, PIEs can be one of the appropriate candidates for solving scattering and radiation problems at a broad spectrum of frequencies, including low frequencies [49–52,77,78,94–96,109,110]. In this chapter, derivation and MoM implementation of PIEs are discussed in details.

4.2 Derivation of Potential Integral Equations

Fig. 4.1 illustrates a scatterer S with a unit outward normal vector $\hat{\boldsymbol{n}}$ in free-space illuminated by a source. The PIEs are derived using the Green's function, the Lorenz gauge, and the surface equivalence principle for the magnetic vector and electric scalar potentials. In this formulation, boundary conditions are satisfied for the electric

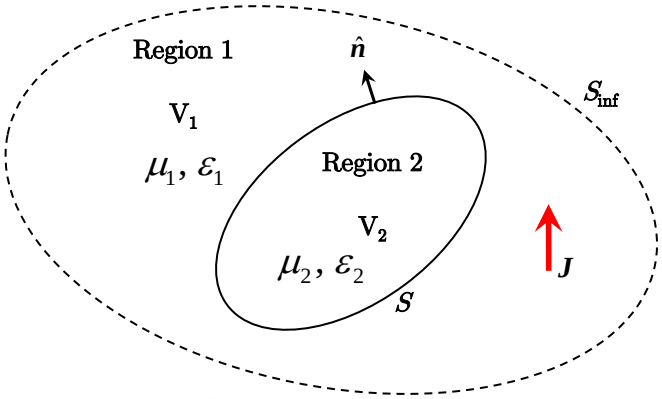


Figure 4.1: Geometry to obtain the surface PIEs.

scalar potential, $\Phi(\boldsymbol{r})$, and the tangential component of the magnetic vector potential, $\hat{\boldsymbol{n}} \times \boldsymbol{A}(\boldsymbol{r})$, over the surface of an arbitrarily shaped scatterer. Both the current and the contribution of charge are considered as unknowns. Two equations should be formulated based upon the tangential component of the magnetic vector potential and the electric scalar potential. We start our derivation by substituting (2.7) and (2.9) into (2.3b) which leads to

$$\nabla \times \frac{1}{\mu_1} \nabla \times \boldsymbol{A}(\boldsymbol{r}) = -i\omega\varepsilon_1 \left[i\omega \boldsymbol{A}(\boldsymbol{r}) - \nabla\phi(\boldsymbol{r}) \right] + \boldsymbol{J}(\boldsymbol{r}). \tag{4.1}$$

We assume that the constitutive parameters of Region 1 (μ_1 and ε_1) are constant. Using the vector identity ($\nabla \times \nabla \times \boldsymbol{a} = \nabla\nabla \cdot \boldsymbol{a} - \nabla^2 \boldsymbol{a}$), (4.1) can be simplified to

$$\nabla \times \nabla \times \boldsymbol{A}(\boldsymbol{r}) = \omega^2 \mu_1 \varepsilon_1 \boldsymbol{A}(\boldsymbol{r}) + i\omega\mu_1\varepsilon_1 \nabla\phi(\boldsymbol{r}) + \mu_1 \boldsymbol{J}(\boldsymbol{r}) \tag{4.2a}$$

$$\nabla\nabla \cdot \boldsymbol{A}(\boldsymbol{r}) - \nabla^2 \boldsymbol{A}(\boldsymbol{r}) = k^2 \boldsymbol{A}(\boldsymbol{r}) + i\omega\mu_1\varepsilon_1 \nabla\phi(\boldsymbol{r}) + \mu_1 \boldsymbol{J}(\boldsymbol{r}), \tag{4.2b}$$

where $k^2 = \omega^2 \mu_1 \varepsilon_1$ and (4.2b) can be rewritten by using the gauge condition given in (2.12a) as

$$\nabla^2 \boldsymbol{A}(\boldsymbol{r}) + k^2 \boldsymbol{A}(\boldsymbol{r}) = -\mu_1 \boldsymbol{J}(\boldsymbol{r}). \tag{4.3}$$

In addition, taking the divergence of (2.9) and using the gauge condition given in (2.12a), the scalar wave equation in terms of the scalar potential is obtained as

$$\nabla^2 \phi(\boldsymbol{r}) + k^2 \phi(\boldsymbol{r}) = -\frac{1}{\varepsilon_1} \rho(\boldsymbol{r}). \tag{4.4}$$

Equations (4.3) and (4.4) are the same as the ones given by (2.13b) and (2.13c) without

considering magnetic sources in Region 1 as presented in Fig. 4.1. To derive the equivalence principle and extinction theorem for the magnetic vector potential, we will consider vector wave equation in (4.2a) and define a dyadic Green's function in the first region as

$$\nabla \times \nabla \times \boldsymbol{A}(\boldsymbol{r}) - \nabla\nabla \cdot \boldsymbol{A}(\boldsymbol{r}) - k^2 \boldsymbol{A}(\boldsymbol{r}) = \mu_1 \boldsymbol{J}(\boldsymbol{r}) \tag{4.5a}$$

$$\nabla \times \nabla \times \bar{\boldsymbol{G}}(\boldsymbol{r}, \boldsymbol{r'}) - \nabla\nabla \cdot \bar{\boldsymbol{G}}(\boldsymbol{r}, \boldsymbol{r'}) - k^2 \bar{\boldsymbol{G}}(\boldsymbol{r}, \boldsymbol{r'}) = \bar{\boldsymbol{I}}\delta(\boldsymbol{r} - \boldsymbol{r'}), \tag{4.5b}$$

where $\bar{\boldsymbol{G}}(\boldsymbol{r}, \boldsymbol{r'}) = \bar{\boldsymbol{I}} g(\boldsymbol{r}, \boldsymbol{r'}) = \bar{\boldsymbol{I}} \dfrac{e^{ik|\boldsymbol{r}-\boldsymbol{r'}|}}{4\pi|\boldsymbol{r}-\boldsymbol{r'}|}$, and $\bar{\boldsymbol{I}}$ is an identity matrix. Taking the dot product of (4.5a) with the dyadic Green's function, and (4.5b) with the magnetic vector potential

$$\begin{aligned} &\nabla \times \nabla \times \boldsymbol{A}(\boldsymbol{r}) \cdot \bar{\boldsymbol{G}}(\boldsymbol{r}, \boldsymbol{r'}) - \nabla\nabla \cdot \boldsymbol{A}(\boldsymbol{r}) \cdot \bar{\boldsymbol{G}}(\boldsymbol{r}, \boldsymbol{r'}) \\ &\qquad - k^2 \boldsymbol{A}(\boldsymbol{r}) \cdot \bar{\boldsymbol{G}}(\boldsymbol{r}, \boldsymbol{r'}) = \mu_1 \boldsymbol{J}(\boldsymbol{r}) \cdot \bar{\boldsymbol{G}}(\boldsymbol{r}, \boldsymbol{r'}) \end{aligned} \tag{4.6a}$$

$$\begin{aligned} &\boldsymbol{A}(\boldsymbol{r}) \cdot \nabla \times \nabla \times \bar{\boldsymbol{G}}(\boldsymbol{r}, \boldsymbol{r'}) - \boldsymbol{A}(\boldsymbol{r}) \cdot \nabla\nabla \cdot \bar{\boldsymbol{G}}(\boldsymbol{r}, \boldsymbol{r'}) \\ &\qquad - k^2 \boldsymbol{A}(\boldsymbol{r}) \cdot \bar{\boldsymbol{G}}(\boldsymbol{r}, \boldsymbol{r'}) = \boldsymbol{A}(\boldsymbol{r}) \cdot \bar{\boldsymbol{I}}\delta(\boldsymbol{r} - \boldsymbol{r'}), \end{aligned} \tag{4.6b}$$

and then subtracting (4.6a) from (4.6b), we obtain

$$\begin{aligned} &\boldsymbol{A}(\boldsymbol{r}) \cdot \bar{\boldsymbol{I}}\delta(\boldsymbol{r} - \boldsymbol{r'}) - \mu_1 \boldsymbol{J}(\boldsymbol{r}) \cdot \bar{\boldsymbol{G}}(\boldsymbol{r}, \boldsymbol{r'}) = \boldsymbol{A}(\boldsymbol{r}) \cdot \nabla \times \nabla \times \bar{\boldsymbol{G}}(\boldsymbol{r}, \boldsymbol{r'}) \\ &- \nabla \times \nabla \times \boldsymbol{A}(\boldsymbol{r}) \cdot \bar{\boldsymbol{G}}(\boldsymbol{r}, \boldsymbol{r'}) - \boldsymbol{A}(\boldsymbol{r}) \cdot \nabla\nabla \cdot \bar{\boldsymbol{G}}(\boldsymbol{r}, \boldsymbol{r'}) + \nabla\nabla \cdot \boldsymbol{A}(\boldsymbol{r}) \cdot \bar{\boldsymbol{G}}(\boldsymbol{r}, \boldsymbol{r'}). \end{aligned} \tag{4.7}$$

First and second terms in the right-hand side of (4.7) can be simplified as

$$\begin{aligned} &\boldsymbol{A}(\boldsymbol{r}) \cdot \nabla \times \nabla \times \bar{\boldsymbol{G}}(\boldsymbol{r}, \boldsymbol{r'}) - \nabla \times \nabla \times \boldsymbol{A}(\boldsymbol{r}) \cdot \bar{\boldsymbol{G}}(\boldsymbol{r}, \boldsymbol{r'}) \\ &\qquad = \nabla \times \boldsymbol{A}(\boldsymbol{r}) \cdot \nabla \times \bar{\boldsymbol{G}}(\boldsymbol{r}, \boldsymbol{r'}) - \nabla \cdot \left[\boldsymbol{A}(\boldsymbol{r}) \times \nabla \times \bar{\boldsymbol{G}}(\boldsymbol{r}, \boldsymbol{r'})\right] \\ &\qquad - \nabla \cdot \left[\nabla \times \boldsymbol{A}(\boldsymbol{r}) \times \bar{\boldsymbol{G}}(\boldsymbol{r}, \boldsymbol{r'})\right] - \nabla \times \boldsymbol{A}(\boldsymbol{r}) \cdot \nabla \times \bar{\boldsymbol{G}}(\boldsymbol{r}, \boldsymbol{r'}) \\ &\qquad = -\nabla \cdot [\boldsymbol{A}(\boldsymbol{r}) \times \nabla \times \bar{\boldsymbol{G}}(\boldsymbol{r}, \boldsymbol{r'}) + \nabla \times \boldsymbol{A}(\boldsymbol{r}) \times \bar{\boldsymbol{G}}(\boldsymbol{r}, \boldsymbol{r'})], \end{aligned} \tag{4.8}$$

where the third and the fourth terms can be rewritten as

$$\begin{aligned}\nabla\nabla\cdot\boldsymbol{A}(\boldsymbol{r})\cdot\bar{\boldsymbol{G}}(\boldsymbol{r},\boldsymbol{r'})-\boldsymbol{A}(\boldsymbol{r})\cdot\nabla\nabla\cdot\bar{\boldsymbol{G}}(\boldsymbol{r},\boldsymbol{r'}) \qquad (4.9)\\ =\nabla\cdot\left[\nabla\cdot\boldsymbol{A}(\boldsymbol{r})\bar{\boldsymbol{G}}(\boldsymbol{r},\boldsymbol{r'})\right]-\left[\nabla\cdot\boldsymbol{A}(\boldsymbol{r})\nabla\cdot\bar{\boldsymbol{G}}(\boldsymbol{r},\boldsymbol{r'})-\boldsymbol{A}(\boldsymbol{r})\cdot\nabla\nabla\cdot\bar{\boldsymbol{G}}(\boldsymbol{r},\boldsymbol{r'})\right]\\ =\nabla\cdot\left[\nabla\cdot\boldsymbol{A}(\boldsymbol{r})\bar{\boldsymbol{G}}(\boldsymbol{r},\boldsymbol{r'})\right]-\nabla\cdot\left[\boldsymbol{A}(\boldsymbol{r})\nabla\cdot\bar{\boldsymbol{G}}(\boldsymbol{r},\boldsymbol{r'})\right]\\ =\nabla\cdot\left[\nabla\cdot\boldsymbol{A}(\boldsymbol{r})\bar{\boldsymbol{G}}(\boldsymbol{r},\boldsymbol{r'})-\boldsymbol{A}(\boldsymbol{r})\nabla\cdot\bar{\boldsymbol{G}}(\boldsymbol{r},\boldsymbol{r'})\right].\end{aligned}$$

Inserting (4.8) and (4.9) into (4.7), a new expression is obtained as

$$\begin{aligned}\boldsymbol{A}(\boldsymbol{r})\cdot\bar{\boldsymbol{I}}\delta(\boldsymbol{r}-\boldsymbol{r'})-\mu_1\boldsymbol{J}(\boldsymbol{r})\cdot\bar{\boldsymbol{G}}(\boldsymbol{r},\boldsymbol{r'})= \qquad (4.10)\\ -\nabla\cdot\left[\boldsymbol{A}(\boldsymbol{r})\times\nabla\times\bar{\boldsymbol{G}}(\boldsymbol{r},\boldsymbol{r'})+\nabla\times\boldsymbol{A}(\boldsymbol{r})\times\bar{\boldsymbol{G}}(\boldsymbol{r},\boldsymbol{r'})\right]\\ +\nabla\cdot\left[\nabla\cdot\boldsymbol{A}(\boldsymbol{r})\bar{\boldsymbol{G}}(\boldsymbol{r},\boldsymbol{r'})-\boldsymbol{A}(\boldsymbol{r})\nabla\cdot\bar{\boldsymbol{G}}(\boldsymbol{r},\boldsymbol{r'})\right].\end{aligned}$$

Equation (4.10) can be rewritten by taking the volume integration of its both sides

$$\begin{aligned}\int\limits_{V=V_1}dv[\boldsymbol{A}(\boldsymbol{r})\cdot\bar{\boldsymbol{I}}\delta(\boldsymbol{r}-\boldsymbol{r'})-\mu_1\boldsymbol{J}(\boldsymbol{r})\cdot\bar{\boldsymbol{G}}(\boldsymbol{r},\boldsymbol{r'})]= \qquad (4.11)\\ -\int\limits_V dv\nabla\cdot\left[\boldsymbol{A}(\boldsymbol{r})\times\nabla\times\bar{\boldsymbol{G}}(\boldsymbol{r},\boldsymbol{r'})+\nabla\times\boldsymbol{A}(\boldsymbol{r})\times\bar{\boldsymbol{G}}(\boldsymbol{r},\boldsymbol{r'})\right]\\ +\int\limits_V dv\nabla\cdot\left[\nabla\cdot\boldsymbol{A}(\boldsymbol{r})\bar{\boldsymbol{G}}(\boldsymbol{r},\boldsymbol{r'})-\boldsymbol{A}(\boldsymbol{r})\nabla\cdot\bar{\boldsymbol{G}}(\boldsymbol{r},\boldsymbol{r'})\right],\end{aligned}$$

and then applying the divergence theorem to (4.11) resulting

$$\begin{aligned}\int\limits_V dv[\boldsymbol{A}(\boldsymbol{r})\cdot\bar{\boldsymbol{I}}\delta(\boldsymbol{r}-\boldsymbol{r'})-\mu_1\boldsymbol{J}(\boldsymbol{r})\cdot\bar{\boldsymbol{G}}(\boldsymbol{r},\boldsymbol{r'})]= \qquad (4.12)\\ +\oint\limits_S ds\hat{\boldsymbol{n}}\cdot\left[\boldsymbol{A}(\boldsymbol{r})\times\nabla\times\bar{\boldsymbol{G}}(\boldsymbol{r},\boldsymbol{r'})+\nabla\times\boldsymbol{A}(\boldsymbol{r})\times\bar{\boldsymbol{G}}(\boldsymbol{r},\boldsymbol{r'})\right]\\ -\oint\limits_S ds\hat{\boldsymbol{n}}\cdot\left[\nabla\cdot\boldsymbol{A}(\boldsymbol{r})\bar{\boldsymbol{G}}(\boldsymbol{r},\boldsymbol{r'})-\boldsymbol{A}(\boldsymbol{r})\nabla\cdot\bar{\boldsymbol{G}}(\boldsymbol{r},\boldsymbol{r'})\right],\end{aligned}$$

where $\hat{\boldsymbol{n}}$ is an unit outward normal vector on the surface S. As shown in Fig. 4.1, for the calculation of the magnetic vector potential in Region 1, the closed surface can be

decomposed into $S + S_{\text{inf}}$, where S_{inf} is at infinity. Therefore, (4.12) can be written as

$$\int_V dv[\boldsymbol{A}(\boldsymbol{r}) \cdot \bar{\boldsymbol{I}}\delta(\boldsymbol{r}-\boldsymbol{r'}) - \mu_1 \boldsymbol{J}(\boldsymbol{r}) \cdot \bar{\boldsymbol{G}}(\boldsymbol{r},\boldsymbol{r'})] = \tag{4.13}$$

$$+ \oint_{S+S_{\text{inf}}} ds\hat{\boldsymbol{n}} \cdot \left[\boldsymbol{A}(\boldsymbol{r}) \times \nabla \times \bar{\boldsymbol{G}}(\boldsymbol{r},\boldsymbol{r'}) + \nabla \times \boldsymbol{A}(\boldsymbol{r}) \times \bar{\boldsymbol{G}}(\boldsymbol{r},\boldsymbol{r'})\right]$$

$$- \oint_{S+S_{\text{inf}}} ds\hat{\boldsymbol{n}} \cdot \left[\nabla \cdot \boldsymbol{A}(\boldsymbol{r})\bar{\boldsymbol{G}}(\boldsymbol{r},\boldsymbol{r'}) - \boldsymbol{A}(\boldsymbol{r})\nabla \cdot \bar{\boldsymbol{G}}(\boldsymbol{r},\boldsymbol{r'})\right].$$

Result of the integration over S_{inf} is zero due to the radiation boundary condition. Therefore, (4.13) becomes

$$\boldsymbol{A}(\boldsymbol{r'}) - \int_V dv\mu_1 \boldsymbol{J}(\boldsymbol{r}) \cdot \bar{\boldsymbol{G}}(\boldsymbol{r},\boldsymbol{r'}) = \tag{4.14}$$

$$+ \int_S ds \left\{[\hat{\boldsymbol{n}} \times \boldsymbol{A}(\boldsymbol{r})] \cdot \nabla \times \bar{\boldsymbol{G}}(\boldsymbol{r},\boldsymbol{r'}) + [\hat{\boldsymbol{n}} \times \nabla \times \boldsymbol{A}(\boldsymbol{r})] \cdot \bar{\boldsymbol{G}}(\boldsymbol{r},\boldsymbol{r'})\right\}$$

$$- \int_S ds\hat{\boldsymbol{n}} \cdot \left[\nabla \cdot \boldsymbol{A}(\boldsymbol{r})\bar{\boldsymbol{G}}(\boldsymbol{r},\boldsymbol{r'}) - \boldsymbol{A}(\boldsymbol{r})\nabla \cdot \bar{\boldsymbol{G}}(\boldsymbol{r},\boldsymbol{r'})\right].$$

Using $\bar{\boldsymbol{G}}(\boldsymbol{r},\boldsymbol{r'}) = \bar{\boldsymbol{I}}g(\boldsymbol{r},\boldsymbol{r'})$ in (4.14), we obtain

$$\begin{aligned}
\boldsymbol{A}(\boldsymbol{r'}) - \int_V dv\mu_1 \boldsymbol{J}(\boldsymbol{r}) \cdot \bar{\boldsymbol{I}}g(\boldsymbol{r},\boldsymbol{r'}) &= \boldsymbol{A}(\boldsymbol{r'}) - \int_V dv\mu_1 \boldsymbol{J}(\boldsymbol{r})g(\boldsymbol{r},\boldsymbol{r'}) \\
&= \int_S ds \left\{[\hat{\boldsymbol{n}} \times \boldsymbol{A}(\boldsymbol{r})] \cdot \nabla \times \bar{\boldsymbol{I}}g(\boldsymbol{r},\boldsymbol{r'}) + [\hat{\boldsymbol{n}} \times \nabla \times \boldsymbol{A}(\boldsymbol{r})] \cdot \bar{\boldsymbol{I}}g(\boldsymbol{r},\boldsymbol{r'})\right\} \\
&- \int_S ds\hat{\boldsymbol{n}} \cdot \left[\nabla \cdot \boldsymbol{A}(\boldsymbol{r})\bar{\boldsymbol{I}}g(\boldsymbol{r},\boldsymbol{r'}) - \boldsymbol{A}(\boldsymbol{r})\nabla \cdot \bar{\boldsymbol{I}}g(\boldsymbol{r},\boldsymbol{r'})\right] \\
&= \int_S ds \left\{[\hat{\boldsymbol{n}} \times \boldsymbol{A}(\boldsymbol{r})] \cdot \left[\nabla g(\boldsymbol{r},\boldsymbol{r'}) \times \bar{\boldsymbol{I}} + g(\boldsymbol{r},\boldsymbol{r'})\nabla \times \bar{\boldsymbol{I}}\right] + [\hat{\boldsymbol{n}} \times \nabla \times \boldsymbol{A}(\boldsymbol{r})]\, g(\boldsymbol{r},\boldsymbol{r'})\right\} \\
&- \int_S ds \left[\hat{\boldsymbol{n}}\nabla \cdot \boldsymbol{A}(\boldsymbol{r})g(\boldsymbol{r},\boldsymbol{r'}) - \hat{\boldsymbol{n}} \cdot \boldsymbol{A}(\boldsymbol{r}) \left(\nabla g(\boldsymbol{r},\boldsymbol{r'}) \cdot \bar{\boldsymbol{I}} + g(\boldsymbol{r},\boldsymbol{r'})\nabla \cdot \bar{\boldsymbol{I}}\right)\right] \\
&= \int_S ds \left\{[\hat{\boldsymbol{n}} \times \boldsymbol{A}(\boldsymbol{r})] \times \nabla g(\boldsymbol{r},\boldsymbol{r'}) + [\hat{\boldsymbol{n}} \times \nabla \times \boldsymbol{A}(\boldsymbol{r})]\, g(\boldsymbol{r},\boldsymbol{r'})\right\} \\
&- \int_S ds \left[\hat{\boldsymbol{n}}\nabla \cdot \boldsymbol{A}(\boldsymbol{r})g(\boldsymbol{r},\boldsymbol{r'}) - \hat{\boldsymbol{n}} \cdot \boldsymbol{A}(\boldsymbol{r})\nabla g(\boldsymbol{r},\boldsymbol{r'})\right].
\end{aligned} \tag{4.15}$$

Equation (4.15) can be alternatively written as

$$\begin{aligned}\boldsymbol{A}(\boldsymbol{r}) - \int_V dv' \mu_1 \boldsymbol{J}(\boldsymbol{r'}) g(\boldsymbol{r}, \boldsymbol{r'}) = \\ = \int_S ds' \left\{ \left[\hat{\boldsymbol{n}}' \times \boldsymbol{A}(\boldsymbol{r'})\right] \times \nabla' g(\boldsymbol{r}, \boldsymbol{r'}) + \left[\hat{\boldsymbol{n}}' \times \nabla' \times \boldsymbol{A}(\boldsymbol{r'})\right] g(\boldsymbol{r}, \boldsymbol{r'}) \right\} \\ - \int_S ds' \left[\hat{\boldsymbol{n}}' \nabla' \cdot \boldsymbol{A}(\boldsymbol{r'}) g(\boldsymbol{r}, \boldsymbol{r'}) - \hat{\boldsymbol{n}}' \cdot \boldsymbol{A}(\boldsymbol{r'}) \nabla' g(\boldsymbol{r}, \boldsymbol{r'})\right]. \end{aligned} \tag{4.16}$$

where $\boldsymbol{r}$ and $\boldsymbol{r'}$ are swapped due to the reciprocity theorem (as a consequence of the symmetry in a mathematical sense as explained in [81] where $\hat{\boldsymbol{n}}'$ is an unit outward normal vector on the surface S). As given in Fig. 4.1, $\boldsymbol{J}(\boldsymbol{r'})$ radiates in Region 1 and creates the induced current on the surface of the scatterer S $\left[\hat{\boldsymbol{n}}' \times \boldsymbol{H}(\boldsymbol{r'})\right]$. Hence, using

$$\boldsymbol{A}_{\text{inc}}(\boldsymbol{r}) = \int_V dv' \mu_1 \boldsymbol{J}(\boldsymbol{r'}) g(\boldsymbol{r}, \boldsymbol{r'}) \tag{4.17a}$$

$$\boldsymbol{H}(\boldsymbol{r'}) = \frac{1}{\mu_1} \nabla' \times \boldsymbol{A}(\boldsymbol{r'}), \tag{4.17b}$$

and substituting (4.17) into (4.16), the following equation is obtained;

$$\begin{aligned}\boldsymbol{A}(\boldsymbol{r}) = \boldsymbol{A}_{\text{inc}}(\boldsymbol{r}) + \int_S ds' \left[\mu_1 g(\boldsymbol{r}, \boldsymbol{r'}) \hat{\boldsymbol{n}}' \times \boldsymbol{H}(\boldsymbol{r'}) - \nabla' g(\boldsymbol{r}, \boldsymbol{r'}) \times \left(\hat{\boldsymbol{n}}' \times \boldsymbol{A}(\boldsymbol{r'})\right)\right] \\ + \int_S ds' \left[\hat{\boldsymbol{n}}' \cdot \boldsymbol{A}(\boldsymbol{r'}) \nabla' g(\boldsymbol{r}, \boldsymbol{r'}) - \hat{\boldsymbol{n}}' g(\boldsymbol{r}, \boldsymbol{r'}) \nabla' \cdot \boldsymbol{A}(\boldsymbol{r'})\right]. \end{aligned} \tag{4.18}$$

The above equation is obtained for Region 1, where the term $\boldsymbol{A}(\boldsymbol{r})$ is zero if $\boldsymbol{r} \in V_2$ because of the shifting property of the delta function. Hence, (4.18) can be written as

$$\begin{aligned}\left.\begin{array}{ll} \boldsymbol{r} \in V_1 & \boldsymbol{A}(\boldsymbol{r}) \\ \boldsymbol{r} \in V_2 & 0 \end{array}\right\} = \boldsymbol{A}_{\text{inc}}(\boldsymbol{r}) + \int_S ds' \left\{\mu_1 g(\boldsymbol{r}, \boldsymbol{r'}) \hat{\boldsymbol{n}}' \times \boldsymbol{H}(\boldsymbol{r'}) - \nabla' g(\boldsymbol{r}, \boldsymbol{r'}) \times \left[\hat{\boldsymbol{n}}' \times \boldsymbol{A}(\boldsymbol{r'})\right]\right\} \\ + \int_S ds' \left[\hat{\boldsymbol{n}}' \cdot \boldsymbol{A}(\boldsymbol{r'}) \nabla' g(\boldsymbol{r}, \boldsymbol{r'}) - \hat{\boldsymbol{n}}' g(\boldsymbol{r}, \boldsymbol{r'}) \nabla' \cdot \boldsymbol{A}(\boldsymbol{r'})\right]. \end{aligned} \tag{4.19}$$

Equation (4.19) states the integral equation for the magnetic vector potential, and it is the building block of the surface integral equation for the potentials. The physical meaning of (4.19) is that the total magnetic vector potential $\boldsymbol{A}(\boldsymbol{r})$ in V_1

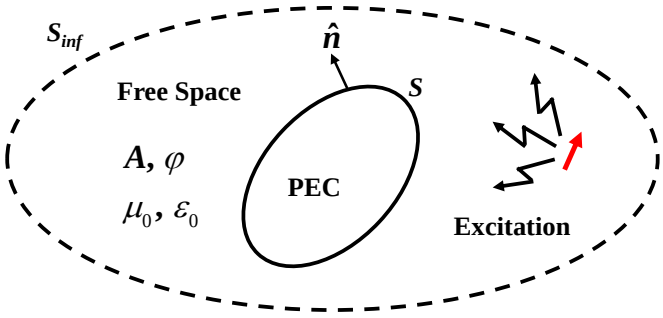


Figure 4.2: Configuration of region and medium to obtain surface PIEs for a PEC scatterer.

can be decomposed into the incident potential $\boldsymbol{A}_{\text{inc}}(\boldsymbol{r})$ on the right-hand side which is generated by the actual source $\boldsymbol{J}(\boldsymbol{r})$, plus potentials generated by the equivalent sources $\boldsymbol{J}_{\text{s}}(\boldsymbol{r'}) = \hat{\boldsymbol{n}}' \times \boldsymbol{H}(\boldsymbol{r'})$, $\hat{\boldsymbol{n}}' \times \boldsymbol{A}(\boldsymbol{r'})$, $\hat{\boldsymbol{n}}' \cdot \boldsymbol{A}(\boldsymbol{r'})$ and $\hat{\boldsymbol{n}}' \nabla' \cdot \boldsymbol{A}(\boldsymbol{r'})$ induced on the surface S. Moreover, the lower term on left-hand side of (4.19) known as the extinction theorem reflects that the total magnetic vector potential is zero if the observation point is in V_2. This implies that the equivalent sources on the surfaces produce a potential that exactly cancels $\boldsymbol{A}_{\text{inc}}(\boldsymbol{r})$ in V_2. The governing equation for the calculation of the potential in V_2 can be obtained in a similar way.

Fig. 4.2 in contrast to Fig. 4.1 presents a scattering problem involving a PEC scatterer in free space illuminated by an incident magnetic vector potential. Surface electric current and charge densities, which are known as surface equivalent sources, will be induced on the surface of the scatterer as derived in (4.19). In the equivalent problem, these sources should produce a potential that exactly cancels the incident potential inside the scatterer. In addition to cancelling the incident potential, the equivalent sources also generate electromagnetic fields outside the scatterer yielding the scattered fields. Therefore, utilizing the surface equivalence formula given in (4.19), PIEs for PECs are obtained by satisfying the boundary conditions for the scalar and vector potentials on the surface of the PEC scatterer as follows:

$$\hat{\boldsymbol{n}} \times \boldsymbol{E}(\boldsymbol{r}) = \hat{\boldsymbol{n}} \times [i\omega \boldsymbol{A}(\boldsymbol{r}) - \nabla\phi(\boldsymbol{r})] = 0 \rightarrow \begin{cases} \hat{\boldsymbol{n}} \times \boldsymbol{A}(\boldsymbol{r}) = 0 \\ \hat{\boldsymbol{n}} \times \nabla\phi(\boldsymbol{r}) = 0 \end{cases} . \tag{4.20}$$

One can choose $\phi(\boldsymbol{r}) = 0$, on the surface of PEC. Therefore, all boundary conditions

for the potentials on the surface of PEC can be summarized as

$$\hat{\boldsymbol{n}} \times \boldsymbol{A}(\boldsymbol{r}) = 0 \tag{4.21a}$$

$$\hat{\boldsymbol{n}} \times \nabla\phi(\boldsymbol{r}) = 0 \tag{4.21b}$$

$$\phi(\boldsymbol{r}) = 0 \tag{4.21c}$$

$$\nabla \cdot \boldsymbol{A}(\boldsymbol{r}) = i\omega\mu_0\varepsilon_0\phi(\boldsymbol{r}) = 0. \tag{4.21d}$$

Considering the geometry in Fig. 4.2, and substituting (4.21) into (4.19) when $\boldsymbol{r}$ approaches $\boldsymbol{r'}$ leads to

$$\left.\begin{array}{ll} \boldsymbol{r} \in V_1 & \boldsymbol{A}(\boldsymbol{r}) \\ \boldsymbol{r} \in V_2 & 0 \end{array}\right\} = \boldsymbol{A}_{\text{inc}}(\boldsymbol{r}) + \int_S ds' \left[\mu_0 g(\boldsymbol{r},\boldsymbol{r'})\hat{\boldsymbol{n}}' \times \boldsymbol{H}(\boldsymbol{r'}) + \hat{\boldsymbol{n}}' \cdot \boldsymbol{A}(\boldsymbol{r'})\nabla' g(\boldsymbol{r},\boldsymbol{r'})\right]. \tag{4.22}$$

Then, the PIE for the magnetic vector potential $\boldsymbol{A}(\boldsymbol{r})$ in the presence of a PEC scatterer is obtained in a tangential form of (4.22) as

$$-\hat{\boldsymbol{n}} \times \hat{\boldsymbol{n}} \times \boldsymbol{A}_{\text{inc}}(\boldsymbol{r}) = \hat{\boldsymbol{n}} \times \hat{\boldsymbol{n}} \times \int_S ds' \left[\mu_0 g(\boldsymbol{r},\boldsymbol{r'})\boldsymbol{J}_{\text{s}}(\boldsymbol{r'}) + \Sigma(\boldsymbol{r'})\nabla' g(\boldsymbol{r},\boldsymbol{r'})\right] \quad \boldsymbol{r} \in S^+, \tag{4.23}$$

where S^+ is a surface approaching S from the outside and it is slightly larger than S, in other words, the potentials are zero when $\boldsymbol{r} \in S^-$. In addition, $\boldsymbol{J}_{\text{s}}(\boldsymbol{r'}) = \hat{\boldsymbol{n}}' \times \boldsymbol{H}(\boldsymbol{r'})$ and $\Sigma(\boldsymbol{r'}) = \hat{\boldsymbol{n}}' \cdot \boldsymbol{A}(\boldsymbol{r'})$ are equivalent unknown sources on the surface of the PEC scatterer. $\Sigma(\boldsymbol{r'})$ is related to the distribution of the electric charge density due to the fact that $[\hat{\boldsymbol{n}} \cdot \varepsilon_0 \boldsymbol{E}(\boldsymbol{r}) = i\omega\varepsilon_0 \hat{\boldsymbol{n}} \cdot \boldsymbol{A}(\boldsymbol{r}) - \varepsilon_0 \hat{\boldsymbol{n}} \cdot \nabla\phi(\boldsymbol{r})]$. There are two types of unknowns in (4.23) that require to be expanded in terms of linearly independent basis functions using MoM. Therefore, a second equation is required to be solved in tandem with (4.23) to match the number of unknowns. This can be achieved by taking the normal component of (4.22)

$$\hat{\boldsymbol{n}} \cdot \boldsymbol{A}(\boldsymbol{r}) = \hat{\boldsymbol{n}} \cdot \boldsymbol{A}_{\text{inc}}(\boldsymbol{r}) + \hat{\boldsymbol{n}} \cdot \int_S ds' \left[\mu_0 g(\boldsymbol{r},\boldsymbol{r'})\boldsymbol{J}_s(\boldsymbol{r'}) + \Sigma(\boldsymbol{r'})\nabla' g(\boldsymbol{r},\boldsymbol{r'})\right] \quad \boldsymbol{r} \in S^+. \tag{4.24}$$

The equivalent current and charge in (4.23) and (4.24) can be expanded in term of RWG and pulse functions, respectively. However, normal testing of (4.22) requires the expansion of charge with higher-order basis functions instead of pulse functions to obtain more accurate results [92]. Using higher-order basis functions increases the complexity of the implementation. Instead, the calculation can be accomplished

by attaining the surface equivalence theorem for the scalar potential or taking the divergence of (4.22) and using the Lorenz gauge. By taking the divergence of (4.22), the scalar potential for a PEC scatterer can be obtained as

$$\left.\begin{array}{ll} \boldsymbol{r}\in V_1 & \nabla\cdot\boldsymbol{A}(\boldsymbol{r}) \\ \boldsymbol{r}\in V_2 & 0 \end{array}\right\} = \nabla\cdot\boldsymbol{A}_{\text{inc}}(\boldsymbol{r}) + \int\limits_S ds'\nabla\cdot\left[\mu_0 g(\boldsymbol{r},\boldsymbol{r'})\boldsymbol{J}_s(\boldsymbol{r'}) + \Sigma(\boldsymbol{r'})\nabla' g(\boldsymbol{r},\boldsymbol{r'})\right]. \quad (4.25)$$

By invoking the Lorenz gauge and applying the boundary conditions for the potentials, from (4.25) the following equation can be obtained:

$$\begin{aligned} 0 =& i\omega\mu_0\varepsilon_0\phi_{\text{inc}} + \int\limits_S ds'\left\{\nabla\cdot\left[\mu_0 g(\boldsymbol{r},\boldsymbol{r'})\boldsymbol{J}_s(\boldsymbol{r'})\right] + \nabla\cdot\left[\Sigma(\boldsymbol{r'})\nabla' g(\boldsymbol{r},\boldsymbol{r'})\right]\right\} \\ =& i\omega\mu_0\varepsilon_0\phi_{\text{inc}} + \int\limits_S ds'\left[\mu_0\nabla\cdot\boldsymbol{J}_s(\boldsymbol{r'})g(\boldsymbol{r},\boldsymbol{r'}) + \mu_0\boldsymbol{J}_s(\boldsymbol{r'})\cdot\nabla g(\boldsymbol{r},\boldsymbol{r'}) + \Sigma(\boldsymbol{r'})\nabla\cdot\nabla' g(\boldsymbol{r},\boldsymbol{r'})\right] \\ =& i\omega\mu_0\varepsilon_0\phi_{\text{inc}} + \int\limits_S ds'\left[\mu_0\boldsymbol{J}_s(\boldsymbol{r'})\cdot\nabla g(\boldsymbol{r},\boldsymbol{r'}) - \Sigma(\boldsymbol{r'})\nabla^2 g(\boldsymbol{r},\boldsymbol{r'})\right] \\ =& i\omega\mu_0\varepsilon_0\phi_{\text{inc}} + \int\limits_S ds'\left\{\mu_0\nabla'\cdot\boldsymbol{J}_s(\boldsymbol{r'})g(\boldsymbol{r},\boldsymbol{r'}) - \mu_0\nabla'\cdot\left[\boldsymbol{J}_s(\boldsymbol{r'})g(\boldsymbol{r},\boldsymbol{r'})\right] - \Sigma(\boldsymbol{r'})\nabla^2 g(\boldsymbol{r},\boldsymbol{r'})\right\} \\ =& i\omega\mu_0\varepsilon_0\phi_{\text{inc}} + \int\limits_S ds'\left[\mu_0\nabla'\cdot\boldsymbol{J}_s(\boldsymbol{r'})g(\boldsymbol{r},\boldsymbol{r'}) - \Sigma(\boldsymbol{r'})\nabla^2 g(\boldsymbol{r},\boldsymbol{r'})\right] \\ =& i\omega\mu_0\varepsilon_0\phi_{\text{inc}} + \int\limits_S ds'\left[\mu_0\nabla'\cdot\boldsymbol{J}_s(\boldsymbol{r'})g(\boldsymbol{r},\boldsymbol{r'}) + k^2 g(\boldsymbol{r},\boldsymbol{r'})\Sigma(\boldsymbol{r'})\right] \quad \boldsymbol{r}\in S. \end{aligned} \quad (4.26)$$

It can be shown [52] that equation (4.26) is a weak form of the current continuity equation given in (2.4a). For this purpose, solution of the scalar potential wave equation in the first region using the scalar Green's function can be written as

$$\phi(\boldsymbol{r'}) = \frac{1}{\varepsilon_0}\int\limits_{V_1} dv g(\boldsymbol{r},\boldsymbol{r'})\rho(\boldsymbol{r}) - \int\limits_{S+S_{\text{inf}}} ds\,\hat{\boldsymbol{n}}\cdot\left[g(\boldsymbol{r},\boldsymbol{r'})\nabla\phi(\boldsymbol{r}) - \phi(\boldsymbol{r})\nabla g(\boldsymbol{r},\boldsymbol{r'})\right]. \quad (4.27)$$

By swapping $\boldsymbol{r}\rightarrow\boldsymbol{r'}$ due to the reciprocity theorem [81], and invoking the radiation boundary condition which results in vanishing of the integral over S_{inf}, (4.26) is modified as

$$\left.\begin{array}{ll} r\in V_1 & \phi(\boldsymbol{r}) \\ r\in V_2 & 0 \end{array}\right\} = \phi_{\text{inc}}(\boldsymbol{r}) - \int\limits_S ds'\,\hat{\boldsymbol{n}}'\cdot\left[g(\boldsymbol{r},\boldsymbol{r'})\nabla'\phi(\boldsymbol{r'}) - \phi(\boldsymbol{r'})\nabla' g(\boldsymbol{r},\boldsymbol{r'})\right], \quad (4.28)$$

where $\phi_{\text{inc}}(\boldsymbol{r})$ is the incident scalar potential generated by the charge source in V_1 as

$$\phi_{\text{inc}}(\boldsymbol{r}) = \frac{1}{\varepsilon_0} \int\limits_V dv g(\boldsymbol{r}, \boldsymbol{r'}) \rho(\boldsymbol{r'}) \quad \text{when} \quad \boldsymbol{r} \in V_1. \tag{4.29}$$

Equation (4.28) is the integral equation used for the scalar potential. The lower term on the left-hand side of (4.28) reflects that the total electric scalar potential is zero if the observation point is in V_2. This implies that the equivalent sources on the boundary produce potentials that exactly cancel $\phi_{\text{inc}}(\boldsymbol{r})$ in V_2, which is known as the extinction theorem. On the surface of the conductor, (4.28) is reduced to

$$\phi_{\text{inc}}(\boldsymbol{r}) = \int\limits_S ds' \hat{\boldsymbol{n}}' \cdot \nabla' \phi(\boldsymbol{r'}) g(\boldsymbol{r}, \boldsymbol{r'}) \quad \text{when} \quad \boldsymbol{r} \in S. \tag{4.30}$$

Substituting (4.29) into (4.26) yields

$$\begin{aligned}
0 =& i\omega\mu\varepsilon_0 \int\limits_S ds' \hat{\boldsymbol{n}}' \cdot \nabla' \phi(\boldsymbol{r'}) g(\boldsymbol{r}, \boldsymbol{r'}) + \int\limits_S ds' \left[\mu_0 \nabla' \cdot \boldsymbol{J}(\boldsymbol{r'}) g(\boldsymbol{r}, \boldsymbol{r'}) + k^2 g(\boldsymbol{r}, \boldsymbol{r'}) \Sigma(\boldsymbol{r'}) \right] \\
=& \int\limits_S ds' \left[\hat{\boldsymbol{n}}' \cdot i\omega\mu_0\varepsilon_0 \nabla' \phi(\boldsymbol{r'}) g(\boldsymbol{r}, \boldsymbol{r'}) + \mu_0 \nabla' \cdot \boldsymbol{J}(\boldsymbol{r}) g(\boldsymbol{r}, \boldsymbol{r'}) + k^2 g(\boldsymbol{r}, \boldsymbol{r'}) \Sigma(\boldsymbol{r'}) \right] \\
=& \int\limits_S ds' g(\boldsymbol{r}, \boldsymbol{r'}) \left[i\omega\mu_0\varepsilon_0 \hat{\boldsymbol{n}}' \cdot \nabla' \phi(\boldsymbol{r'}) + \mu_0 \nabla' \cdot \boldsymbol{J}(\boldsymbol{r}) + k^2 \Sigma(\boldsymbol{r'}) \right] \\
=& \int\limits_S ds' \mu_0 g(\boldsymbol{r}, \boldsymbol{r'}) \left[i\omega \left(\varepsilon_0 \hat{\boldsymbol{n}}' \cdot \nabla' \phi(\boldsymbol{r'}) - i\omega\varepsilon_0 \underbrace{\Sigma(\boldsymbol{r'})}_{\hat{\boldsymbol{n}}' \cdot \boldsymbol{A}(\boldsymbol{r'})} \right) + \nabla' \cdot \boldsymbol{J}(\boldsymbol{r'}) \right] \\
=& \int\limits_S ds' g(\boldsymbol{r}, \boldsymbol{r'}) \left[-i\omega\rho(\boldsymbol{r'}) + \nabla' \cdot \boldsymbol{J}(\boldsymbol{r'}) \right]
\end{aligned} \tag{4.31}$$

Therefore, it is shown that (4.26) is satisfying the weak continuity equation, and when the incident scalar potential is zero in (4.30) (which will be discussed later in the excitation section), it leads to $\hat{\boldsymbol{n}} \cdot \nabla \phi(\boldsymbol{r}) = 0$ on the surface of a PEC scatterer. Therefore, the charge contribution can be written as $\hat{\boldsymbol{n}} \cdot \varepsilon \boldsymbol{E}(\boldsymbol{r}) = \hat{\boldsymbol{n}} \cdot [i\omega\varepsilon \boldsymbol{A}(\boldsymbol{r}) - \varepsilon \nabla \phi(\boldsymbol{r})] = i\omega\varepsilon \hat{\boldsymbol{n}} \cdot \boldsymbol{A}(\boldsymbol{r}) = i\omega\varepsilon \Sigma(\boldsymbol{r})$.

Eventually, the obtained integral equations for the tangential component of the magnetic vector potential (4.23) and the scalar potential (4.26) can be solved simultaneously using MoM. Discretization of the geometry and the details of the MoM formulation for (4.23) and (4.26) are provided in the following section.

4.2.1 Method of Moments

SIEs are usually constituted by linear integro-differential operators which can be represented in a general form as

$$\mathcal{L}\{\boldsymbol{f}(\boldsymbol{r})\} = \boldsymbol{g}(\boldsymbol{r}). \tag{4.32}$$

In (4.32), $\mathcal{L}$ is a linear integro-differential operator that will be applied to the scalar or vector function $\boldsymbol{f}(\boldsymbol{r})$, and $\boldsymbol{g}(\boldsymbol{r})$ is considered as a known scalar/vector excitation function. Usually, the IEs for electromagnetic problems cannot be solved analytically. However, using MoM these IEs are converted to matrix equations which can be solved numerically [3,4]. The MoM procedure starts by expanding the unknown function $\boldsymbol{f}(\boldsymbol{r})$ in terms of linearly independent basis functions $\boldsymbol{b}_n(\boldsymbol{r})$ as

$$\boldsymbol{f}(\boldsymbol{r}) \approx \sum_{n=1}^{N} \alpha_n \boldsymbol{b}_n(\boldsymbol{r}), \tag{4.33}$$

where α_n, $n = 1, 2, ..., N$ are the unknown coefficients, and finite number of basis functions (N) are used for the expansion. Substituting (4.33) into (4.32) leads to

$$\sum_{n=1}^{N} \alpha_n \mathcal{L}\{\boldsymbol{b}_n\}(\boldsymbol{r}) = \boldsymbol{g}(\boldsymbol{r}). \tag{4.34}$$

Expansion of $\boldsymbol{f}(\boldsymbol{r})$ using linearly independent basis functions $\boldsymbol{b}_n(\boldsymbol{r})$ with the corresponding unknown coefficients α_n results in an equation with N unknowns. Therefore, in order to obtain sufficient number of equations (i.e., N equations with N unknowns) and so a unique solution, it requires to test (4.34) with N different testing functions $\boldsymbol{t}_m(\boldsymbol{r})$ for $m = 1, 2, ..., N$, leading to

$$\int d\boldsymbol{r} \boldsymbol{t}_m(\boldsymbol{r}) \cdot \sum_{n=1}^{N} \alpha_n \mathcal{L}\{\boldsymbol{b}_n\}(\boldsymbol{r}) = \int d\boldsymbol{r} \boldsymbol{t}_m(\boldsymbol{r}) \cdot \boldsymbol{g}(\boldsymbol{r}) \quad (m = 1, 2, ..., N). \tag{4.35}$$

By changing the order of integration and summation, the final matrix equation can be written as

$$\bar{\boldsymbol{Z}} \boldsymbol{I} = \boldsymbol{V}, \tag{4.36}$$

where $\bar{\boldsymbol{Z}}$ and $\boldsymbol{V}$ are the impedance matrix and the excitation vector, respectively. The entries of $\bar{\boldsymbol{Z}}$, $[\bar{\boldsymbol{Z}}]_{m,n}$ and the entries of $\boldsymbol{V}$, $[\boldsymbol{V}]_m$, are given by

$$[\bar{\boldsymbol{Z}}]_{m,n} = \int d\boldsymbol{r} \boldsymbol{t}_m(\boldsymbol{r}) \cdot \mathcal{L}\{\boldsymbol{b}_n\}(\boldsymbol{r}) \tag{4.37a}$$

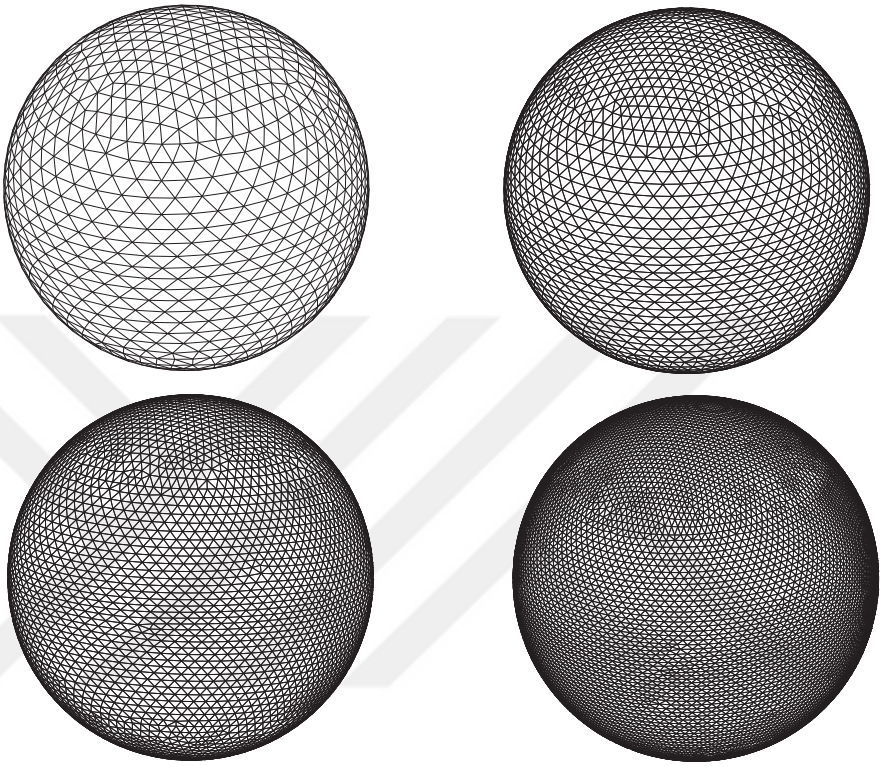
$$[\boldsymbol{V}]_m = \int d\boldsymbol{r} \boldsymbol{t}_m(\boldsymbol{r}) \cdot \boldsymbol{g}(\boldsymbol{r}). \tag{4.37b}$$

The implementation of MoM requires the discretization of the geometries so that we can model arbitrarily shaped electromagnetic problems. For this purpose, planar triangular meshes are usually used as a common approach to discretize the surfaces of a given geometry. Different triangular mesh sizes for the surface discretization of a sphere and a benchmark object known as stealth airborne target Flamme are presented in Fig. 4.3 [5]. As a result, solution of SIEs using MoM requires basis functions defined on the surface of the planar triangles. For this purpose, RWG functions [111] are the usual basis functions which are defined on surfaces of planar triangles and used for the popular SIEs as shown in Fig. 4.4. An RWG function is defined on two triangles with a common edge as

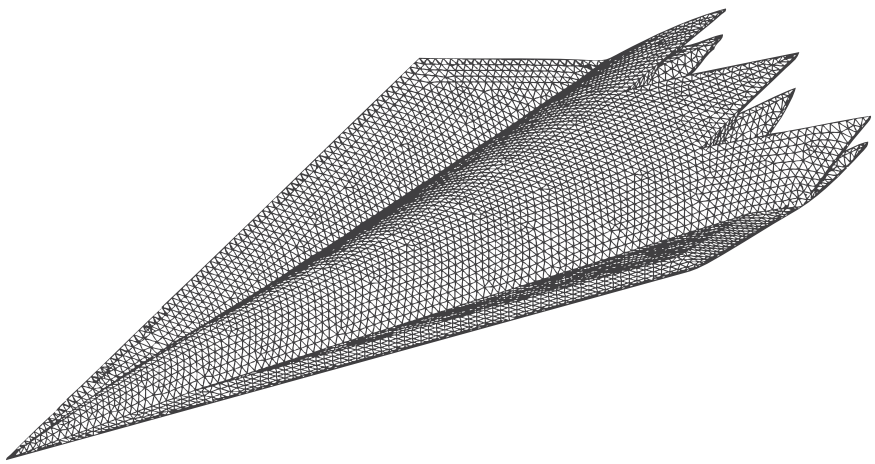
$$\boldsymbol{b}_n^{\mathrm{RWG}}(\boldsymbol{r}) = \begin{cases} \dfrac{l_n}{2A_{n1}}(\boldsymbol{r} - \boldsymbol{r}_{n1}), & \boldsymbol{r} \in S_{n1} \\ \dfrac{l_n}{2A_{n2}}(\boldsymbol{r}_{n2} - \boldsymbol{r}), & \boldsymbol{r} \in S_{n2} \\ 0, & \boldsymbol{r} \notin S_n \end{cases}, \tag{4.38}$$

where l_n is length of the common edge between the paired triangles. A_{n1} and A_{n2} represent the areas of the first triangle (S_{n1}) and the second triangle (S_{n2}), respectively. In addition, $\boldsymbol{r}_{n1}$ and $\boldsymbol{r}_{n2}$ are position vectors from the origin to the free vertices of the first and second triangles, respectively, where the surface current starts and ends its distribution. In addition, the RWG function should be divergence conforming (not to add fictitious charges to electromagnetic problems) because the divergence of the surface current density expanded in terms of RWG functions is proportional to the surface charge density through the equation of continuity. As a result, the divergence of (4.38) is obtained as

$$\nabla \cdot \boldsymbol{b}_n^{\mathrm{RWG}}(\boldsymbol{r}) = \begin{cases} \dfrac{l_n}{A_{n1}}, & \boldsymbol{r} \in S_{n1} \\ -\dfrac{l_n}{A_{n2}}, & \boldsymbol{r} \in S_{n2} \\ 0, & \boldsymbol{r} \notin S_n \end{cases}. \tag{4.39}$$



(a)



(b)

Figure 4.3: (a) Triangular discretization of a sphere using various mesh sizes. (b) Modeling of a complicated benchmark object known as stealth airborne target Flamme with planar triangular meshes [5].

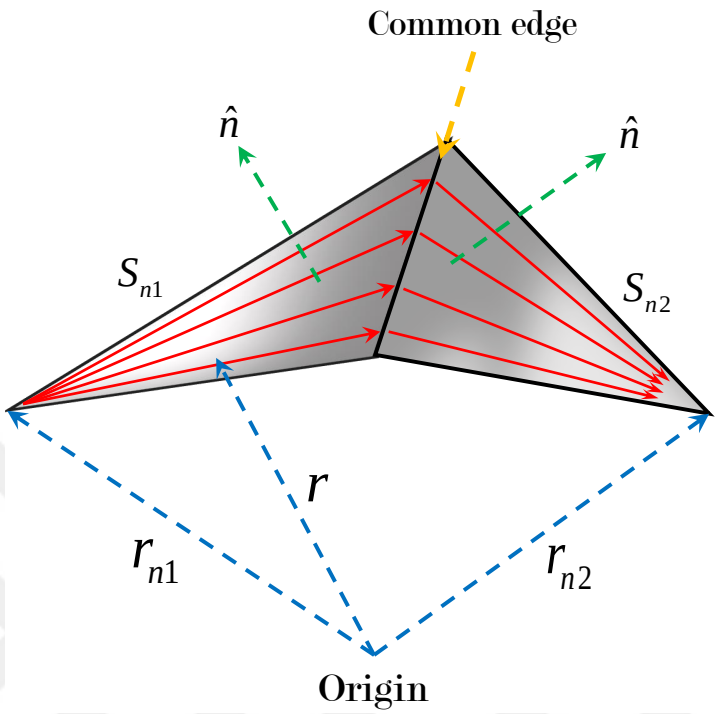


Figure 4.4: An RWG function defined on a pair of triangles sharing an edge.

In (4.39), the total charge density associated with an adjacent triangle pairs is zero. Therefore, there is no accumulation of charges on the edge and the RWG function is divergence conforming.

4.2.2 Discretization of Potential Integral Equations

For numerical solutions of PIEs using MoM, small planar triangles are among the promising choices for the surface discretization of arbitrarily-shaped objects where the basis functions are defined on triangular domains to expand unknown surface currents and charge contributions. In this subsection, discretization of PIEs will be explained. For the sake of simplicity, PIEs that are going to be discretized are repeated as

$$-\hat{\boldsymbol{n}} \times \hat{\boldsymbol{n}} \times \boldsymbol{A}_{\text{inc}}(\boldsymbol{r}) = \hat{\boldsymbol{n}} \times \hat{\boldsymbol{n}} \times \int_S ds' \left[\mu_0 g(\boldsymbol{r}, \boldsymbol{r'}) \boldsymbol{J}(\boldsymbol{r'}) + \Sigma(\boldsymbol{r'}) \nabla' g(\boldsymbol{r}, \boldsymbol{r'})\right] \tag{4.40a}$$

$$-i\omega\mu_0\varepsilon_0\phi_{\text{inc}} = \int_S ds' \left[\mu_0 g(\boldsymbol{r}, \boldsymbol{r'}) \nabla' \cdot \boldsymbol{J}(\boldsymbol{r'}) + \omega^2 \mu_0 \varepsilon_0 g(\boldsymbol{r}, \boldsymbol{r'}) \Sigma(\boldsymbol{r'})\right], \tag{4.40b}$$

where the surface current density $\boldsymbol{J}(\boldsymbol{r})$ and the normal component of magnetic vector potential $\Sigma(\boldsymbol{r}) = \hat{\boldsymbol{n}} \cdot \boldsymbol{A}(\boldsymbol{r})$ (as charge contribution) are the unknowns and expanded in a series of RWG and pulse functions with unknown coefficients, respectively, as follows:

$$\boldsymbol{J}(\boldsymbol{r}) = \sum_{n=1}^{N_{\mathrm{RWG}}} j_n \boldsymbol{b}_n^{\mathrm{RWG}}(\boldsymbol{r}), \qquad \boldsymbol{b}_n^{\mathrm{RWG}}(\boldsymbol{r}) = \begin{cases} \dfrac{l_n}{2A_{n1}}(\boldsymbol{r} - \boldsymbol{r}_{n1}), & \boldsymbol{r} \in S_{n1} \\ \dfrac{l_n}{2A_{n2}}(\boldsymbol{r}_{n2} - \boldsymbol{r}), & \boldsymbol{r} \in S_{n2} \\ 0, & \boldsymbol{r} \notin S_n, \end{cases} \tag{4.41a}$$

$$\Sigma(\boldsymbol{r}) = \sum_{m=1}^{M_{\mathrm{PLS}}} s_m \sigma_m^{\mathrm{PLS}}(\boldsymbol{r}), \quad \sigma_m^{\mathrm{PLS}}(\boldsymbol{r}) = \begin{cases} 1, & \boldsymbol{r} \in S_{n1} \\ 0, & \boldsymbol{r} \in S_{n2} \end{cases}, \tag{4.41b}$$

where $n = 0, 1, ...N_{\mathrm{RWG}}$ is the number of RWGs and $m = 0, 1, ...M_{\mathrm{PLS}}$ is the number of pulse functions with triangular supports. Testing (4.40a) with RWGs and (4.40b) with pulse functions, we have:

$$\begin{aligned} -\left\langle \boldsymbol{t}_{n'}^{\mathrm{RWG}}(\boldsymbol{r}), \hat{\boldsymbol{n}} \times \hat{\boldsymbol{n}} \times \boldsymbol{A}_{\mathrm{inc}}(\boldsymbol{r}) \right\rangle &= \left\langle \boldsymbol{t}_{n'}^{\mathrm{RWG}}(\boldsymbol{r}), \hat{\boldsymbol{n}} \times \hat{\boldsymbol{n}} \times \sum_{n=1}^{N_{\mathrm{RWG}}} j_n \mu_0 \int_S ds' g(\boldsymbol{r}, \boldsymbol{r'}) \boldsymbol{b}_n^{\mathrm{RWG}}(\boldsymbol{r'}) \right\rangle \\ &+ \left\langle \boldsymbol{t}_{n'}^{\mathrm{RWG}}(\boldsymbol{r}), \hat{\boldsymbol{n}} \times \hat{\boldsymbol{n}} \times \sum_{m=1}^{M_{\mathrm{PLS}}} s_m \int_S ds' \nabla' g(\boldsymbol{r}, \boldsymbol{r'}) {\sigma_m}^{\mathrm{PLS}}(\boldsymbol{r'}) \right\rangle \end{aligned} \tag{4.42a}$$

$$\begin{aligned} -\left\langle \sigma_{m'}^{\mathrm{PLS}}(\boldsymbol{r}), i\omega\varepsilon_0 \phi_{\mathrm{inc}}(\boldsymbol{r}) \right\rangle &= \left\langle \sigma_{m'}^{\mathrm{PLS}}(\boldsymbol{r}), \sum_{n=1}^{N_{\mathrm{RWG}}} j_n \int_S ds' g(\boldsymbol{r}, \boldsymbol{r'}) \nabla' \cdot \boldsymbol{b}_n^{\mathrm{RWG}}(\boldsymbol{r'}) \right\rangle \\ &+ \left\langle \sigma_{m'}^{\mathrm{PLS}}(\boldsymbol{r}), \sum_{m=1}^{M_{\mathrm{PLS}}} s_m \omega^2 \varepsilon_0 \int_S ds' \sigma_m^{\mathrm{PLS}}(\boldsymbol{r'}) g(\boldsymbol{r}, \boldsymbol{r'}) \right\rangle. \end{aligned} \tag{4.42b}$$

Finally, a 2 by 2 block matrix equation is obtained for the formulas given in (4.42)

$$\begin{bmatrix} \mu_0 \bar{\boldsymbol{\Gamma}}_{\boldsymbol{J},\boldsymbol{J}(N_{\mathrm{RWG}} \times N_{\mathrm{RWG}})} & \bar{\boldsymbol{\Gamma}}_{\boldsymbol{J},\sigma(N_{\mathrm{RWG}} \times M_{\mathrm{PLS}})} \\ \bar{\boldsymbol{\Gamma}}_{\sigma,\boldsymbol{J}(M_{\mathrm{PLS}} \times N_{\mathrm{RWG}})} & \omega^2 \varepsilon_0 \bar{\boldsymbol{\Gamma}}_{\sigma,\sigma(M_{\mathrm{PLS}} \times M_{\mathrm{PLS}})} \end{bmatrix} \begin{bmatrix} \boldsymbol{j}_{(N_{\mathrm{RWG}} \times 1)} \\ \boldsymbol{s}_{(M_{\mathrm{PLS}} \times 1)} \end{bmatrix} = - \begin{bmatrix} \boldsymbol{a}_{\mathrm{inc}(N_{\mathrm{RWG}} \times 1)} \\ i\omega\varepsilon_0 \boldsymbol{\varphi}_{\mathrm{inc}(M_{\mathrm{PLS}} \times 1)} \end{bmatrix} \tag{4.43}$$

where $\boldsymbol{j}$ and $\boldsymbol{s}$ are the unknown coefficient vectors. In addition, $\boldsymbol{a}_{\mathrm{inc}}$ and $\boldsymbol{\varphi}_{\mathrm{inc}}$ are the discretized and tested vectors of the incident magnetic and scalar potentials, respectively. Each element of the submatrix $\bar{\boldsymbol{\Gamma}}_{\boldsymbol{J},\boldsymbol{J}}$ in (4.43) is given by

$$
\begin{aligned}
\bar{\mathbf{\Gamma}}_{\boldsymbol{J},\boldsymbol{J}_{(\boldsymbol{t}_{n'},\boldsymbol{b}_n)}} &= \left\langle \boldsymbol{t}_{n'}^{\mathrm{RWG}}(\boldsymbol{r}), -\hat{\boldsymbol{n}}\times\hat{\boldsymbol{n}}\times \int\limits_{S} ds' g(\boldsymbol{r},\boldsymbol{r'}) \boldsymbol{b}_n^{\mathrm{RWG}}(\boldsymbol{r'}) \right\rangle \\
&= -\int\limits_{S_{n'}} ds\, \boldsymbol{t}_{n'}^{\mathrm{RWG}}(\boldsymbol{r}) \cdot \left[\hat{\boldsymbol{n}}\times\hat{\boldsymbol{n}}\times \int\limits_{S_n} ds' g(\boldsymbol{r},\boldsymbol{r'}) \boldsymbol{b}_n^{\mathrm{RWG}}(\boldsymbol{r'}) \right] \\
&= \int\limits_{S_{n'}} ds\, \boldsymbol{t}_{n'}^{\mathrm{RWG}}(\boldsymbol{r}) \cdot \left[\hat{\boldsymbol{n}}\cdot\hat{\boldsymbol{n}} \int\limits_{S_n} ds' g(\boldsymbol{r},\boldsymbol{r'}) \boldsymbol{b}_n^{\mathrm{RWG}}(\boldsymbol{r'}) - \hat{\boldsymbol{n}}\hat{\boldsymbol{n}}\cdot \int\limits_{S_n} ds' g(\boldsymbol{r},\boldsymbol{r'}) \boldsymbol{b}_n^{\mathrm{RWG}}(\boldsymbol{r'}) \right] \\
&= \int\limits_{S_{n'}} ds\, \boldsymbol{t}_{n'}^{\mathrm{RWG}}(\boldsymbol{r}) \cdot \left[\int\limits_{S_n} ds' g(\boldsymbol{r},\boldsymbol{r'}) \boldsymbol{b}_n^{\mathrm{RWG}}(\boldsymbol{r'}) - \underbrace{\left(\boldsymbol{t}_{n'}^{\mathrm{RWG}}(\boldsymbol{r})\cdot\hat{\boldsymbol{n}}\right)}_{\text{zero}} \hat{\boldsymbol{n}} \cdot \int\limits_{S_n} ds' g(\boldsymbol{r},\boldsymbol{r'}) \boldsymbol{b}_n^{\mathrm{RWG}}(\boldsymbol{r'}) \right] \\
&= \int\limits_{S_{n'}} ds\, \boldsymbol{t}_{n'}^{\mathrm{RWG}}(\boldsymbol{r}) \cdot \int\limits_{S_n} ds' g(\boldsymbol{r},\boldsymbol{r'}) \boldsymbol{b}_n^{\mathrm{RWG}}(\boldsymbol{r'}) \\
&= \left\langle \boldsymbol{t}_{n'}^{\mathrm{RWG}}(\boldsymbol{r}), g(\boldsymbol{r},\boldsymbol{r'}), \boldsymbol{b}_n^{\mathrm{RWG}}(\boldsymbol{r'}) \right\rangle .
\end{aligned} \tag{4.44}
$$

Similarly, each element of the submatrix $\bar{\mathbf{\Gamma}}_{\boldsymbol{J},\sigma}$ in (4.43) is calculated via

$$
\begin{aligned}
\bar{\mathbf{\Gamma}}_{\boldsymbol{J},\sigma_{(\boldsymbol{t}_{n'},\sigma_m)}} &= \left\langle \boldsymbol{t}_{n'}^{\mathrm{RWG}}(\boldsymbol{r}), -\hat{\boldsymbol{n}}\times\hat{\boldsymbol{n}}\times \int\limits_{S} ds' \sigma_m(\boldsymbol{r'}) \nabla' g(\boldsymbol{r},\boldsymbol{r'}) \right\rangle \\
&= -\int\limits_{S_{n'}} ds\ \boldsymbol{t}_{n'}^{\mathrm{RWG}}(\boldsymbol{r}) \cdot \int\limits_{S_m} ds' \sigma_m(\boldsymbol{r'}) \hat{\boldsymbol{n}}\times\hat{\boldsymbol{n}}\times\nabla' g(\boldsymbol{r},\boldsymbol{r'}) \\
&= \int\limits_{S_{n'}} ds\ \boldsymbol{t}_{n'}^{\mathrm{RWG}}(\boldsymbol{r}) \cdot \int\limits_{S_m} ds' \sigma_m(\boldsymbol{r'}) \left[\hat{\boldsymbol{n}}\cdot\hat{\boldsymbol{n}}\nabla' g(\boldsymbol{r},\boldsymbol{r'}) - \hat{\boldsymbol{n}}\hat{\boldsymbol{n}}\cdot\nabla' g(\boldsymbol{r},\boldsymbol{r'}) \right] \\
&= \int\limits_{S_{n'}} ds\ \boldsymbol{t}_{n'}^{\mathrm{RWG}}(\boldsymbol{r}) \cdot (\hat{\boldsymbol{n}}\cdot\hat{\boldsymbol{n}}) \int\limits_{S_m} ds' \sigma_m(\boldsymbol{r'}) \nabla' g(\boldsymbol{r},\boldsymbol{r'}) \\
&\quad - \int\limits_{S_{n'}} ds\ \boldsymbol{t}_{n'}^{\mathrm{RWG}}(\boldsymbol{r}) \cdot \hat{\boldsymbol{n}} \int\limits_{S_m} ds' \sigma_m(\boldsymbol{r'}) \hat{\boldsymbol{n}}\cdot\nabla' g(\boldsymbol{r},\boldsymbol{r'}) \\
&= \int\limits_{S_{n'}} ds\ \boldsymbol{t}_{n'}^{\mathrm{RWG}}(\boldsymbol{r}) \cdot \int\limits_{S_m} ds' \sigma_m(\boldsymbol{r'})\, \nabla' g(\boldsymbol{r},\boldsymbol{r'}) \\
&= \left\langle \boldsymbol{t}_{n'}^{\mathrm{RWG}}(\boldsymbol{r}), \nabla' g(\boldsymbol{r},\boldsymbol{r'}), \sigma_m(\boldsymbol{r'}) \right\rangle .
\end{aligned} \tag{4.45}
$$

Equation (4.45) can be rewritten by transferring the gradient operator of the free-space Green's function as a divergence operator over the testing function as follows:

$$
\begin{aligned}
\bar{\mathbf{\Gamma}}_{\boldsymbol{J},\sigma_{(\boldsymbol{t}_{n'},\sigma_m)}} &= \left\langle \boldsymbol{t}_{n'}^{\mathrm{RWG}}(\boldsymbol{r}), \nabla' g(\boldsymbol{r},\boldsymbol{r'}), \sigma_m(\boldsymbol{r'}) \right\rangle \\
&= \int\limits_{S_{n'}} ds\, \boldsymbol{t}_{n'}^{\mathrm{RWG}}(\boldsymbol{r}) \cdot \int\limits_{S_m} ds'\, \sigma_m(\boldsymbol{r'}) \nabla' g(\boldsymbol{r},\boldsymbol{r'}) = \int\limits_{S_{n'}} ds \int\limits_{S_m} ds'\, \sigma_m(\boldsymbol{r'}) \boldsymbol{t}_{n'}^{\mathrm{RWG}}(\boldsymbol{r}) \cdot \nabla' g(\boldsymbol{r},\boldsymbol{r'}) \\
&= -\int\limits_{S_m} ds'\, \sigma_m(\boldsymbol{r'}) \int\limits_{S_{n'}} ds\ \nabla \cdot \left[\boldsymbol{t}_{n'}^{\mathrm{RWG}}(\boldsymbol{r}) g(\boldsymbol{r},\boldsymbol{r'}) \right] + \int\limits_{S_m} ds'\, \sigma_m(\boldsymbol{r'}) \int\limits_{S_{n'}} ds\ g(\boldsymbol{r},\boldsymbol{r'}) \nabla \cdot \boldsymbol{t}_{n'}^{\mathrm{RWG}}(\boldsymbol{r}) \\
&= -\int\limits_{S_m} ds'\, \sigma_m(\boldsymbol{r'}) \underbrace{\oint\limits_{l_{n'}} dl\, g(\boldsymbol{r},\boldsymbol{r'}) \boldsymbol{t}_{n'}^{\mathrm{RWG}}(\boldsymbol{r}) \cdot \hat{\boldsymbol{u}}}_{\text{zero}} + \int\limits_{S_m} ds'\, \sigma_m(\boldsymbol{r'}) \int\limits_{S_{n'}} ds\ g(\boldsymbol{r},\boldsymbol{r'}) \nabla \cdot \boldsymbol{t}_{n'}^{\mathrm{RWG}}(\boldsymbol{r}) \\
&= \int\limits_{S_{n'}} ds \nabla \cdot \boldsymbol{t}_{n'}^{\mathrm{RWG}}(\boldsymbol{r}) \int\limits_{S_m} ds'\, \sigma_m(\boldsymbol{r'}) g(\boldsymbol{r},\boldsymbol{r'}) \\
&= \left\langle \nabla \cdot \boldsymbol{t}_{n'}^{\mathrm{RWG}}(\boldsymbol{r}), g(\boldsymbol{r},\boldsymbol{r'}), \sigma_m\left(\boldsymbol{r'}\right) \right\rangle . \qquad (4.46)
\end{aligned}
$$

For the lower submatrices, each element of the submatrix $\bar{\mathbf{\Gamma}}_{\sigma,\boldsymbol{J}}$ in (4.43) is obtained as

$$
\begin{aligned}
\bar{\mathbf{\Gamma}}_{\sigma,\boldsymbol{J}_{(\sigma_{m'},\boldsymbol{b}_n)}} &= \left\langle \sigma_{m'}\left(\boldsymbol{r}\right), \int\limits_S ds' g(\boldsymbol{r},\boldsymbol{r'})\, \nabla' \cdot \boldsymbol{b}_n^{\mathrm{RWG}}(\boldsymbol{r'}) \right\rangle \\
&= \int\limits_{S_{m'}} ds\, \sigma_{m'}\left(\boldsymbol{r}\right) \int\limits_{S_n} ds'\, g(\boldsymbol{r},\boldsymbol{r'}) \nabla' \cdot \boldsymbol{b}_n^{\mathrm{RWG}}(\boldsymbol{r'}) \\
&= \left\langle \sigma_{m'}\left(\boldsymbol{r}\right), g(\boldsymbol{r},\boldsymbol{r'}), \nabla' \cdot \boldsymbol{b}_n^{\mathrm{RWG}}(\boldsymbol{r'}) \right\rangle , \qquad (4.47)
\end{aligned}
$$

and finally, each element of the submatrix $\bar{\mathbf{\Gamma}}_{\sigma,\sigma}$ in (4.43) is given by

$$
\begin{aligned}
\bar{\mathbf{\Gamma}}_{\sigma,\sigma_{(\sigma_{m'},\sigma_m)}} &= \left\langle \sigma_{m'}\left(\boldsymbol{r}\right), \int\limits_S ds' \sigma_m(\boldsymbol{r'}) g(\boldsymbol{r},\boldsymbol{r'}) \right\rangle \\
&= \int\limits_{S_{m'}} ds\, \sigma_{m'}\left(\boldsymbol{r}\right) \int\limits_{S_m} ds'\, g(\boldsymbol{r},\boldsymbol{r'})\, \sigma_m(\boldsymbol{r'}) \\
&= \left\langle \sigma_{m'}\left(\boldsymbol{r}\right), g(\boldsymbol{r},\boldsymbol{r'}), \sigma_m(\boldsymbol{r'}) \right\rangle . \qquad (4.48)
\end{aligned}
$$

The discretized incident magnetic vector and scalar potentials forming the right hand side vector in (4.43) are obtained via (4.49a) and (4.49b), respectively, as follows:

$$\begin{aligned}\left\langle \boldsymbol{t}_{n'}^{\mathrm{RWG}}(\boldsymbol{r}), -\hat{\boldsymbol{n}}\times\hat{\boldsymbol{n}}\times\boldsymbol{A}_{\mathrm{inc}}(\boldsymbol{r})\right\rangle &= \int\limits_{S_{n'}} ds\ \boldsymbol{t}_{n'}^{\mathrm{RWG}}(\boldsymbol{r})\cdot(-\hat{\boldsymbol{n}}\times\hat{\boldsymbol{n}}\times\boldsymbol{A}_{\mathrm{inc}}(\boldsymbol{r})) \\ &= \int\limits_{S_{n'}} ds\ \boldsymbol{t}_{n'}^{\mathrm{RWG}}(\boldsymbol{r})\cdot(\hat{\boldsymbol{n}}\cdot\hat{\boldsymbol{n}}\boldsymbol{A}_{\mathrm{inc}}(\boldsymbol{r}) - \hat{\boldsymbol{n}}\hat{\boldsymbol{n}}\cdot\boldsymbol{A}_{\mathrm{inc}}(\boldsymbol{r})) \\ &= \int\limits_{S_{n'}} ds\ \boldsymbol{t}_{n'}^{\mathrm{RWG}}(\boldsymbol{r})\cdot\boldsymbol{A}_{\mathrm{inc}}(\boldsymbol{r}) - \underbrace{\boldsymbol{t}_{n'}^{\mathrm{RWG}}(\boldsymbol{r})\cdot\hat{\boldsymbol{n}}}_{\text{zero}}\hat{\boldsymbol{n}}\cdot\boldsymbol{A}_{\mathrm{inc}}(\boldsymbol{r}) \\ &= \int\limits_{S_{n'}} ds\ \boldsymbol{t}_{n'}^{\mathrm{RWG}}(\boldsymbol{r})\cdot\boldsymbol{A}_{\mathrm{inc}}(\boldsymbol{r}) = \left\langle \boldsymbol{t}_{n'}^{\mathrm{RWG}}(\boldsymbol{r}), \boldsymbol{A}_{\mathrm{inc}}(\boldsymbol{r})\right\rangle \quad (4.49a)\end{aligned}$$

$$\langle \sigma_{m'}(\boldsymbol{r}), -i\omega\varepsilon_0\phi_{\mathrm{inc}}(\boldsymbol{r})\rangle = -i\omega\varepsilon_0 \int\limits_{S_{m'}} ds\ \sigma_{m'}(\boldsymbol{r})\phi_{\mathrm{inc}}(\boldsymbol{r}). \quad (4.49b)$$

As it is seen, each element of the submatrices given in (4.43) should be calculated using double surface integrals over the testing and basis functions and the free-space Green's function. For this purpose, the calculation of the outer integral over the testing triangle domain can be accomplished using a numerical integration method. However, due to the singular behaviour of the free-space Green's function as the kernel of the integral equation, a singularity extraction technique should be applied over the triangle domain of basis function when the observation and source points are close to each other. Therefore, we will involve in analytical and numerical integration techniques according to the distance between the observation and source points. Therefore, in the implementation, the integrals are evaluated numerically [112] and singularity extraction technique [113, 114] is used when necessary.

4.2.3 Electromagnetic Excitation

In the solution of scattering/radiation problems using PIEs, different types of excitation can be considered as a right-hand side vector for the matrix equation obtained in (4.43). The utilized excitations in PIEs are

- Hertzian-dipole excitation,
- Plane-wave excitation,

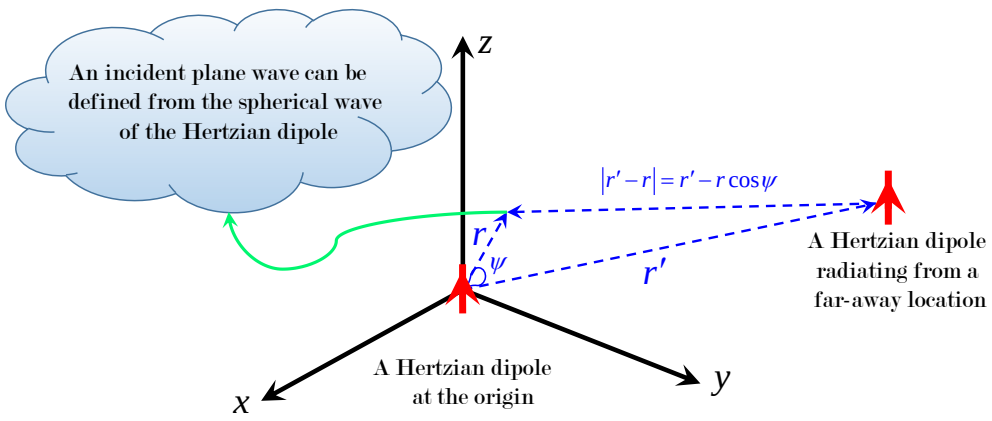


Figure 4.5: Configuration of a Hertzian dipole at the origin and a Hertzian dipole radiating from its far zone.

- Delta-gap excitation.

In contrary to EFIE and MFIE where incident fields are in the form of electric- and magnetic-field intensities, in PIEs, the excitations are in the form of incident (incoming) potentials. Therefore, the definition of $\boldsymbol{A}_{\text{inc}}(\boldsymbol{r})$ and $\phi_{\text{inc}}(\boldsymbol{r})$ as incident potentials should be clarified. For a Hertzian-dipole excitation as presented in Fig. 4.5, lets assume we have a Hertzian dipole with a current density $\boldsymbol{J}(\boldsymbol{r}) = \hat{\boldsymbol{a}}_z lI\delta(\boldsymbol{r})$ that is located at the origin and oriented along the z-axis. Then, the incident magnetic vector potential and incident scalar potential [using Lorenz gauge (2.12a)] can be written as

$$\boldsymbol{A}_{\text{inc}}(\boldsymbol{r}) = \hat{\boldsymbol{a}}_z lI\mu_0 \frac{e^{ikr}}{4\pi r}, \tag{4.50a}$$

$$\phi_{\text{inc}}(\boldsymbol{r}) = lI \frac{\left(-e^{ikr} + ikre^{ikr}\right)}{4\pi i\omega\varepsilon_0 r^2}\cos\theta. \tag{4.50b}$$

where k is the wavenumber of the medium. In (4.50), the incident magnetic vector potential has only r dependence while the incident scalar potential is a function of both r and θ.

Incident plane-wave potentials can be obtained by considering a spherical wave of a Hertzian dipole radiating from a far-away location as also shown in Fig. 4.5. Therefore, when $\boldsymbol{R} = \boldsymbol{r} - \boldsymbol{r'}$ and $|\boldsymbol{r'}| >> |\boldsymbol{r}|$, (4.50a) can be written as

$$\boldsymbol{A}_{\text{inc}}(\boldsymbol{r}) = \hat{\boldsymbol{a}}_z \mu_0 lI \frac{e^{ik|\boldsymbol{r'}-\boldsymbol{r}|}}{4\pi|\boldsymbol{r'}-\boldsymbol{r}|} \approx \hat{\boldsymbol{a}}_z \mu_0 lI \frac{e^{ik\boldsymbol{r'}}}{4\pi\boldsymbol{r'}} e^{i\boldsymbol{k}\cdot\boldsymbol{r}} = \boldsymbol{a}e^{i\boldsymbol{k}\cdot\boldsymbol{r}}, \tag{4.51}$$

where $\boldsymbol{k} = k\hat{\boldsymbol{a}}_{\boldsymbol{r'}}$ and $\hat{\boldsymbol{a}}_{\boldsymbol{r'}}$ is the unit vector in the direction of $\boldsymbol{r'}$. In addition, $\boldsymbol{a} = \hat{\boldsymbol{a}}_z \mu_0 l I \dfrac{e^{ik\boldsymbol{r'}}}{4\pi \boldsymbol{r'}}$ is a vector in the direction of $\hat{\boldsymbol{a}}_z$ and can be decomposed into its perpendicular and parallel components in the direction of propagation ($\hat{\boldsymbol{k}} = \hat{\boldsymbol{a}}_{\boldsymbol{r'}}$) leading to the following equation;

$$\boldsymbol{A}_{\text{inc}}(\boldsymbol{r}) = \boldsymbol{a} e^{i\boldsymbol{k}\cdot\boldsymbol{r}} = \left(\boldsymbol{a}_\perp + \boldsymbol{a}_\parallel\right) e^{i\boldsymbol{k}\cdot\boldsymbol{r}}. \tag{4.52}$$

In (4.52) $\boldsymbol{a}_\perp = (\hat{\boldsymbol{a}}_\theta \hat{\boldsymbol{a}}_\theta \cdot \boldsymbol{a} + \hat{\boldsymbol{a}}_\varphi \hat{\boldsymbol{a}}_\varphi \cdot \boldsymbol{a})$ and $\boldsymbol{a}_\parallel = \hat{\boldsymbol{k}}\hat{\boldsymbol{k}} \cdot \boldsymbol{a}$. Therefore, taking the divergence and curl of (4.52), the following equations are obtained

$$\nabla \cdot \boldsymbol{A}_{\text{inc}}(\boldsymbol{r}) = i\hat{\boldsymbol{k}} \cdot \boldsymbol{a}_\parallel e^{i\boldsymbol{k}\cdot\boldsymbol{r}} \tag{4.53a}$$

$$\nabla \times \boldsymbol{A}_{\text{inc}}(\boldsymbol{r}) = i\hat{\boldsymbol{k}} \times \boldsymbol{a}_\perp e^{i\boldsymbol{k}\cdot\boldsymbol{r}} = \mu_0 \boldsymbol{H}_{\text{inc}}(\boldsymbol{r}). \tag{4.53b}$$

In (4.52), based on the decomposition into perpendicular and parallel components, two cases can be considered. The first case follows as

$$\underbrace{\begin{cases} \boldsymbol{a}_\perp \neq 0 \\ \boldsymbol{a}_\parallel = 0 \end{cases} \Rightarrow \begin{cases} \nabla \cdot \boldsymbol{A}_{\text{inc}}(\boldsymbol{r}) = 0 \\ \nabla \times \boldsymbol{A}_{\text{inc}}(\boldsymbol{r}) = i\hat{\boldsymbol{k}} \times \boldsymbol{a}_\perp e^{i\boldsymbol{k}\cdot\boldsymbol{r}} \\ \phi_{\text{inc}}(\boldsymbol{r}) = 0 \end{cases}}_{\Downarrow}$$

$$\boldsymbol{E}_{\text{inc}}(\boldsymbol{r}) = i\omega \boldsymbol{A}_{\text{inc}}(\boldsymbol{r}) - \nabla\phi_{\text{inc}}(\boldsymbol{r}) = i\omega \boldsymbol{A}_{\text{inc}}(\boldsymbol{r})$$

$$\boldsymbol{H}_{\text{inc}}(\boldsymbol{r}) = \frac{1}{\eta}\boldsymbol{k} \times \boldsymbol{E}_{\text{inc}}(\boldsymbol{r}) = \frac{i\omega}{\eta}\boldsymbol{k} \times \boldsymbol{A}_{\text{inc}}(\boldsymbol{r}). \tag{4.54}$$

Based on (4.54), the plane-wave excitation in terms of the incident magnetic vector potential and incident scalar potential can be calculated from the perpendicular component of $\boldsymbol{a}$ ($\boldsymbol{a}_\perp \neq 0$). Using (4.54), the incident magnetic vector potential for an x-polarized uniform plane wave propagating along the z-direction can be written as

$$\boldsymbol{E}_{\text{inc}}(\boldsymbol{r}) = \hat{\boldsymbol{e}}_x e^{(ikz)} = i\omega \boldsymbol{A}_{\text{inc}}(\boldsymbol{r}) \rightarrow \boldsymbol{A}_{\text{inc}}(\boldsymbol{r}) = \hat{\boldsymbol{e}}_x \frac{1}{i\omega} e^{(ikz)}, \tag{4.55}$$

while $\phi_{\text{inc}}(\boldsymbol{r}) = 0$ and $\hat{\boldsymbol{e}}$ is the electric field polarization along the x-axis. For the second

case, we have

$$\underbrace{\begin{cases} \boldsymbol{a}_\perp = 0 \\ \boldsymbol{a}_\parallel \neq 0 \end{cases} \quad \Rightarrow \quad \begin{cases} \nabla \cdot \boldsymbol{A}_{\text{inc}}(\boldsymbol{r}) = i\hat{\boldsymbol{k}} \cdot \boldsymbol{a}_\parallel e^{i\boldsymbol{k}\cdot\boldsymbol{r}} \\ \nabla \times \boldsymbol{A}_{\text{inc}}(\boldsymbol{r}) = 0 \\ \phi_{\text{inc}}(\boldsymbol{r}) = \boldsymbol{k} \cdot \boldsymbol{a}_\parallel e^{i\boldsymbol{k}\cdot\boldsymbol{r}} / \left(i\omega\mu_0\varepsilon_0\right) \end{cases}}_{\Downarrow} \tag{4.56}$$

$$\boldsymbol{H}_{\text{inc}}(\boldsymbol{r}) = \frac{1}{\mu_0}\nabla \times \boldsymbol{A}_{\text{inc}}(\boldsymbol{r}) = \frac{1}{\mu_0}\, i\boldsymbol{k} \times \boldsymbol{a}_\perp e^{i\boldsymbol{k}\cdot\boldsymbol{r}} = 0$$

$$\boldsymbol{E}_{\text{inc}}(\boldsymbol{r}) = -\frac{\nabla \times \boldsymbol{H}_{\text{inc}}(\boldsymbol{r})}{i\omega\varepsilon_0} = \frac{i\boldsymbol{k} \times (\boldsymbol{k} \times \boldsymbol{A}_{\text{inc}}(\boldsymbol{r}))}{\omega\mu_0\varepsilon_0} = i\omega\, \boldsymbol{a}_\perp\, e^{i\boldsymbol{k}\cdot\boldsymbol{r}} = 0.$$

In the second case when only parallel (longitudinal) component of $\boldsymbol{a}$ is nonzero ($\boldsymbol{a}_\parallel \neq 0$), the incident plan wave electromagnetic field is zero. However, another expression dependent on $\boldsymbol{r}$ can be considered for the longitudinal component in such a way that the electric and magnetic fields would not be zero and the Lorenz gauge condition is also satisfied [110]. For this purpose, $\boldsymbol{A}_{\text{inc}}(\boldsymbol{r})$ and $\phi_{\text{inc}}(\boldsymbol{r})$ and the associated electric and magnetic fields can be defined as (rigorous proof can be found in [110])

$$\boldsymbol{A}_{\text{inc}}(\boldsymbol{r}) = \hat{\boldsymbol{k}}\,(\boldsymbol{r}\cdot\hat{\boldsymbol{e}})\,\sqrt{\mu_0\varepsilon_0}e^{i\boldsymbol{k}\cdot\boldsymbol{r}} \tag{4.57a}$$

$$\phi_{\text{inc}}(\boldsymbol{r}) = -\,(\boldsymbol{r}\cdot\hat{\boldsymbol{e}})\,e^{i\boldsymbol{k}\cdot\boldsymbol{r}} \tag{4.57b}$$

$$\begin{aligned} \boldsymbol{H}_{\text{inc}}(\boldsymbol{r}) &= \frac{1}{\mu_0}\nabla \times \boldsymbol{A}_{\text{inc}}(\boldsymbol{r}) = \frac{1}{\mu_0}\nabla \times \left(-\hat{\boldsymbol{k}}\,(\boldsymbol{r}\cdot\hat{\boldsymbol{e}})\,\sqrt{\mu_0\varepsilon_0}e^{i\boldsymbol{k}\cdot\boldsymbol{r}}\right) \\ &= \frac{-1}{\eta_0}\nabla \times \left[\hat{\boldsymbol{k}}\,(\boldsymbol{r}\cdot\hat{\boldsymbol{e}})\,e^{i\boldsymbol{k}\cdot\boldsymbol{r}}\right] = \frac{-1}{\eta_0}\left[(\boldsymbol{r}\cdot\hat{\boldsymbol{e}})\,e^{i\boldsymbol{k}\cdot\boldsymbol{r}}\nabla \times \hat{\boldsymbol{k}} - \hat{\boldsymbol{k}} \times \nabla\left((\boldsymbol{r}\cdot\hat{\boldsymbol{e}})\,e^{i\boldsymbol{k}\cdot\boldsymbol{r}}\right)\right] \\ &= \frac{1}{\eta_0}\hat{\boldsymbol{k}} \times \nabla\left((\boldsymbol{r}\cdot\hat{\boldsymbol{e}})\,e^{i\boldsymbol{k}\cdot\boldsymbol{r}}\right) = \frac{1}{\eta_0}\hat{\boldsymbol{k}} \times \hat{\boldsymbol{e}}e^{i\mathbf{k}\cdot\boldsymbol{r}} \end{aligned} \tag{4.57c}$$

$$\boldsymbol{E}_{\text{inc}}(\boldsymbol{r}) = \hat{\boldsymbol{e}}e^{i\mathbf{k}\cdot\boldsymbol{r}}. \tag{4.57d}$$

In (4.57), $\hat{\boldsymbol{e}}$ is the electric-field polarization, $\hat{\boldsymbol{k}}$ is the unit vector in the propagation direction that is perpendicular to $\hat{\boldsymbol{e}}$. Similar to the previous case, for an x-polarized uniform plane wave propagating along the z-direction, (4.57) leads to

$$\boldsymbol{A}_{\text{inc}}(\boldsymbol{r}) = \hat{\boldsymbol{a}}_z\,(\boldsymbol{r}\cdot\hat{\boldsymbol{a}}_x)\,\sqrt{\mu_0\varepsilon_0}e^{ikz} \tag{4.58a}$$

$$\phi_{\text{inc}}(\boldsymbol{r}) = -\,(\boldsymbol{r}\cdot\hat{\boldsymbol{a}}_x)\,e^{ikz}. \tag{4.58b}$$

Both expressions given in (4.54) and (4.57) define the same plane wave. However, the second expression is more suitable to be exploited when $\omega \to 0$ since it is bounded.

Unlike plane-wave and Hertzian dipole excitations, which are completely external

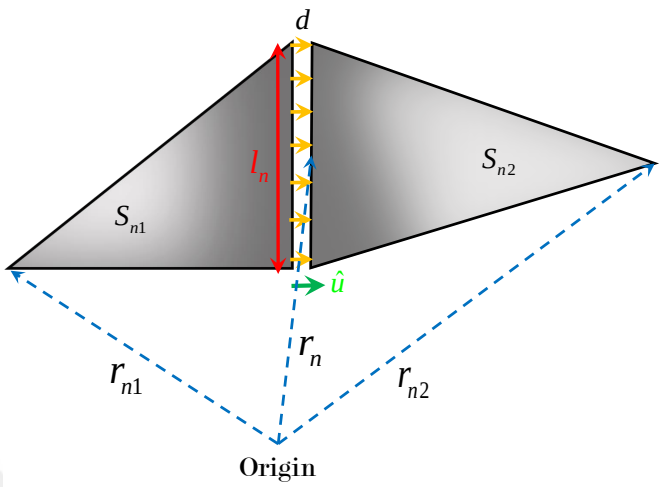


Figure 4.6: An illustration of a delta-gap source defined on a pair of triangles.

sources without a physical connection to objects, in antenna problems and some applications involving metallic objects, voltage sources are required. A voltage source can be modelled as a delta-gap excitation, which is considered as an infinitesimally narrow opening between paired triangles of the discretization as presented in Fig. 4.6. The local electric field created by such a voltage source can be defined as

$$\boldsymbol{E}_{\text{inc}}(\boldsymbol{r}) = I \lim_{d\to 0} \frac{\hat{\boldsymbol{u}}\delta(\boldsymbol{r}, \boldsymbol{r}_n)}{d} \rightarrow \boldsymbol{A}_{\text{inc}}(\boldsymbol{r}) = \frac{1}{i\omega}\boldsymbol{E}_{\text{inc}}(\boldsymbol{r}), \tag{4.59}$$

where d is the gap width between the paired triangles, and $\hat{\boldsymbol{u}}$ is a normal unit vector to the common edge in the plane of triangles as shown in Fig. 4.6. The strength of the feed is defined by I, which can be a complex value, and $\boldsymbol{r}_n$ is any point on the edges. The delta function represents that only the value of n^{th} edge is nonzero and the voltage source is located between the paired triangles of the n^{th} edge.

4.2.4 Iterative Solvers and Condition Number

Resultant matrix equation of PIEs can be solved using direct solvers with the computational complexity of $\mathcal{O}(N^3)$, where N is the number of unknowns. These solvers require direct access to the elements or blocks of the impedance matrix, and they are exact except for rounding errors. They do not need any convergence analysis. However, due to the high computational complexity, they are not useful for large

numbers of unknowns. On the other hand, Krylov subspace iterative solvers with the computational complexity of $\mathcal{O}(N^2)$ are developed to solve the matrix equation ($\bar{\boldsymbol{Z}}\boldsymbol{I} = \boldsymbol{V}$) efficiently [115–118]. The iterative solvers can improve the complexity issue since these methods start from an initial guess of the solution $\boldsymbol{I}_0$, and evaluate the error by multiplying it with $\bar{\boldsymbol{Z}}$ and checking the difference $\left\|\bar{\boldsymbol{Z}}\boldsymbol{I}_0 - \boldsymbol{V}\right\|$. Then, based on the constructed sequence of vectors expanded in a Krylov subspace which is specific to the type of the iterative solver, a new guess $\boldsymbol{I}_1$ is determined. The new guess is usually closer to the actual solution than $\boldsymbol{I}_0$ and hopefully by repeating the procedure, in the p^{th} iteration the solver converges to a value such that the error tolerance is below the predetermined threshold. Due to p iterations, the computational complexity of an iterative solution method is $\mathcal{O}(pN^2)$. For well-conditioned problems, the number of iterations p is small, which means a reduction of the computational cost. It is understood that iterative solvers require access to the elements or blocks of the impedance matrix only via its action on vectors and often require a preconditioner for fast convergence. The performance of iterative solvers (in terms of the number of iteration and accuracy of the final result) depends on the shape of the geometry, discretization, and the type of formulation, and there is no well-performing algorithm for all electromagnetic problems [5]. In this dissertation, we use the generalized minimal residual method (GMRES) with a preconditioner [119] due to its flexibility in solving a wide range of electromagnetic problems.

In a typical matrix equation $\bar{\boldsymbol{Z}}\boldsymbol{I} = \boldsymbol{V}$, the number of iterations in an iterative solver directly depends on the condition number of the matrix $\bar{\boldsymbol{Z}}$ [115]. The condition number is defined to find out how a small change in $\boldsymbol{V}$ affects the final solution $\boldsymbol{I}$. The condition number $\kappa(\bar{\boldsymbol{Z}}) \geq 1$ is calculated using matrix norm as

$$\kappa(\bar{\boldsymbol{Z}}) = \left\|\bar{\boldsymbol{Z}}\right\| \left\|\bar{\boldsymbol{Z}}^{-1}\right\| \tag{4.60}$$

where $\|\cdot\|$ denotes a matrix norm. The definition of the condition number depends on the choice of the norm. For example, using the 2-norm to calculate the condition number of $\bar{\boldsymbol{Z}}$, (4.60) is simplified as

$$\kappa(\bar{\boldsymbol{Z}}) = \frac{\sigma_{max}(\bar{\boldsymbol{Z}})}{\sigma_{min}(\bar{\boldsymbol{Z}})}, \tag{4.61}$$

where σ_{min} and σ_{max} are the minimum and maximum singular values of $\bar{\boldsymbol{Z}}$, respectively. Definition of the condition number of $\bar{\boldsymbol{Z}}$ in terms of its minimum and maximum

eigenvalues is also possible if it is a normal matrix ($\bar{\boldsymbol{Z}}$ is a normal matrix when $\bar{\boldsymbol{Z}}^*\bar{\boldsymbol{Z}} = \bar{\boldsymbol{Z}}\bar{\boldsymbol{Z}}^*$). In this case, the condition number is given by

$$\kappa(\bar{\boldsymbol{Z}}) = \left| \frac{\lambda_{max}(\bar{\boldsymbol{Z}})}{\lambda_{min}(\bar{\boldsymbol{Z}})} \right|, \tag{4.62}$$

where λ_{min} and λ_{max} are the minimum and maximum eigenvalues of $\bar{\boldsymbol{Z}}$, respectively. In (4.62), if eigenvalues of matrix $\bar{\boldsymbol{Z}}$ are sensitive to perturbations, then, small changes in the matrix elements can lead to large changes in the eigenvalues. It means that even small roundoff errors which can be introduced during the numerical computation of matrix elements with floating-point arithmetic are magnified in the computed values of sensitive eigenvalues. Therefore, a matrix is well-conditioned if the condition number is not much larger than 1 (it also depends on the size of the matrix). Small condition number means that iterative solution of a matrix equation converges rapidly. On the other hand, a matrix is ill-conditioned if the condition number is very large. Practically, such a matrix is almost singular, and the solution of the corresponding linear system of equations converges very slowly or is prone to large numerical errors. A singular matrix is not invertible and has a condition number equals to infinity.

In this thesis, the elements of the submatrices in (4.43) shows that the calculated elements are in the same order of values. However, existence of the constitutive parameters (μ_0 and ε_0) and the square of operating frequency (ω^2) cause imbalances among the element values of the diagonal block submatrices where the off-diagonal submatrices are balanced and are the transpose of each other ($\bar{\boldsymbol{\Gamma}}_{\boldsymbol{J},\sigma} = \bar{\boldsymbol{\Gamma}}^T_{\sigma,\boldsymbol{J}}$). Therefore, in order to have better-conditioned matrix equations for PIEs in comparison to (4.43), a coefficient normalization is considered in (4.43) as follows

$$\begin{bmatrix} \bar{\boldsymbol{\Gamma}}_{\boldsymbol{J},\boldsymbol{J}} & \bar{\boldsymbol{\Gamma}}_{\boldsymbol{J},\sigma} \\ \bar{\boldsymbol{\Gamma}}_{\sigma,\boldsymbol{J}} & k_0^2\bar{\boldsymbol{\Gamma}}_{\sigma,\sigma} \end{bmatrix} \begin{bmatrix} \boldsymbol{j}/c_0 \\ \boldsymbol{s}/\eta_0 \end{bmatrix} = - \begin{bmatrix} \boldsymbol{a}_{\text{inc}}/\eta_0 \\ ik_0\varepsilon_0\boldsymbol{\varphi}_{\text{inc}} \end{bmatrix}, \tag{4.63}$$

where k_0, η_0, and c_0 are the wavenumber, light velocity, and the characteristic impedance of the medium, respectively.

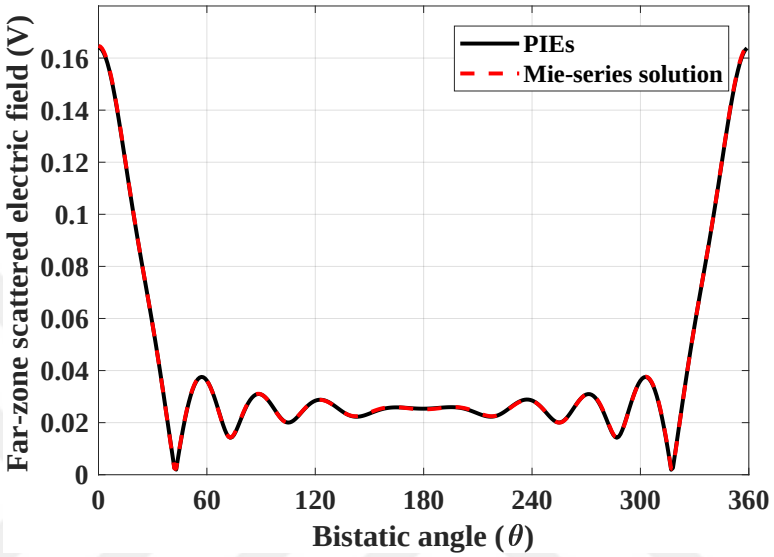
4.2.5 Numerical Results

In this section, numerical results obtained via the MoM solution of PIEs are presented to demonstrate the accuracy of the PIEs where GMRES with an error tolerance of 10^{-4} is used. The solver uses left preconditioner obtained via the approximate near-field matrix of its own [52]. For the simulation, scattering from a PEC sphere with a diameter of 0.1 m is considered when the size of the object is 1λ at 3 GHz. The sphere is discretized with 2700 triangles leading to a total number of 21850 unknowns with the average edge size of 5 mm. The object is illuminated by an x-polarized uniform plane wave propagating along the z-direction at different operating frequencies. The physical size of the sphere is kept the same in all simulations (i.e., all frequencies). Table 4.1 shows the operating frequency and the corresponding wavelength, the electrical size of the sphere, the mesh sizes, the number of iterations with (w) using preconditioner, and the condition number of the resultant impedance matrices with and without (w/o) using the preconditioner.

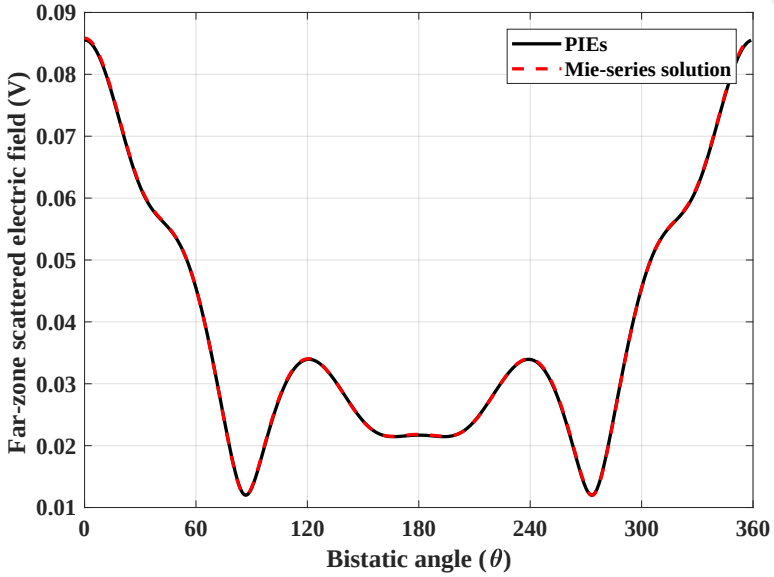
Figs. 4.7 and 4.8 show the far-zone scattered electric-field results as a function of the bistatic angle on the z-x plane (0° and 180° represent the forward and the backward scattering directions, respectively) compared with the Mie series results when the operating frequency varies from 6 GHz down to 1 Hz. The definition of the far-zone electric field is given in (2.26) where the electric field is multiplied by the distance from the object as the distance goes to infinity. All results agree well with each other, which numerically demonstrate that PIEs are a good candidate to solve the scattering problems, particularly at low frequencies.

Table 4.1: Information for a uniformly discretized PEC sphere with the diameter of 0.1 m, which is illuminated by an x-polarized uniform plane wave propagating along the z-direction at different frequencies.

Frequency	Wavelength	Diameter of the sphere	Mesh size	# iterations (w)	Condition number (w/o)
6 GHz	50 mm	2λ	$1e{-}1\lambda$	78	3.351e+03/7.963e+06
3 GHz	$1e2$ mm	1λ	$5e{-}2\lambda$	36	1.022e+03/1.342e+06
300 MHz	$1e3$ mm	$1e{-}1\lambda$	$5e{-}3\lambda$	12	359.73/2.833e+04
30 MHz	$1e4$ mm	$2e{-}2\lambda$	$5e{-}4\lambda$	10	416.863/1.618e+04
3 MHz	$1e5$ mm	$2e{-}3\lambda$	$5e{-}5\lambda$	10	418.947/2.219e+04
1 KHz	$3e8$ mm	$0.334e{-}6\lambda$	$1.667e{-}8\lambda$	10	303.214/1.992e+11
100 Hz	$3e9$ mm	$0.334e{-}7\lambda$	$1.667e{-}9\lambda$	9	286.949/1.994e+13
10 Hz	$3e10$ mm	$0.334e{-}8\lambda$	$1.667e{-}10\lambda$	7	463.989/1.438e+15
1 Hz	$3e11$ mm	$0.334e{-}9\lambda$	$1.667e{-}11\lambda$	8	3.403e+04/9.141e+14



(a)



(b)

Figure 4.7: Far-zone scattered electric-field result obtained via PIE/MoM, for the uniformly discretized PEC sphere illuminated by an x-polarized uniform plane wave propagating along the z-direction (a) at 6 GHz. (b) at 3 GHz.

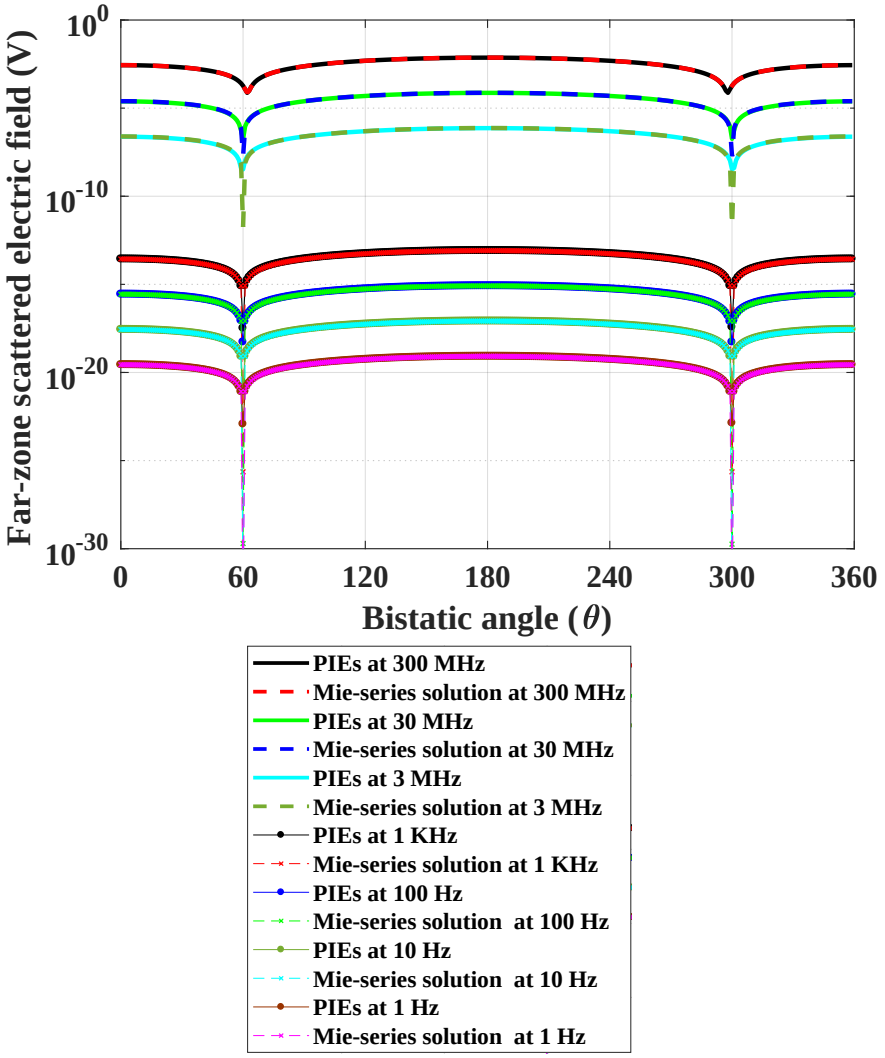


Figure 4.8: Far-zone scattered electric-field result obtained via PIE/MoM, for the uniformly discretized PEC sphere illuminated by an x-polarized uniform plane wave propagating along the z-direction at different frequencies.

Chapter 5

Multilevel Fast Multipole Algorithm

5.1 Introduction and Concept

Solutions of SIEs using the MoM procedure yield matrix equations as presented in (4.36). The resultant impedance matrix $\bar{\boldsymbol{Z}}$ is entirely populated by the fact that every testing function receives fields from every basis function due to the nonzero value of the free-space Green's function throughout the entire space. When the dimension of the $\bar{\boldsymbol{Z}}$ matrix becomes prohibitively large, the memory requirements and the MVM computation times during an iterative solution process become intractable. Therefore, various fast algorithms have been developed to reduce the $\mathcal{O}(N^2)$ storage requirements of the $\bar{\boldsymbol{Z}}$ matrix, and to accelerate the MVMs with $\mathcal{O}(N^2)$ operation complexity per iteration. Among the fast algorithms, FMM can reduce the memory requirements as well as the computational complexity from $\mathcal{O}(N^2)$ to $\mathcal{O}(N^{3/2})$ and to $\mathcal{O}(N\log N)$ via its multilevel version called MLFMA. In the following, basic implementation steps of the conventional MLFMA are summarized.

MLFMA starts by ***i***) enclosing the entire geometry in a fictitious cubic box and dividing the box into eight identical subboxes (hierarchy of boxes called the tree structure as presented in Fig. 5.1(a)), and ***ii***) invoking a multipole or propagating

plane-wave decomposition of the free-space Green's function. Only the nonempty cubic boxes (the boxes containing unknowns) are considered and are recursively divided into eight subboxes until a stopping criterion such as a predetermined number of levels [$L = \mathcal{O}(\log N)$] is met or given minimal box size is reached [see Fig. 5.1(b)]. Meanwhile, empty boxes at any stage are omitted, and each box at the lowest level contains some of the discretization elements [see Fig. 5.1(c) and see Fig. 5.1(d)]. Using the tree structure and the one-box-buffer scheme as presented in Fig. 5.1(e), the impedance matrix can be splitted into near-field and far-field matrices as follows:

$$\bar{\boldsymbol{Z}} \cdot \boldsymbol{I} = \bar{\boldsymbol{Z}}_{NF} \cdot \boldsymbol{I} + \bar{\boldsymbol{Z}}_{FF} \cdot \boldsymbol{I} = \boldsymbol{V}, \tag{5.1}$$

where near-field interactions denoted by $\bar{\boldsymbol{Z}}_{NF}$ are computed directly using MoM due to the strong interactions among the basis and testing functions (hence it requires accurate calculation). The near-field interactions are stored in memory to perform the first part of the multiplications $\bar{\boldsymbol{Z}}_{NF} \cdot \boldsymbol{I}$. The far-field interactions denoted by $\bar{\boldsymbol{Z}}_{FF}$ are computed via FMM/MLFMA (due to the weak interactions among the basis and testing functions) in the MVM part in such a way that the unknown current coefficients for far-field interactions are updated in each iteration. The computation of far-field interactions in the MVM part is possible since the decomposition of the free-space Green's function permits the separation of basis and testing functions from each other. The separation leads to compute far-field interactions in a group-by-group manner consisting of three main stages called aggregation, translation, and disaggregation. The stages are performed on the tree structures in a multilevel scheme and in each MVM operation of an iterative solver.

The one-box-buffer scheme will be used for defining the near- and far-zone boxes and their corresponding interactions according to the following procedure:

- All same-size boxes touching a given box of interest are considered as near-zone boxes, where the interactions are computed using MoM at the deepest level. The total number of near-zone boxes for a given box of interest in a three-dimensional FMM (MLFMA) is $3^3 = 27$ (see the two-dimensional case in Fig. 5.1(e)).
- The other same-size boxes (that their parent boxes are in the near zone of the parent box of the given box) are considered as far-zone boxes where the translations occur among them in the same level, and the interactions are

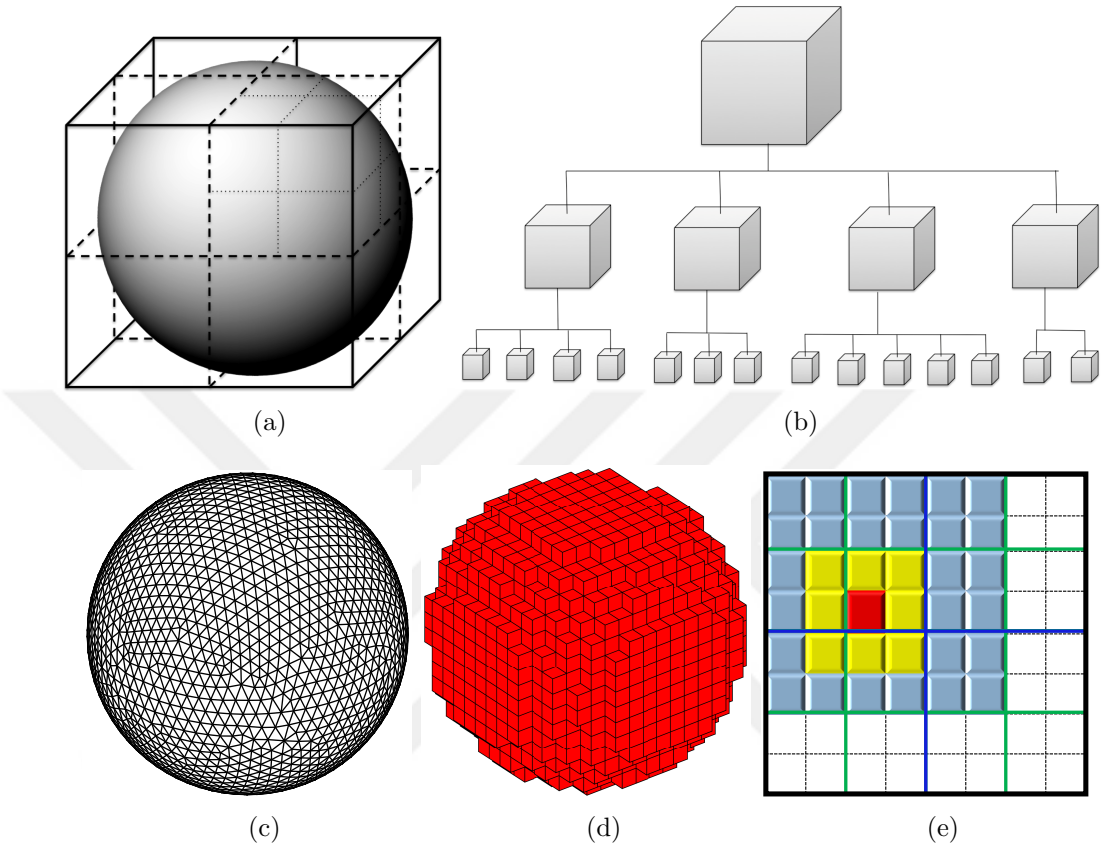


Figure 5.1: (a) A spherical object enclosed by a cubic box and recursive clustering based on dividing the box into eight identical subboxes. (b) Construction of a hierarchy of boxes called as tree structures. (c) A discretized sphere and (d) its corresponding clustering where the empty boxes are omitted. (e) Near-zone boxes colored in yellow and far-zone boxes colored in blue for a given testing box (in red) based on the one-box-buffer scheme.

computed explicitly in a group-wise manner using MLFMA. The total number of far-zone boxes for a given box is $6^3 - 3^3 = 189$, and the total number of translations is $7^3 - 3^3 = 316$.

- Very-far-zone boxes are defined when there is not any explicit interaction among the group of testing and basis functions, and the translations occur at higher levels depending upon the location of testing and basis functions.

It is seen that a large number of matrix elements is located inside $\bar{\boldsymbol{Z}}_{FF}$ and a relatively small number of matrix elements is computed and stored in $\bar{\boldsymbol{Z}}_{NF}$. Therefore, FMM (MLFMA) can change an original dense impedance matrix to a highly sparse matrix,

and group-wise computations replace the one-by-one computations, which leads to a considerable amount of saving in the memory consumption and CPU time.

Multipole representation of the free-space Green's function can be utilized in MLFMA where an infinite number of spherical wave modes at a single point is required to describe the single spherical wave mode from another point. This representation is suitable when the frequency is sufficiently low. Instead, the conventional MLFMA can also use diagonalized form of the free-space Green's function where a plane-wave mode at a single point is required to describe a plane-wave mode from another point. The conventional MLFMA is suitable to be exploited at higher frequencies or when the leaf box sizes are larger than $\lambda/8$. This is due to the fact that diagonalization makes MLFMA suffer from a numerical instability at low frequencies (when the leaf box sizes are smaller than $< \lambda/8$) which is called the LF breakdown of MLFMA.

In this chapter, with regard to the capabilities and practicality of the conventional MLFMA, the extension of the conventional MLFMA for PIEs will be discussed.

5.2 Basic Steps in MLFMA

For the first step, we construct the general solution of the scalar Helmholtz wave equation given in (2.15). General solution of (2.15) using the separation-of-variables method in Cartesian coordinate system leads to the following plane-wave solution;

$$f(\boldsymbol{r}) = \sum_{n} F(\boldsymbol{k}_n) e^{i\boldsymbol{k}_n \cdot \boldsymbol{r}}, \tag{5.2}$$

where all the wave vectors should satisfy $\boldsymbol{k}_n \cdot \boldsymbol{k}_n = k^2$. In spherical coordinates, separation of variables leads to the following general solution;

$$f(\boldsymbol{r}) = \sum_{l=0}^{\infty} \sum_{m=-l}^{+l} \left[a_{l,m} \underbrace{j_l(kr) Y_{l,m}\left(\hat{\boldsymbol{r}}\left(\theta,\varphi\right)\right)}_{Z^{j}_{l,m}(k\boldsymbol{r})} + b_{l,m} \underbrace{h_l^{(1)}(kr) Y_{l,m}\left(\hat{\boldsymbol{r}}\left(\theta,\varphi\right)\right)}_{Z^{h}_{l,m}(k\boldsymbol{r})} \right], \tag{5.3}$$

where $j_l(kr)$ and $h_l^{(1)}(kr)$ are the spherical Bessel and Hankel functions of the first kind, respectively. The spherical Bessel function is finite at the origin and it is originally

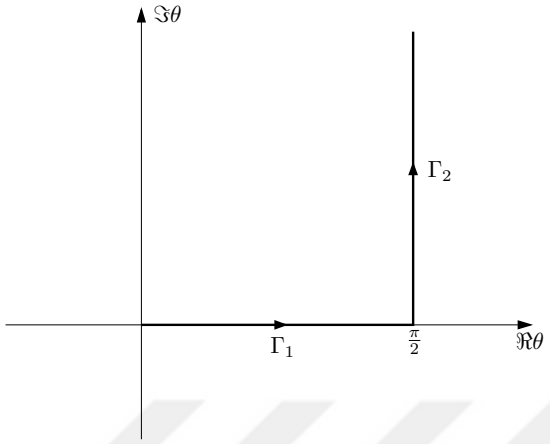


Figure 5.2: Integration path for the equation given in (5.5b) [120].

used to represent radial standing waves while spherical Hankel function represents the outward radial traveling waves. The spherical harmonics $Y_{l,m}\left(\hat{\boldsymbol{r}}\left(\theta,\varphi\right)\right)$ is defined as

$$Y_{l,m}\left(\hat{\boldsymbol{r}}\left(\theta,\varphi\right)\right)=(-1)^m\sqrt{\frac{(2l+1)}{4\pi}\frac{(l-m)!}{(l+m)!}}(\hat{x}+i\hat{y})P_l^m(\hat{z}) \quad \text{for} \tag{5.4a}$$

$$=(-1)^m\sqrt{\frac{(2l+1)}{4\pi}\frac{(l-m)!}{(l+m)!}}P_l^m(\cos\theta)e^{im\varphi} \quad \text{for} \quad \begin{cases} l=0,1,2,3,... \\ m=-l,....,+l, \end{cases} \tag{5.4b}$$

where $\hat{x}=\frac{x}{r}$, $\hat{y}=\frac{y}{r}$, and $\hat{z}=\frac{z}{r}$ and they satisfy $\hat{x}^2+\hat{y}^2+\hat{z}^2=1$. In (5.4b), $P_l^m(\cos\theta)$ is the associated Legendre function of the first kind. Note that the solution of (2.15) using the spatial Fourier transform method gives the following important relations;

$$Z_{l,m}^j(k\boldsymbol{r})=j_l(kr)Y_{l,m}\left(\hat{\boldsymbol{r}}\left(\theta,\varphi\right)\right)=\frac{i^{-l}}{4\pi}\int_{\varphi=0}^{2\pi}\int_{\theta=0}^{\pi}d^2\hat{\boldsymbol{k}}Y_{l,m}\left(\hat{\boldsymbol{k}}\left(\theta,\varphi\right)\right)e^{ik\hat{\boldsymbol{k}}\cdot\boldsymbol{r}} \tag{5.5a}$$

$$Z_{l,m}^h(k\boldsymbol{r})=h_l^{(1)}(kr)Y_{l,m}\left(\hat{\boldsymbol{r}}\left(\theta,\varphi\right)\right)=\frac{i^{-l}}{2\pi}\int_{\varphi=0}^{2\pi}\int_{\Gamma}d^2\hat{\boldsymbol{k}}Y_{l,m}\left(\hat{\boldsymbol{k}}\left(\theta,\varphi\right)\right)e^{ik\hat{\boldsymbol{k}}\cdot\boldsymbol{r}}, \tag{5.5b}$$

where $d^2\hat{\boldsymbol{k}}=\sin\theta d\theta d\varphi$ (integration over a unit sphere), $\hat{\boldsymbol{k}}=\hat{\boldsymbol{a}}_x\sin\theta\cos\varphi+\hat{\boldsymbol{a}}_y\sin\theta\sin\varphi+\hat{\boldsymbol{a}}_z\cos\theta$, and the integration path $\Gamma=\Gamma_1+\Gamma_2$ is defined as shown in Fig. 5.2.

5.2.1 Multipole Expansions of a Plane Wave

General solutions of (2.15) in Cartesian and spherical coordinate systems imply that, a plane wave can be expanded in terms of spherical-wave functions (due to the orthogonality of spherical harmonics) which is also called as the multipole expansion of a plane wave. By utilizing the completeness property of the spherical harmonics given by

$$F\left(\hat{\boldsymbol{k}}\left(\theta,\varphi\right)\right)=\sum_{l=0}^{\infty}\sum_{m=-l}^{+l}Y_{l,m}\left(\hat{\boldsymbol{k}}\left(\theta,\varphi\right)\right)\int_{\varphi=0}^{2\pi}\int_{\theta=0}^{\pi}d^{2}\hat{\boldsymbol{k}}'F\left(\hat{\boldsymbol{k}}'\left(\theta',\varphi'\right)\right)Y_{l,m}^{*}\left(\hat{\boldsymbol{k}}'\left(\theta',\varphi'\right)\right), \tag{5.6}$$

and the relation given in (5.5a), a plane wave can be expanded in terms of spherical harmonics (spherical waves) as

$$e^{ik\hat{\boldsymbol{k}}\cdot\boldsymbol{r}}=\sum_{l=0}^{\infty}\sum_{m=-l}^{+l}Y_{l,m}\left(\hat{\boldsymbol{k}}\left(\theta,\varphi\right)\right)\int_{\varphi=0}^{2\pi}\int_{\theta=0}^{\pi}d^{2}\hat{\boldsymbol{k}}'e^{ik\hat{\boldsymbol{k}}'\cdot\boldsymbol{r}}Y_{l,m}^{*}\left(\hat{\boldsymbol{k}}'\left(\theta',\varphi'\right)\right) \tag{5.7a}$$

$$=\sum_{l=0}^{\infty}\sum_{m=-l}^{+l}Y_{l,m}\left(\hat{\boldsymbol{k}}\left(\theta,\varphi\right)\right)\underbrace{\int_{\varphi=0}^{2\pi}\int_{\theta=0}^{\pi}d^{2}\hat{\boldsymbol{k}}'e^{ik\hat{\boldsymbol{k}}'\cdot\boldsymbol{r}}(-1)^{m}Y_{l,m}\left(\hat{\boldsymbol{k}}'\left(\theta',\varphi'\right)\right)}_{Z_{l,-m}^{j}(k\boldsymbol{r})} \tag{5.7b}$$

$$=4\pi\sum_{l=0}^{\infty}\sum_{m=-l}^{+l}(-1)^{m}i^{l}Y_{l,m}\left(\hat{\boldsymbol{k}}\left(\theta,\varphi\right)\right)Z_{l,-m}^{j}(k\boldsymbol{r}) \tag{5.7c}$$

$$=4\pi\sum_{l=0}^{\infty}\sum_{m=-l}^{+l}(-1)^{m}i^{l}Y_{l,m}\left(\hat{\boldsymbol{k}}\left(\theta,\varphi\right)\right)j_{l}(kr)Y_{l,-m}\left(\hat{\boldsymbol{r}}\left(\theta,\varphi\right)\right) \tag{5.7d}$$

$$=\sum_{l=0}^{\infty}i^{l}(2l+1)j_{l}(kr)P_{l}\left(\hat{\boldsymbol{k}}\left(\theta,\varphi\right)\cdot\hat{\boldsymbol{r}}\left(\theta,\varphi\right)\right), \tag{5.7e}$$

where the following property

$$P_{l}\left(\hat{\boldsymbol{k}}\cdot\hat{\boldsymbol{r}}\right)=\frac{4\pi}{2l+1}\sum_{m=-l}^{+l}(-1)^{m}Y_{l,m}(\hat{\boldsymbol{k}})Y_{l,-m}(\hat{\boldsymbol{r}}) \tag{5.8}$$

is used in (5.7d) as an expansion of Legendre function in terms of spherical harmonics.

5.2.2 Addition Theorem

The addition theorem for spherical waves is used for transformations from one spherical coordinate system to another spherical coordinate system. Since it is the fundamental formulation for the implementation of FMM and MLFMA, for clear understanding, the multipole expansion of a plane wave is considered to derive the addition theorem for spherical waves, where the rigorous proof can be found in the literature [5]. Consider (5.7e) and rewrite it as

$$e^{ik\hat{\boldsymbol{w}}\cdot\boldsymbol{v}} = \sum_{l=0}^{\infty} i^l (2l+1) j_l(kv) P_l(\hat{\boldsymbol{w}}\cdot\hat{\boldsymbol{v}}) \tag{5.9a}$$

$$\underbrace{\frac{e^{ik\hat{\boldsymbol{w}}\cdot\boldsymbol{v}} e^{ikw}}{w}}_{|\boldsymbol{v}+\boldsymbol{w}|\approx\hat{\boldsymbol{w}}\cdot\boldsymbol{v}+w} = \sum_{l=0}^{\infty} \underbrace{(-i)^l \frac{e^{ikw}}{ikw}}_{\approx h_l^{(1)}(kw)} ik(-1)^l(2l+1) j_l(kv) P_l(\hat{\boldsymbol{w}}\cdot\hat{\boldsymbol{v}}) \tag{5.9b}$$

$$\frac{e^{ik|\boldsymbol{w}+\boldsymbol{v}|}}{4\pi|\boldsymbol{w}+\boldsymbol{v}|} = \frac{ik}{4\pi} \sum_{l=0}^{\infty} (-1)^l (2l+1) j_l(kv) h_l^{(1)}(kw) P_l(\hat{\boldsymbol{w}}\cdot\hat{\boldsymbol{v}}) \tag{5.9c}$$

$$h_0^{(1)}(k|\boldsymbol{w}+\boldsymbol{v}|) = \sum_{l=0}^{\infty} (-1)^l (2l+1) j_l(kv) h_l^{(1)}(kw) P_l(\hat{\boldsymbol{w}}\cdot\hat{\boldsymbol{v}}). \tag{5.9d}$$

Equation given in (5.9d) is known as the addition theorem (when $|\boldsymbol{w}| > |\boldsymbol{v}|$) and can be written in the following familiar form;

$$h_0^{(1)}(k|\boldsymbol{r}-\boldsymbol{r'}|) = \begin{cases} \displaystyle\sum_{l=0}^{\infty} (-1)^l (2l+1) j_l(k\boldsymbol{r}) h_l^{(1)}(k\boldsymbol{r'}) P_l(\hat{\boldsymbol{r}}\cdot\hat{\boldsymbol{r}}') & \boldsymbol{r} < \boldsymbol{r'} \\ \displaystyle\sum_{l=0}^{\infty} (-1)^l (2l+1) j_l(k\boldsymbol{r'}) h_l^{(1)}(k\boldsymbol{r}) P_l(\hat{\boldsymbol{r}}\cdot\hat{\boldsymbol{r}}') & \boldsymbol{r} > \boldsymbol{r'}. \end{cases} \tag{5.10}$$

By substituting (5.8) into (5.9d), there is a possibility to separate the variables $\boldsymbol{w}$ and $\boldsymbol{v}$ from each other as

$$h_0^{(1)}(k|\boldsymbol{w}+\boldsymbol{v}|) = 4\pi \sum_{l=0}^{\infty} \sum_{l=-m}^{+m} (-1)^{l+m} j_l(kv) h_l^{(1)}(kw) Y_{l,m}(\hat{\boldsymbol{w}}) Y_{l,-m}(\hat{\boldsymbol{v}}) \tag{5.11a}$$

$$\frac{e^{ik|\boldsymbol{w}+\boldsymbol{v}|}}{4\pi|\boldsymbol{w}+\boldsymbol{v}|} = ik \sum_{l=0}^{\infty} \sum_{l=-m}^{+m} (-1)^{l+m} \underbrace{[j_l(kv) Y_{l,-m}(\hat{\boldsymbol{v}})]}_{\text{depends on } \hat{\boldsymbol{v}} \text{ only}} \underbrace{[h_l^{(1)}(kw) Y_{l,m}(\hat{\boldsymbol{w}})]}_{\text{depends on } \hat{\boldsymbol{w}} \text{ only}}. \tag{5.11b}$$

5.2.3 Diagonalization of the Free-Space Green's Function

Efficient implementation of MLFMA is based on the diagonalization of the free-space Green's function. This can be accomplished by converting the spherical waves into plane waves. By multiplying both sides of (5.9a) with $P_t(\hat{\boldsymbol{w}}\cdot\hat{\boldsymbol{z}})$ and integrating over $\hat{\boldsymbol{w}}$, we obtain

$$\int d^2\hat{\boldsymbol{w}} P_t(\hat{\boldsymbol{w}}\cdot\hat{\boldsymbol{z}}) e^{ik\hat{\boldsymbol{w}}\cdot\boldsymbol{v}} = \int d^2\hat{\boldsymbol{w}} \sum_{l=0}^{\infty} i^l(2l+1) j_l(kv) P_l(\hat{\boldsymbol{w}}\cdot\hat{\boldsymbol{v}}) P_t(\hat{\boldsymbol{w}}\cdot\hat{\boldsymbol{z}}) \tag{5.12a}$$

$$\int d^2\hat{\boldsymbol{w}} P_t(\hat{\boldsymbol{w}}\cdot\hat{\boldsymbol{z}}) e^{ik\hat{\boldsymbol{w}}\cdot\boldsymbol{v}} = \sum_{l=0}^{\infty} i^l(2l+1) j_l(kv) \int d^2\hat{\boldsymbol{w}} P_l(\hat{\boldsymbol{w}}\cdot\hat{\boldsymbol{v}}) P_t(\hat{\boldsymbol{w}}\cdot\hat{\boldsymbol{z}}) \tag{5.12b}$$

$$\int d^2\hat{\boldsymbol{w}} P_t(\hat{\boldsymbol{w}}\cdot\hat{\boldsymbol{z}}) e^{ik\hat{\boldsymbol{w}}\cdot\boldsymbol{v}} = \sum_{l=0}^{\infty} i^l(2l+1) j_l(kv) \frac{4\pi}{(2l+1)} P_t(\hat{\boldsymbol{v}}\cdot\hat{\boldsymbol{z}}) \delta_{lt} \tag{5.12c}$$

$$\int d^2\hat{\boldsymbol{w}} P_t(\hat{\boldsymbol{w}}\cdot\hat{\boldsymbol{z}}) e^{ik\hat{\boldsymbol{w}}\cdot\boldsymbol{v}} = 4\pi i^t j_t(kv) P_t(\hat{\boldsymbol{v}}\cdot\hat{\boldsymbol{z}}) \tag{5.12d}$$

$$j_t(kv) P_t(\hat{\boldsymbol{v}}\cdot\hat{\boldsymbol{z}}) = \frac{(-i)^t}{4\pi} \int d^2\hat{\boldsymbol{w}} P_t(\hat{\boldsymbol{w}}\cdot\hat{\boldsymbol{z}}) e^{ik\hat{\boldsymbol{w}}\cdot\boldsymbol{v}}, \tag{5.12e}$$

where $\int d^2\hat{\boldsymbol{w}}$ is a double integral over θ and φ components. The following identity for Legendre function is used to obtain (5.12c) from (5.12b)

$$\int d^2\hat{\boldsymbol{w}} P_l(\hat{\boldsymbol{w}}\cdot\hat{\boldsymbol{v}}) P_t(\hat{\boldsymbol{w}}\cdot\hat{\boldsymbol{z}}) = \frac{4\pi}{(2l+1)} P_t(\hat{\boldsymbol{v}}\cdot\hat{\boldsymbol{z}}) \delta_{lt}, \tag{5.13}$$

where δ_{lt} is the Kronecker delta function. Changing $\hat{\boldsymbol{w}} \to \hat{\boldsymbol{k}}$ and $\hat{\boldsymbol{z}} \to \hat{\boldsymbol{w}}$, (5.12e) becomes

$$j_l(kv) P_l(\hat{\boldsymbol{w}}\cdot\hat{\boldsymbol{v}}) = \frac{(-i)^l}{4\pi} \int d^2\hat{\boldsymbol{k}} P_l(\hat{\boldsymbol{k}}\cdot\hat{\boldsymbol{w}}) e^{ik\hat{\boldsymbol{k}}\cdot\boldsymbol{v}}. \tag{5.14}$$

The final equation in (5.14) can be interpreted as the expansion of spherical waves in terms of plane waves. Substituting (5.14) into (5.9c) where $|\boldsymbol{w}| > |\boldsymbol{v}|$, we have

$$\frac{e^{ik|\boldsymbol{w}+\boldsymbol{v}|}}{4\pi|\boldsymbol{w}+\boldsymbol{v}|} = \frac{ik}{4\pi} \sum_{l=0}^{\infty} (-1)^l(2l+1) h_l^{(1)}(kw) \frac{(-i)^l}{4\pi} \int d^2\hat{\boldsymbol{k}} P_l(\hat{\boldsymbol{k}}\cdot\hat{\boldsymbol{w}}) e^{ik\hat{\boldsymbol{k}}\cdot\boldsymbol{v}} \tag{5.15a}$$

$$\frac{e^{ik|\boldsymbol{w}+\boldsymbol{v}|}}{4\pi|\boldsymbol{w}+\boldsymbol{v}|} = \frac{ik}{(4\pi)^2} \int d^2\hat{\boldsymbol{k}} \underbrace{e^{ik\hat{\boldsymbol{k}}\cdot\boldsymbol{v}}}_{\substack{\text{depends on} \\ \boldsymbol{v} \text{ only}}} \sum_{l=0}^{\infty} \underbrace{(i)^l(2l+1) h_l^{(1)}(kw) P_l(\hat{\boldsymbol{k}}\cdot\hat{\boldsymbol{w}})}_{\text{depends on } \hat{\boldsymbol{w}} \text{ only}} \tag{5.15b}$$

$$\frac{e^{ik|\boldsymbol{w}+\boldsymbol{v}|}}{4\pi|\boldsymbol{w}+\boldsymbol{v}|} = \frac{ik}{(4\pi)^2} \int d^2\hat{\boldsymbol{k}} \beta(\boldsymbol{k},\boldsymbol{v}) T(\boldsymbol{k},\boldsymbol{w}) \quad |\boldsymbol{w}| > |\boldsymbol{v}|. \tag{5.15c}$$

In (5.15c), $\beta(\boldsymbol{k},\boldsymbol{v})$ and $T(\boldsymbol{k},\boldsymbol{w})$ are, respectively, called as the diagonal shift and translation functions, and are defined as

$$\beta(\boldsymbol{k},\boldsymbol{v}) = e^{ik\hat{\boldsymbol{k}}\cdot\boldsymbol{v}} \tag{5.16a}$$

$$T(\boldsymbol{k},\boldsymbol{w}) = \sum_{l=0}^{\infty}(i)^l(2l+1)h_l^{(1)}(kw)P_l(\hat{\boldsymbol{k}}\cdot\hat{\boldsymbol{w}}). \tag{5.16b}$$

Equation (5.15c) is known as the diagonalized form of the free-space Green's function, and it is a fundamental equation in the implementation of the conventional MLFMA. Note that in the numerical implementation, the translation function given in (5.16b) should be truncated. The truncation number (also called as the number of harmonics and it is recognized by L in this thesis) can be determined by the excess bandwidth formula given in [5, 6].

5.2.4 Tree Structure and Stages of MLFMA

For a given object, a tree structure can be constructed by putting the object in a fictitious cubic box and recursively dividing it into eight identical subboxes as mentioned before. Empty boxes are omitted, and only nonempty boxes are considered in the tree structure. At the lowest level, each box contains a part of the discretized object as shown in Fig. 5.3. For the time being, just consider a pair of basis and testing functions and the interactions among the triangles. The calculation of the free-space Green's function using (5.15b) according to Fig. 5.3 can be written as

$$\begin{aligned}\frac{e^{ik|\boldsymbol{r}-\boldsymbol{r'}|}}{4\pi|\boldsymbol{r}-\boldsymbol{r'}|} \simeq & \frac{ik}{(4\pi)^2}\int d^2\hat{\boldsymbol{k}}[e^{ik\hat{\boldsymbol{k}}\cdot(\boldsymbol{r}_{C'}-\boldsymbol{r'})}e^{ik\hat{\boldsymbol{k}}\cdot(\boldsymbol{r}-\boldsymbol{r}_C)} \\ & \cdot\sum_{l=0}^{L}(i)^l(2l+1)h_l^{(1)}(k|\boldsymbol{r}_C-\boldsymbol{r}_{C'}|)P_l(\hat{\boldsymbol{k}}\cdot(\boldsymbol{r}_C-\boldsymbol{r}_{C'}))]\end{aligned} \tag{5.17a}$$

$$\boldsymbol{R} = \boldsymbol{r}-\boldsymbol{r'} = \underbrace{(\boldsymbol{r}_{C'}-\boldsymbol{r'})}_{\boldsymbol{v}_1} + \underbrace{(\boldsymbol{r}_C-\boldsymbol{r}_{C'})}_{\boldsymbol{w}} + \underbrace{(\boldsymbol{r}-\boldsymbol{r}_C)}_{\boldsymbol{v}_2}, \tag{5.17b}$$

where $\boldsymbol{r}$ and $\boldsymbol{r'}$ represent the observation and source points (on the surface of the triangles), respectively. Furthermore, $\boldsymbol{r}'_C$ and $\boldsymbol{r}_C$ are the position vectors of the centers of the far boxes containing the basis and testing triangles as shown in Fig. 5.3. Equation

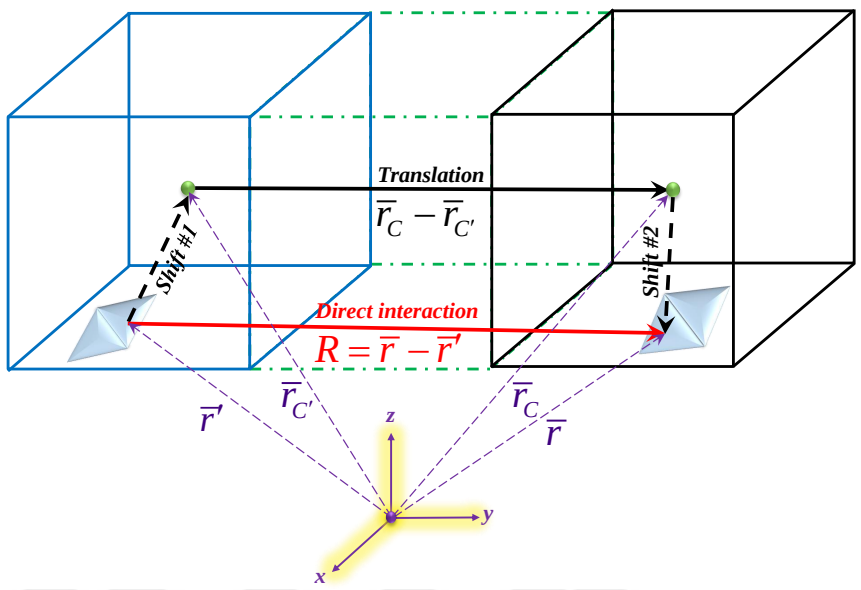


Figure 5.3: A schematic description of the diagonalized form of the free-space Green's function and calculation of interaction between a pair of RWG functions located at far boxes based on the one-box-buffer scheme.

(5.17) can be written in terms of the diagonal shift and translation functions as follows:

$$\frac{e^{ik|\boldsymbol{r}-\boldsymbol{r'}|}}{4\pi|\boldsymbol{r}-\boldsymbol{r'}|} \simeq \frac{ik}{(4\pi)^2}\int d^2\hat{\boldsymbol{k}}\beta(\boldsymbol{k},\boldsymbol{v}_1=\boldsymbol{r}_{C'}-\boldsymbol{r'})T(\boldsymbol{k},\boldsymbol{w}=\boldsymbol{r}_C-\boldsymbol{r}_{C'})\beta(\boldsymbol{k},\boldsymbol{v}_2=\boldsymbol{r}-\boldsymbol{r}_C), \tag{5.18}$$

where

$$\beta(\boldsymbol{k},\boldsymbol{v}_1) = e^{ik\hat{\boldsymbol{k}}\cdot(\boldsymbol{r}_{C'}-\boldsymbol{r'})} \tag{5.19a}$$

$$T(\boldsymbol{k},\boldsymbol{w}) \simeq \sum_{l=0}^{L}(i)^l(2l+1)h_l^{(1)}(k|\boldsymbol{r}_C-\boldsymbol{r}_{C'}|)P_l(\hat{\boldsymbol{k}}\cdot(\boldsymbol{r}_C-\boldsymbol{r}_{C'})) \tag{5.19b}$$

$$\beta(\boldsymbol{k},\boldsymbol{v}_2) = e^{ik\hat{\boldsymbol{k}}\cdot(\boldsymbol{r}-\boldsymbol{r}_C)} \tag{5.19c}$$

$$|\boldsymbol{w}| > |\boldsymbol{v}| = |\boldsymbol{v}_1+\boldsymbol{v}_2|. \tag{5.19d}$$

Therefore, instead of direct computation of the free-space Green's function between the observation and source points, the diagonalized form can be utilized for indirect computation which benefits the separation of source and observation points from each other by using two shift functions (later called as aggregation and disaggregation functions) and a translation function.

Imagine the calculation of interactions among a group of basis and testing functions as shown in Fig. 5.4. Parent boxes located in the same level are labeled as (A), (B), and (C), and their child boxes located in one deeper level are labeled as (a), (b), and (c). The interaction between the child boxes (a) and (b) is calculated using MLFMA in such a way that the radiation of all basis functions is aggregated (red arrows) at the center of the child box (a), then the aggregated radiation pattern is translated (green arrows) to the center of the child-box (b) where at the disaggregation stage (purple arrows), the translated radiation pattern will be received by each testing function inside the child box (b). This occurs since the child boxes (a) and (b) are in the far zone of each other. Calculating the interaction between child box (a) and (c) can be done at one upper level since they are located at the very far-zone region of each other. The calculation is accomplished in such a way that, first the aggregated radiation pattern at the center of the child box (a) is shifted again to the center of the parent box (A) (aggregation at the higher level), then the radiation pattern is translated from the center of the parent box (A) to the center of the parent box (C) (translation at the higher level), and at the end, the translated pattern shifted to the center of the child box (c) which is called disaggregation at the higher level, and the pattern at the center of the child box (c) is received by each testing function due to the disaggregation at the deepest level.

There are two important issues that should be noted here. First, translations among the boxes located at very far-zone regions of each other will occur at the highest level. Then, aggregation from lower to the higher levels or disaggregation from higher to the lower levels require interpolation and anterpolation techniques due to the differences in the number of harmonics for each level, and so the number of sample points for the integration.

5.3 Fast Implementations of Potential Integral Equations

Fast solution of PIEs using the conventional MLFMA requires to find the interactions among basis and testing functions belonging to far-zone and very far-zone boxes. For each submatrix in (4.43) and the corresponding interactions obtained from (4.44) to (4.48), the free-space Green's function can be replaced with its diagonalized form as

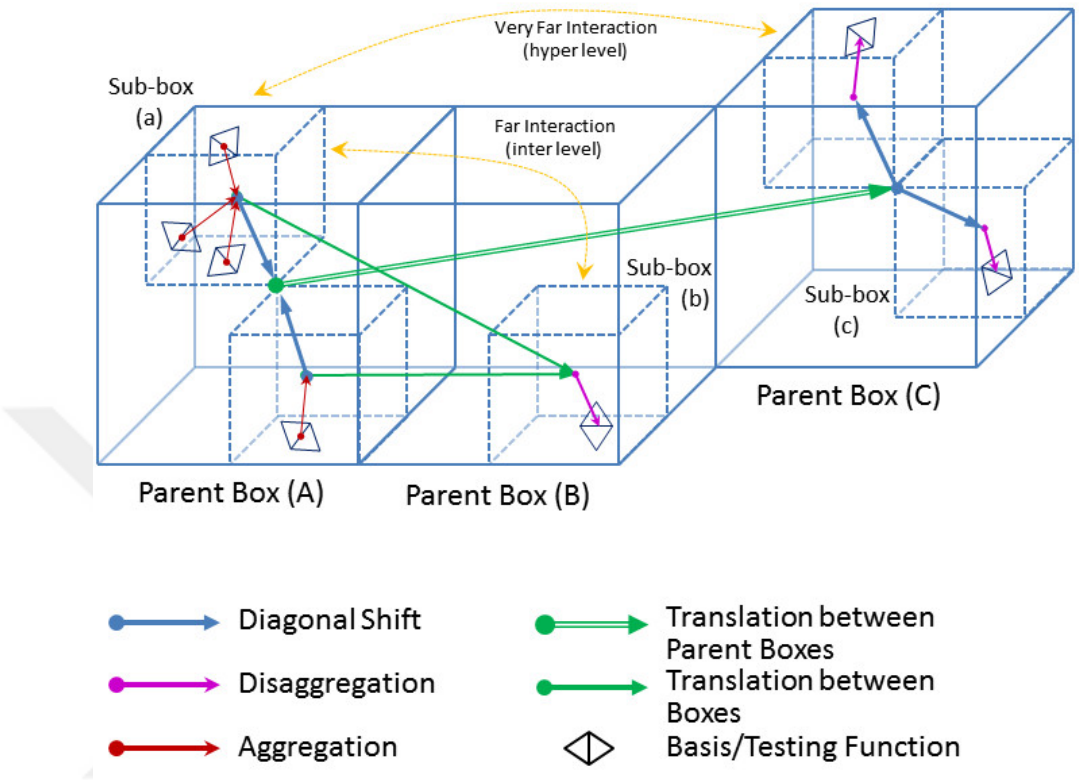


Figure 5.4: Aggregation, translation, and disaggregation processes inside a typical MLFMA scenario [121].

follows:

$$
\begin{aligned}
\bar{\mathbf{\Gamma}}_{\boldsymbol{J},\boldsymbol{J}_{(\boldsymbol{t}_{n'},\boldsymbol{b}_n)}} &= \mu_0 \left\langle \boldsymbol{t}_{n'}^{\mathrm{RWG}}(\boldsymbol{r}), g(\boldsymbol{r},\boldsymbol{r'}), \boldsymbol{b}_{n}^{\mathrm{RWG}}(\boldsymbol{r'}) \right\rangle = \mu_0 \int\limits_{S_{n'}} d\boldsymbol{r} \boldsymbol{t}_{n'}^{\mathrm{RWG}}(\boldsymbol{r}) \cdot \int\limits_{S_n} d\boldsymbol{r'} g(\boldsymbol{r},\boldsymbol{r'}) \boldsymbol{b}_{n}^{\mathrm{RWG}}(\boldsymbol{r'}) \\
&= \mu_0 \int\limits_{S_{n'_a}} d\boldsymbol{r} \frac{l'_n}{2A_{n'_a}} \gamma_{n'_a}\left(\boldsymbol{r}-\boldsymbol{r}_{n'_a}\right) \\
&\cdot \int\limits_{S_{n_b}} d\boldsymbol{r'} \frac{ik}{(4\pi)^2} \int d^2\hat{\boldsymbol{k}} \beta_1\left(\boldsymbol{k},\boldsymbol{v}_1\right) T\left(\boldsymbol{k},\boldsymbol{w}\right) \beta_2\left(\boldsymbol{k},\boldsymbol{v}_2\right) \frac{l_n}{2A_{n_b}} \gamma_{n_b}\left(\boldsymbol{r'}-\boldsymbol{r}_{n_b}\right) \\
&= \mu_0 \frac{ik}{(4\pi)^2} \int d^2\hat{\boldsymbol{k}} \left[\int\limits_{S_{n'_a}} d\boldsymbol{r} \frac{l_{n'}}{2A_{n'_a}} \gamma_{n'_a}\left(\boldsymbol{r}-\boldsymbol{r}_{n'_a}\right) \beta_1\left(\boldsymbol{k},\boldsymbol{v}_1\right) \right] \\
&\cdot T\left(\boldsymbol{k},\boldsymbol{w}\right) \left[\int\limits_{S_{n_b}} d\boldsymbol{r'} \frac{l_n}{2A_{n_b}} \gamma_{n_b}\left(\boldsymbol{r'}-\boldsymbol{r}_{n_b}\right) \beta_2\left(\boldsymbol{k},\boldsymbol{v}_2\right) \right] \\
&= \mu_0 \frac{ik}{(4\pi)^2} \int d^2\hat{\boldsymbol{k}} F_{n'_a}^{\mathrm{RWG}\times\mathrm{RWG}}\left(\boldsymbol{k},\boldsymbol{r},\boldsymbol{v}_1\right) \cdot T\left(\boldsymbol{k},\boldsymbol{w}\right) S_{n_b}^{\mathrm{RWG}\times\mathrm{RWG}}\left(\boldsymbol{k},\boldsymbol{r'},\boldsymbol{v}_2\right),
\end{aligned}
\tag{5.20}
$$

where $F_{n'_a}^{\mathrm{RWG}\times\mathrm{RWG}}(\boldsymbol{k},\boldsymbol{r},\boldsymbol{v}_1)$ and $S_{n_b}^{\mathrm{RWG}\times\mathrm{RWG}}(\boldsymbol{k},\boldsymbol{r'},\boldsymbol{v}_2)$ are known as radiating and receiving patterns of ${n'_a}^{th}$ and ${n_b}^{th}$ triangles. The elements belonging to other submatrices are calculated as follows

$$\begin{aligned}
\bar{\boldsymbol{\Gamma}}_{\boldsymbol{J},\sigma_{(\boldsymbol{t}_{n'},\sigma_m)}} &= \left\langle \nabla\cdot\boldsymbol{t}_{n'}^{\mathrm{RWG}}(\boldsymbol{r}), g(\boldsymbol{r},\boldsymbol{r'}), \sigma_m\left(\boldsymbol{r'}\right)\right\rangle = \int\limits_{S_{n'}} d\boldsymbol{r}\nabla\cdot\boldsymbol{t}_{n'}^{\mathrm{RWG}}(\boldsymbol{r}) \int\limits_{S_m} d\boldsymbol{r'}\sigma_m(\boldsymbol{r'})g(\boldsymbol{r},\boldsymbol{r'}) \\
&= \int\limits_{S_{n'_a}} d\boldsymbol{r}\frac{l_{n'}}{A_{n'_a}}\gamma_{n'_a}\int\limits_{S_m} d\boldsymbol{r'}\frac{ik}{(4\pi)^2}\int d^2\hat{\boldsymbol{k}}\beta_1\left(\boldsymbol{k},\boldsymbol{v}_1\right)T\left(\boldsymbol{k},\boldsymbol{w}\right)\beta_2\left(\boldsymbol{k},\boldsymbol{v}_2\right)\sigma_m\left(\boldsymbol{r'}\right) \\
&= \frac{ik}{(4\pi)^2}\int d^2\hat{\boldsymbol{k}}\left[\int\limits_{S_{n'_a}} d\boldsymbol{r}\frac{l'_n}{A_{n'_a}}\gamma_{n'_a}\beta_1\left(\boldsymbol{k},\boldsymbol{v}_1\right)\right]T\left(\boldsymbol{k},\boldsymbol{w}\right)\left[\int\limits_{S_m} d\boldsymbol{r'}\sigma_m\left(\boldsymbol{r'}\right)\beta_2\left(\boldsymbol{k},\boldsymbol{v}_2\right)\right] \\
&= \frac{ik}{(4\pi)^2}\int d^2\hat{\boldsymbol{k}}F_{n'_a}^{\mathrm{RWG}\times\mathrm{PLS}}\left(\boldsymbol{k},\boldsymbol{r},\boldsymbol{v}_1\right)T\left(\boldsymbol{k},\boldsymbol{w}\right)S_m^{\mathrm{RWG}\times\mathrm{PLS}}\left(\boldsymbol{k},\boldsymbol{r'},\boldsymbol{v}_2\right), \quad (5.21)
\end{aligned}$$

$$\begin{aligned}
\bar{\boldsymbol{\Gamma}}_{\sigma,\boldsymbol{J}_{(\sigma_{m'},\boldsymbol{b}_n)}} &= \left\langle \sigma_{m'}\left(\boldsymbol{r}\right), g(\boldsymbol{r},\boldsymbol{r'}), \nabla'\cdot\boldsymbol{b}_n^{\mathrm{RWG}}(\boldsymbol{r'})\right\rangle = \int\limits_{S_{m'}} d\boldsymbol{r}\sigma_{m'}\left(\boldsymbol{r}\right)\int\limits_{S_n} d\boldsymbol{r'}g(\boldsymbol{r},\boldsymbol{r'})\nabla'\cdot\boldsymbol{b}_n^{\mathrm{RWG}}(\boldsymbol{r'}) \\
&= \int\limits_{S_{m'}} d\boldsymbol{r}\sigma_{m'}\left(\boldsymbol{r}\right)\int\limits_{S_{n_b}} d\boldsymbol{r'}\frac{l_n}{A_{n_b}}\gamma_{n_b}\frac{ik}{(4\pi)^2}\int d^2\hat{\boldsymbol{k}}\beta_1\left(\boldsymbol{k},\boldsymbol{v}_1\right)T\left(\boldsymbol{k},\boldsymbol{w}\right)\beta_2\left(\boldsymbol{k},\boldsymbol{v}_2\right) \\
&= \frac{ik}{(4\pi)^2}\int d^2\hat{\boldsymbol{k}}\left[\int\limits_{S_{m'}} d\boldsymbol{r}\sigma_{m'}\left(\boldsymbol{r}\right)\beta_1\left(\boldsymbol{k},\boldsymbol{v}_1\right)\right]T\left(\boldsymbol{k},\boldsymbol{w}\right)\left[\int\limits_{S_{n_b}} d\boldsymbol{r'}\frac{l_n}{A_{n_b}}\gamma_{n_b}\beta_2\left(\boldsymbol{k},\boldsymbol{v}_2\right)\right] \\
&= \frac{ik}{(4\pi)^2}\int d^2\hat{\boldsymbol{k}}F_{m'}^{\mathrm{PLS}\times\mathrm{RWG}}\left(\boldsymbol{k},\boldsymbol{r},\boldsymbol{v}_1\right)T\left(\boldsymbol{k},\boldsymbol{w}\right)S_{n_b}^{\mathrm{PLS}\times\mathrm{RWG}}\left(\boldsymbol{k},\boldsymbol{r'},\boldsymbol{v}_2\right), \quad (5.22)
\end{aligned}$$

$$\begin{aligned}
\bar{\boldsymbol{\Gamma}}_{\sigma,\sigma_{(\sigma_{m'},\sigma_m)}} &= \omega^2\varepsilon_0\left\langle \sigma_{m'}\left(\boldsymbol{r}\right), g(\boldsymbol{r},\boldsymbol{r'}), \sigma_m(\boldsymbol{r'})\right\rangle = \omega^2\varepsilon_0\int\limits_{S_{m'}} d\boldsymbol{r}\sigma_{m'}\left(\boldsymbol{r}\right)\int\limits_{S_m} d\boldsymbol{r'}g(\boldsymbol{r},\boldsymbol{r'})\sigma_m(\boldsymbol{r'}) \\
&= \omega^2\varepsilon_0\int\limits_{S_{m'}} d\boldsymbol{r}\sigma_{m'}\left(\boldsymbol{r}\right)\int\limits_{S_m} d\boldsymbol{r'}\frac{ik}{(4\pi)^2}\int d^2\hat{\boldsymbol{k}}\beta_1\left(\boldsymbol{k},\boldsymbol{v}_1\right)T\left(\boldsymbol{k},\boldsymbol{w}\right)\beta_2\left(\boldsymbol{k},\boldsymbol{v}_2\right)\sigma_m\left(\boldsymbol{r'}\right) \\
&= \frac{ik\omega^2\varepsilon_0}{(4\pi)^2}\int d^2\hat{\boldsymbol{k}}\left[\int\limits_{S_{m'}} d\boldsymbol{r}\sigma_{m'}\left(\boldsymbol{r}\right)\beta_1\left(\boldsymbol{k},\boldsymbol{v}_1\right)\right]T\left(\boldsymbol{k},\boldsymbol{w}\right)\left[\int\limits_{S_m} d\boldsymbol{r'}\sigma_m\left(\boldsymbol{r'}\right)\beta_2\left(\boldsymbol{k},\boldsymbol{v}_2\right)\right] \\
&= \frac{ik\omega^2\varepsilon_0}{(4\pi)^2}\int d^2\hat{\boldsymbol{k}}F_{m'}^{\mathrm{PLS}\times\mathrm{PLS}}\left(\boldsymbol{k},\boldsymbol{r},\boldsymbol{v}_1\right)T\left(\boldsymbol{k},\boldsymbol{w}\right)S_{n_b}^{\mathrm{PLS}\times\mathrm{PLS}}\left(\boldsymbol{k},\boldsymbol{r'},\boldsymbol{v}_2\right), \quad (5.23)
\end{aligned}$$

5.3.1 Low-frequency Breakdown of MLFMA

The diagonalization of the free-space Green's function (conversion of spherical waves into plane waves) causes MLFMA to suffer from inaccuracies at low frequencies called as the LF breakdown of MLFMA. The LF breakdown of MLFMA occurs since spherical Hankel function $h_l^{(1)}(x)$ in the translation function [see equation (5.15b)] grows rapidly for small argument when $l > x$ and cannot be compensated with any other components due to the plane wave expansion (the summation is based on the multiplication of spherical Hankel functions with the Legendre polynomials). Therefore, the LF breakdown of MLFMA is a numerically round-off error occurs at lower frequencies. Contrarily, in an infinite summation representation shown in (5.9d), both involved spherical Bessel $j_l(x)$ and Hankel functions $h_l^{(1)}(x)$ can balance each other even at low frequencies. The argument of the spherical Hankel function (x) is dependent on the box size. Hence, MLFMA will suffer form the LF breakdown at deeper levels which contain electrically smaller boxes sizes. MLFMA also becomes inefficient for small electromagnetic problems with a large number of unknowns since the lowest-level boxes may involve many discretization elements. This problem also occurs when multiscale objects including fine geometrical details are simulated using the conventional MLFMA [5, 73–76, 79, 80].

There are two common approaches to solve the LF-breakdown problem of MLFMA efficiently. The first approach is based on a spectral representation of the free-space Green's function, where evanescent waves together with propagating waves are considered in the radiated fields. Evanescent waves are employed to compute the interactions between small boxes (usually smaller than $\lambda/8$) separated by short distances. The second approach is based on the multipole representation of the free-space Green's function, where the multipoles (spherical waves) are not converted into plane waves. In both approaches, there is not any restriction on the box size, and they allow simulating the problem at deeper levels with the box size becoming much smaller than the wavelength.

Consequently, as a heart of this thesis, in the next chapters broadband, fast, and efficient implementations of PIEs using a mixed-form MLFMA will be discussed where NSPWMLFMA is used to circumvent the LF breakdown problem of the conventional MLFMA.

Chapter 6

Broadband Solutions of Potential Integral Equations With Mixed-form MLFMA

6.1 Introduction

In this chapter, a mixed-form MLFMA is combined with PIEs to obtain an efficient and accurate broadband solver that can be used for the solution of electromagnetic scattering from perfectly conducting surfaces over a wide frequency range including low frequencies. The mixed-form MLFMA uses Nondirective Stable Plane Wave MLFMA (NSPWMLFMA) at low frequencies and the conventional MLFMA at middle/high frequencies. Various numerical examples are presented to assess the validity, efficiency, and accuracy of the developed solver. NSPWMLFMA is preferred in this study due to its error controllability, and suitability for being combined with the conventional MLFMA to obtain a robust broadband mixed-form MLFMA solver for $\boldsymbol{A}$-Φ formulations.

6.2 Nondirective Stable Plane Wave MLFMA (NSPWMLFMA) for PIEs

The derivation of the conventional MLFMA implies that only the propagating part of the plane-wave spectrum is included for sufficient accuracy. This is simply achieved via use of the diagonalized form of the Green's function given in (5.15c). Unfortunately, the conventional MLFMA exhibits LF breakdown as a result of numerical round-off errors which occur at the deeper levels in the corresponding tree structure when the box size is smaller than $\lambda/8$ [29, 30]. This drawback of the conventional MLFMA is solved by using NSPWMLFMA [53] in this thesis. Briefly, the evanescent waves are taken into account in NSPWMLFMA by shifting the integration path into the complex plane for electrically short distances. The details are as follows:

As the first step, the θ direction of the integration over the Ewald sphere given in (5.15c) is changed from $[0, \pi]$ to $[0, 2\pi]$. Then, the Fourier spectrum in θ is calculated analytically for the smooth translation $\tilde{T}_z\left(kw\hat{\boldsymbol{a}}_z, \theta, \varphi\right)$ along the z-direction as follows:

$$\begin{aligned}\tilde{T}_z\left(kw\hat{\boldsymbol{a}}_z, \theta, \varphi\right) &= T_z\left(kw\hat{\boldsymbol{a}}_z, \theta, \varphi\right)\left|\sin\left(\theta\right)\right| \\ &\simeq \sum_{l=0}^{L} (i)^l (2l+1) h_l^{(1)}(kw) P_l(\cos\left(\theta\right))\left|\sin\left(\theta\right)\right| \\ &= \sum_{n=-L}^{L} b_n e^{(in\theta)},\end{aligned} \tag{6.1}$$

where $T_z\left(kw\hat{\boldsymbol{a}}_z, \theta, \varphi\right)$ is the conventional translation function [see (5.16b)] along the z-direction. The translation function given in (5.16b) should be truncated due to the numerical calculation. Accordingly, in (6.1), L is the truncation number and is a fixed value at low frequencies [55, 97] and can be determined by using the excess bandwidth formula given in [5,6] at high frequencies. In (6.1), b_n represents the Fourier coefficients

and the analytical expression of b_n are provided in [53] as follows:

$$b_n = \frac{1}{2\pi}\sum_{l=0}^{L}(i)^l(2l+1)h_l^{(1)}(kw) \cdot \begin{cases} l \neq 0 : -2^{l+1}\sum_{k=0}^{\infty}(2k+l)\dfrac{(2k-3)!!\,(l+k-1)!}{k!\,(2l+2k+1)!!}[\delta_{l+2k,n}+\delta_{l+2k,-n}] \\ l = 0, n \neq 0 : 4\sum_{k=0}^{\infty}\dfrac{1}{1-4k^2}\;[\delta_{l+2k,n}+\delta_{l+2k,-n}] \\ l = 0, n = 0 : 4 \end{cases} . \tag{6.2}$$

Next, the integration path is deformed into the complex plane to include the evanescent waves for electrically short distances. Finally, translations along other directions are calculated using the rotation matrix $\bar{\boldsymbol{R}}_v$ leading to an expression for the free space Green's function as

$$\frac{e^{ik|\boldsymbol{r}-\boldsymbol{r'}|}}{4\pi|\boldsymbol{r}-\boldsymbol{r'}|} \simeq \frac{ik}{(4\pi)^2}\int_{\varphi=0}^{2\pi}\int_{\theta=0+i\chi_v}^{2\pi+i\chi_v} d\theta d\varphi e^{i\left(\bar{\boldsymbol{R}}_v\cdot k\hat{\boldsymbol{k}}_v(\theta+i\chi_v,\varphi)\right)\cdot\boldsymbol{v}} \cdot \sum_{n=-L}^{L} b_n e^{in(\theta+i\chi_v)}, \tag{6.3}$$

where $\bar{\boldsymbol{R}}_v$ represents rotation matrix for the v^{th} translation and χ_v indicates the magnitude of the shifting into the complex plane for the v^{th} translation. Because of different translations in one FMM level, we have various shifting paths (χ_v) due to dependency of b_n to the translation distances. Since the radiation patterns contain enough information for the shorter translations, it can be concluded that the same shifting path can also support the longer translations. Therefore, biggest χ corresponding to the smallest translation will be used for all translations in one FMM level which leads to $\hat{\boldsymbol{k}}_v(\theta+i\chi_v,\varphi) = \hat{\boldsymbol{k}}(\theta+i\chi,\varphi)$. Optimal χ can be calculated via $\frac{1}{L}\ln|\frac{2b_L}{b_0}|$ as given in [53]. Making use of uniform integration for both θ and φ directions, the discretized form of (6.3) is obtained as

$$\frac{e^{ik|\boldsymbol{r}-\boldsymbol{r'}|}}{4\pi|\boldsymbol{r}-\boldsymbol{r'}|} \simeq \frac{ikC}{(4\pi)^2}\sum_{n_\varphi=1}^{N_\varphi}\sum_{n_\theta=1}^{N_\theta} e^{i(\bar{\boldsymbol{R}}_v\cdot k\hat{\boldsymbol{k}}_n(\theta_{n_\theta}+i\chi,\varphi_{n_\varphi})\cdot\boldsymbol{v}} \sum_{n=-L}^{L} b_n e^{in(\theta_{n_\theta}+i\chi)}, \tag{6.4}$$

where C is a constant, and N_θ and N_φ indicate the number of discretization points for θ and φ directions, respectively. At this point, use of (6.3) [or its discretized form (6.4)] for all translations is inefficient as it requires the rotation of k-space and all vectors for each translation (which is equivalent to the rotation of the entire integration points during the numerical integration) [53]. Moreover, aggregation and disaggregation at deeper levels are not possible since it requires re-aggregation and re-disaggregation of

basis and testing patterns, respectively, for each specific translation [53]. As a first step to solve the aforementioned problems, the shift functions in (6.3) are expanded in terms of spherical harmonics. Therefore, for p distinct sources (basis functions), J_p, to be aggregated, and disaggregated to one single testing function, the expression can be written as

$$\psi^{\text{old}}(\bar{\boldsymbol{R}}_v \cdot \hat{\boldsymbol{k}}) = \underbrace{\sum_{p} J_p e^{i(\bar{\boldsymbol{R}}_v \cdot \boldsymbol{k}) \cdot \boldsymbol{v}_1^p}}_{\text{Aggregation}} \underbrace{e^{i(\bar{\boldsymbol{R}}_v \cdot \boldsymbol{k}) \cdot \boldsymbol{v}_2}}_{\text{Disaggregation}} = \sum_{l=0}^{\infty} \sum_{m=-l}^{+l} a_{l,m} Y_{l,m} \left(\bar{\boldsymbol{R}}_v \cdot \hat{\boldsymbol{k}} \right), \tag{6.5}$$

where $a_{l,m}$ is an unknown coefficient, and $Y_{l,m}$ is a spherical harmonic function of degree l and order m [see (5.4b)]. In (6.5), $\psi^{\text{old}}(\bar{\boldsymbol{R}}_v \cdot \hat{\boldsymbol{k}})$ represents the diagonal shift functions from p distinct basis functions to a single testing function. Discretized form of (6.5) including all discretization points in one level is given by

$$\boldsymbol{\Psi}^{\text{old}} \left(\bar{\boldsymbol{R}}_v \cdot \hat{\boldsymbol{k}}_n(\theta_{n_\theta} + i\chi, \varphi_{n_\varphi}) \right)_{(N_t N_\theta N_\varphi) \times 1} = \bar{\boldsymbol{Y}}_{(N_t N_\theta N_\varphi) \times (L+1)^2} \cdot \boldsymbol{a}_{(L+1)^2 \times 1} \tag{6.6}$$

$$\forall n \in [1, N_\varphi N_\theta], \forall v \in [1, N_t],$$

where, N_t represents the total number of rotated translations in the corresponding level. Each element in (6.6) is calculated by

$$\begin{aligned} \left[\bar{\boldsymbol{Y}}\right]_{n_t \times (N_\varphi(n_\theta - 1) + n_\varphi), l(l+1)+m+1} &= j_l(2kr_C) Y_{l,m} \left(\bar{\boldsymbol{R}}_v \cdot \hat{\boldsymbol{k}}_n \left(\theta_{n_\theta} + i\chi, \varphi_{n_\varphi} \right) \right) \\ \left[\boldsymbol{\Psi}^{\text{old}}\right]_{n_t \times (N_\varphi(n_\theta - 1) + n_\varphi), 1} &= \psi^{\text{old}} \left(\bar{\boldsymbol{R}}_v \cdot \hat{\boldsymbol{k}}_n \left(\theta_{n_\theta} + i\chi, \varphi_{n_\varphi} \right) \right) \\ [\boldsymbol{a}]_{l(l+1)+m+1,1} &= a_{l,m} / j_l(2kr_C), \end{aligned} \tag{6.7}$$

where spherical Bessel function $j_l(2kr_C)$ is multiplied as a scaling factor in order to compensate the grow of the spherical function at higher degree, and r_C represents the distance from the center of cube to its vertex which varies at different levels due to various box sizes. Due to the specific rotation matrix for each translation, whole rotated discretization points in each level should be considered in (6.6) which is equal to $(N_t \times N_\theta \times N_\varphi)$. Integration of all spherical harmonics up to a certain degree L in (6.3) requires $(L+1)^2$ discretization points [112]. Therefore, in the next step, $(L+1)^2$ new discretization points should be obtained from the QR-decomposition method to cover all information for whole translations. Newly discretized k-vectors are defined as a span of the entire k-space in such a way that to have stable translations in all other directions without rotating basis and testing vectors and k-space [55]. Applying the

QR-decomposition method for $\bar{\boldsymbol{Y}}$ matrix leads to the following equation;

$$\underbrace{\bar{\boldsymbol{Y}}^T}_{(L+1)^2\times N} \cdot \underbrace{\bar{\boldsymbol{P}}}_{N\times N} = \underbrace{\bar{\boldsymbol{Q}}}_{(L+1)^2\times(L+1)^2} \cdot \underbrace{\bar{\boldsymbol{R}}}_{(L+1)^2\times N}, \tag{6.8}$$

where $\bar{\boldsymbol{P}}$, $\bar{\boldsymbol{Q}}$, and $\bar{\boldsymbol{R}}$ are permutation, unitary, and upper triangle matrices, and $N = N_t \times N_\theta \times N_\varphi$. Equation (6.8) can be expressed in terms of block submatrices with $(L+1)^2$ elements as

$$\begin{bmatrix} \bar{\boldsymbol{Y}}_{11} & \bar{\boldsymbol{Y}}_{12} \end{bmatrix}^T \cdot \begin{bmatrix} \bar{\boldsymbol{P}}_{11} & \bar{\boldsymbol{P}}_{12} \\ \bar{\boldsymbol{P}}_{21} & \bar{\boldsymbol{P}}_{22} \end{bmatrix} = \bar{\boldsymbol{Q}}_{11} \cdot \begin{bmatrix} \bar{\boldsymbol{R}}_{11} & \bar{\boldsymbol{R}}_{12} \end{bmatrix}. \tag{6.9}$$

where $\bar{\boldsymbol{P}}_{11}$ and $\bar{\boldsymbol{R}}_{11}$ with dimensions of $(L+1)^2 \times (L+1)^2$ are extracted submatrices from the permutation and upper triangular matrices, respectively. Newly discretized k-vectors $\hat{\boldsymbol{k}}_{n_s}$ based on the obtained discretization points from the QR-decomposition method can be determined by

$$\hat{\boldsymbol{k}}_{n_s}\left(\theta_{n_{s_\theta}}, \varphi_{n_{s_\varphi}}\right) = \bar{\boldsymbol{K}}_{3\times N} \cdot \boldsymbol{P}^{n_s}_{N\times 1}, \quad \text{where} \quad \begin{cases} \forall n_s \in \left[1, (L+1)^2\right] \\ \forall n_{s_\theta} \in [1, (L+1)] \\ \forall n_{s_\varphi} \in [1, (L+1)] \end{cases}, \tag{6.10}$$

where $\hat{\boldsymbol{k}}_{n_s} = \hat{\boldsymbol{a}}_x \sin\theta_{n_s}\cos\varphi_{n_s} + \hat{\boldsymbol{a}}_y \sin\theta_{n_s}\sin\varphi_{n_s} + \hat{\boldsymbol{a}}_z \cos\theta_{n_s}$, and $\boldsymbol{P}^{n_s}_{N\times 1}$ represents the ${n_s}^{\text{th}}$ column of $\bar{\boldsymbol{P}}$ matrix. Each column of $\bar{\boldsymbol{K}}_{n'}$ is defined as

$$\hat{\boldsymbol{K}}_{n'} = \bar{\boldsymbol{R}}_v \cdot \hat{\boldsymbol{k}}_n\left(\theta_{n_\theta} + i\chi, \varphi_{n_\varphi}\right), \quad \text{where} \quad \begin{cases} \forall n' \in [1, N_t N_\theta N_\varphi] \\ \forall n \in [1, N_\theta N_\varphi] \\ \forall v \in [1, N_t] \end{cases}. \tag{6.11}$$

Utilizing (6.6) and (6.8), the newly discretized shift function $\boldsymbol{\Psi}^{\text{new}}$ (from p distinct basis functions to a single testing function) based on the new set of discretized wave vectors, $\hat{\boldsymbol{k}}_{n_s}\left(\theta_{n_{s\theta}}, \varphi_{n_{s\varphi}}\right)$, can be defined as

$$\boldsymbol{\Psi}^{\text{new}}\left(\hat{\boldsymbol{k}}_{n_s}(\theta_{n_{s\theta}}, \varphi_{n_{s_\varphi}})\right)_{(L+1)^2\times 1} = \left[\bar{\boldsymbol{P}}^T_{11} \quad \bar{\boldsymbol{P}}^T_{21}\right]_{(L+1)^2\times N} \cdot \boldsymbol{\Psi}^{\text{old}}\left(\bar{\boldsymbol{R}}_v \cdot \hat{\boldsymbol{k}}_n(\theta_{n_\theta} + i\chi, \varphi_{n_\varphi})\right)_{N\times 1}$$

$$\tag{6.12a}$$

$$= \left[\bar{\boldsymbol{Q}}_{11} \cdot \bar{\boldsymbol{R}}_{11}\right]^T \cdot \boldsymbol{a}. \tag{6.12b}$$

Expression of the old discretized shift function ($\boldsymbol{\Psi}^{\text{old}}$) with respect to the new one ($\boldsymbol{\Psi}^{\text{new}}$) for a single specific translation can be accomplished by reconstructing $\bar{\boldsymbol{Y}}$ in (6.6) for the corresponding translation and representing it with $\bar{\boldsymbol{y}}$. Therefore, using (6.6) and (6.12b), the following expression can be obtained

$$\begin{aligned}\boldsymbol{\Psi}^{\text{old}}\left(\bar{\boldsymbol{R}}_v\cdot\hat{\boldsymbol{k}}_n(\theta_{n_\theta}+i\chi,\varphi_{n_\varphi})\right)_{N_\varphi N_\theta\times 1} &= \bar{\boldsymbol{y}}_{N_\varphi N_\theta\times(L+1)^2}\cdot\boldsymbol{a}_{(L+1)^2\times 1}\\ &= \left(\bar{\boldsymbol{R}}_{11}^{-1}\cdot\bar{\boldsymbol{Q}}_{11}^{-1}\cdot\bar{\boldsymbol{y}}^T\right)^T\cdot\boldsymbol{\Psi}^{\text{new}}\left(\hat{\boldsymbol{k}}_{n_s}\right).\end{aligned}\tag{6.13}$$

Substituting (6.13) into (6.6) and then substituting the resultant expression into (6.4) yields the final expression at the end of the QR-decomposition algorithm. As a result, for p distinct sources, J_p, to be aggregated, translated, and disaggregated to one single testing function, the expression is obtained as

$$\begin{aligned}\sum_p J_p\frac{e^{ikR}}{4\pi R} &= \frac{ik}{(4\pi)^2}\int_0^{2\pi}\int_{0+i\chi}^{2\pi+i\chi}\underbrace{\sum_p J_p e^{i\left(\bar{\boldsymbol{R}}_v\cdot k\hat{\boldsymbol{k}}(\theta+i\chi,\varphi)\right)\cdot\boldsymbol{v}}}_{\substack{\text{Aggregation and Disaggregation}\\ \text{where } \boldsymbol{v}=\boldsymbol{v}_1^b+\boldsymbol{v}_2}}\underbrace{\left[\sum_{n=-L}^{L}b_n e^{in(\theta+i\chi)}\right]}_{\substack{\text{Translation along}\\ \text{the } z\text{-direction}}}d\theta d\varphi\\ &= \frac{ikC}{(4\pi)^2}\boldsymbol{\Psi}^{\text{old}}\left(\bar{\boldsymbol{R}}_v\cdot\hat{\boldsymbol{k}}_n\left(\theta_{n_\theta}+i\chi,\varphi_{n_\varphi}\right)\right)^T\tilde{\boldsymbol{T}}_z\left(kw\boldsymbol{a}_z,\theta_{n_\theta},\varphi_{n_\phi}\right)\\ &= \frac{ikC}{(4\pi)^2}\boldsymbol{\Psi}^{\text{new}}\left(\hat{\boldsymbol{k}}_{n_s}\left(\theta_{n_{s_\theta}},\varphi_{n_{s_\varphi}}\right)\right)^T\underbrace{\left(\bar{\boldsymbol{R}}_{11}^{-1}\cdot\bar{\boldsymbol{Q}}_{11}^{-1}\cdot\bar{\boldsymbol{y}}^T\right)\cdot\tilde{\boldsymbol{T}}_z\left(kw\boldsymbol{a}_z,\theta_{n_\theta},\theta_{n_\theta}\right)}_{\text{New translation}}.\end{aligned}\tag{6.14}$$

Hence, $\left(\bar{\boldsymbol{R}}_{11}^{-1}\cdot\bar{\boldsymbol{Q}}_{11}^{-1}\cdot\boldsymbol{y}^T\right)\cdot\tilde{\boldsymbol{T}}_z\left(kw\boldsymbol{a}_z,\theta_{n_\theta}+i\chi,\varphi_{n_\varphi}\right)$ represents the new translation in the desired direction which does not suffer from the LF breakdown and has stable translations in all directions. Consequently, besides obtaining a set of basis k-vectors using the QR-decomposition method and decreasing the number of integration points, new translation operator is defined which does not require rotation of k-space.

Although the number of harmonics approaches a constant number at low frequencies, interpolation and anterpolation operations for the multilevel version of NSPWMLFMA are unavoidable due to existence of different integration paths (χ) in each level [55]. Interpolation and anterpolation techniques are based on the applied QR-decomposition method. Considering aggregation from a deeper level ($m+1$) to one upper level (m)

leads to

$$\underbrace{\boldsymbol{A}^{L_m}}_{(L_m+1)^2\times 1} = \underbrace{\bar{\boldsymbol{I}}_{L_{m+1}}^{L_m}}_{(L_m+1)^2\times(L_{m+1}+1)^2} \cdot \underbrace{\boldsymbol{A}^{L_{m+1}}}_{(L_{m+1}+1)^2\times 1} , \tag{6.15}$$

where L_m and L_{m+1} are the number of the harmonics at level m and $m+1$, respectively. The interpolation matrix $\bar{\boldsymbol{I}}_{L_{m+1}}^{L_m}$ is defined as

$$\begin{aligned}\underbrace{\left(\bar{\boldsymbol{I}}_{L_{m+1}}^{L_m}\right)^T}_{(L_{m+1}+1)^2\times(L_m+1)^2} = &\underbrace{\left(\bar{\boldsymbol{R}}_{11}^{m+1}\right)^{-1}}_{(L_{m+1}+1)^2\times(L_{m+1}+1)^2} \\ &\cdot \underbrace{\left(\bar{\boldsymbol{Q}}_{11}^{L_{m+1}}\right)^{-1}}_{(L_{m+1}+1)^2\times(L_{m+1}+1)^2} \cdot \underbrace{\bar{\boldsymbol{S}}}_{(L_{m+1}+1)^2\times(L_m+1)^2} ,\end{aligned} \tag{6.16}$$

where

$$\begin{aligned}&\left[\bar{\boldsymbol{S}}\right]_{l(l+1)+m+1,n_s} = j_l(2kr_C)^{L_{m+1}} Y_{l,m}\left(\hat{\boldsymbol{k}}_{n_s}^{L_m}\left(\theta_{n_{s_\theta}},\varphi_{n_{s_\varphi}}\right)\right) \\ &\forall n_s \in \left[1,(L_m+1)^2\right],\ \forall l \in [0,L_{m+1}],\ \ m \in [-l,+l] .\end{aligned} \tag{6.17}$$

It should be noted here that the anterpolation is the transpose of the interpolation matrix.

Implementation of NSPWMLFMA for the solution of PIEs requires the construction of two separate tree structures for the RWG and pulse basis functions. It should be noted that the box indices in tree structures are not identical, which requires to uniquely define translations among the boxes containing RWGs and the boxes containing pulses. In other words, in addition to translations among the boxes containing RWG basis functions (i.e., RWG to RWG), new translations among the boxes containing pulses (i.e., pulse to pulse), and from the boxes containing RWG basis functions to boxes containing pulse basis functions (i.e., RWG to pulse) and vice versa (i.e., pulse to RWG) are uniquely defined, thereby assuring the desired accuracy.

6.3 Preconditioning for PIEs solved via Mixed-Form MLFMA

In a similar fashion to [52], where a comprehensive study for conditioning properties of PIEs has been provided, a left constraint preconditioner $\bar{\mathbf{P}}_C^{-1}$ is used for $\bar{\boldsymbol{Z}} = \begin{bmatrix} \bar{\boldsymbol{\Gamma}}_{\boldsymbol{J},\boldsymbol{J}} & \bar{\boldsymbol{\Gamma}}_{\boldsymbol{J},\sigma} \\ \bar{\boldsymbol{\Gamma}}_{\sigma,\boldsymbol{J}} & k_0^2\bar{\boldsymbol{\Gamma}}_{\sigma,\sigma} \end{bmatrix}$ to reduce the number of iterations. Briefly, $\bar{\mathbf{P}}_C^{-1}$ is obtained as

$$\bar{\mathbf{P}}_C^{-1} = \begin{bmatrix} \bar{\mathbf{I}} & -\bar{\mathbf{D}}^{-1}\bar{\boldsymbol{\Gamma}}_{\boldsymbol{J},\sigma} \\ \bar{\mathbf{0}} & \bar{\mathbf{I}} \end{bmatrix} \begin{bmatrix} \bar{\mathbf{D}}^{-1} & \bar{\mathbf{0}} \\ \bar{\mathbf{0}} & \bar{\mathbf{S}}^{-1} \end{bmatrix} \begin{bmatrix} \bar{\mathbf{I}} & \bar{\mathbf{0}} \\ -\bar{\boldsymbol{\Gamma}}_{\sigma,\boldsymbol{J}}\bar{\mathbf{D}}^{-1} & \bar{\mathbf{I}} \end{bmatrix}, \tag{6.18}$$

where $\bar{\mathbf{S}} = -\left(-k_0^2\bar{\boldsymbol{\Gamma}}_{\sigma,\sigma} + \bar{\boldsymbol{\Gamma}}_{\sigma,\boldsymbol{J}}\big(\bar{\mathbf{D}}\big)^{-1}\bar{\boldsymbol{\Gamma}}_{\boldsymbol{J},\sigma}\right)$ is the Schur complement of $\bar{\mathbf{P}}_C$, and $\bar{\mathbf{D}}$ is the diagonal form of $\bar{\boldsymbol{\Gamma}}_{\boldsymbol{J},\boldsymbol{J}}$ as an approximation. Note that instead of $\bar{\mathbf{D}}$, one can use $\bar{\mathbf{D}}'$ formed from the block diagonal elements of $\bar{\boldsymbol{\Gamma}}_{\boldsymbol{J},\boldsymbol{J}}$ that are obtained from near-field interactions as explained in [119]. This can reduce the number of iterations even further. Other matrices will remain intact which are obtained from their corresponding near-field interactions. For a PEC sphere discretized with 826 triangles (including 2065 unknowns), Fig. 6.1 shows both the diagonal and block diagonal terms of $\bar{\boldsymbol{\Gamma}}_{\boldsymbol{J},\boldsymbol{J}}$ used in $\bar{\mathbf{P}}_C^{-1}$ at different mixed-form MLFMA levels, where the generalized minimal residual method (GMRES) iterative solver with an error tolerance of 10^{-3} is used with maximum number of iterations fixed to 1000. Table 6.1 shows the number of iterations when there is no preconditioner, and when $\bar{\mathbf{D}}$ and $\bar{\mathbf{D}}'$ as a diagonal and block diagonal approximations are used in (6.18), respectively. Here, level 2 corresponds to the MoM solution. It can be seen that the use of $\bar{\mathbf{D}}'$ reduces the total iteration counts to reasonable numbers.

Table 6.1: Number of iterations based on the residual error 10^{-3} for the solution of the PEC sphere problem.

Sphere Problem		Potential Based Integral Equations		
Level	Unknowns	NP	D	BD
2	2065	488	27	19
3	2065	491	30	18
4	2065	492	23	21
NP: No preconditioner, D: Diagonal, BD: Block diagonal				

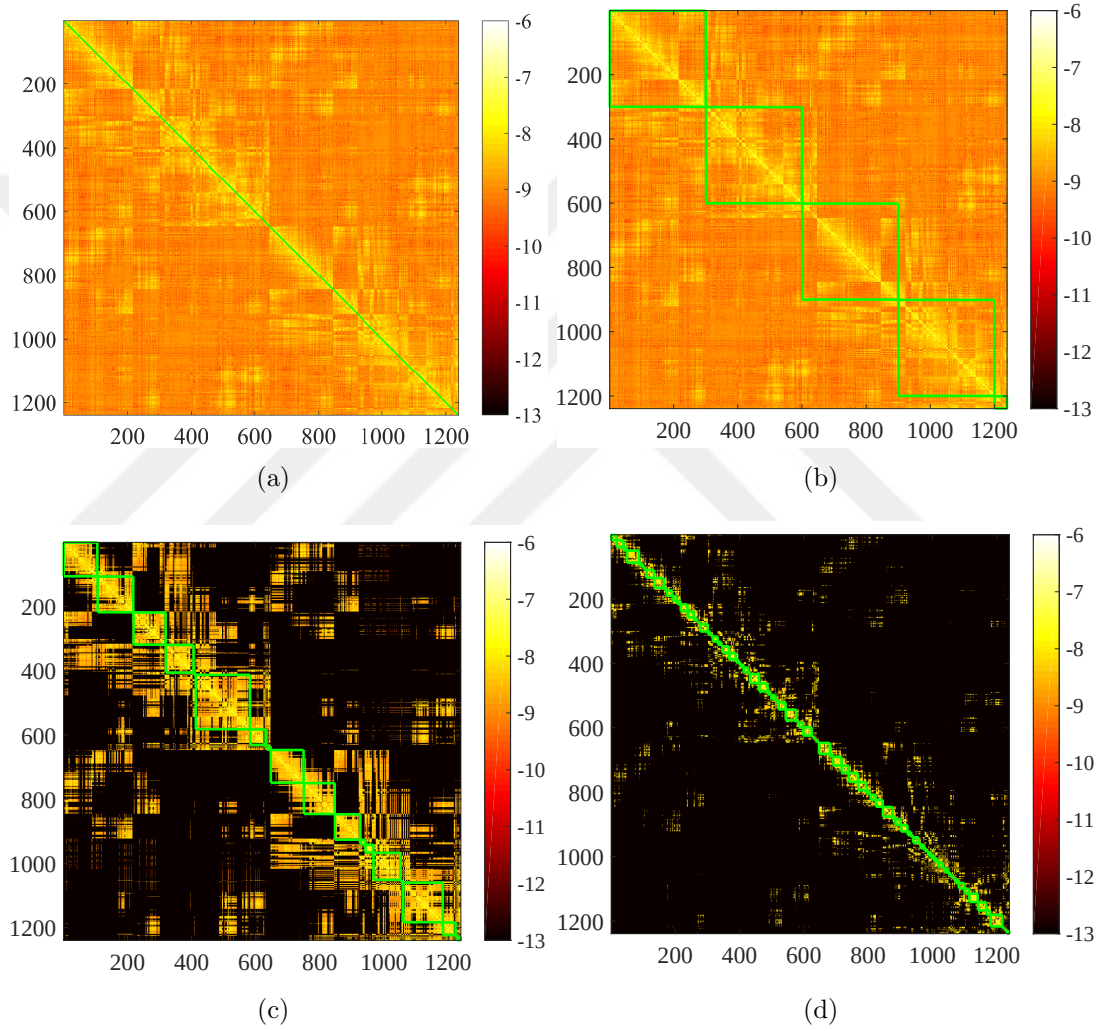


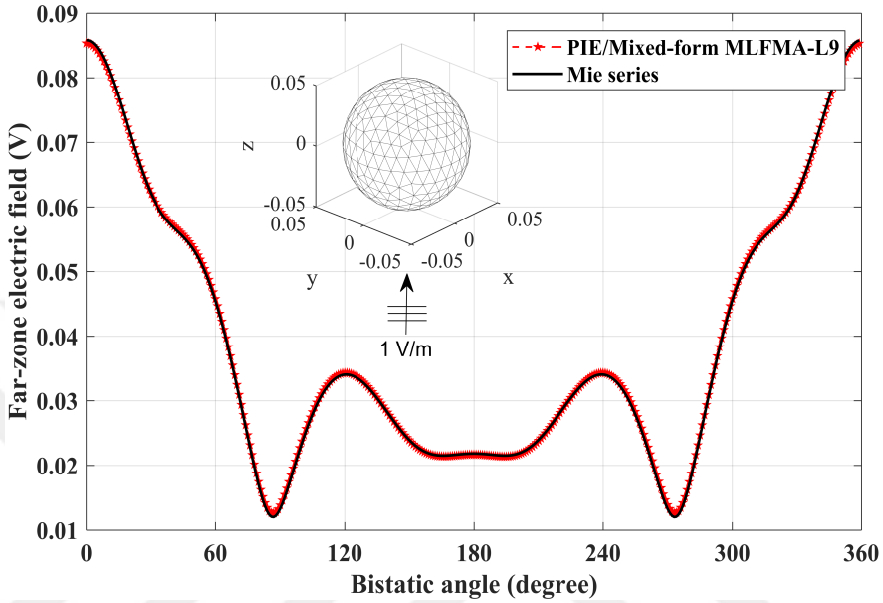
Figure 6.1: (a) Diagonal terms of near-field matrix ($\bar{\mathbf{\Gamma}}_{\boldsymbol{J},\boldsymbol{J}}$) which are used to construct the left preconditioner at level 2, (b) Block diagonal terms of near-field matrix ($\bar{\mathbf{\Gamma}}_{\boldsymbol{J},\boldsymbol{J}}$) which are used to construct the left preconditioner at level 2, (c) level 3, and (d) level 4 according to (6.18).

6.4 Numerical Results

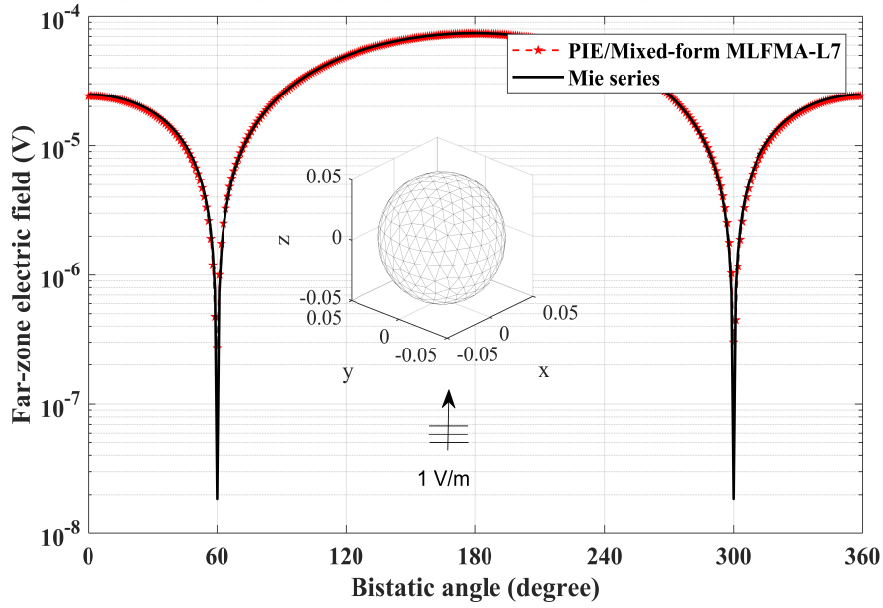
Numerical results are presented to illustrate the capability of the proposed mixed-form MLFMA solver for PIEs, where GMRES with an error tolerance of 10^{-4} is used as the iterative solver. Number of harmonics, L, at low frequencies (i.e., electrically small boxes) is fixed (regardless of the box size) [55, 97], and is selected to be 25 for all the numerical examples presented in this thesis. At middle and high frequencies, where the box sizes are comparable to the wavelength, excess bandwidth formula is used [6]. In the simulations, $2L + 2$ integration points are used both for θ and φ directions. All results are obtained by a double-precision program on a cluster of Intel(R) Xeon(R) X5472 processors with 3.00 GHz clock rate and 32 GB RAM.

The first example is a PEC sphere with a diameter of 0.1 m, which is illuminated by an x-polarized uniform plane wave propagating along the z-direction. Fig. 6.2(a) shows the far-zone scattered electric field as a function of the bistatic angle on the z-x plane (0° and 180° represent forward and backward scattering directions, respectively) compared with the Mie series result when the operating frequency is 3 GHz. As mentioned in chapter 2 (section 2.3), the far-zone electric field is defined as the electric-field intensity multiplied by the distance from the object when the distance goes to infinity. At this frequency, the diameter of the sphere, d_λ, corresponds to λ and each triangle has an approximate edge length, l_λ, of $\lambda/150$. A total of 364865 unknowns are solved using 9-level mixed-form MLFMA. Fig. 6.2(b) shows a similar result when the frequency is 30 MHz, where $d_\lambda = \lambda/100$ and $l_\lambda = \lambda/5600$. In this case, 54365 unknowns are solved with a 7-level mixed-form MLFMA. The number of iterations is 86 and 59 at 3 GHz and 30 MHz, respectively. In both cases a very good agreement is obtained that verifies the accuracy of the proposed method at both high and low frequencies.

A tilted 10 cm $\times$ 10 cm PEC plate, illuminated by an x-polarized uniform plane wave propagating along the z-direction, is the second example. Similar to the PEC sphere case, two different operating frequencies are selected as 3 GHz and 3 MHz. At 3 GHz, the plate is $\lambda \times \lambda$ and discretized with triangles of edge size $l_\lambda = \lambda/320$. A total 511360 unknowns are solved with a 9-level mixed-form MLFMA in 79 iterations. The scattered far-field result is compared with both PIEs and EFIE solved with MoM by using coarse discretization ($l_\lambda = \lambda/10$) as shown in Fig. 6.3(a), where an excellent agreement can be seen. The same plate is $\lambda/1000 \times \lambda/1000$ at 3 MHz, and discretized with triangles of

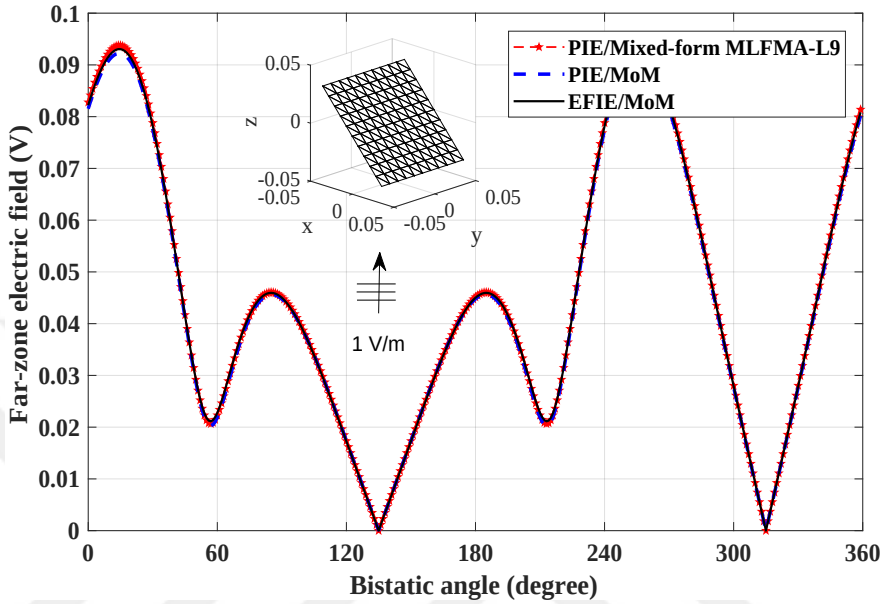


(a)

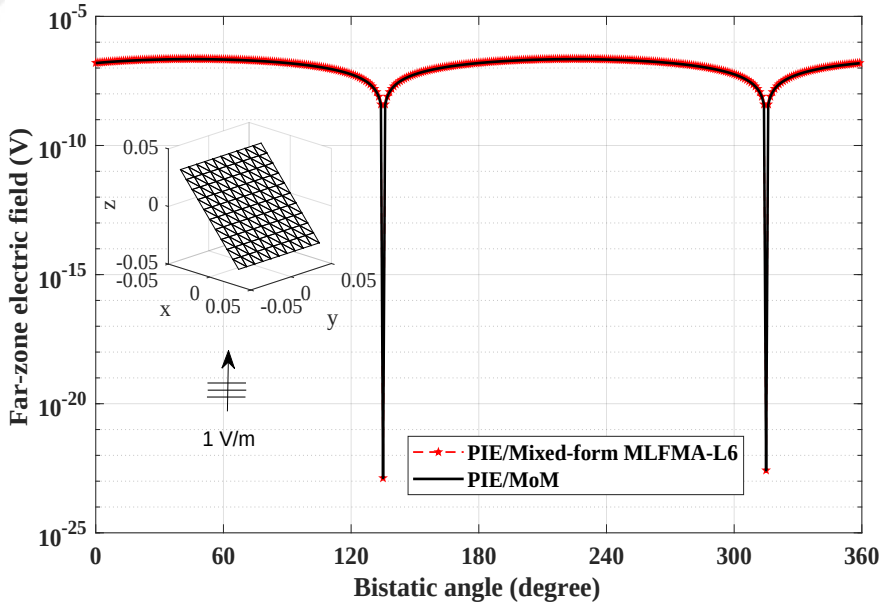


(b)

Figure 6.2: Far-zone scattered electric field results obtained from numerical and analytical solutions for a PEC sphere of diameter 10 cm (a) at 3 GHz and (b) 30 MHz.



(a)



(b)

Figure 6.3: Far-zone scattered electric field results obtained from numerical solutions for a PEC plate with edge size of 10 cm discretized with different mesh sizes including fine and coarse cases (a) at 3 GHz and (b) 3 MHz.

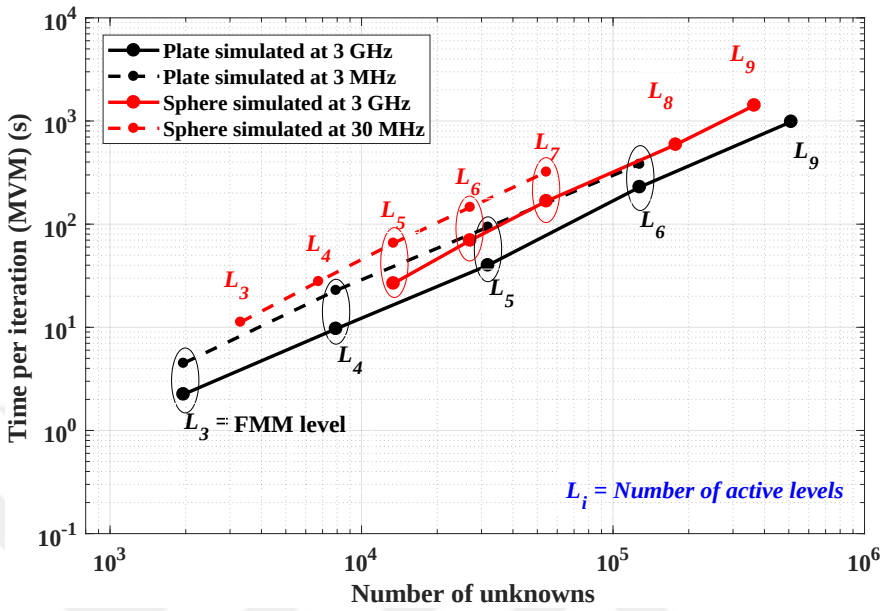


Figure 6.4: Matrix-vector multiplication times for both a PEC tilted plate and a PEC sphere at two different frequencies (3 GHz and 3 MHz for tilted PEC plate, and 3 GHz and 30 MHz for the PEC sphere). For the PEC tilted plate, the number of unknowns is increasing from 1960 to 511360 by refining the discretization from $\lambda/20$ to $\lambda/320$ at 3 GHz and from 1960 to 127680 by refining the discretization from $\lambda/20000$ to $\lambda/160000$ at 3 MHz. Minimum box sizes in the tree structures for 3 GHz and 3 MHz are $\lambda/256$ and $\lambda/32000$, respectively. For the PEC sphere, these numbers are as follows: the number of unknowns is increasing by refining the discretizations from 13405 ($l_\lambda = \lambda/30$) to 364865 ($l_\lambda = \lambda/150$) at 3 GHz, and from 3305 ($l_\lambda = \lambda/1400$) to 54365 ($l_\lambda = \lambda/5600$) at 30 MHz. Minimum box sizes in the tree structures for 3 GHz and 30 MHz are $\lambda/256$ and $\lambda/6400$, respectively.

edge size $l_\lambda = \lambda/160000$ leading to 127680 unknowns, which are solved with a 6-level mixed-form MLFMA. For the solution, 55 iterations are required to reach 10^{-4} residual error. The far-field result is compared with PIE/MoM in Fig. 6.3(b), where an excellent agreement is obtained.

Fig. 6.4 presents the running time per iteration versus the number of unknowns both for the PEC sphere and the tilted PEC plate examples at two different frequencies (3 GHz and 30 MHz for the PEC sphere and 3 GHz and 3 MHz for tilted PEC plate). An $O(NL)$ complexity, where L is the number of levels, can be observed for the CPU time.

The third example is a 2-D periodic electromagnetic band gap structure formed of

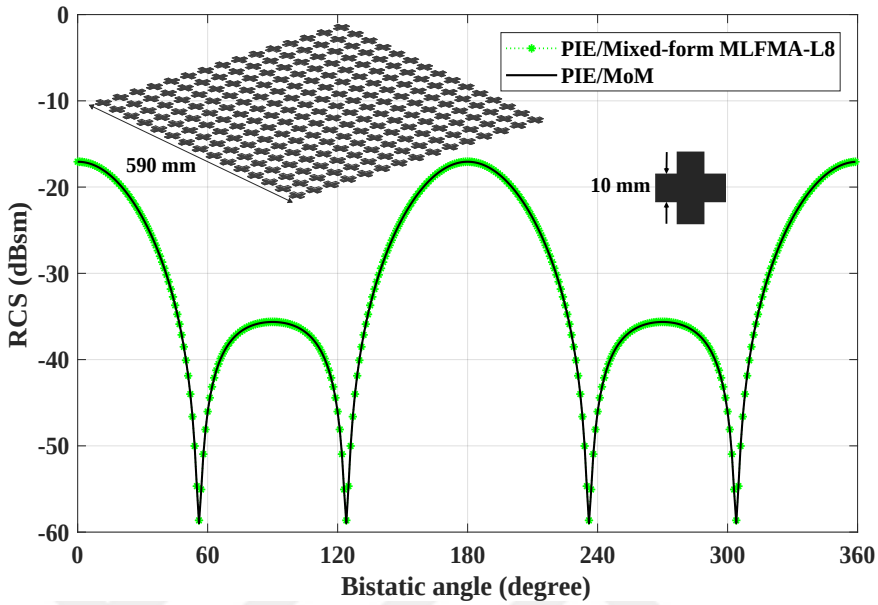


Figure 6.5: RCS results obtained by using two different mesh sizes $l_\lambda = \lambda/100$ and $l_\lambda = \lambda/200$, which are corresponding to 23175 and 119175 unknowns at 600 MHz. The coarse and fine discretized objects are solved by using MoM and 8-level mixed-form MLFMA with approximate minimum box sizes of $\lambda/128$ in the tree structure.

PEC cross-shaped elements as shown in Fig. 6.5. The PEC structure is illuminated by a uniform plane wave polarized in both x- and y-directions and propagating along the $-z$ direction [i.e., $\boldsymbol{E} = \frac{1}{\sqrt{2}}(\hat{\boldsymbol{a}}_x + \hat{\boldsymbol{a}}_y)$ and $\hat{\boldsymbol{k}} = -\hat{\boldsymbol{a}}_z$] at 600 MHz. Radar cross section (RCS) is obtained both with MoM (used to solve PIEs) and 8-level mixed-form MLFMA. Excellent agreement is obtained as can be seen from Fig. 6.5. A total of 119175 unknowns are used in this example for the mixed-form MLFMA solver. Note that, because of memory and CPU time restrictions, a coarser mesh with 23175 unknowns is used for the MoM solution.

Final example is grounded mushroom type structure with total dimensions of 10.68 cm $\times$ 10.68 cm $\times$ 0.8 cm as shown in Fig. 6.6 [122]. The structure is discretized with a total of 394710 unknowns, corresponding to 1 mm triangle edge, and solved with 8-level mixed-form MLFMA at 3 GHz for an x-polarized plane wave propagating along the $-z$ direction. Far-zone scattered electric field and linear current distribution results are presented in Figs. 6.7 and 6.8, respectively.

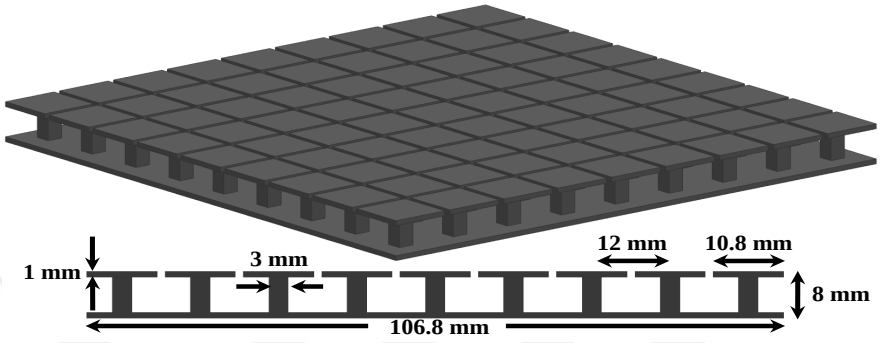


Figure 6.6: Geometry of a mushroom-type structure.

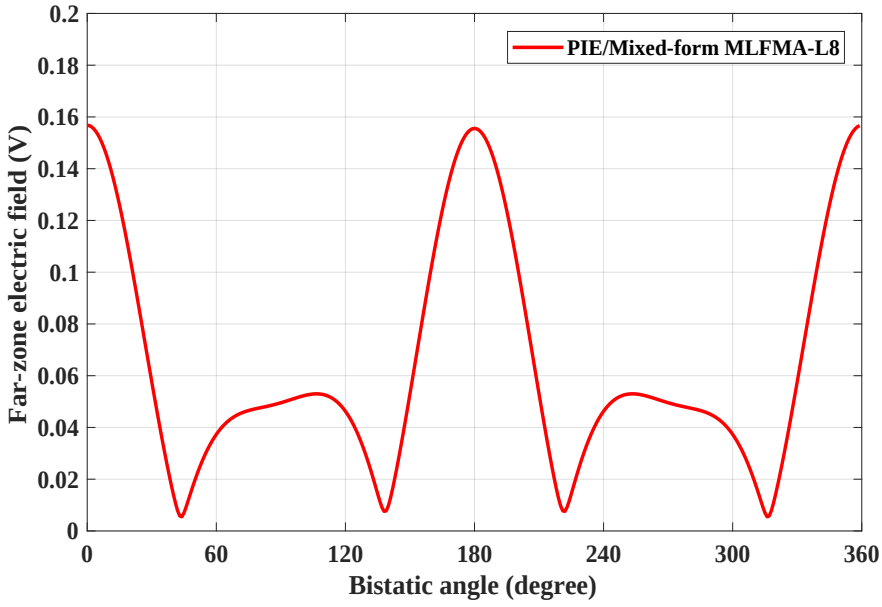


Figure 6.7: Far-zone scattered electric field result obtained from 8-level mixed-form MLFMA solution of the PEC mushroom-type structure at 3 GHz.

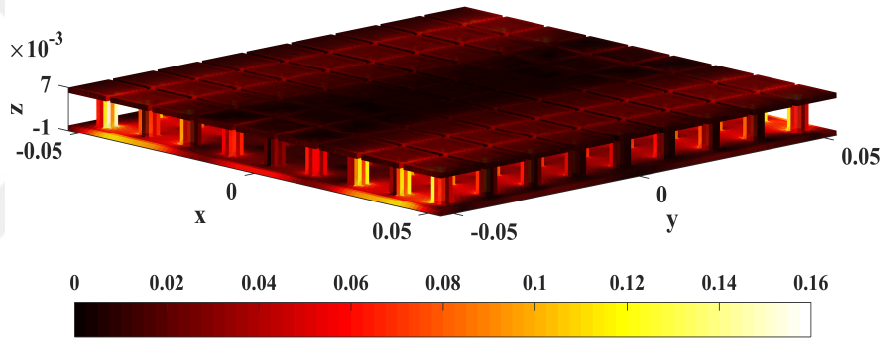


Figure 6.8: Linear current distribution of the mushroom-type structure illuminated by a uniform plane wave polarized in x-direction.

Chapter 7

Solutions of Multiscale Electromagnetic Problems

7.1 Introduction

In this chapter, recently introduced incomplete-tree structures for MFIE [73] are modified and used in conjunction with the proposed mixed-form MLFMA that is presented in the previous chapter to employ a novel broadband incomplete-leaf (IL) MLFMA (IL-MLFMA) to the solution of PIEs for scattering/radiation from multiscale open and closed surfaces. This population based algorithm deploys a nonuniform clustering that enables to use deep levels safely and, when necessary, without compromising the accuracy, and hence the error is controllable. As a result, by using the proposed IL-MLFMA for PIEs (i) the efficiency is improved and (ii) the memory requirements are significantly reduced (order of magnitude) while the accuracy is maintained. The superiority of this algorithm in terms of efficiency, accuracy and in particular memory requirements is demonstrated by means of canonical and several real-life multiscale geometries.

7.2 Implementations

As explained in chapter 4, for a PEC in free space (ε_0, μ_0) with a surface S and a normal unit vector $\hat{\boldsymbol{n}}$ on its surface as shown in Fig. 4.2, PIEs can be expressed as relationships between scattered and incident fields by satisfying the boundary conditions on S for the electric scalar potential Φ and the tangential component of the magnetic vector potential $(\hat{\boldsymbol{n}} \times \boldsymbol{A})$ [49, 110]. The surface electric-current density, $\boldsymbol{J}$, and the normal component of the magnetic vector potential, $\Sigma = \hat{\boldsymbol{n}} \cdot \boldsymbol{A}$, are the unknowns expanded with RWG [111] and pulse functions [49–52], respectively. Using a Galerkin method of MoM solution for the resulting PIEs, a matrix equation of the form

$$\begin{bmatrix} \bar{\boldsymbol{\Gamma}}_{\boldsymbol{J},\boldsymbol{J}} & \bar{\boldsymbol{\Gamma}}_{\boldsymbol{J},\sigma} \\ \bar{\boldsymbol{\Gamma}}_{\sigma,\boldsymbol{J}} & k_0^2 \bar{\boldsymbol{\Gamma}}_{\sigma,\sigma} \end{bmatrix} \begin{bmatrix} \boldsymbol{\zeta}/c_0 \\ \boldsymbol{\psi}/\eta_0 \end{bmatrix} = - \begin{bmatrix} \boldsymbol{a}_{\text{inc}}/\eta_0 \\ ik_0\varepsilon_0\boldsymbol{\varphi}_{\text{inc}} \end{bmatrix} \tag{7.1}$$

is obtained (for details see chapter 4). In (7.1), k_0, η_0, and c_0 are the free-space wavenumber, intrinsic impedance, and wave velocity, respectively, while $\boldsymbol{\zeta}$ and $\boldsymbol{\psi}$ contain the unknown coefficients of RWG and pulse basis functions, respectively. $\boldsymbol{a}_{\text{inc}}$ contains the discrete tested form of the known incident magnetic vector potential whereas $\boldsymbol{\varphi}_{\text{inc}}$ contains that of the electric scalar potential. Finally, the matrix entries of each submatrix in (7.1) are given as

$$\begin{aligned} [\Gamma_{\boldsymbol{J},\boldsymbol{J}}]_{mn} &= \langle \boldsymbol{t}_m, g, \boldsymbol{b}_n \rangle\,; \qquad [\Gamma_{\boldsymbol{J},\sigma}]_{mn} = \langle \nabla.\boldsymbol{t}_m, g, \sigma_n \rangle \\ [\Gamma_{\sigma,\boldsymbol{J}}]_{mn} &= \langle \sigma_m, g, \nabla'.\boldsymbol{b}_n \rangle\,; \quad [\Gamma_{\sigma,\sigma}]_{mn} = \langle \sigma_m, g, \sigma_n \rangle \end{aligned} \tag{7.2}$$

where

$$\left\langle \boldsymbol{f}\left(\boldsymbol{r}\right), g\left(\boldsymbol{r}, \boldsymbol{r'}\right), \boldsymbol{h}\left(\boldsymbol{r'}\right) \right\rangle = \int_S ds \boldsymbol{f}\left(\boldsymbol{r}\right) \cdot \int_{S'} ds' g\left(\boldsymbol{r}, \boldsymbol{r'}\right) \boldsymbol{h}\left(\boldsymbol{r'}\right) \tag{7.3}$$

with $g\left(\boldsymbol{r}, \boldsymbol{r'}\right)$ being the free-space Green's function. In (7.3) $\boldsymbol{f}\left(\boldsymbol{r}\right)$ and $\boldsymbol{h}\left(\boldsymbol{r}\right)$ can be replaced by scalar functions.

The fast and accurate solution of (7.1) using the conventional MLFMA is not feasible for multiscale problems due to the need of electrically small boxes at deeper levels of the constructed tree structures giving rise to the well-known LF breakdown. As a remedy, the mixed-form MLFMA [78] presented in the previous chapter, as a conventional

broadband MLFMA solver, uses NSPWMLFMA at low frequencies (i.e., box sizes $< \lambda/8$; λ: free-space wavelength). Although stable computations of near- and far-field interactions can be performed via PIEs and the conventional broadband MLFMAs, such as the mixed-form MLFMA, they employ the standard tree structure with fixed-size boxes and regular division of parent boxes into at most eight subboxes, and thus offer only the following two inaccurate/inefficient options for multiscale structures modeled with highly nonuniform discretizations:

- To use extended number of levels with small leaf-level boxes that would lead to inaccurate interactions since many of these boxes cannot enclose relatively larger discretization elements especially in the coarsely discretized regions.
- To use a limited number of levels, and hence larger leaf-level boxes that would lead to a high computational cost due to $\mathcal{O}(N^2)$ complexity in self- and near-field interactions among these boxes in locally over-discretized regions.

Therefore, to obtain a truly broadband MLFMA implementation that can tackle the above-mentioned issues, we use the incomplete-tree structures in conjunction with the mixed-form MLFMA resulting a population based and hence a nonuniform clustering based algorithm. Similar to [73–76], first a predetermined threshold, called as the maximum box population (MBP), is selected to handle such a nonuniform clustering scheme. Then, three different types of boxes are defined for PIEs. The first two types, namely the overcrowded boxes (OCBs) with a population equal to or more than the given threshold (OCBs are the ones that are recursively divided into subboxes in the incomplete-tree structures), and truncated boxes (TBs) with a population less than the given threshold (TBs may exist at any level with no box branches and they are not recursively divided into subboxes), have already been introduced in [73]. However, because PIEs include both RWGs and pulse basis functions, correct organization of near- and far-field interactions as well as their efficient and accurate computations necessitate a third type of boxes called as pruned boxes (PBs). A PB is a virtual box, which was supposed to be one of the extensions for a TB. For better understanding, Fig. 7.1(a) illustrates the 2-D nonuniform clustering where only OCBs are divided into four small subboxes in each level, and TBs will stay at upper levels. The clustering process is continuing until the assigned maximum level is being reached or populations of the leaf boxes do not exceed the predetermined threshold as well as preventing a

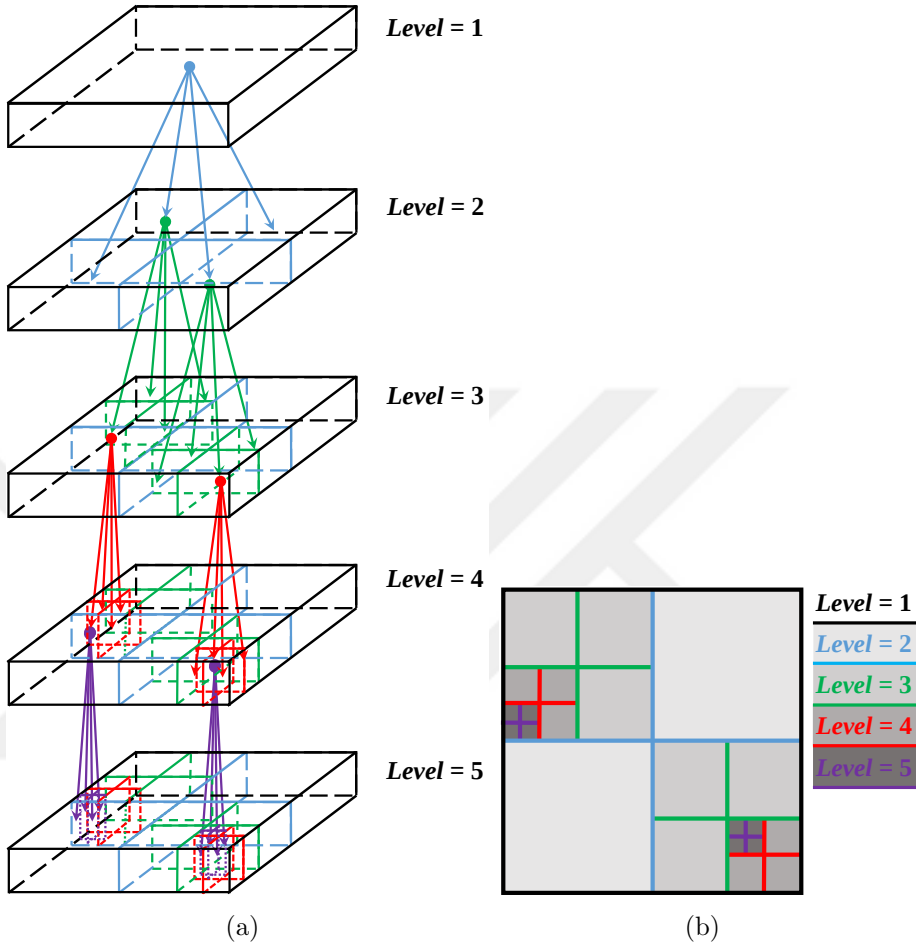


Figure 7.1: (a) 3-D view and corresponding (b) 2-D view of nonuniform clustering in incomplete-tree structure where overpopulated boxes require more divisions to reach the assigned population threshold (overpopulated (or OCBs) are colored with darker gray in the same level).

situation that triangles are sticking out the enclosing boxes. The 2-D view of Fig. 7.1(a) is presented in Fig. 7.1(b) where the boxes are colored based on the population density. The darker regions are equivalent to denser discretizations and hence, deeper levels. The borders for the first to fifth levels are also given in the figure. According to Fig. 7.1, TBs with variable box sizes are distributed across the whole tree structure not only at the leaf level, and only OCBs are divided into subboxes which results in an incomplete-tree structure. For understanding the concept behind PBs, a typical 2D incomplete-tree structure where OCBs, TBs, and PBs can be recognized according to the color and definitions is given in Fig. 7.2.

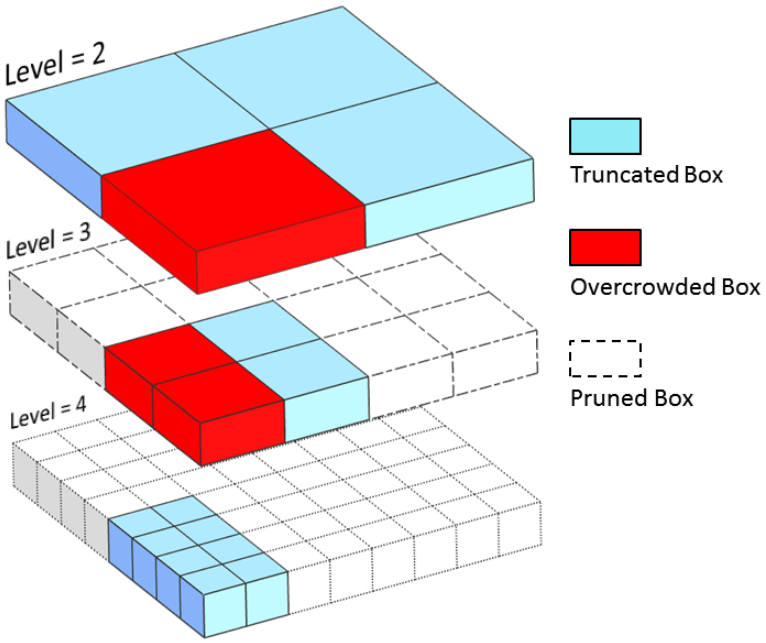


Figure 7.2: A typical 2-D incomplete-tree structure with recognized OCBs, TBs, and PBs [121].

At this point it should be noted that one can define two separate incomplete-tree structures; one for RWG and one for pulse basis functions, and implement the algorithm proposed in [73] that does not require PBs. Such an implementation is performed in [78] for mixed-form MLFMA that uses the standard tree structure. Unfortunately, in such an implementation for incomplete-tree structures, all near-, pseudonear- and far-interactions for the submatrices in (7.1) should be redefined and calculated separately (including 4 QR-decompositions for small boxes), which will significantly increase the complexity of the algorithm especially for $\bar{\mathbf{\Gamma}}_{\boldsymbol{J},\sigma}$ and $\bar{\mathbf{\Gamma}}_{\sigma,\boldsymbol{J}}$ submatrices. Hence, we proceed with a novel single incomplete-tree structure by selecting the threshold over the RWG functions and implement the algorithm as follows:

(i) *Identifying the Parent TB of RWG and Pulse (i.e., triangle) Functions*: The incomplete-tree structure is constructed based on the MBP of RWG functions, and thus the parent TBs of RWG functions are identified using the same algorithm presented in [73]. Very often, however, a triangle may fall into a different parent TB from its pair and/or the corresponding RWG function, and its occurrence increases significantly for multiscale geometries at each and every level. Moreover, these different parent TBs can even be located at different levels (usually observed for geometries with large

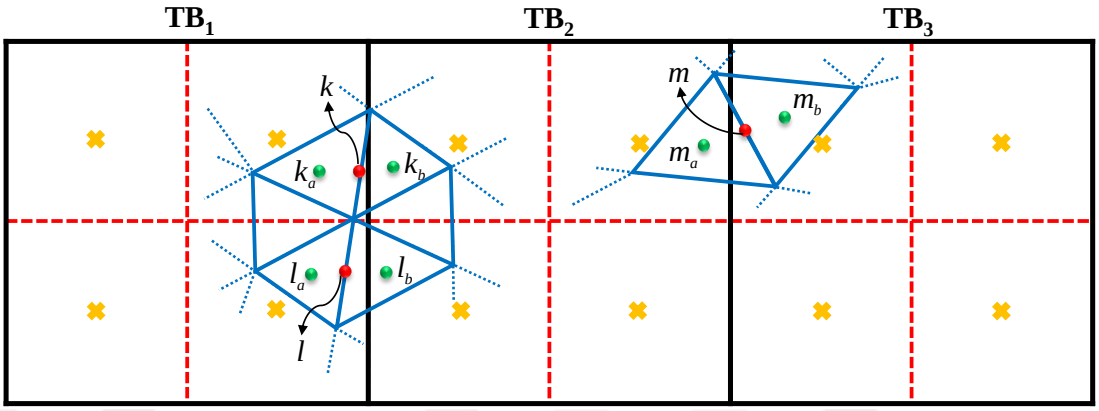


Figure 7.3: A pictorial example to illustrate (*i*) the parent TBs of RWG and pulse basis functions, and (*ii*) how their interactions are classified (i.e., near- or far-field interactions).

multiscale factors). A simple example for such a scenario is illustrated in Fig. 7.3, where three leaf-level TBs (solid lines) and the associated virtual PBs (dashed lines, centers marked with $\times$) contain part of an arbitrarily discretized geometry (i.e., RWG and pulse functions). Consider the RWG k and l together with the associated pair of triangles (k_a,k_b) and (l_a,l_b), respectively (centroids are marked with dots). It can be clearly seen that k_b and l_b remain in TB_2 while their pair triangles k_a and l_a as well as the corresponding RWG functions (k and l) remain in TB_1. To identify the parent TB of a given triangle and hence the total triangle population in a TB in a robust manner, we first determine its parent PB by finding the minimum of the shortest distances between the centroid of the triangle and the center of the PBs containing the three edges (i.e., the associated RWGs) of that triangle, and then find the parent TB of the corresponding PB. Because this implementation is performed only in the leaf level, it does not bring any extra computational cost (see the time (in seconds) "Incomplete-tree constructions" in numerical examples). The pseudo code shown in Algorithm 1 in Appendix A is used to identify the parent TBs of pulse functions (i.e., triangles).

(*ii*) *List of Near and Far Boxes*: The implementation of incomplete-tree structure requires detailed investigation on box-to-box interactions and careful organizations of near- and far-zone boxes for obtaining better efficiency and accuracy. Therefore, near-zone and far-zone boxes are redefined in the incomplete-tree structure. Construction of a list for near boxes, pseudonear boxes, and far boxes are presented in [73]. However, for the sake of clarity it is also explained here. As an example, a

nonuniform clustering is considered in Fig. 7.4 for several scenarios, where small purple boxes are the testing boxes and the surrounding yellow and blue boxes denote near- and far-zone basis boxes, respectively. All touching boxes with equal or larger sizes are considered as near-zone boxes. In addition to considering the touching boxes of any testing box as near-zone boxes whether they are distinct in sizes and truncated at different levels, non-touching TBs (TBs that are touching the parent or grandparent boxes of the testing boxes) located at any upper level are also defined as pseudonear boxes and considered as near-zone boxes of the same testing box. Pseudonear boxes are larger than the testing box since they usually contain larger basis functions and hence larger interactions. Although pseudonear boxes may be located farther than some of the far-zone boxes, they can have bigger interactions in comparison with the basis functions located in the far-zone boxes of the same testing box. Therefore, pseudonear box definition is for justifying accurate calculation of the interactions among different sizes of basis and testing functions regardless of their distance from each other.

Construction of far-zone boxes of the given testing box is determined according to one-box-buffer scheme (the same scenario in the conventional MLFMA) applied to the rest of the same-size boxes (at the same level). Due to considering uniform size boxes in determining far-zone boxes, the far-field computations look like the conventional MLFMA without any extra interpolation and anterpolation techniques.

(*iii*) *Near- and Far-Field interactions*: All near- and far-field interactions (based on the one-buffer-box criterion) must be calculated for each and every submatrix of (7.1) (i.e., $\bar{\mathbf{\Gamma}}_{\boldsymbol{J},\boldsymbol{J}} = \bar{\mathbf{\Gamma}}^N_{\boldsymbol{J},\boldsymbol{J}} + \bar{\mathbf{\Gamma}}^F_{\boldsymbol{J},\boldsymbol{J}}$, $\bar{\mathbf{\Gamma}}_{\boldsymbol{J},\sigma} = \bar{\mathbf{\Gamma}}^N_{\boldsymbol{J},\sigma} + \bar{\mathbf{\Gamma}}^F_{\boldsymbol{J},\sigma}$, $\bar{\mathbf{\Gamma}}_{\sigma,\boldsymbol{J}} = \bar{\mathbf{\Gamma}}^N_{\sigma,\boldsymbol{J}} + \bar{\mathbf{\Gamma}}^F_{\sigma,\boldsymbol{J}}$, $\bar{\mathbf{\Gamma}}_{\sigma,\sigma} = \bar{\mathbf{\Gamma}}^N_{\sigma,\sigma} + \bar{\mathbf{\Gamma}}^F_{\sigma,\sigma}$; N: near-field calculation, F: far-field calculation). Yet, the possibility that the parent TB of a triangle can be different than its pair triangle and/or the corresponding RWG function, as explained in step (*i*), should be taken into account in these calculations. As an example, consider the k^{th} and the m^{th} RWG functions in Fig. 7.3. They are in the far-zone of each other and their interaction, $\langle \boldsymbol{t}_k, g, \boldsymbol{b}_m \rangle$, must be in $\bar{\mathbf{\Gamma}}^F_{\boldsymbol{J},\boldsymbol{J}}$. On the other hand, when we consider the interactions between the pulses on the triangles that form these two RWG functions, k_a and m_b are in the far-zone of each other and their interaction $\langle \sigma_{k_a}, g, \sigma_{m_b} \rangle$ must be in $\bar{\mathbf{\Gamma}}^F_{\sigma,\sigma}$. However, m_a is in the near-zone of both k_a and k_b, and m_b is in the near zone of k_b. Thus all, $\langle \sigma_{k_a}, g, \sigma_{m_a} \rangle$, $\langle \sigma_{k_b}, g, \sigma_{m_a} \rangle$, and $\langle \sigma_{k_b}, g, \sigma_{m_b} \rangle$ must be in $\bar{\mathbf{\Gamma}}^N_{\sigma,\sigma}$. Similarly, when we consider the interactions between these RWG functions and the pulses on the triangles that form these RWG functions, k_a and m_b are in the far-zone of m and k, respectively. Hence, $\langle \nabla.\boldsymbol{t}_k, g, \sigma_{m_b} \rangle$ and

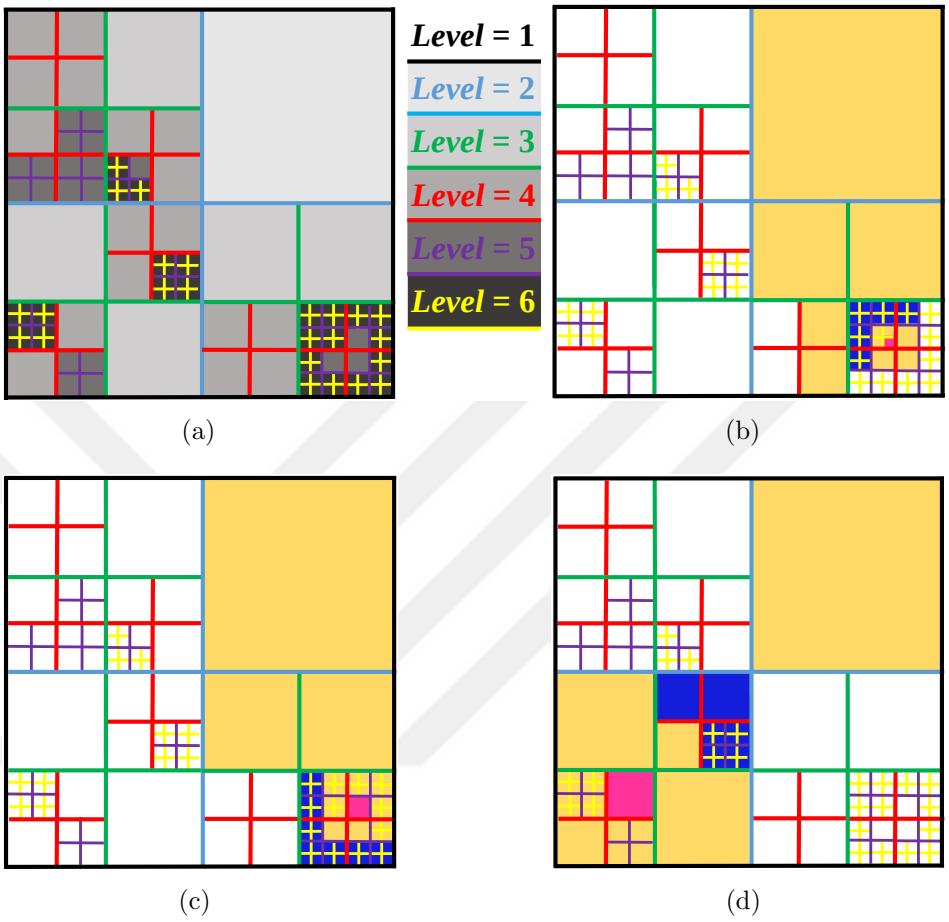


Figure 7.4: (a) 2-D view of a nonuniform clustering where the darker regions correspond to the denser discretizations. (b-d) Several representations of near-field and far-field boxes of different testing boxes colored in pink.

$\langle \nabla.\boldsymbol{t}_m, g, \sigma_{k_a} \rangle$ must be in $\bar{\boldsymbol{\Gamma}}^F_{\boldsymbol{J},\sigma}$ (and $\langle \sigma_{m_b}, g, \nabla'.\boldsymbol{b}_k \rangle$ and $\langle \sigma_{k_a}, g, \nabla'.\boldsymbol{b}_m \rangle$ must be in $\bar{\boldsymbol{\Gamma}}^F_{\sigma,\boldsymbol{J}}$). However, $\langle \nabla.\boldsymbol{t}_k, g, \sigma_{m_a} \rangle$ and $\langle \nabla.\boldsymbol{t}_m, g, \sigma_{k_b} \rangle$ must be in $\bar{\boldsymbol{\Gamma}}^N_{\boldsymbol{J},\sigma}$ (and $\langle \sigma_{m_a}, g, \nabla'.\boldsymbol{b}_k \rangle$ and $\langle \sigma_{k_b}, g, \nabla'.\boldsymbol{b}_m \rangle$ must be in $\bar{\boldsymbol{\Gamma}}^N_{\sigma,\boldsymbol{J}}$).

After organizing all types of interactions, matrices with high degree of sparsity are calculated for all near-field submatrices in (7.1). The pseudocode shown in Algorithm 2 in Appendix A shows all key steps of this implementation.

Regarding the far-field interactions, incomplete-tree structures are used in conjunction with the mixed-form MLFMA, which uses NSPWMLFMA at the LF regime (i.e., for box sizes smaller than $\lambda/8$). Therefore, aggregation, translation, and disaggregation at LF differ from those presented in [73]. Algorithm 3 and Algorithm 4

in Appendix A present the important features of aggregation and translation operations in the LF regime, respectively. An algorithm similar to Algorithm 3 can be used for disaggregation in the LF regime. On the other hand, aggregation, translation, and disaggregation operations at the high frequency regime are similar to those presented in [73].

7.3 Numerical Results

Numerical results are presented to assess the efficiency/accuracy and memory requirements of the proposed IL-MLFMA for PIEs (referred to as PIE/IL-MLFMA) by means of both canonical (multiscale sphere) and real-life multiscale geometries. For comparison purpose, the analytical Mie series solutions (for sphere), the mixed-form MLFMA for PIEs that uses the conventional tree structure (referred to as PIE/mixed-form MLFMA) [78], and a commercial software Ansoft high-frequency structural simulator (HFSS) v 15.0.0 [123] are used. In all simulations both PIE/IL-MLFMA and PIE/mixed-form MLFMA use the same iterative solver (GMRES method with an error tolerance of 10^{-4}) and the same conventional MLFMA/NSPWMLFMA parameters (number of harmonics, number of interpolation points in θ and φ, etc.) as specified in [78] together with a second order Gaussian quadrature for the integration over the surfaces of triangles. Moreover, both MLFMA solvers use left and right preconditioners obtained via the incomplete lower upper decomposition (ILU) of the approximate near-field matrices of their own. However, because the definition of near-field boxes are significantly different for the conventional and incomplete-tree structures, the sparsity of these preconditioners also differ for PIE/mixed-form MLFMA and PIE/IL-MLFMA. Finally, all results are generated in MATLAB. All MLFMA results are obtained on a cluster of Intel® Xeon® X5472 processors with 3.00 GHz clock rate and 32 GB RAM. MoM results, which are used as reference results for multiscale PEC cone and NASA Almond geometries, are obtained on a cluster of Intel® Xeon® CLX6230 20-core processors with 2.10 GHz clock rate and 512 GB RAM.

Scattering from a λ diameter PEC sphere at 3 GHz, illuminated by an x-polarized uniform plane wave propagating along the z-direction, is used to assess the accuracy, efficiency, and memory requirements as well as the computational details of the

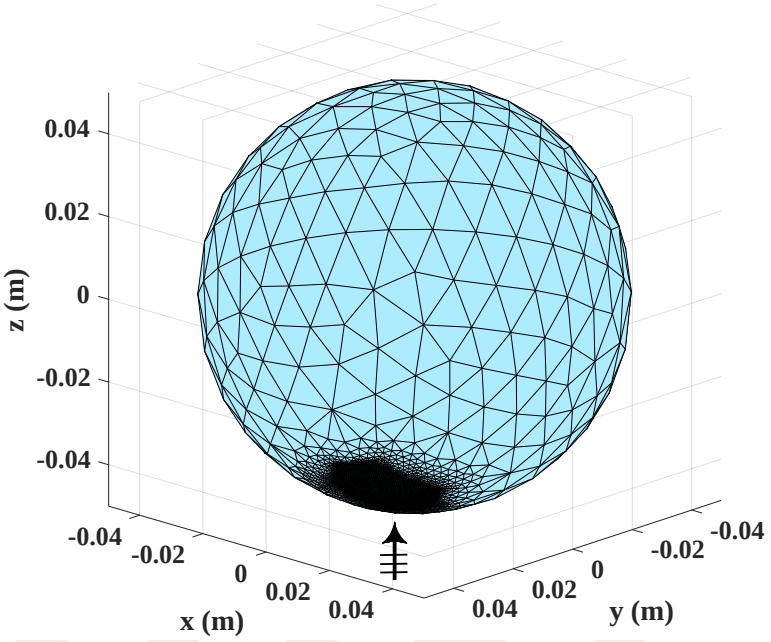


Figure 7.5: Geometry of nonuniformly discretized sphere with a multiscale factor of 100 possessing a dense discretization around the south pole.

PIE/IL-MLFMA. The sphere, as illustrated in Fig. 7.5, is meshed nonuniformly. It possesses a dense discretization around the south pole (edge size of triangles varies from 0.05 mm ($\lambda/2000$) at the south pole to 5 mm ($\lambda/20$) around the north pole) leading to a total number of 21850 unknowns. The results obtained via the PIE/IL-MLFMA are compared with those of the Mie series solution and the PIE/mixed-form MLFMA. The relative root mean square (RMS) error given by

$$\text{Relative RMS Error} = \sqrt{\frac{\sum_{i=1}^{N} \left| E_{\theta_i}^{\text{Sim}} - E_{\theta_i}^{\text{Ref}} \right|^2}{\sum_{i=1}^{N} \left| E_{\theta_i}^{\text{Ref}} \right|^2}}, \tag{7.4}$$

is used to determine the accuracy. In (7.4), $E_{\theta_i}^{\text{Sim}}$ and $E_{\theta_i}^{\text{Ref}}$ are the dominant θ components of the far-zone scattered electric field obtained via PIE/IL-MLFMA (or PIE/mixed-form MLFMA) and the Mie series solution, respectively.

Table 7.1 shows the run times, the relative RMS errors and the memory requirements of the PIE/IL-MLFMA for this PEC sphere geometry as a function MBP. Note that MBP automatically determines the deepest level attained by PIE/IL-MLFMA. The

same performance metrics of PIE/mixed-form MLFMA are also given as a function of level in the same table for comparison purposes. Similar to [73–76], the optimal MBP value is between 50 and 250 (for different problems) for the best efficiency, and this value may be changed if memory requirement is an issue. The memory requirement decreases significantly as the MBP decreases (from 7693 MByte to 22 MByte) in the expense of longer run times for very small MBP values. On the other hand, the error remains almost constant except a slight increase for very small MBP values that may not be preferred from the efficiency point of view. Also note that the incomplete tree construction time is negligible compared to the total run time.

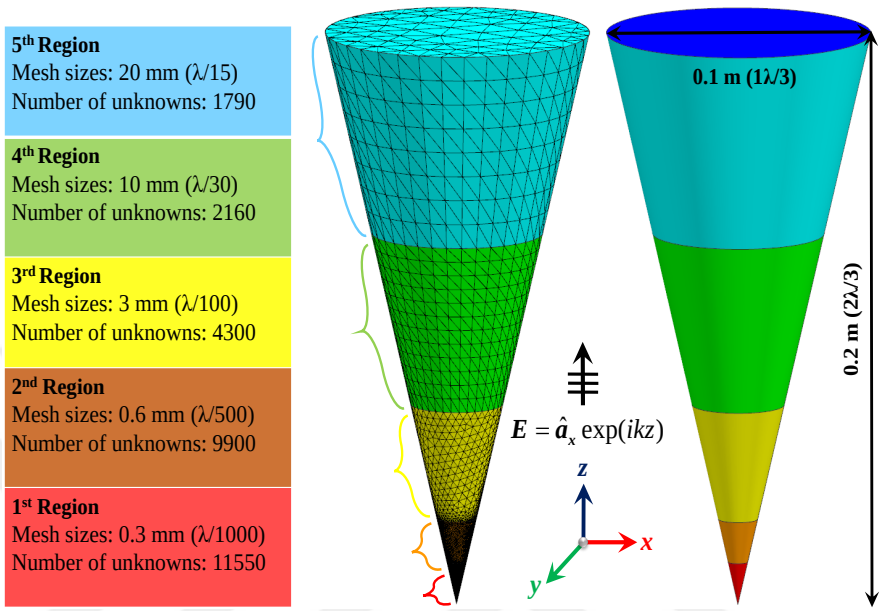
When we compare the performance of PIE/IL-MLFMA with that of PIE/mixed-form MLFMA, the followings are observed: If we use a 5-level PIE/mixed-form MLFMA, the relative RMS error is 0.55% (comparable to that of PIE/IL-MLFMA), the total run time is 6045 seconds and it requires 3414 MByte memory. If the number of level is increased to 6, the relative RMS error increases to 2.06% and the run time increases to 7742 seconds (run time increases as error grows due to convergence problems) while the required memory decreases to 2525 MByte. A 7-level PIE/mixed-form MLFMA does not work for this problem as seen from Table 7.1. On the other hand, the relative RMS error of PIE/IL-MLFMA for MBP = 60 is 0.47%, its run time is 4170 seconds and its memory requirement is only 439 MByte demonstrating the superiority of PIE/IL-MLFMA. Furthermore, if we sacrifice the efficiency and reduce MBP to 10, the run time becomes 6470 seconds, which is comparable to that of a 5-level PIE/mixed-form MLFMA, the relative RMS error remains as 0.47% but the required memory becomes only 47 MByte.

The far-zone scattered electric field (defined as the electric field intensity multiplied by the distance from the object when the distance goes to infinity), and the normalized near-zone electric field of a nonuniformly discretized PEC circular cone form the second numerical example. The cone has a radius of 5 cm and its height is 20 cm, as shown in Fig. 7.6(a), and is illuminated by an x-polarized uniform plane wave propagating along the z-direction at 1 GHz. It is discretized with 11880 triangles (resulting 29700 unknowns), where the size of triangles varies from $\lambda/1000$ at its apex to $\lambda/15$ at its flat base as can be seen from Fig. 7.6(a), where the number of unknowns and the corresponding mesh size at each region are also highlighted. Fig. 7.6(b) shows the far-zone scattered electric fields as functions of bistatic angle (θ) on the x-z plane ($\theta = 0^\circ$ and $\theta = 180^\circ$ represent the forward and backward

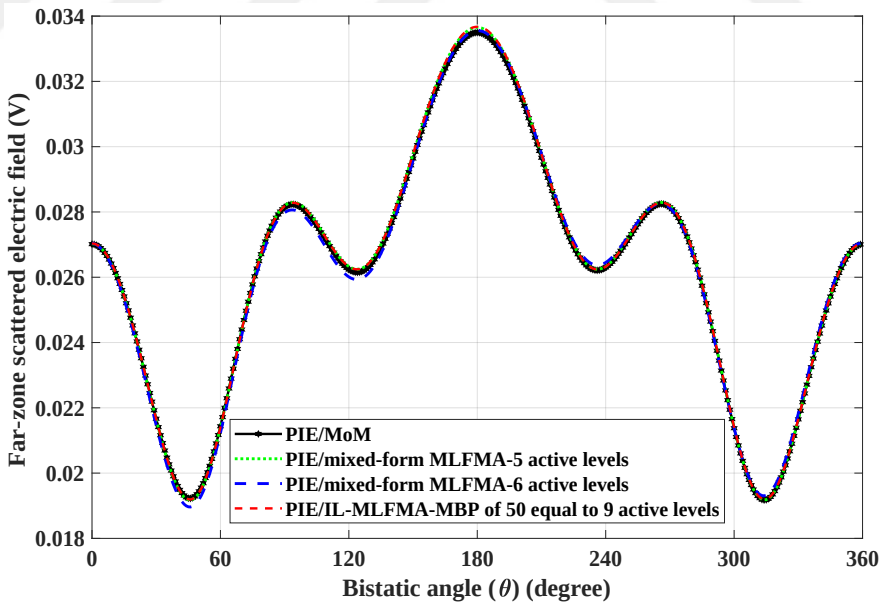
Table 7.1: Statistics for scattering simulations of a nonuniform discretized sphere with diameter of 10 cm and multiscale factor of 100 illuminated by an x-polarized uniform plane wave propagating along the z-direction at 3 GHz. Different number of RWGs populations (corresponding to the different simulation levels) are chosen for the simulation with error tolerance of 1e-4

Maximum Box Population	8000	6500	5000	3500	2000	1000	500	250	100	80	**60**	50	40	30	20	10	5
Number of Levels	3	5	**6**	**6**	**7**	8	8	9	10	10	**10**	11	11	11	11	12	13
Incomplete Tree Construction (s)	2	3	4	4	5	6	6	7	10	10	**10**	13	15	15	19	32	67
Near-field Construction (s)	4113	4113	4113	4113	4113	3682	1498	1321	969	714	**391**	350	305	227	216	232	566
Relative RMS Error for PIE/IL-MLFMA (%)	0.67	0.67	0.67	0.67	0.67	0.71	0.47	0.47	0.48	0.49	**0.49**	0.91	1.01	1.17	1.12	0.47	1.45
Total Run-time for PIE/IL-MLFMA (s)	9940	9940	9940	9940	9940	9710	6740	6610	6070	5390	**4170**	4210	4210	4370	4790	6470	14540
Total Memory Requirement for PIE/IL-MLFMA (MByte)	7639	7639	7639	7639	7639	6527	2543	2158	1457	1022	**519**	439	358	213	129	47	22
Relative RMS Error for PIE/mixed-form MLFMA (%)	0.5	**0.55**	**2.06**	**2.06**	**100.4**	–*	–	–	–	–	–	–	–	–	–	–	–
Total Run-time for PIE/mixed-form MLFMA (s)	7130	**6045**	**7742**	**7742**	**41713**	–	–	–	–	–	–	–	–	–	–	–	–
Total Memory Requirement for PIE/mixed-form MLFMA (MByte)	4686	**3414**	**2525**	**2525**	**1356**	–	–	–	–	–	–	–	–	–	–	–	–

* All hyphens '–' mean that the solver does not converge



(a)



(b)

Figure 7.6: (a) The geometry of PEC circular cone including the number of unknowns and mesh sizes for each colored region. (b) Far-zone scattered electric-field results obtained via PIE/MoM, PIE/mixed-form MLFMA and PIE/IL-MLFMA for the nonuniformly discretized PEC circular cone illuminated by an x-polarized uniform plane wave propagating along the z-direction at 1 GHz.

scattering directions, respectively) obtained via PIE/MoM (used as the reference solution), PIE/IL-MLFMA with MBP = 50 and PIE/mixed-form MLFMAs (5 and 6 levels). The far-zone relative RMS error (with respect to MoM) for PIE/IL-MLFMA is 0.42%. This number is 0.44% for the 5-level PIE/mixed-form MLFMA and it increases to 1.08% if a 6-level PIE/mixed-form MLFMA is used. A 7-level PIE/mixed-form MLFMA does not converge. As seen in Fig. 7.6(b), all results agree well with each other except small discrepancies in the 6-level PIE/mixed-form MLFMA results. If we look at the normalized near-zone electric fields for this geometry, as depicted in Fig. 7.7(a)-Fig. 7.7(d) [where the magnitudes of the total electric fields on the x-z plane, inside the PEC circular cone as well its vicinity, are illustrated (apex of the cone is assumed to be at the origin)], the near-zone relative RMS error for PIE/IL-MLFMA is 0.28% while it is 0.31% for the 5-level PIE/mixed-form MLFMA. However, this error increases to 11.75% if the level is increased to 6. As seen in Fig. 7.7(d) the 6-level PIE/mixed-form MLFMA suffers from inaccuracies especially at the flat base portion of the cone, where many of the larger basis functions (both RWGs and pulses) stick out from their parent boxes as the box size becomes smaller especially at the leaf level. On the other hand regarding the efficiency, PIE/IL-MLFMA is 3.48 times faster and requires nearly 21 times less memory than those of the 5-level PIE/mixed-form MLFMA, which is impressive. Furthermore, it is 1.4 times faster and requires 12 times less memory than those of 6-level PIE/mixed-form MLFMA despite the big difference in relative RMS errors (both near- and far-zone errors). Note that similar to the sphere example, by keeping the relative RMS error the same and sacrificing from the run time, memory requirement of PIE/IL-MLFMA can be decreased further.

A 2.5λ PEC NASA Almond geometry, illuminated by a pair of Hertzian dipoles at 5 GHz, as shown in Fig. 7.8 and Fig. 7.9, is our third numerical example. The geometry is located on the x-y plane and is discretized nonuniformly with a mesh size varying from $\lambda/675$ around the sharp tip and curved sides to $\lambda/15$ at smooth regions resulting a total number of 45650 unknowns. The first Hertzian dipole is located at $\boldsymbol{r'} = 4\lambda\left(\hat{\boldsymbol{a}}_x + \hat{\boldsymbol{a}}_z\right)$ (on the x-z plane) with a polarization $\hat{\boldsymbol{l}} = \left(-\hat{\boldsymbol{a}}_x + \hat{\boldsymbol{a}}_z\right)/\sqrt{2}$, and the second one is located at $\boldsymbol{r'} = 4\lambda\left(\hat{\boldsymbol{a}}_y + \hat{\boldsymbol{a}}_z\right)$ (on the y-z plane) with a polarization $\hat{\boldsymbol{l}} = \left(-\hat{\boldsymbol{a}}_y + \hat{\boldsymbol{a}}_z\right)/\sqrt{2}$. These Hertzian dipoles are expected to create stronger fields (and hence stronger surface currents) on the NASA Almond's surface. The far-zone scattered electric-field components, E_θ and E_ϕ, obtained via PIE/MoM, PIE/IL-MLFMA with MBP = 50 (deepest level = 10) and 5-level PIE/mixed-form

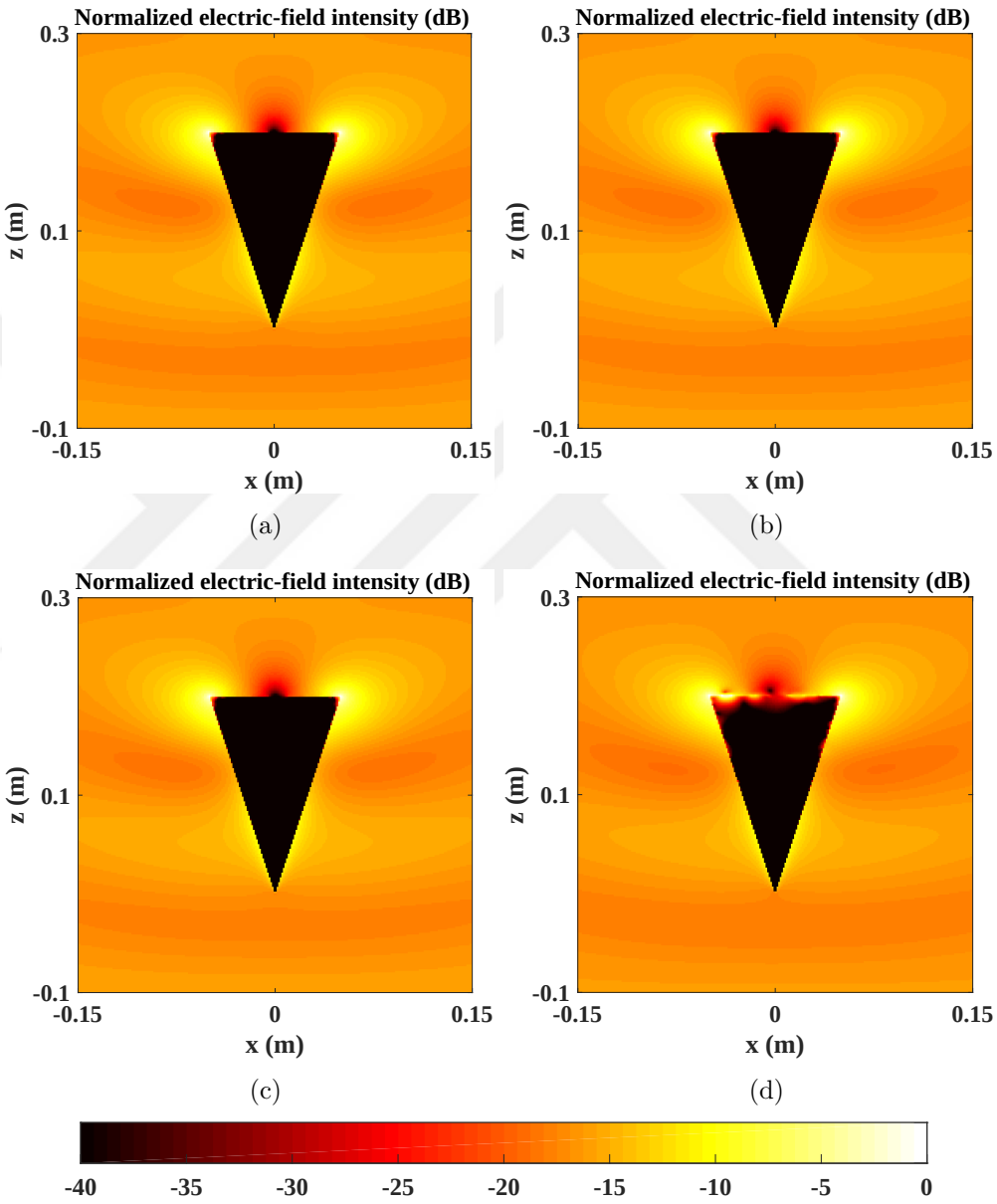


Figure 7.7: Normalized electric-field intensities in dB on the x-z plane for the circular cone geometry with the plane-wave illumination at 1 GHz. The near-field results are obtained via (a) PIE/MoM, (b) PIE/IL-MLFMA with MBP of 50 (corresponding to 9 active levels), (c) 5-level PIE/mixed-form MLFMA, and (d) 6-level PIE/mixed-form MLFMA.

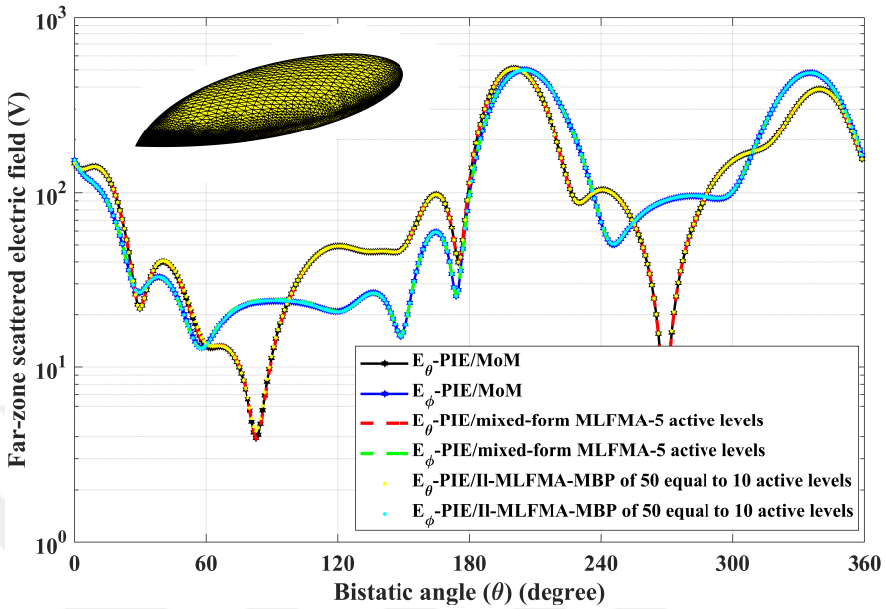


Figure 7.8: Far-zone scattered electric-field results obtained by using PIE/MoM, PIE/mixed-form MLFMA and PIE/IL-MLFMA for the nonuniformly discretized NASA Almond geometry illuminated by two Hertzian dipoles at 5 GHz.

MLFMA are presented with respect to the bistatic angle (θ) on the x-z plane in Fig. 7.8. Both PIE/IL-MLFMA and PIE/mixed-form MLFMA results agree well with the reference PIE/MoM results as seen in Fig. 7.8. The far-zone relative RMS error for both PIE/IL-MLFMA and the 5-level PIE/mixed-form MLFMA is approximately 0.32%. If we use a 6-level PIE/mixed-form MLFMA, this error increases to 1.41%, which is still reasonable, but a 7-level PIE/mixed-form MLFMA does not converge. Fig. 7.9(a)-Fig. 7.9(d) show the current distribution on this NASA Almond geometry obtained via PIE/MoM, PIE/IL-MLFMA, 5-level PIE/mixed-form MLFMA, and 6-level PIE/mixed-form MLFMA, respectively. The relative RMS current error for PIE/IL-MLFMA and the 5-level PIE/mixed-form MLFMA is again nearly the same, 2.2%. This error increases to 8.7% and exhibits itself in the form of discontinuities in Fig. 7.9(d) when a 6-level PIE/mixed-form MLFMA is used. On the other hand, PIE/IL-MLFMA requires nearly one-tenth of the memory that 5-level PIE/mixed-form MLFMA requires, and it is nearly 4 times faster. Even if we sacrifice from the accuracy and use the 6-level PIE/mixed-form MLFMA, it still requires 4.6 times more memory and is slightly slower (1.2 times slower) than PIE/IL-MLFMA.

An antenna problem, namely a cavity backed slot antenna based on the substrate

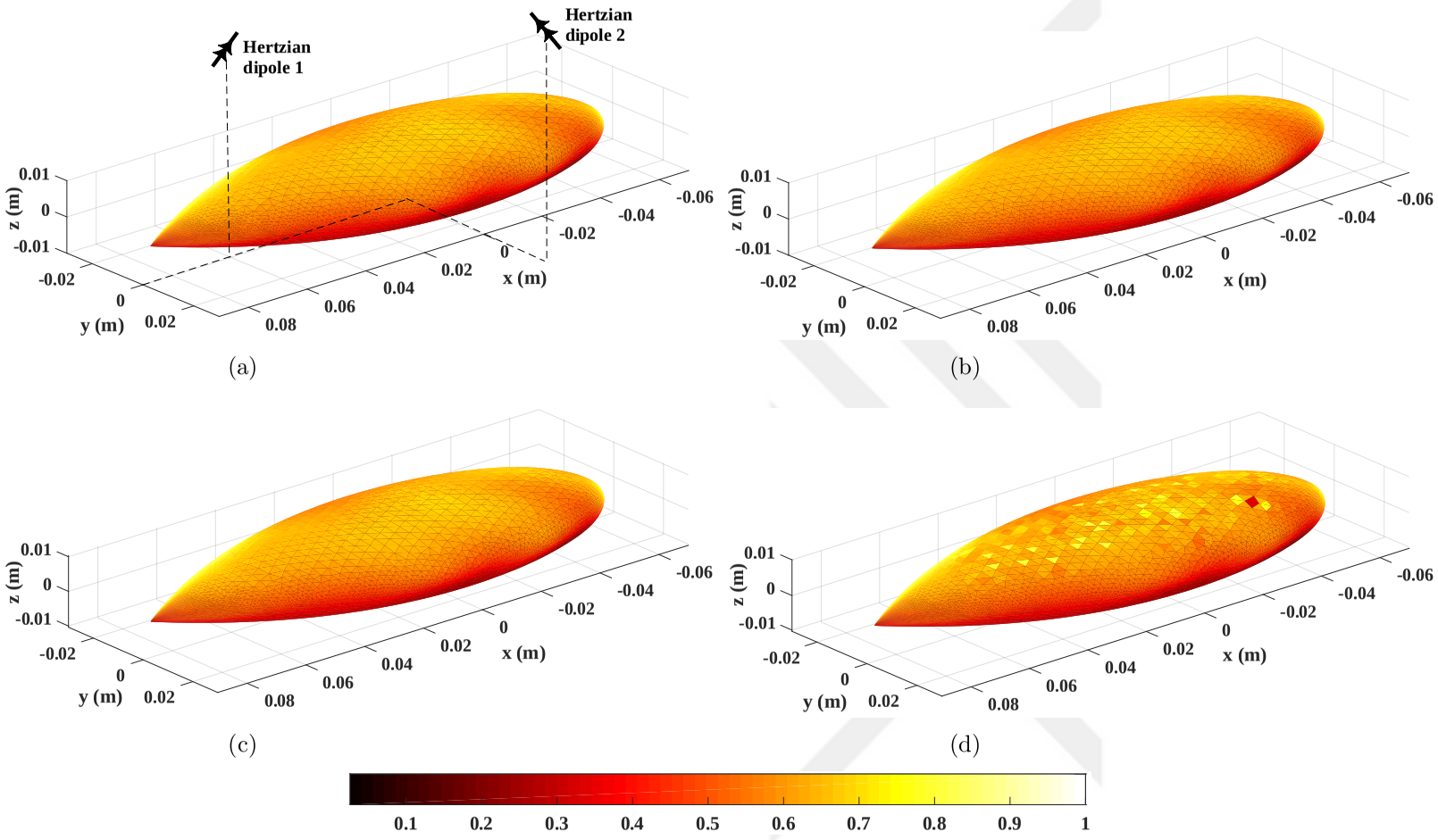


Figure 7.9: (a) Absolute value of the normalized current distributions over the nouniformly discretized NASA Almond geometry at 5 GHz excited by a pair of Hertzian Dipoles. The results are obtained by using (a) PIE/MoM, (b) PIE/IL-MLFMA, (c) 5-level PIE/mixed-form MLFMA, and (d) 6-level PIE/mixed-form MLFMA.

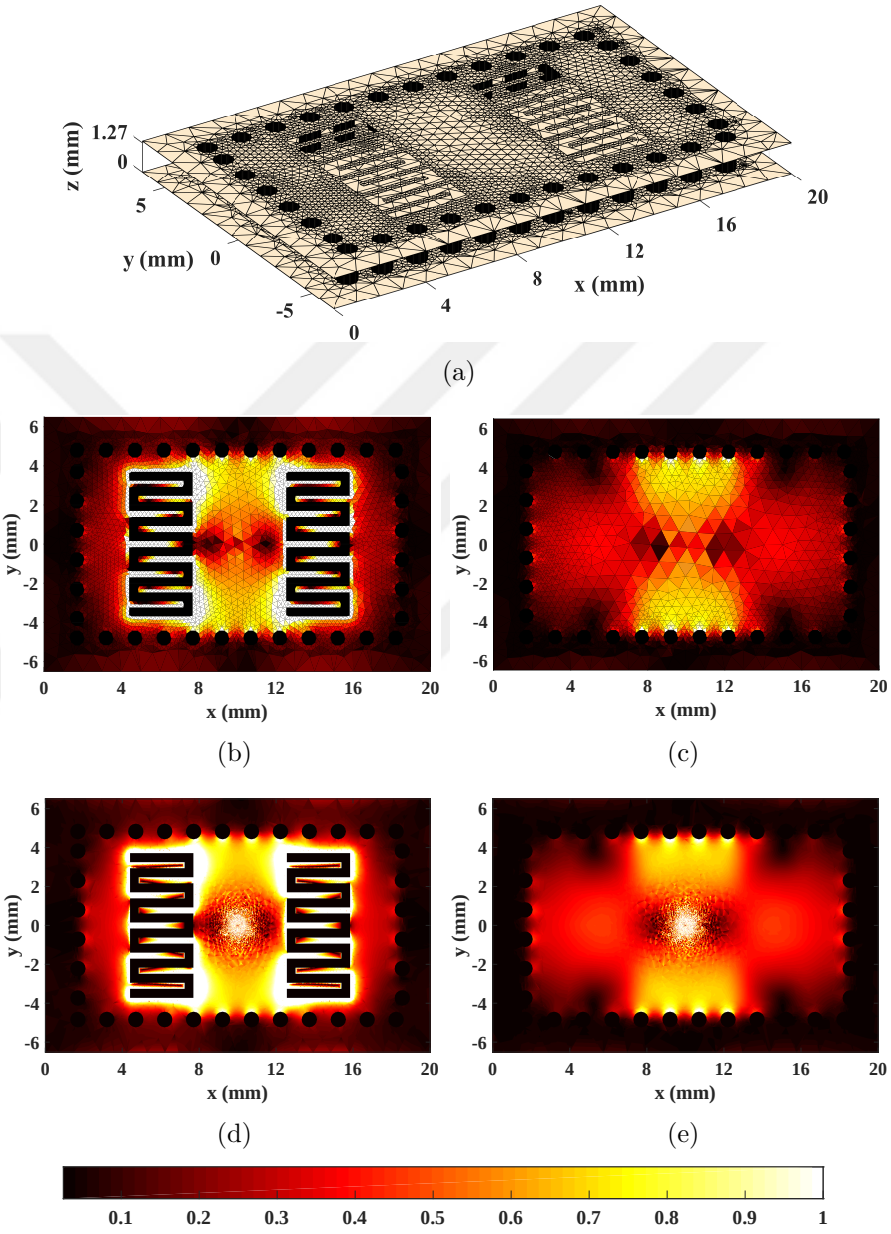


Figure 7.10: (a) A cavity-backed slot antenna based on the SIW technology excited by a Hertzian dipole located in the middle of the structure. Absolute value of the normalized current distributions on the (b) top and (c) bottom surfaces obtained via PIE/IL-MLFMA, and the same current distributions on the (d) top and (e) bottom surfaces of the antenna obtained by using HFSS at 9 GHz. (f) Normalized radiation patterns with respect to θ when $\phi = 0$, and π (i.e., over x-z plane) obtained via PIE/IL-MLFMA and FEM.

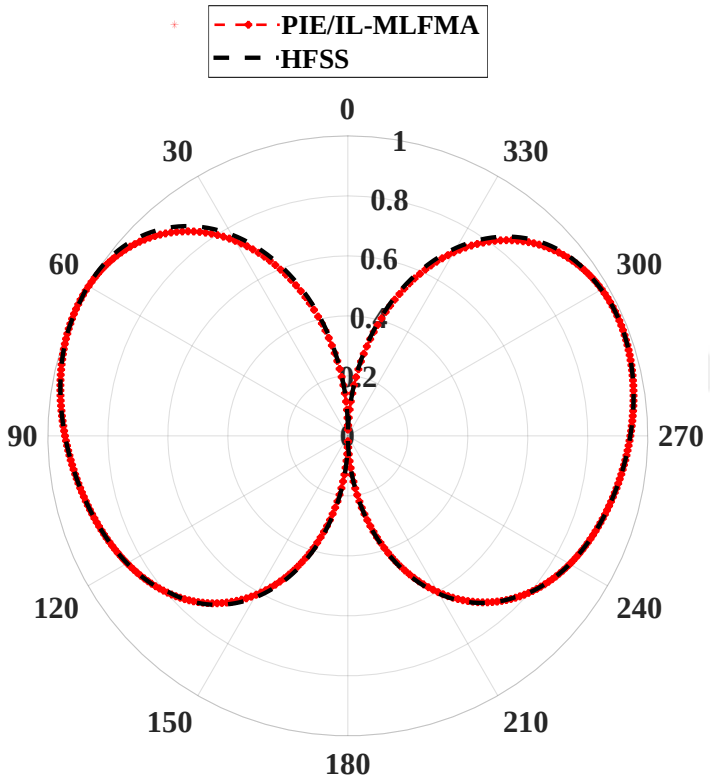
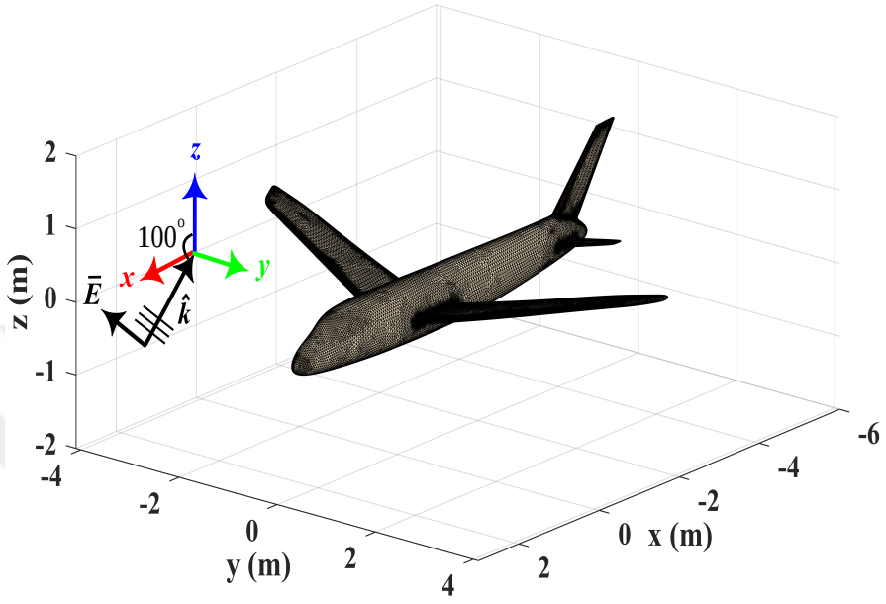
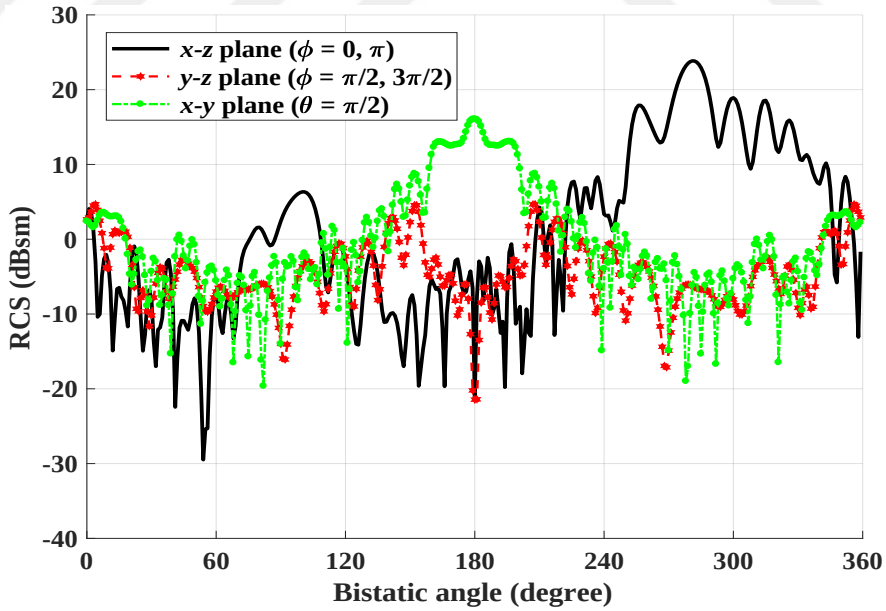


Figure 7.11: Normalized radiation patterns with respect to θ when $\phi = 0$, and π (i.e., over x-z plane) obtained via PIE/IL-MLFMA and FEM.



(a)



(b)

Figure 7.12: (a) A nonuniformly discretized $16\lambda \times 16\lambda \times 3.8\lambda$ airplane illuminated by a uniform plane wave propagating parallel to the x-z plane (with an angle of incidence 100° with respect to the z-axis) at 600 MHz. (b) RCS (in dBsm) patterns of this airplane at x-z, y-z and x-y planes.

integrated waveguide (SIW) technology [124–126], as shown in Fig. 7.10(a), is considered as the next numerical example. The geometry is taken from [127] with the same dimensions except the dielectric substrate is replaced by air. The antenna is excited via a z-directed Hertzian dipole, located in the middle of the structure, and the operating frequency is 9 GHz. The metallic vias and the inter-digital capacitor slots on the top surface of the structure are densely discretized with a mesh size of 0.04 mm and the mesh size is gradually increased to 2 mm for flat parts leading to a total number of 82040 unknowns. Fig. 7.10(b) and Fig. 7.10(c) present the absolute value of the normalized current distributions on the top and bottom surfaces, respectively, obtained via PIE/IL-MLFMA with MBP = 50. The same type results obtained via a finite element method based commercial software HFSS are shown in Fig. 7.10(d) and Fig. 7.10(e). Good agreement between these results also demonstrates the accuracy of PIE/IL-MLFMA. The radiation pattern of this antenna on the x-z plane obtained via both PIE/IL-MLFMA and HFSS are depicted in Fig. 7.11, where an excellent agreement can be seen.

Our final numerical example is the radar-cross-section (RCS) of a $16\lambda \times 16\lambda \times 3.8\lambda$ airplane, as illustrated in Fig. 7.12(a), which is illuminated by a uniform plane wave at 600 MHz. The incident plane wave is propagating parallel to the x-z plane with an angle of incidence 100° with respect to the z-axis. The airplane is discretized with 80476 triangles leading to a total number of 201190 unknowns. Fig. 7.12(b) shows the RCS (in dBsm) obtained via PIE/IL-MLFMA versus bistatic angle (280° being the forward and 100° being the backward scattering directions) at three different planes. The symmetry in x-y and y-z planes agree with our expectations.

Chapter 8

Conclusion and Future Work

8.1 Conclusion

In this thesis, we introduce a state-of-the-art algorithm and develop a broadband electromagnetic solver that enables us to investigate real-life multiscale problems including open surfaces and/or closed objects in an efficient and accurate way. As a first step, we propose a method to solve densely discretized PEC objects over a wide frequency range including low frequencies by incorporating a mixed-form MLFMA with the recently introduced PIEs. The proposed mixed-form MLFMA uses NSPWMLFMA at lower frequencies (i.e., at the deeper levels in the tree structures when the box sizes are less than $\lambda/8$) and the conventional MLFMA for middle/higher frequencies. NSPWMLFMA is preferred in this thesis due to its error controllability, and suitability for being combined with the conventional MLFMA to obtain a robust broadband mixed-form MLFMA solver for $\boldsymbol{A}-\Phi$ formulations which are also demonstrated to be very successful in handling the low-frequency problems. Consequently, the proposed method does not suffer from the LF-breakdown problem of the conventional MLFMA and SIEs. The accuracy of the proposed method in terms of scattered fields and current distribution are verified for various canonical and non-canonical geometries by comparing the numerical results with the ones obtained via analytical and MoM solutions, respectively. Furthermore, the efficiency of the proposed algorithm with an $\mathcal{O}(NL)$ complexity is demonstrated at different frequencies for various geometries.

Stable computations of near- and far-field interactions can be performed via PIEs

and the proposed mixed-form MLFMA. However, the method utilizes the standard tree structure with fixed-size boxes and regular division of parent boxes into at most eight subboxes, and thus the method can be inaccurate or inefficient for multiscale structures where capturing the fine but important features of structures requires nonuniform discretization. Meanwhile, uniform discretization of such kind of structures leads to very tiny triangular meshes which increases the required number of unknowns tremendously. Accordingly, in the second step, a modified incomplete tree structures are used in conjunction with the proposed mixed-form MLFMA for the solution of PIEs leading to an algorithm that can perform an accurate and efficient analysis of electromagnetic scattering/radiation for multiscale open and closed objects. The presented algorithm is population based and deploys nonuniform clustering for multiscale geometries that are often modeled by using highly variable discretizations. However, it is significantly modified from its predecessor by introducing pruned boxes, and reorganizing box-to-box as well as near- and far-field interactions in order to be combined with PIEs, which include both RWG and pulse basis functions. Numerical results obtained from the scattering/radiation analysis of canonical and real-life multiscale geometries clearly demonstrate the superiority of the algorithm. It is accurate, where the error is controllable, and is very efficient in terms of run-time and especially memory requirements, where more than an order of magnitude saving in memory can be achieved.

8.2 Future Work

PIEs are suffered from the spurious internal resonance problem when applied to perfect electric conducting bodies with closed surfaces and electrical dimension of bigger than the operating wavelength. In this case, MoM solutions of PIEs lead to singular matrices, and hence, nontrivial solutions introduce errors on the near-field results. The internal resonance problem of PIEs can be alleviated by linear combination of PIEs and MFIE where the boundary conditions are enforced for the scalar potential and both tangential components of the total magnetic vector potential and the magnetic field. However, even with this solution, the internal resonance problem of PIEs is not eliminated completely, and solutions of PIEs at resonant frequencies are problematic and require more investigations. As a future work, dual-surface PIEs can be a promising research topic for solving the internal resonance problem of PIEs.

Bibliography

[1] R. F. Harrington, *Time-harmonic electromagnetic fields*. Wiley-IEEE Press, 1961.

[2] C. A. Balanis, *Advanced engineering electromagnetics*. John Wiley & Sons, 2012.

[3] R. F. Harrington, *Field computation by moment methods*. Wiley-IEEE Press, 1993.

[4] W. C. Gibson, *The method of moments in electromagnetics*. CRC press, 2014.

[5] Ö. Ergül and L. Gürel, *The multilevel fast multipole algorithm (MLFMA) for solving large-scale computational electromagnetic problems*. IEEE Press, 2014.

[6] W. C. Chew, E. Michielssen, J. Song, and J.-M. Jin, *Fast and efficient algorithms in computational electromagnetics*. Artech House, Inc., 2001.

[7] A. Taflove and S. C. Hagness, *Computational electrodynamics: the finite-difference time-domain method*. Artech house, 2005.

[8] J.-M. Jin, *The finite element method in electromagnetics*. John Wiley & Sons, 2015.

[9] J. Zhu, S. Omar, and D. Jiao, "Solution of the electric field integral equation when it breaks down," *IEEE Transactions on Antennas and Propagation*, vol. 62, no. 8, pp. 4122–4134, 2014.

[10] J.-S. Zhao and W. C. Chew, "Integral equation solution of maxwell's equations from zero frequency to microwave frequencies," *IEEE Transactions on Antennas and Propagation*, vol. 48, no. 10, pp. 1635–1645, 2000.

[11] M. E. Bautista, M. A. Francavilla, F. Vipiana, and G. Vecchi, "A hierarchical fast solver for EFIE-MoM analysis of multiscale structures at very low frequencies,"

IEEE Transactions on Antennas and Propagation, vol. 62, no. 3, pp. 1523–1528, 2014.

[12] Y. Zhang, T. J. Cui, W. C. Chew, and J.-S. Zhao, "Magnetic field integral equation at very low frequencies," *IEEE Transactions on Antennas and Propagation*, vol. 51, no. 8, pp. 1864–1871, 2003.

[13] K. Cools, F. P. Andriulli, D. De Zutter, and E. Michielssen, "Accurate and conforming mixed discretization of the MFIE," *IEEE Antennas and Wireless Propagation Letters*, vol. 10, pp. 528–531, 2011.

[14] L. Gürel and Ö. Ergül, "Singularity of the magnetic-field integral equation and its extraction," *IEEE Antennas and Wireless Propagation Letters*, vol. 4, pp. 229–232, 2005.

[15] Ö. Ergül and L. Gürel, "Solid-angle factor in the magnetic-field integral equation," *Microwave and Optical Technology Letters*, vol. 45, no. 5, pp. 452–456, 2005.

[16] Ö. Ergül and L. Gürel, "Improved testing of the magnetic-field integral equation," *IEEE Microwave and Wireless Components Letters*, vol. 15, no. 10, pp. 615–617, 2005.

[17] K. Cools, F. P. Andriulli, F. Olyslager, and E. Michielssen, "Nullspaces of MFIE and Calderón preconditioned EFIE operators applied to toroidal surfaces," *IEEE Transactions on Antennas and Propagation*, vol. 57, no. 10, pp. 3205–3215, 2009.

[18] V. Rokhlin, "Rapid solution of integral equations of classical potential theory," *Journal of computational physics*, vol. 60, no. 2, pp. 187–207, 1985.

[19] R. Coifman, V. Rokhlin, and S. Wandzura, "The fast multipole method for the wave equation: A pedestrian prescription," *IEEE Antennas and Propagation Magazine*, vol. 35, no. 3, pp. 7–12, 1993.

[20] W. C. Chew, J.-M. Jin, C.-C. Lu, E. Michielssen, and J. M. Song, "Fast solution methods in electromagnetics," *IEEE Transactions on Antennas and Propagation*, vol. 45, no. 3, pp. 533–543, 1997.

[21] J. Carrier, L. Greengard, and V. Rokhlin, "A fast adaptive multipole algorithm for particle simulations," *SIAM Journal on Scientific and Statistical Computing*, vol. 9, no. 4, pp. 669–686, 1988.

[22] J.-S. Zhao and W. C. Chew, "Applying matrix rotation to the three-dimensional low-frequency multilevel fast multipole algorithm," *Microwave and Optical Technology Letters*, vol. 26, no. 2, pp. 105–110, 2000.

[23] J. Zhao and W. C. Chew, "Applying LF–MLFMA to solve complex pec structures," *Microwave and Optical Technology Letters*, vol. 28, no. 3, pp. 155–160, 2001.

[24] L. J. Jiang and W. C. Chew, "A mixed-form fast multipole algorithm," *IEEE Transactions on Antennas and Propagation*, vol. 53, no. 12, pp. 4145–4156, 2005.

[25] C.-C. Lu and W. C. Chew, "A multilevel algorithm for solving a boundary integral equation of wave scattering," *Microwave and Optical Technology Letters*, vol. 7, no. 10, pp. 466–470, 1994.

[26] J. M. Song and W. C. Chew, "Multilevel fast-multipole algorithm for solving combined field integral equations of electromagnetic scattering," *Microwave and Optical Technology Letters*, vol. 10, no. 1, pp. 14–19, 1995.

[27] S. Velamparambil, W. C. Chew, and J. Song, "10 million unknowns: is it that big?[computational electromagnetics]," *IEEE Antennas and Propagation Magazine*, vol. 45, no. 2, pp. 43–58, 2003.

[28] K. C. Donepudi, J.-M. Jin, and W. C. Chew, "A higher order multilevel fast multipole algorithm for scattering from mixed conducting/dielectric bodies," *IEEE Transactions on Antennas and Propagation*, vol. 51, no. 10, pp. 2814–2821, 2003.

[29] Ö. Ergül and B. Karaosmanoğlu, "Broadband multilevel fast multipole algorithm based on an approximate diagonalization of the Green's function," *IEEE Transactions on Antennas and Propagation*, vol. 63, no. 7, pp. 3035–3041, July 2015.

[30] B. Dembart and E. Yip, "The accuracy of fast multipole methods for maxwell's equations," *IEEE Computational Science and Engineering*, vol. 5, no. 3, pp. 48–56, 1998.

[31] C. A. Balanis, *Antenna theory: analysis and design*. John wiley & sons, 2016.

[32] A. Sadeghi-Tarakameh, A. Torrado-Carvajal, R. L. Lagore, S. Moen, X. Wu, G. Adriany, G. J. Metzger, L. DelaBarre, K. Ugurbil, E. Atalar, *et al.*, "Toward

human head imaging at 10.5 T using an eight-channel transmit/receive array of bumped fractionated dipoles," in *Proceedings of the 27th Annual Meeting of ISMRM, Montreal, QC, Canada*, p. 430, 2019.

[33] A. Etminan, A. Sadeghi, and L. Gürel, "Electromagnetic imaging of three-dimensional dielectric objects with newton minimization," in *2014 IEEE Antennas and Propagation Society International Symposium (APSURSI)*, pp. 876–877, IEEE, 2014.

[34] P. Goktas, I. O. Sukharevsky, S. Larkin, F. A. Kuypers, O. Yalcin, and A. Altintas, "Image-based flow cytometry and angle-resolved light scattering to define the sickling process," *Cytometry Part A*, vol. 95, no. 5, pp. 488–498, 2019.

[35] P. Goktas, I. O. Sukharevsky, S.-J. Jang, S.-H. Yun, and A. Altintas, "Cell morphology-based classification in red blood cells by angle-resolved electromagnetic scattering approach," in *2018 IEEE International Symposium on Antennas and Propagation & USNC/URSI National Radio Science Meeting*, pp. 19–20, IEEE, 2018.

[36] P. Goktas, I. O. Sukharevsky, and A. Altintas, "Electromagnetic scattering by several 2-D single biological cell models," in *2018 United States National Committee of URSI National Radio Science Meeting (USNC-URSI NRSM)*, pp. 1–2, IEEE, 2018.

[37] E. Kazemivalipour, A. Sadeghi-Tarakameh, and E. Atalar, "Eigenmode analysis of the scattering matrix for the design of mri transmit array coils," *Magnetic Resonance in Medicine*, 2020.

[38] E. Kazemivalipour, J. Vu, S. Lin, B. Bhusal, B. T. Nguyen, J. Kirsch, B. Elahi, J. Rosenow, E. Atalar, and L. Golestanirad, "RF heating of deep brain stimulation implants during MRI in 1.2 T vertical scanners versus 1.5 T horizontal systems: A simulation study with realistic lead configurations," in *2020 42nd Annual International Conference of the IEEE Engineering in Medicine & Biology Society (EMBC)*, pp. 6143–6146, IEEE, 2020.

[39] L. Golestanirad, E. Kazemivalipour, D. Lampman, H. Habara, E. Atalar, J. Rosenow, J. Pilitsis, and J. Kirsch, "RF heating of deep brain stimulation implants in open-bore vertical MRI systems: A simulation study with realistic

device configurations," *Magnetic Resonance in Medicine*, vol. 83, no. 6, pp. 2284–2292, 2020.

[40] L. Golestanirad, E. Kazemivalipour, B. Keil, S. Downs, J. Kirsch, B. Elahi, J. Pilitsis, and L. L. Wald, "Reconfigurable MRI coil technology can substantially reduce RF heating of deep brain stimulation implants: First in-vitro study of RF heating reduction in bilateral dbs leads at 1.5 T," *PloS one*, vol. 14, no. 8, p. e0220043, 2019.

[41] E. Kazemivalipour, B. Keil, A. Vali, S. Rajan, B. Elahi, E. Atalar, L. L. Wald, J. Rosenow, J. Pilitsis, and L. Golestanirad, "Reconfigurable MRI technology for low-SAR imaging of deep brain stimulation at 3T: Application in bilateral leads, fully-implanted systems, and surgically modified lead trajectories," *NeuroImage*, vol. 199, pp. 18–29, 2019.

[42] A. Sadeghi-Tarakameh, G. Adriany, G. J. Metzger, R. L. Lagore, S. Jungst, L. DelaBarre, P.-F. Van de Moortele, K. Ugurbil, E. Atalar, and Y. Eryaman, "Improving radiofrequency power and specific absorption rate management with bumped transmit elements in ultra-high field MRI," *Magnetic Resonance in Medicine*, 2020.

[43] A. Sadeghi-Tarakameh, A. Torrado-Carvajal, C. Ariyurek, E. Atalar, G. Adriany, G. J. Metzger, R. L. Lagore, L. DelaBarre, A. Grant, P.-F. Van de Moortele, *et al.*, "Optimizing the topography of transmit coils for SAR management," in *Proceedings of the 26th Joint Annual Meeting of ISMRM-ESMRMB, Paris, France*, p. 297, 2018.

[44] A. Sadeghi-Tarakameh, X. Wu, F. Ulus, Y. Eryaman, and E. Atalar, "Ultimate intrinsic specific absorption rate efficiency," in *Proceedings of the 27th Annual Meeting of ISMRM, Montreal, QC, Canada*, p. 4166, 2019.

[45] A. Sadeghi-Tarakameh, E. Kazemivalipour, T. Demir, U. Gundogdu, and E. Atalar, "Accelerating the co-simulation method for fast design of transmit array coils: An example study on a degenerate birdcage coil," in *Proceedings of the 26th Joint Annual Meeting of ISMRM-ESMRMB, Paris, France*, p. 4404, 2018.

[46] A. Sadeghi-Tarakameh, E. Kazemivalipour, U. Gundogdu, S. Erdogan, and E. Atalar, "Accelerating the co-simulation method for the design of transmit

array coils for MRI," *Magnetic Resonance Materials in Physics, Biology and Medicine*, pp. 1–14, 2020.

[47] A. Sadeghi-Tarakameh, L. DelaBarre, R. L. Lagore, A. Torrado-Carvajal, X. Wu, A. Grant, G. Adriany, G. J. Metzger, P.-F. Van de Moortele, K. Ugurbil, *et al.*, "In vivo human head MRI at 10.5 T: A radiofrequency safety study and preliminary imaging results," *Magnetic Resonance in Medicine*, vol. 84, no. 1, pp. 484–496, 2020.

[48] A. Sadeghi-Tarakameh, S. Jungst, X. Wu, M. Lanagan, G. Adriany, G. J. Metzger, P.-F. Van de Moortele, K. Ugurbil, E. Atalar, and Y. Eryaman, "A new coil element for highly-dense transmit arrays: An introduction to non-uniform dielectric substrate (nodes) antenna," in *Proceedings of the 27th Annual Meeting of ISMRM, Montreal, Canada*, p. 732, 2019.

[49] W. C. Chew, "Vector potential electromagnetics with generalized gauge for inhomogeneous media: Formulation," *Progress In Electromagnetics Research*, vol. 149, pp. 69–84, 2014.

[50] Q. S. Liu, S. Sun, and W. C. Chew, "A vector potential integral equation method for electromagnetic scattering," in *2015 31st International Review of Progress in Applied Computational Electromagnetics (ACES)*, pp. 1–2, IEEE, 2015.

[51] Q. S. Liu, S. Sun, and W. C. Chew, "An integral equation method based on vector and scalar potential formulations," in *2015 IEEE International Symposium on Antennas and Propagation & USNC/URSI National Radio Science Meeting*, pp. 744–745, IEEE, 2015.

[52] Q. S. Liu, S. Sun, and W. C. Chew, "A potential-based integral equation method for low-frequency electromagnetic problems," *IEEE Transactions on Antennas and Propagation*, vol. 66, no. 3, pp. 1413–1426, 2018.

[53] I. Bogaert, J. Peeters, and F. Olyslager, "A nondirective plane wave MLFMA stable at low frequencies," *IEEE Transactions on Antennas and Propagation*, vol. 56, no. 12, pp. 3752–3767, 2008.

[54] I. Bogaert and F. Olyslager, "A low frequency stable plane wave addition theorem," *Journal of Computational Physics*, vol. 228, no. 4, pp. 1000–1016, 2009.

[55] I. Bogaert, J. Peeters, and D. De Zutter, "Error control of the vectorial nondirective stable plane wave multilevel fast multipole algorithm," *Progress In Electromagnetics Research*, vol. 111, pp. 271–290, 2011.

[56] B. Khalichi, Ö. Ergül, and V. B. Ertürk, "Error analysis of QR-decomposition-based nondirective stable plane wave MLFMA," in *2018 IEEE AP-S Symposium on Antennas and Propagation & USNC-URSI Radio Science Meeting*, 2018.

[57] L. Greengard, J. Huang, V. Rokhlin, and S. Wandzura, "Accelerating fast multipole methods for the helmholtz equation at low frequencies," *IEEE Computational Science and Engineering*, vol. 5, no. 3, pp. 32–38, 1998.

[58] J.-S. Zhao and W. C. Chew, "Three-dimensional multilevel fast multipole algorithm from static to electrodynamic," *Microwave and Optical Technology Letters*, vol. 26, no. 1, pp. 43–48, 2000.

[59] L. Jiang and W. C. Chew, "Low-frequency fast inhomogeneous plane-wave algorithm LF-FIPWA," *Microwave and Optical Technology Letters*, vol. 40, no. 2, pp. 117–122, 2004.

[60] E. Darve and P. Havé, "Efficient fast multipole method for low-frequency scattering," *Journal of Computational Physics*, vol. 197, no. 1, pp. 341–363, 2004.

[61] E. Darve and P. Havé, "A fast multipole method for maxwell equations stable at all frequencies," *Philosophical Transactions of the Royal Society of London. Series A: Mathematical, Physical and Engineering Sciences*, vol. 362, no. 1816, pp. 603–628, 2004.

[62] H. Wallen and J. Sarvas, "Translation procedures for broadband MLFMA," *Progress In Electromagnetics Research*, vol. 55, pp. 47–78, 2005.

[63] D. T. Schobert and T. F. Eibert, "Low-frequency surface integral equation solution by multilevel Green's function interpolation with fast fourier transform acceleration," *IEEE Transactions on Antennas and Propagation*, vol. 60, no. 3, pp. 1440–1449, 2012.

[64] W.-B. Kong, H.-X. Zhou, K.-L. Zheng, and W. Hong, "Analysis of multiscale problems using the MLFMA with the assistance of the FFT-based method," *IEEE Transactions on Antennas and Propagation*, vol. 63, no. 9, pp. 4184–4188, 2015.

[65] H. Cheng, L. Greengard, and V. Rokhlin, "A fast adaptive multipole algorithm in three dimensions," *Journal of computational physics*, vol. 155, no. 2, pp. 468–498, 1999.

[66] B. Shanker, A. A. Ergin, M. Lu, and E. Michielssen, "Fast analysis of transient electromagnetic scattering phenomena using the multilevel plane wave time domain algorithm," *IEEE Transactions on Antennas and Propagation*, vol. 51, no. 3, pp. 628–641, 2003.

[67] H. Cheng, W. Y. Crutchfield, Z. Gimbutas, L. F. Greengard, J. F. Ethridge, J. Huang, V. Rokhlin, N. Yarvin, and J. Zhao, "A wideband fast multipole method for the helmholtz equation in three dimensions," *Journal of Computational Physics*, vol. 216, no. 1, pp. 300–325, 2006.

[68] M. Vikram and B. Shanker, "Fast evaluation of time domain fields in sub-wavelength source/observer distributions using accelerated cartesian expansions (ACE)," *Journal of Computational Physics*, vol. 227, no. 2, pp. 1007–1023, 2007.

[69] M. Vikram, H. Huang, B. Shanker, and T. Van, "A novel wideband FMM for fast integral equation solution of multiscale problems in electromagnetics," *IEEE Transactions on Antennas and Propagation*, vol. 57, no. 7, pp. 2094–2104, 2009.

[70] M. Vikram, B. Shanker, S. Seal, and S. Aluru, "A scalable parallel wideband MLFMA for efficient electromagnetic simulations on large scale clusters," *IEEE Transactions on Antennas and Propagation*, vol. 59, no. 7, pp. 2565–2577, 2011.

[71] S. Hughey, H. Aktulga, M. Vikram, M. Lu, B. Shanker, and E. Michielssen, "Parallel wideband MLFMA for analysis of electrically large, nonuniform, multiscale structures," *IEEE Transactions on Antennas and Propagation*, vol. 67, no. 2, pp. 1094–1107, 2019.

[72] W.-B. Kong, H.-X. Zhou, W.-D. Li, G. Hua, and W. Hong, "The MLFMA equipped with a hybrid tree structure for the multiscale EM scattering," *International Journal of Antennas and Propagation*, vol. 2014, pp. 1–6, 2014.

[73] M. Takrimi, Ö. Ergül, and V. B. Ertürk, "A novel broadband multilevel fast multipole algorithm with incomplete-leaf tree structures for multiscale electromagnetic problems," *IEEE Transactions on Antennas and Propagation*, vol. 64, no. 6, pp. 2445–2456, 2016.

[74] M. Takrimi, Ö. Ergül, and V. B. Ertürk, "A broadband multilevel fast multipole algorithm with incomplete-leaf tree structures for multiscale electromagnetic problems," in *2016 10th European Conference on Antennas and Propagation (EuCAP)*, pp. 1–2, Apr. 2016.

[75] Ö. Ergül, B. Karaosmanoğlu, M. Takrimi, and V. B. Ertürk, "Broadband multilevel fast multipole algorithm for large-scale problems with nonuniform discretizations," in *2016 URSI International Symposium on Electromagnetic Theory (EMTS)*, pp. 284–287, Aug. 2016.

[76] M. Takrimi, Ö. Ergül, and V. B. Ertürk, "Incomplete-leaf multilevel fast multipole algorithm for multiscale penetrable objects formulated with volume integral equations," *IEEE Transactions on Antennas and Propagation*, vol. 65, no. 9, pp. 4914–4918, Sept. 2017.

[77] B. Khalichi, Ö. Ergül, M. Takrimi, and V. B. Ertürk, "Solution of potential integral equations with NSPWMLFMA," in *2018 IEEE AP-S Symposium on Antennas and Propagation and USNC-URSI Radio Science Meeting*, 2018.

[78] B. Khalichi, Ö. Ergül, and V. B. Ertürk, "Broadband solutions of potential integral equations with NSPWMLFMA," *IEEE Transactions on Antennas and Propagation*, vol. 67, no. 6, pp. 4307–4312, 2019.

[79] B. Khalichi, V. B. Ertürk, and Ö. Ergül, "Fast solutions of multiscale electromagnetic problems using potential integral equations," in *2020 IEEE AP-S Symposium on Antennas and Propagation and USNC-URSI Radio Science Meeting*, 2020.

[80] B. Khalichi, Ö. Ergül, M. Takrimi, and V. B. Ertürk, "Broadband analysis of multiscale electromagnetic problems: Novel incomplete-leaf MLFMA for potential integral equations," *Submitted to IEEE Transactions on Antennas and Propagation*, 2020.

[81] W. C. Chew, M. S. Tong, and B. Hu, "Integral equation methods for electromagnetic and elastic waves," *Synthesis Lectures on Computational Electromagnetics*, vol. 3, no. 1, pp. 1–241, 2008.

[82] F. P. Andriulli, K. Cools, I. Bogaert, and E. Michielssen, "On a well-conditioned electric field integral operator for multiply connected geometries," *IEEE Transactions on Antennas and Propagation*, vol. 61, no. 4, pp. 2077–2087, 2012.

[83] G. Vecchi, "Loop-star decomposition of basis functions in the discretization of the EFIE," *IEEE Transactions on Antennas and Propagation*, vol. 47, no. 2, pp. 339–346, 1999.

[84] J.-F. Lee, R. Lee, and R. J. Burkholder, "Loop star basis functions and a robust preconditioner for efie scattering problems," *IEEE Transactions on Antennas and Propagation*, vol. 51, no. 8, pp. 1855–1863, 2003.

[85] F. P. Andriulli, F. Vipiana, and G. Vecchi, "Hierarchical bases for nonhierarchic 3-d triangular meshes," *IEEE Transactions on Antennas and Propagation*, vol. 56, no. 8, pp. 2288–2297, 2008.

[86] J. Peeters, K. Cools, I. Bogaert, F. Olyslager, and D. De Zutter, "Embedding calderón multiplicative preconditioners in multilevel fast multipole algorithms," *IEEE Transactions on Antennas and Propagation*, vol. 58, no. 4, pp. 1236–1250, 2010.

[87] S. Sun, Y. G. Liu, W. C. Chew, and Z. Ma, "Calderón multiplicative preconditioned EFIE with perturbation method," *IEEE Transactions on Antennas and Propagation*, vol. 61, no. 1, pp. 247–255, 2012.

[88] M. Taskinen and P. Yla-Oijala, "Current and charge integral equation formulation," *IEEE Transactions on Antennas and Propagation*, vol. 54, no. 1, pp. 58–67, 2006.

[89] M. Taskinen and S. Vänskä, "Current and charge integral equation formulations and picard's extended maxwell system," *IEEE Transactions on Antennas and Propagation*, vol. 55, no. 12, pp. 3495–3503, 2007.

[90] Z.-G. Qian and W. C. Chew, "Fast full-wave surface integral equation solver for multiscale structure modeling," *IEEE Transactions on Antennas and Propagation*, vol. 57, no. 11, pp. 3594–3601, 2009.

[91] Z.-G. Qian and W. C. Chew, "Enhanced A-EFIE with perturbation method," *IEEE Transactions on Antennas and Propagation*, vol. 58, no. 10, pp. 3256–3264, 2010.

[92] S. Yan, J.-M. Jin, and Z. Nie, "Analysis of electrically large problems using the augmented EFIE with a calderón preconditioner," *IEEE Transactions on Antennas and Propagation*, vol. 59, no. 6, pp. 2303–2314, 2011.

[93] A. Das and D. Gope, "Modified separated potential integral equation for low-frequency EFIE conditioning," *IEEE Transactions on Antennas and Propagation*, vol. 64, no. 4, pp. 1394–1403, 2016.

[94] A. Farshkaran and O. Ergül, "Equivalence principle algorithm for potential integral equations," in *2018 International Conference on Electromagnetics in Advanced Applications (ICEAA)*, pp. 189–192, IEEE, 2018.

[95] A. Farshkaran and Ö. Ergül, "Numerical implementation of equivalence principle algorithm for potentials," in *2018 IEEE International Symposium on Antennas and Propagation & USNC/URSI National Radio Science Meeting*, pp. 2405–2406, IEEE, 2018.

[96] A. Farshkaran and Ö. Ergül, "Implementation of the equivalence principle algorithm for potential integral equations," *IEEE Transactions on Antennas and Propagation*, vol. 67, no. 5, pp. 3249–3255, 2019.

[97] M. Kalfa, Ö. Ergül, and V. B. Ertürk, "Error control of multiple-precision MLFMA," *IEEE Transactions on Antennas and Propagation*, vol. 66, no. 10, pp. 5651–5656, 2018.

[98] M. Kalfa, O. Ergül, and V. B. Ertürk, "Error control in MLFMA with multiple-precision arithmetic," in *12th European Conference on Antennas and Propagation (EuCAP 2018), 2018 page*, pp. 286–288, IET, 2018.

[99] M. Kalfa, V. B. Ertürk, and Ö. Ergül, "Error control of MLFMA within a multiple-precision arithmetic framework," in *2018 IEEE International Symposium on Antennas and Propagation & USNC/URSI National Radio Science Meeting*, pp. 2299–2300, IEEE, 2018.

[100] L. Xuan, A. Zhu, R. Adams, and S. Gedney, "A broadband multilevel fast multipole algorithm," in *IEEE antennas and propagation society symposium (June 20-25, 2004, Monterey, California)*, pp. 1195–1198, 2004.

[101] H. Shao, J. Hu, Z. Nie, and L. Jiang, "Simulation of multiscale structures using equivalence principle algorithm with grid-robust higher order vector basis," *J. Electromagn. Waves and Appl.*, vol. 28, no. 11, pp. 1333–1346, 2014.

[102] Z. Nie, W. Ma, Y. Ren, Y. Zhao, J. Hu, and Z. Zhao, "A wideband electromagnetic scattering analysis using MLFMA with higher order hierarchical

vector basis functions," *IEEE Transactions on Antennas and Propagation*, vol. 57, no. 10, pp. 3169–3178, 2009.

[103] X. Zhao, H. Zhang, Y. Zhang, T. K. Sarkar, and S.-W. Ting, "Efficient modeling of multiscale structures using higher-order method of moments," *IEEE J. Multiscale Multiphys. Comput. Tech.*, vol. 2, pp. 78–83, 2017.

[104] Y.-N. Liu, X.-M. Pan, and X.-Q. Sheng, "Skeletonization accelerated MLFMA solution of volume integral equation for plasmonic structures," *IEEE Transactions on Antennas and Propagation*, vol. 66, no. 3, pp. 1590–1594, 2018.

[105] C. Wang, Z. Jiang, X. Qiao, and T. Wan, "Efficient performance of MLSSM-MLFMA algorithm using adaptive grouping technique for electromagnetic problems," *IEEE Transactions on Antennas and Propagation*, vol. 66, no. 1, pp. 493–496, 2017.

[106] X.-M. Pan, J.-G. Wei, Z. Peng, and X.-Q. Sheng, "A fast algorithm for multiscale electromagnetic problems using interpolative decomposition and multilevel fast multipole algorithm," *Radio Science*, vol. 47, no. 01, pp. 1–11, 2012.

[107] J.-G. Wei, Z. Peng, and J.-F. Lee, "Multiscale electromagnetic computations using a hierarchical multilevel fast multipole algorithm," *Radio Science*, vol. 49, no. 11, pp. 1022–1040, 2014.

[108] W. C. Chew and J. Song, "Gedanken experiments to understand the internal resonance problems of electromagnetic scattering," *Electromagnetics*, vol. 27, no. 8, pp. 457–471, 2007.

[109] U. M. Gür and Ö. Ergül, "Accuracy of sources and near-zone fields when using potential integral equations at low frequencies," *IEEE Antennas and Wireless Propagation Letters*, vol. 16, pp. 2783–2786, 2017.

[110] F. Vico, M. Ferrando, L. Greengard, and Z. Gimbutas, "The decoupled potential integral equation for time-harmonic electromagnetic scattering," *Communications on Pure and Applied Mathematics*, vol. 69, no. 4, pp. 771–812, 2016.

[111] S. Rao, D. Wilton, and A. Glisson, "Electromagnetic scattering by surfaces of arbitrary shape," *IEEE Transactions on Antennas and Propagation*, vol. 30, no. 3, pp. 409–418, 1982.

[112] C. H. Beentjes, "Quadrature on a spherical surface," *Working note available on the website http://people. maths. ox. ac. uk/beentjes/Essays*, 2015.

[113] D. Wilton, S. Rao, A. Glisson, D. Schaubert, O. Al-Bundak, and C. Butler, "Potential integrals for uniform and linear source distributions on polygonal and polyhedral domains," *IEEE Transactions on Antennas and Propagation*, vol. 32, no. 3, pp. 276–281, 1984.

[114] R. D. Graglia, "On the numerical integration of the linear shape functions times the 3-d green's function or its gradient on a plane triangle," *IEEE Transactions on Antennas and Propagation*, vol. 41, no. 10, pp. 1448–1455, 1993.

[115] R. Barrett, M. Berry, T. F. Chan, J. Demmel, J. Donato, J. Dongarra, V. Eijkhout, R. Pozo, C. Romine, and H. Van der Vorst, *Templates for the solution of linear systems: building blocks for iterative methods*. SIAM, 1994.

[116] M. R. Hestenes, E. Stiefel, *et al.*, "Methods of conjugate gradients for solving linear systems," *Journal of research of the National Bureau of Standards*, vol. 49, no. 6, pp. 409–436, 1952.

[117] C. F. Smith, A. F. Peterson, and R. Mittra, "The biconjugate gradient method for electromagnetic scattering," *IEEE Transactions on Antennas and Propagation*, vol. 38, no. 6, pp. 938–940, 1990.

[118] Y. Saad and M. H. Schultz, "GMRES: A generalized minimal residual algorithm for solving nonsymmetric linear systems," *SIAM Journal on scientific and statistical computing*, vol. 7, no. 3, pp. 856–869, 1986.

[119] T. Malas and L. Gürel, "Schur complement preconditioners for surface integral-equation formulations of dielectric problems solved with the multilevel fast multipole algorithm," *SIAM Journal on Scientific Computing*, vol. 33, no. 5, pp. 2440–2467, 2011.

[120] I. Bogaert, *Broadband multilevel fast multipole methods*. PhD thesis, Ghent University, 2008.

[121] M. Takrimi, *Implementation of a broadband multilevel fast multipole algorithm for multiscale electromagnetics problems*. PhD thesis, bilkent university, 2016.

[122] O. Luukkonen, M. G. Silveirinha, A. B. Yakovlev, C. R. Simovski, I. S. Nefedov, and S. A. Tretyakov, "Effects of spatial dispersion on reflection from

mushroom-type artificial impedance surfaces," *IEEE Transactions on Microwave Theory and Techniques*, vol. 57, no. 11, pp. 2692–2699, 2009.

[123] Ansoft HFSS $v15.0.0$, 2012, Pittsburgh, PA: Ansoft Corp.

[124] B. Khalichi, S. Nikmehr, and A. Pourziad, "Reconfigurable SIW antenna based on RF-MEMS switches," *Progress In Electromagnetics Research*, vol. 142, pp. 189–206, 2013.

[125] B. Khalichi, S. Nikmehr, A. Pourziad, and M. Ebrahimpouri, "Designing wideband tapered-slot antennas: A novel method using SIW technology," *IEEE Antennas and Propagation Magazine*, vol. 57, no. 3, pp. 60–70, 2015.

[126] B. Khalichi, S. Nikmehr, and A. Pourziad, "Development of novel wideband H-plane horn antennas by employing asymmetrical slots based on SIW technology," *AEU - International Journal of Electronics and Communications*, vol. 69, no. 9, pp. 1374–1380, 2015.

[127] Y. Dong and T. Itoh, "Miniaturized substrate integrated waveguide slot antennas based on negative order resonance," *IEEE Transactions on Antennas and Propagation*, vol. 58, no. 12, pp. 3856–3864, Dec. 2010.

Appendix A

The algorithms used for the fast and efficient solution of PIEs using IL-MLFMA are given below:

Algorithm 1: Identifying the Unique Triangle Population of each TB

UniqueTriPerLeafBox;
Input : Lists of TBs, OCBs, PBs, and Δs
Output : *UniqueTriPerLeafBox* := List of unique Δs per leaf boxes or TBs
forall Δs **do**
    Calculate midpoint of each examined Δ;
    foreach edge ∈ examined Δ **do**
        Calculate the distances between the centroid of the examined Δ and the center of the PBs containing the three edges;
    Find the shortest distance;
    Identify the PB that contains the examined Δ and construct new variable as *tri2prunedbox*;
Sort *tri2prunedbox* to have sorted locations of all Δs with new indices;
forall Δs **do**
    Find the total number of Δs inside each PB and identify first and last sorted indices of Δs in the corresponding PB;
forall TBs and OCBs **do**
    Find the total number of Δs inside all TBs and OCBs and identify first and last sorted indices of Δs in the corresponding boxes;
foreach *ExaminedBox* ∈ list of TBs **do**
    if ∼isempty (Number of Δs ∈ *ExaminedBox*) **then**
        Determine sorted indices of all Δs inside the *ExaminedBox*;
        Allocate real indices for each *ExaminedBox* to construct *UniqueTriPerLeafBox*;

Algorithm 2: Near-Field Sparse Matrix Calculation

```
1  constructnearfield-IL;
   Input  : IL-List of Near Field Boxes
   Output : Near-FieldSparseMatrix-(J, J), Near-FieldSparseMatrix-(J, σ),
            Near-FieldSparseMatrix-(σ, J), and Near-FieldSparseMatrix-(σ, σ)
2  foreach TestingBox ∈ TBs array do
3      NearBox-List = List of near boxes of the selected TestingBox;
4      NearTB-List = All TBs ∈ NearBox-List;
5      NearOCB-List = All TBs inside OCBs ∈ NearBox-List;
6      NearBox-List = NearTB-List ∪ NearOCB-List;
7      TestingTriList = List of all Δs in the selected TestingBox;
8      if ∼isempty(TestingTriList) then
9          foreach BasisBox ∈ NearBox-List do
10             if ∼isempty(BasisBox) then
11                 BasisTriList := List of all Δs in the selected BasisBox;
12                 if ∼isempty(BasisTriList) then
13                     foreach nonempty TestingTri ∈ TestingTriList do
14                         foreach nonempty BasisTri ∈ BasisTriList do
15                             Calculate the interaction between the TestingTri and BasisTri;
16                             forall the valid TestingFunctions do
17                                 forall the valid BasisFunctions do
18                                     Update Near-FieldSparseMatrix-(J, J);
19                 UniqueBasisTriList := List of all unique Δs in the selected BasisBox;
20                 if ∼isempty(UniqueBasisTriList) then
21                     foreach nonempty TestingTri ∈ TestingTriList do
22                         foreach nonempty BasisTri ∈ UniqueBasisTriList do
23                             Calculate the interaction between the TestingTri and BasisTri;
24                             forall the valid TestingFunctions do
25                                 Update Near-FieldSparseMatrix-(J, σ);
26             else
27                 Break;
28     UniqueTestingTriList := List of all unique Δs in the selected TestingBox;
29     if ∼isempty(UniqueTestingTriList) then
30         foreach BasisBox ∈ NearBox-List do
31             if ∼isempty(BasisBox) then
32                 BasisTriList := List of all Δs in the selected BasisBox;
33                 if ∼isempty(BasisTriList) then
34                     foreach nonempty TestingTri ∈ UniqueTestingTriList do
35                         foreach nonempty BasisTri ∈ BasisTriList do
36                             Calculate the interaction between the TestingTri and BasisTri;
37                             forall the valid BasisFunctions do
38                                 Update Near-FieldSparseMatrix-(σ, J);
39                 UniqueBasisTriList := List of all unique Δs in the selected BasisBox;
40                 if ∼isempty(UniqueBasisTriList) then
41                     foreach nonempty TestingTri ∈ UniqueTestingTriList do
42                         foreach nonempty BasisTri ∈ UniqueBasisTriList do
43                             Calculate the interaction between the TestingTri and BasisTri;
44                             Update Near-FieldSparseMatrix-(σ, σ);
45             else
46                 Break;
```

Algorithm 3: Aggregation in the Low Frequency Regime

AggregationVectors-LF;
Input : List of TBs and OCBs
Output : Aggregation-Vector-$(\boldsymbol{J},\boldsymbol{J})$, *Aggregation-Vector*-$(\boldsymbol{J},\sigma)$, *Aggregation-Vector*-$(\sigma,\boldsymbol{J})$, and *Aggregation-Vector*-(σ,σ)
foreach *level* $\in$ LF levels when $B_\lambda < \lambda/8$) **do**
  Determine the optimized number of harmonics [29] and the number of uniform integration points as explained in [53, 78];
  BasisBoxList = Concatenated list of the TBs and OCBs;
  foreach *BasisBox* $\in$ *BasisBoxList* **do**
    foreach *BasisFunction* $\in$ *BasisBox* **do**
      Determine *BasisTri* $\in$ examined *BasisFunction*;
      forall integration points over *BasisTri*s **do**
        foreach new (θ_i,φ_j) $i=1:N_\theta; j=1:N_\varphi$ obtained via QR-decomposition method **do**
          Update *Aggregation-Vector*-$(\boldsymbol{J},\boldsymbol{J})$;
          Update *Aggregation-Vector*-$(\sigma,\boldsymbol{J})$;
    UniqueBasisTriList := List of all unique Δs in the selected *BasisBox*;
    if $\sim$isempty(*UniqueBasisTriList*) **then**
      foreach *BasisTri* $\in$ *UniqueBasisTriList* **do**
        forall integration points over *BasisTri* **do**
          foreach new (θ_i,φ_j) $i=1:N_\theta; j=1:N_\varphi$ obtained via QR-decomposition method **do**
            Update *Aggregation-Vector*-$(\boldsymbol{J},\sigma)$;
            Update *Aggregation-Vector*-(σ,σ);

Algorithm 4: Translation in the Low Frequency Regime

TranslationVector-LF;
Input : Lists of TBs, OCBs, and FFBs (Far-field Boxes)
Output : *new-translationoperator-LF* := Translation operator in a vector format
foreach *level* $\in$ LF levels when $B_\lambda < \lambda/8$) **do**
  TestingBoxList = Concatenated list of the TBs and OCBs;
  foreach *TestingBox* $\in$ *TestingBoxList* **do**
    FFBList = List of FFBs of the examined *TestingBox*;
    foreach *Basisbox* $\in$ *FFBList* **do**
      if $\sim$isempty(*Basisbox*) **then**
        1) Find the translation distance between the examined *TestingBox* and *Basisbox*;
        2) Construct an index for the corresponding translation function;
  Apply QR-decomposition algorithm to obtain a new set of basis integration points for all discretized translation functions in the entire space in the selected level;
  foreach constructed index for the corresponding translation function **do**
    1) Calculate the rotation matrix for the translation function;
    2) Rotate the translation function along the z-direction;
    3) Calculate the Fourier spectrum of the rotated translation function along the z-directions;
    4) Shift the integration path to the comlex plane to include evanescent waves (normalize the Fourier coefficients);
    foreach (θ_i,φ_j) $i=1:N_\theta; j=1:N_\varphi$ **do**
      5) Calculate the discretized translation operator called as *translationoperator-LF*;
    6) Construct *new-translationoperator-LF* (based on eq. (10) in [78]) for the new set of basis integration points obtained via QR-decomposition method [53, 78];